

RADIOWAVE PROPAGATION IN THE POLAR IONOSPHERE

Thesis submitted for the degree of
Doctor of Philosophy
at the University of Leicester

by

Mariyam Jamilah Homam
Department of Engineering
University of Leicester

June 2011

Mariyam Jamilah Homam

Radiowave Propagation in the Polar Ionosphere

Abstract

A dual-frequency GPS receiver, GSV4004B, has been installed at Alert, Canada since May 2008 to study the ionospheric variability at a high-latitude location. This Ionospheric Scintillation and TEC Monitor (GISTM) receiver is able to measure amplitude and phase scintillation, and also Total Electron Content (TEC). In addition, a High Frequency (HF) link has been established from Qaanaaq to Svalbard since March 2009 to study the channel characteristics, including Doppler spreads. This study covers from end of May 2008 to February 2011 where it was mostly during the minimum state of solar activity. During the period of where both GISTM and HF data were available (i.e. March 2009-July 2010), data from both links are compared to see any relation between TEC variations and scintillation effects and also Doppler spreads. Data from the GISTM receivers at Svalbard were also utilised.

Winter months expectedly show lower mean vertical TEC (VTEC) than in other months. Higher mean VTEC was observed in 2010 that could be related to the increase of solar activity. In 2010, both small and large patches of moderate-high intensity were found to be more than twice as common in February and March than in other months. The difference in the occurrences of small patches between months of the same year was about 1-2% (for low intensity patches) and 1-10% (moderate-high intensity). This difference increased to 1-4% (low intensity) and 1-12% (moderate-high intensity) for large patches. UT dependence can be seen where ~80 large and ~300 small patches were identified ~1000 to 2000 UT from June to October in both 2008 and 2009, and they doubled in 2010. Amplitude scintillations index, S4 were very low where at least ~99% were between 0 and 0.1, which is insignificant. Meanwhile, phase scintillations index, σ_ϕ were from 0 to 0.1 rad for at least 93% of the time. The relationship of TEC fluctuations/increase and phase scintillations is complex. There are few events where phase scintillations occurred simultaneously with slant TEC increases, but this is not frequent. The magnitude of the irregularities was generally independent of geomagnetic indices, Interplanetary Magnetic Field (IMF) components, and local magnetic fields at Eureka and Resolute Bay.

Monthly upper decile of Doppler spreads generally varied from 1 to 5.5 Hz. High upper decile normally occurred from around September/October to March, from ~0000 to 1700 UT on 6.95 and 8.01 MHz. The hourly upper decile reached up to 7-8.5 Hz (6.95 MHz) and 7-9.5 Hz (8.01 MHz). Upper decile on these frequencies was mostly 0.5-4.5 Hz larger in October 2010-February 2011 than in the same months of the previous year which possibly related to the increase in solar activity. However, Doppler spreads were generally independent of independent of geomagnetic indices, IMF components, and local magnetic fields. The relation between the irregularities observed via transionospheric link and HF link is also complex. Large TEC fluctuations/increases and/or phase scintillations observed on satellite(s) close to HF midpoint may correspond to either small or large Doppler spreads.

Acknowledgements

Firstly, I extend my gratitude to The Almighty Allah, for giving me the strength to face all the obstacles and challenges in completing my study.

A huge thank to my supervisor, Prof. E.M. Warrington for his invaluable guidance, advice and support. I also thank my co-supervisor, Dr. A.J. Stocker for his aide and insightful comments. I gratefully thank Prof. F. Honary and Dr. D.R. Siddle for the constructive critiques they have made during the viva voce examination. I also appreciate all the help given by the members of Radio Systems Group.

I would also like to thank Universiti Tun Hussein Onn Malaysia and Ministry of Higher Education, Malaysia for giving me the opportunity to further my study and providing the scholarship. I would like to express my gratitude to the data providers from Istituto Nazionale di Geofisica e Vulcanologia (<http://www.eswua.ingv.it>), Space Physics Data Facility of Goddard Space Flight Center (<http://cdaweb.gsfc.nasa.gov>), and Natural Resources Canada (<http://www.geomag.nrcan.gc.ca>).

I also wish to thank my entire family for the encouragement, motivation and support. Not forgetting my best and closest friends who helped me a lot through the tough period of my life during the study. I also offer my regards to everyone else that supported me in any respect in order to successfully complete this thesis.

Lastly, and most importantly, my sincerest thank goes to my parents, Zainab Yusuf and Homam Md Som for their continuous prayers and unconditional love, and for believing in me. To them I dedicate this thesis.

List of Contents

Abstract	ii
Acknowledgements	iii
Chapter One: Introduction	1
Chapter Two: Review of Previous Works	8
2.1 Patches and Arcs	8
2.2 Phase and Amplitude Scintillations	25
2.3 HF Channel Characteristics at High Latitude	37
Chapter Three: Experimental Configuration	43
3.1 Transionospheric Link	46
3.2 HF Link	55
Chapter Four: Variations of TEC and Scintillations at Alert, Canada	58
4.1 TEC Variations	58
4.2 Amplitude Scintillations	68
4.3 Phase Scintillations	73
4.4 Geomagnetic Activity Dependence	79
4.5 Selected Events	97
4.6 Concluding Remarks	149
Chapter Five: Qaanaaq to Ny-Ålesund HF Link	161
5.1 Statistical Analysis of Doppler Spreads	161
5.2 Geomagnetic Activity Dependence	184
5.3 Concluding Remarks	194
Chapter Six: HF Link and Its Relations to Transionospheric Link	197
6.1 Selected Events	197

6.2	Concluding Remarks	262
	Chapter Seven: Summary	268
	References	275

List of Figures

Figure 1.1: Ionospheric regions (Source: <i>Davies</i> [1990]. Reproduced by permission of Institution of Engineering and Technology).....	2
Figure 1.2: Auroral oval on 24 May 2008. Location of Alert is superposed on the map (Source: http://sd-www.jhuapl.edu).....	5
Figure 1.3: Location of HF transmitter (Qaanaaq) and receiver (Ny-Ålesund), HF midpoint (indicated by the blue circle), and GPS receiver (Alert).....	6
Figure 2.1: Polar cap F region structures (Source: <i>Buchau et al.</i> [1983]).....	10
Figure 2.2: Patches identified on the virtual height plot at 4 MHz, critical frequencies, TEC measurements and horizontal drift velocity on 10 April 1998 (Source: <i>Breed et al.</i> [2002])	12
Figure 2.3: A polar map in magnetic coordinate and local time, centred at north magnetic pole. Locations of some polar stations are shown. An auroral oval at 0600 UT and $K_p = 4$ is also shown (Source: <i>McEwen and Harris</i> [1996])	14
Figure 2.4: Appearance of polar cap patches at Qaanaaq on 29 December 1989 and Sondrestromfjord on 20 November 1989. The scale for y-axis extends from 0 to 200×10^4 electron cm^{-3} (Source: <i>Dandekar</i> [2002]). The example shows patches determined using both the old baseline [<i>Dandekar and Bullett</i> , 1999], indicated by dashed curve and the new baseline	15
Figure 2.5: Seasonal behaviour of polar cap patches at Sondrestromfjord and Qaanaaq with respect to daily occurrence. The labels of the curves in each graph refer to levels exceeding the patch strengths. From left to right, the annual average SSN is 150, 125, 40, and 10, respectively (Source: <i>Dandekar</i> [2002]).....	16
Figure 2.6: Map of southern high-latitude GPS stations. The underlined names of stations indicated the station used in the study (Source: <i>Krankowski et al.</i> [2006]) ..	18
Figure 2.7: The magnetic activity at Mawson (the top panel) and the ROT occurrence (the lower panels) at different stations on 21–24 September 2001 for all individual satellite passes (Source: <i>Krankowski et al.</i> [2006])	20
Figure 2.8: Oblique ionogram recorded at Alert on 23 January 1996 (Source: <i>Rogers et al.</i> [2003] © IEE 2003)	22
Figure 2.9: Oblique ionogram recorded at Alert at 0115 UT on 24 February 1996 (Source: <i>Rogers et al.</i> [2003] © IEE 2003)	23
Figure 2.10: Simulated ionograms through the ionosphere containing patches (Source: <i>Zaalov</i> [2004]).....	24

Figure 2.11: Simulated ionograms through the ionosphere containing arcs (Source: <i>Zaalov</i> [2004])	25
Figure 2.12: Worst-case fading depths of scintillation at L-band during solar maximum and minimum (Source: <i>Davies</i> [1990]. Reproduced by permission of the Institution of Engineering and Technology)	26
Figure 2.13 Mean value of scintillation (in dB) observed at Thule for both quiet and disturbed magnetic activity periods in (a) winter (November-January), (b) spring (February-April), (c) summer (May-July), (d) fall (August-October) (Source: <i>Aarons et al.</i> [1981])	27
Figure 2.14: Percentage occurrence of scintillation greater than 6 dB for April-October 1975 (10.7 cm flux of ~45) and April-October 1979 (10.7 cm flux of ~150-225) for both quiet and disturbed magnetic conditions (Source: <i>Aarons et al.</i> [1981])	28
Figure 2.15: Thule scintillation intensity statistics at 250 MHz during 1979-1984 (Source: <i>Basu et al.</i> [1987] © 1987 IEEE)	30
Figure 2.16: Phase scintillation maps of all days (disturbed and quiet) and for each station separately. In grey is the quiet Feldstein oval (i.e. auroral activity, IQ=3), while in red is the disturbed oval (i.e. IQ=6) (Source: <i>Spogli et al.</i> [2009])	31
Figure 2.17: Contour plots of percentage occurrence of amplitude ($S_4 > 0.25$) and phase scintillation ($\sigma_\phi > 15^\circ$ (i.e. 0.26 rad) and 10° (0.17 rad)) as a function of corrected geomagnetic latitude and month for observations made at Ny-Ålesund and Larsemann Hills (Source: <i>Li et al.</i> [2010])	32
Figure 2.18: Percentage occurrence of amplitude ($S_4 > 0.25$) and phase scintillation ($\sigma_\phi > 15^\circ$ (i.e. 0.26 rad) and 10° (0.17 rad)) as a function of corrected geomagnetic (CGM) latitude and MLT observations made at Ny-Ålesund and Larsemann Hills (Source: <i>Li et al.</i> [2010])	33
Figure 2.19: Mean σ_ϕ for Resolute Bay from September 2008 to August 2009. Magnetic local midnight and noon at Resolute Bay is around 0710 and 1940 UT, respectively (Source: <i>Prikryl et al.</i> [2010])	35
Figure 2.20: Map showing the location of four Scandinavian stations. Approximate location of auroral oval during high geomagnetic activity is also illustrated in grey (Source: <i>Angling et al.</i> [1998])	39
Figure 2.21: Map showing the path from Isfjord to Cricklade and from Isfjord to Alert. Auroral oval location is also illustrated at 1500 UT with $K_p=3$ (Source: <i>Warrington et al.</i> [2006])	41
Figure 3.1: Daily Sunspot Number, SSN from June 2008 to February 2011 (Source: http://cdaweb.gsfc.nasa.gov)	44

Figure 3.2: Illustration of sunspot number for the last five cycles (Source: http://www.sidc.be)	44
Figure 3.3: Location of HF transmitter (Qaanaaq) and receiver (Ny-Ålesund), GPS receivers at Alert, Ny-Ålesund and Longyearbyen, and magnetic observatories at Eureka and Resolute Bay. The geomagnetic pole is indicated by the blue circle.	46
Figure 3.4: Geometry for the conversion from slant to vertical TEC (Source: <i>Nava</i> [2007])	48
Figure 3.5: σ_{ϕ} of code/carrier divergence versus corrected S4 for 24 May 2008.....	53
Figure 3.6: Plot of Doppler spreads on 8.01 MHz from 14 March 2009 to 28 February 2011 for various SNR.....	57
Figure 4.1: Hourly mean VTEC for every month from June 2008 to July 2010.....	59
Figure 4.2: Hourly mean vertical TEC values for each year	61
Figure 4.3: The number of occurrence of small patches ($0.2 < \text{ROTI} < 0.5$ (left) and $\text{ROTI} > 0.5$ (right)) in 5-minute interval	62
Figure 4.4: The number of occurrence of large patches ($0.2 < \text{ROTI} < 0.5$ (left) and $\text{ROTI} > 0.5$ (right)) in 30-minute interval	63
Figure 4.5: The percentage of occurrence of small patches ($0.2 < \text{ROTI} < 0.5$ (left) and $\text{ROTI} > 0.5$ (right)) in 5-minute interval.....	64
Figure 4.6: The percentage of occurrence of large patches ($0.2 < \text{ROTI} < 0.5$ (left) and $\text{ROTI} > 0.5$ (right)) in 30-minute interval.....	65
Figure 4.7: Number of 5–minute ROTI data for each month and degree of magnetic latitude (top), and the percentage of these data for which $0.2 < \text{ROTI} < 0.5$ (middle) and $\text{ROTI} > 0.5$ (bottom)	66
Figure 4.8: Number of 30–minute ROTI data for each month and degree of magnetic latitude (top), and the percentage of these data for which $0.2 < \text{ROTI} < 0.5$ (middle) and $\text{ROTI} > 0.5$ (bottom)	68
Figure 4.9: Plot of elevation angle versus S4 for all data $> 25^{\circ}$	70
Figure 4.10: Plot of the standard deviation of carrier/code divergence versus S4 for all data $> 25^{\circ}$	70
Figure 4.11: Percentage of occurrence of S4 for every month (a) June 2008 – June 2009 and (b) July 2009 - July 2010	71
Figure 4.12: Percentage of S4 values greater than 0.15 for every available month from June 2008 to July 2010.....	72

Figure 4.13: Percentage of occurrence of phase scintillations for every month (a) June 2008 – June 2009 and (b) July 2009 - July 2010	75
Figure 4.14: Hourly mean σ_ϕ for every month from June 2008 to July 2010	76
Figure 4.15: Percentage of σ_ϕ greater than 0.15 rad for every available month from June 2008 to July 2010	77
Figure 4.16: Number of all data (top) and percentage of $\sigma_\phi > 0.15$ rad (bottom) as a function of geomagnetic latitude and observed months	78
Figure 4.17 (i): (a) σ_ϕ , (b) STEC, (c) ROTI ₅ and (d) ROTI ₃₀ observed on each visible satellite on 5 April 2010 from 0600 to 1200 UT. Note the different values on y-axis for STEC, but grid scale is equal	81
Figure 4.18: Path of all visible satellites for every hour at 350 km ionospheric pierce point on 5 April 2010 from 0600 to 1200 UT. Number on the map refers to satellite number and also marks the start of the path for the period of observation.....	84
Figure 4.19: 1-minute IMF components on 5 April 2010	86
Figure 4.20: 1-minute variation data at (a) Eureka, and (b) Resolute Bay on 5 April 2010. The number at the top right of each frame is the mean of its respective component.....	86
Figure 4.21 (i): (a) σ_ϕ , (b) STEC, (c) ROTI ₅ and (d) ROTI ₃₀ observed on each visible satellite on 11 October 2008 from 1200 to 1800 UT	88
Figure 4.22: Path of all visible satellites for every hour at 350 km ionospheric pierce point on 11 October 2008 from 1200 to 1800 UT	92
Figure 4.23: 1-minute IMF components on 11 October 2008	93
Figure 4.24: : 1-minute variation data at (a) Eureka, and (b) Resolute Bay on 11 October 2008.....	93
Figure 4.25: Hourly IMF components, D_{st} and PC(N) indices, 3-hour K_p index, and daily SSN from 4 April to 12 April 2010 (Source: http://cdaweb.gsfc.nasa.gov).....	95
Figure 4.26: Hourly IMF components, D_{st} and PC(N) indices, 3-hour K_p index, and daily SSN from 24 October to 3 November 2003 (Source: http://cdaweb.gsfc.nasa.gov)	96
Figure 4.27: (a) σ_ϕ , (b) STEC, (c) ROTI ₅ and (d) ROTI ₃₀ observed on each visible satellite on 4 February 2009 from 0200 to 0400 UT. Short-period observations on any satellite from 0300 to 0400 UT are not shown.....	99
Figure 4.28: Path of all visible satellites for every hour between 0300 to 0400 UT on 4 February 2009	100

Figure 4.29: σ_ϕ , STEC, ROT, and ROTI for 5- and 30-min interval of PRN12 on 4 February 2009 from 0200 to 0400 UT. Paths of all visible satellites at 350 km are also shown.....	100
Figure 4.30: σ_ϕ , STEC, ROT, and ROTI for 5- and 30-min interval of PRN30 on 4 February 2009 from 0200 to 0400 UT. Paths of all visible satellites at 350 km are also shown.....	101
Figure 4.31: σ_ϕ , STEC, ROT, and ROTI for 5- and 30-min interval of PRN5 on 4 February 2009 from 0200 to 0400 UT. Paths of all visible satellites at 350 km are also shown.....	101
Figure 4.32: 1-minute IMF components from 1200 UT on 4 February 2009	102
Figure 4.33: 1-minute variation data at (a) Eureka, and (b) Resolute Bay on 4 February 2009	103
Figure 4.34: σ_ϕ , STEC, ROT, and ROTI for 5- and 30-min interval of PRN4 on 8 April 2009 from 1000 to 1300 UT. Paths of all visible satellites from 1100 to 1300 UT at 350 km are also shown	104
Figure 4.35: (a) σ_ϕ , (b) STEC, (c) ROTI ₅ and (d) ROTI ₃₀ observed on each visible satellite on 8 April 2009 from 1100 to 1300 UT. Short-period observations on any satellite are not shown.....	105
Figure 4.36: 1-minute IMF components on 8 April 2009.....	106
Figure 4.37: 1-minute variation data at (a) Eureka, and (b) Resolute Bay on 8 April 2009	106
Figure 4.38: σ_ϕ , STEC, ROT, and ROTI for 5- and 30-min interval of PRN10 on 11 October 2008 from 1400 to 1630 UT. Paths of all visible satellites from 1500 to 1600 UT at 350 km are also shown	108
Figure 4.39: σ_ϕ , STEC, ROT, and ROTI for 5- and 30-min interval of PRN13 on 11 October 2008 from 1200 to 1530 UT. Paths of all visible satellites from 1330 to 1500 UT at 350 km are also shown	108
Figure 4.40: (a) σ_ϕ , (b) STEC, (c) ROTI ₅ and (d) ROTI ₃₀ observed on each visible satellite on 15 February 2010 from 1600 to 2000 UT	110
Figure 4.41: Path of all visible satellites from 1800 to 1900 UT on 15 February 2010	111
Figure 4.42: σ_ϕ , STEC, ROT, and ROTI for 5- and 30-min interval of PRN24 on 15 February 2010 from 1630 to 1930 UT. Paths of all visible satellites from 1700 to 1900 UT at 350 km are also shown	111

Figure 4.43: σ_ϕ , STEC, ROT, and ROTI for 5- and 30-min interval of PRN7 on 15 February 2010 from 1630 to 1930 UT. Paths of all visible satellites from 1700 to 1900 UT at 350 km are also shown	112
Figure 4.44: σ_ϕ , STEC, ROT, and ROTI for 5- and 30-min interval of PRN8 on 15 February 2010 from 1730 to 2000 UT. Paths of all visible satellites from 1800 to 1930 UT at 350 km are also shown	112
Figure 4.45: 1-minute IMF components on 15 February 2010.....	113
Figure 4.46: 1-minute variation data at (a) Eureka, and (b) Resolute Bay on 15 February 2010	114
Figure 4.47: σ_ϕ , STEC, ROT, and ROTI for 5- and 30-min interval of PRN27 on 24 February 2010 from 2000 to 2330 UT. Paths of all visible satellites from 2000 to 2300 UT at 350 km are also shown	115
Figure 4.48 (i): (a) σ_ϕ , (b) STEC, (c) ROTI ₅ and (d) ROTI ₃₀ observed on each visible satellite on 24 February 2010 from 2000 to 2400 UT	116
Figure 4.49: σ_ϕ , STEC, ROT, and ROTI for 5- and 30-min interval of PRN28 on 11 March 2010 from 0600 to 1000 UT. Paths of all visible satellites at 350 km are also shown.....	118
Figure 4.50 (i): (a) σ_ϕ , (b) STEC, (c) ROTI ₅ and (d) ROTI ₃₀ observed on each visible satellite on 11 March 2010 from 0600 to 1000 UT	119
Figure 4.51: 1-minute IMF components on (a) 24 February 2010 and (b) 11 March 2010	121
Figure 4.52: 1-minute variation data at (a) Eureka, and (b) Resolute Bay on 24 February 2010	122
Figure 4.53: 1-minute variation data at (a) Eureka, and (b) Resolute Bay on 11 March 2010.....	123
Figure 4.54: (a) σ_ϕ , (b) STEC, (c) ROTI ₅ and (d) ROTI ₃₀ observed on each visible satellite on 26 January 2009 from 1600 to 1800 UT	125
Figure 4.55: Path for all visible satellites for every hour between 1600 and 1800 UT on 26 January 2009	126
Figure 4.56: σ_ϕ , STEC, ROT, and ROTI for 5- and 30-min interval of PRN5 on 26 January 2009 from 1500 to 1700 UT. Paths of all visible satellites between 1600 and 1700 UT at 350 km are also shown.....	127
Figure 4.57: σ_ϕ , STEC, ROT, and ROTI for 5- and 30-min interval of PRN12 on 26 January 2009 from 1500 to 1700 UT. Paths of all visible satellites between 1600 and 1700 UT at 350 km are also shown.....	127

Figure 4.58: 1-minute IMF components on 26 January 2009.....	128
Figure 4.59 : 1-minute variation data at (a) Eureka, and (b) Resolute Bay on 26 January 2009	129
Figure 4.60: σ_{ϕ} , STEC, ROT, and ROTI for 5- and 30-min interval of PRN3 on 3 December 2008 from 1200 to 1500 UT. Paths of all visible satellites between 1230 and 1330 UT at 350 km are also shown.....	130
Figure 4.61: σ_{ϕ} , STEC, ROT, and ROTI for 5- and 30-min interval of PRN6 on 3 December 2008 from 1100 to 1430 UT. Paths of all visible satellites between 1230 and 1330 UT at 350 km are also shown.....	130
Figure 4.62: (a) σ_{ϕ} , (b) STEC, (c) ROTI ₅ and (d) ROTI ₃₀ observed on each visible satellite on 3 December 2008 from 1130 to 1430 UT	132
Figure 4.63: Comparison of TEC variations for PRN3 (left) and PRN6 (right) on 3 December 2008 (red curve) with previous and following days.....	133
Figure 4.64: 1-minute IMF components on 3 December 2008.....	133
Figure 4.65: 1-minute variation data at (a) Eureka, and (b) Resolute Bay on 3 December 2008	134
Figure 4.66: (a) σ_{ϕ} , (b) STEC, (c) ROTI ₅ and (d) ROTI ₃₀ observed on each visible satellite on 24 May 2008 from 1100 to 1400 UT	135
Figure 4.67: Path for all visible satellites for every hour between 1100 and 1400 UT on 24 May 2008	136
Figure 4.68: σ_{ϕ} , STEC, ROT, and ROTI for 5- and 30-min interval of PRN24 on 24 May 2008 from 1100 to 1430 UT. Paths of all visible satellites between 1200 and 1330 UT at 350 km are also shown	137
Figure 4.69: σ_{ϕ} , STEC, ROT, and ROTI for 5- and 30-min interval of PRN29 on 24 May 2008 from 1000 to 1300 UT. Paths of all visible satellites between 1130 and 1230 UT at 350 km are also shown	138
Figure 4.70: Paths of selected visible satellites (i.e. PRN10, PRN21, PRN24 and PRN29) observed at Alert between 1100 and 1400 UT on 24 May 2008, at the ionospheric pierce point of 350 km. The movement of the satellite is indicated by the satellite's PRN number, where the starting time of the track is also denoted. The dots represent the 30-minute interval of the satellite movement.....	138
Figure 4.71: σ_{ϕ} , STEC, ROT, and ROTI for 5- and 30-min interval of PRN10 on 24 May 2008 from 1100 to 1430 UT. Paths of all visible satellites between 1130 and 1400 UT at 350 km are also shown	139
Figure 4.72: 1-minute IMF components on 24 May 2008.....	140

Figure 4.73: 1-minute variation data at (a) Eureka, and (b) Resolute Bay on 24 May 2008	140
Figure 4.74: (a) σ_ϕ , (b) STEC, (c) ROTI ₅ and (d) ROTI ₃₀ observed on each visible satellite on 18 November 2009 from 1600 to 1900 UT	142
Figure 4.75: STEC, σ_ϕ , ROT, and ROTI of PRN17 on 18 November 2009. Paths of all visible satellites from 1700 to 1900 UT at 350 km are also shown.....	143
Figure 4.76: Comparison of TEC variations for PRN17 on 18 November 2009 (red curve) with previous and following days.....	143
Figure 4.77: 1-minute IMF components on 18 November 2009	144
Figure 4.78: 1-minute variation data at (a) Eureka, and (b) Resolute Bay on 18 November 2009.....	144
Figure 4.79: σ_ϕ , STEC, ROT, and ROTI of PRN19 on 2 October 2009. Paths of all visible satellites from 1800 to 1900 UT at 350 km are also shown.....	145
Figure 4.80: (a) σ_ϕ , (b) STEC, (c) ROTI ₅ and (d) ROTI ₃₀ observed on each visible satellite on 2 October 2009 from 1600 to 1900 UT	146
Figure 4.81: Comparison of TEC variations for PRN19 on 2 October 2009 (red curve) with previous and following days.....	147
Figure 4.82: Comparison of TEC variations for PRN18 on 2 October 2009 (red curve) with previous and following days.....	148
Figure 4.83: 1-minute IMF components on 2 October 2009	148
Figure 4.84: 1-minute variation data at Eureka on 2 October 2009	149
Figure 4.85: No. of patches versus K_p	155
Figure 5.1: Number of all data recorded for each month from March 2009 to February 2011 on each frequency.....	162
Figure 5.2: Number of all data (SNR > 0 dB) recorded for each month from March 2009 to February 2011 on each frequency	163
Figure 5.3: Histogram of Doppler spreads for data from March 2009 to February 2011 on each frequency.....	164
Figure 5.4: Monthly upper decile of Doppler spread from March 2009 to February 2011	172
Figure 5.5: Median of Doppler spread computed hourly for every month from March 2009 to February 2011 on each frequency	175

Figure 5.6: Upper decile of Doppler spread computed hourly for every month from March 2009 to February 2011 on each frequency	177
Figure 5.7 (i): The number of data for all Doppler spreads (left) and for Doppler spreads > 3 Hz (right) on 4.64, 6.95 and 8.01 MHz	180
Figure 5.8: Doppler spreads on 5 April 2010 on (a) 6.95 MHz and (b) 8.01 MHz. The vertical lines represents the period where $K_p \geq 5$	187
Figure 5.9: Doppler spreads from 3 to 4 August 2010 on (a) 8.01 MHz and (b) 14.36 MHz. The vertical lines represents the period of interest where $K_p \geq 5$. Note that $K_p \geq 5$ also occurred at other times	189
Figure 5.10: 1-minute IMF components on 3 August 2010	190
Figure 5.11: 1-minute variation data at (a) Eureka and (b) Resolute Bay on 3 August 2010.....	190
Figure 5.12: Doppler spreads from 4 to 5 February 2011 on 6.95 MHz. The vertical lines represents the period where $K_p \geq 5$	191
Figure 5.13: Doppler spreads from 4 to 5 February 2011 on 8.01 MHz. The vertical lines represents the period where $K_p \geq 5$	192
Figure 5.14: 1-minute IMF components on 4 February 2011.....	192
Figure 5.15: 1-minute variation data at Resolute Bay on 4 February 2011	193
Figure 6.1: Slant TEC (top) and σ_ϕ (bottom) of PRN21 over Ny-Ålesund from 1600 to 2200 UT on 4 February 2011. The vertical lines indicates the period of interest where $K_p \geq 5$	199
Figure 6.2: Colour-coded satellites path over Ny-Ålesund at 350 km on 4 February 2011 from 1800 to 1859 UT (left) and from 1900 to 1959 UT (right). The number denotes specific satellite number and also marks the beginning of the path	199
Figure 6.3: Slant TEC (top) and σ_ϕ (bottom) of PRN21 over Longyearbyen from 1600 to 2200 UT on 4 February 2011. The vertical lines indicates the period of interest where $K_p \geq 5$	200
Figure 6.4: Colour-coded satellites path over Longyearbyen at 350 km on 4 February 2011 from 1800 to 1859 UT (left) and from 1900 to 1959 UT (right). The number denotes specific satellite number and also marks the beginning of the path.	201
Figure 6.5: Doppler spread (top) and SNR (bottom) on 6.95 MHz from 1600 to 2200 UT on 4 February 2011. The vertical lines indicates the period of interest where $K_p \geq 5$	202

Figure 6.6: Doppler spread (top) and SNR (bottom) on 8.01 MHz from 1600 to 2200 UT on 4 February 2011. The vertical lines indicates the period of interest where $K_p \geq 5$	202
Figure 6.7: Selected delay-Doppler spectra on 6.95 MHz between 1900 and 2000 UT on 4 February 2011	203
Figure 6.8: Slant TEC (top) and σ_ϕ (bottom) of PRN18 and PRN22 over Ny-Ålesund from 1800 to 0000 UT on 4 February 2011. The vertical lines indicates the period of interest where $K_p \geq 5$	204
Figure 6.9: Slant TEC (top) and σ_ϕ (bottom) of PRN18 and PRN22 over Longyearbyen from 1800 to 0000 UT on 4 February 2011. The vertical lines indicates the period of interest where $K_p \geq 5$	205
Figure 6.10: Colour-coded satellites path over Ny-Ålesund at 350 km on 4 February 2011 from 2000 to 2059 UT (left) and from 2100 to 2159 UT (right)...	205
Figure 6.11: Slant TEC (top) and σ_ϕ (bottom) of PRN14 over Ny-Ålesund from 2000 UT on 4 February 2011 to 0200 UT on 5 February 2011. The vertical lines indicates the period of interest where $K_p \geq 5$	206
Figure 6.12: Slant TEC (top) and σ_ϕ (bottom) of PRN14 over Longyearbyen from 2000 UT on 4 February 2011 to 0200 UT on 5 February 2011. The vertical lines indicates the period of interest where $K_p \geq 5$	207
Figure 6.13: Colour-coded satellites path over Ny-Ålesund at 350 km on 4 February 2011 from 2200 to 2259 UT (left) and from 2300 to 2359 UT (right)...	207
Figure 6.14: Doppler spread (top) and SNR (bottom) on 6.95 MHz from 2000 UT on 4 February 2011 to 0200 UT on 5 February 2011. The vertical lines indicates the period of interest where $K_p \geq 5$	208
Figure 6.15: Doppler spread (top) and SNR (bottom) on 8.01 MHz from 2000 UT on 4 February 2011 to 0200 UT on 5 February 2011. The vertical lines indicates the period of interest where $K_p \geq 5$	208
Figure 6.16: Slant TEC (top) and σ_ϕ (bottom) of all visible satellites over Ny-Ålesund from 1800 UT to 2359 UT on 4 February 2011	209
Figure 6.17: Slant TEC (top) and σ_ϕ (bottom) of all visible satellites over Longyearbyen from 1800 UT to 2359 UT on 4 February 2011	210
Figure 6.18: 1-minute IMF components from 1200 UT on 4 February 2011 to 1200 UT on 5 February 2011	211
Figure 6.19: 1-minute variation data at Resolute Bay from 1200 UT on 4 February 2011 to 1200 UT on 5 February 2011. The number at the top right of each frame is the mean of its respective component	211

Figure 6.20: Slant TEC (top) and σ_ϕ (bottom) of PRN17 and PRN28 over Longyearbyen from 0400 to 1000 UT on 5 April 2010. The vertical lines indicates the period of interest	212
Figure 6.21: Colour-coded satellites path over Longyearbyen at 350 km on 5 April 2010 from 0600 to 0759 UT	213
Figure 6.22: Slant TEC (top) and σ_ϕ (bottom) of several satellites over Alert from 0400 to 1000 UT on 5 April 2010. The vertical lines indicates the period of interest	214
Figure 6.23: σ_ϕ , STEC, ROT, and ROTI of PRN19 on 5 April 2010. Paths of all visible satellites from 0600 to 0700 UT at 350 km are also shown.....	214
Figure 6.24: σ_ϕ , STEC, ROT, and ROTI of PRN32 on 5 April 2010. Paths of all visible satellites from 0700 to 0800 UT at 350 km are also shown.....	215
Figure 6.25: σ_ϕ , STEC, ROT, and ROTI of PRN14 on 5 April 2010. Paths of all visible satellites from 0700 to 0800 UT at 350 km are also shown.....	216
Figure 6.26: Slant TEC (top) and σ_ϕ (bottom) of PRN28 over Ny-Ålesund from 1600 to 2200 UT on 8 October 2009. The vertical lines indicates the period of interest..	217
Figure 6.27: Colour-coded satellites path over Ny-Ålesund at 350 km on 8 October 2009 from 1800 to 1859 UT	217
Figure 6.28: Slant TEC of PRN28 over Longyearbyen from 1600 to 2200 UT on 8 October 2009. The vertical lines indicates the period of interest	218
Figure 6.29: Satellites path over Alert at 350 km on 8 October 2009 from 1800 to 1900 UT	218
Figure 6.30: Slant TEC (top) and σ_ϕ (bottom) of PRN19 and PRN22 over Alert from 1600 to 2200 UT on 8 October 2009. The vertical lines indicates the period of interest.....	219
Figure 6.31: σ_ϕ , STEC, ROT, and ROTI of PRN19 on 8 October 2009. Paths of all visible satellites from 1800 to 1900 UT at 350 km are also shown.....	219
Figure 6.32: σ_ϕ , STEC, ROT, and ROTI of PRN22 on 8 October 2009. Paths of all visible satellites from 1800 to 1900 UT at 350 km are also shown.....	220
Figure 6.33: Doppler spread (top) and SNR (bottom) on 14.35 MHz from 1700 to 2000 UT on 8 October 2009. The vertical lines indicates the period of interest.....	221
Figure 6.34: Selected delay-Doppler spectra on 14.36 MHz between 1800 and 1900 UT on 8 October 2009	222
Figure 6.35: 1-minute IMF components on 8 October 2009	223

Figure 6.36: 1-minute variation data at Eureka on 8 October 2009	223
Figure 6.37: σ_ϕ , STEC, ROT, and ROTI of PRN21 on 4 October 2009. Paths of all visible satellites from 1500 to 1700 UT at 350 km are also shown.....	224
Figure 6.38: σ_ϕ , STEC, ROT, and ROTI of PRN16 on 4 October 2009. Paths of all visible satellites from 1500 to 1600 UT at 350 km are also shown.....	225
Figure 6.39: σ_ϕ , STEC, ROT, and ROTI of PRN6 on 4 October 2009. Paths of all visible satellites from 1500 to 1700 UT at 350 km are also shown.....	225
Figure 6.40: Slant TEC (top) and σ_ϕ (bottom) of PRN6, 16, 18 and 21 over Alert from 1300 to 1900 UT on 4 October 2009. The vertical lines indicates the period of interest.....	226
Figure 6.41: Satellites path over Alert at 350 km on 4 October 2009 from 1500 to 1700 UT	226
Figure 6.42: Slant TEC (top) and σ_ϕ (bottom) of PRN7, 8 and 25 over Ny-Ålesund from 1300 to 1900 UT on 4 October 2009. The vertical lines indicates the period of interest.....	227
Figure 6.43: Slant TEC (top) and σ_ϕ (bottom) of PRN7, 8 and 25 over Longyearbyen from 1300 to 1900 UT on 4 October 2009. The vertical lines indicates the period of interest.....	228
Figure 6.44: Colour-coded satellites path over Ny-Ålesund at 350 km on 4 October 2009 from 1500 to 1659 UT	228
Figure 6.45: Doppler spread (top) and SNR (bottom) on 10.39 MHz from 1430 to 1730 UT on 4 October 2009. The vertical lines indicates the period of interest.....	229
Figure 6.46: Selected delay-Doppler spectra on 10.39 MHz between 1500 and 1600 UT on 4 October 2009	230
Figure 6.47: Selected delay-Doppler spectra on 10.39 MHz between 1600 and 1700 UT on 4 October 2009	231
Figure 6.48: 1-minute IMF components on 4 October 2009	232
Figure 6.49: 1-minute variation data at (a) Eureka, and (b) Resolute Bay on 4 October 2009.....	233
Figure 6.50: Satellites path over Alert at 350 km on 15 February 2010 from 1600 to 2000 UT	234
Figure 6.51: Slant TEC (top) and σ_ϕ (bottom) of PRN7, 8 and 13 over Alert from 1500 to 2100 UT on 15 February 2010. The vertical lines indicates the period of interest.....	234

Figure 6.52: Doppler spread (top) and SNR (bottom) on 10.39 MHz from 1600 to 2000 UT on 15 February 2010.....	235
Figure 6.53: Doppler spread (top) and SNR (bottom) on 11.12 MHz from 1600 to 2000 UT on 15 February 2010.....	236
Figure 6.54: Selected delay-Doppler spectra on 10.39 MHz between 1700 and 1800 UT on 15 February 2010.....	237
Figure 6.55: Selected delay-Doppler spectra on 10.39 MHz between 1800 and 1900 UT on 15 February 2010.....	238
Figure 6.56: Selected delay-Doppler spectra on 10.39 MHz between 1900 and 2000 UT on 15 February 2010.....	239
Figure 6.57: Slant TEC (top) and σ_ϕ (bottom) of PRN29, 21 and 24 over Ny-Ålesund from 1500 to 2000 UT on 15 February 2010. The vertical lines indicates the period of interest	240
Figure 6.58: Slant TEC (top) and σ_ϕ (bottom) of PRN29, 21 and 24 over Longyearbyen from 1500 to 2000 UT on 15 February 2010. The vertical lines indicates the period of interest.....	240
Figure 6.59: Colour-coded satellites path over Ny-Ålesund at 350 km on 15 February 2010 from 1600 to 1959 UT.....	241
Figure 6.60: (a) σ_ϕ , (b) STEC, (c) ROTI ₅ and (d) ROTI ₃₀ observed on each visible satellite on 11 April 2010 from 1700 to 2000 UT. Note the different values on y-axis for STEC, but grid scale is equal	243
Figure 6.61: Satellites path over Alert at 350 km on 11 April 2010 from 1900 to 2000 UT	244
Figure 6.62: Slant TEC (top) and σ_ϕ (bottom) of PRN27 over Alert from 1700 to 2300 UT on 11 April 2010. The vertical lines indicates the period of interest	244
Figure 6.63: σ_ϕ , STEC, ROT, and ROTI of PRN27 on 11 April 2010. Paths of all visible satellites from 1900 to 2000 UT at 350 km are also shown.....	245
Figure 6.64: Doppler spread (top) and SNR (bottom) on 10.39 MHz from 1700 to 2000 UT on 11 April 2010. The vertical lines indicates the period of interest	245
Figure 6.65: Selected delay-Doppler spectra on 10.39 MHz between 1900 and 2000 UT on 11 April 2010.....	246
Figure 6.66: Slant TEC (top) and σ_ϕ (bottom) of PRN14 over Ny-Ålesund from 1700 to 2300 UT on 11 April 2010. The vertical lines indicates the period of interest	247

Figure 6.67: Slant TEC (top) and σ_ϕ (bottom) of PRN14 over Longyearbyen from 1700 to 2300 UT on 11 April 2010. The vertical lines indicates the period of interest	247
Figure 6.68: Colour-coded satellites path over Ny-Ålesund at 350 km on 11 April 2010 from 1900 to 1959 UT.....	248
Figure 6.69: 1-minute IMF components on 11 April 2010	248
Figure 6.70: 1-minute variation data at (a) Eureka, and (b) Resolute Bay on 11 April 2010.....	249
Figure 6.71: Doppler spread (top) and SNR (bottom) on 14.36 MHz from 1500 to 1800 UT on 8 October 2009. The vertical lines indicates the period of interest.....	250
Figure 6.72: Selected delay-Doppler spectra on 14.36 MHz between 1600 to 1700 UT on 8 October 2009	251
Figure 6.73: Slant TEC (top) and σ_ϕ (bottom) of PRN7 and PRN8 over Ny-Ålesund from 1400 to 2000 UT on 8 October 2009. The vertical lines indicates the period of interest.....	252
Figure 6.74: Colour-coded satellites path over Ny-Ålesund at 350 km on 8 October 2009 from 1600 to 1659 UT	253
Figure 6.75: Slant TEC (top) and σ_ϕ (bottom) of PRN3, 6, 18 and 21 over Alert from 1400 to 2000 UT on 8 October 2009. The vertical lines indicates the period of interest.....	254
Figure 6.76: Satellites path over Alert at 350 km on 8 October 2009 from 1600 to 1700 UT	254
Figure 6.77: σ_ϕ , STEC, ROT, and ROTI for 5- and 30-min interval of PRN6 on 8 October 2009 from 1400 to 1730 UT. Paths of all visible satellites between 1600 and 1700 UT at 350 km are also shown.....	255
Figure 6.78: σ_ϕ , STEC, ROT, and ROTI for 5- and 30-min interval of PRN18 on 8 October 2009 from 1600 to 1830 UT. Paths of all visible satellites between 1600 and 1700 UT at 350 km are also shown.....	255
Figure 6.79: Doppler spread (top) and SNR (bottom) on (a) 6.95 MHz and (b) 8.01 MHz from 0100 to 0400 UT on 11 April 2010. The vertical lines indicates the period of interest	256
Figure 6.80: Slant TEC (top) and σ_ϕ (bottom) of PRN7 over Ny-Ålesund from 0000 to 0600 UT on 13 April 2009. The vertical lines indicates the period of interest	257

Figure 6.81: Slant TEC (top) and σ_ϕ (bottom) of PRN7 over Longyearbyen from 0000 to 0600 UT on 13 April 2009. The vertical lines indicates the period of interest	258
Figure 6.82: Colour-coded satellites path over Ny-Ålesund at 350 km on 13 April 2010 from 0200 to 0259 UT.....	258
Figure 6.83: Slant TEC (top) and σ_ϕ (bottom) of PRN21 and PRN24 over Alert from 0000 to 0600 UT on 13 April 2010. The vertical lines indicates the period of interest	259
Figure 6.84: Satellites path over Alert at 350 km on 13 April 2010 from 0200 to 0300 UT	259
Figure 6.85: σ_ϕ , STEC, ROT, and ROTI for 5- and 30-min interval of (a) PRN21 and (b) PRN24 on 13 April 2010 from 0100 to 0400 UT. Paths of all visible satellites between 0200 and 0300 UT at 350 km are also shown	260
Figure 6.86: 1-minute IMF components on 13 April 2010	261
Figure 6.87: 1-minute variation data at (a) Eureka, and (b) Resolute Bay on 13 April 2010.....	261

List of Tables

Table 2.1: Path lengths of high latitude campaigns observing HF channel characteristics using DAMSON (Source: <i>Angling et al.</i> [1998])	39
Table 3.1: Summary of patches classification	50
Table 4.1: Minimum, lower decile, median, upper decile and maximum values of hourly mean VTEC from June 2008 to July 2010	60
Table 4.2: Number of occurrence of amplitude scintillation index, S4 for every month from June 2008 to July 2010	69
Table 4.3: Number of occurrence of σ_ϕ for every month from June 2008 to July 2010 in 0.1-rad step, except between 0.1 rad and 0.2 rad.....	74
Table 4.4: Summary of geomagnetic activity where $K_p \geq 5$ - from June 2008 to July 2010.....	79
Table 4.5: Description of each event type	97
Table 4.6: Sunspot number (SSN), maximum geomagnetic index (K_p) and maximum polar cap index (PC(N)) for every case in each event type	151
Table 4.7: No. of patches for every case in each event type during a specified 3-hour period (except on Event Type $K_p > 4$)	154
Table 4.8: Minimum values of ROT and each magnetic component of IMF, Eureka (EUA) and Resolute Bay (RES) for every case in each event type during a specified 3-hour period (except on Event Type $K_p > 4$)	157
Table 4.9: Maximum values of σ_ϕ , ROT and each magnetic component of IMF, Eureka (EUA) and Resolute Bay (RES) for every case in each event type during a 3-hour specified period (except on Event Type $K_p > 4$)	158
Table 4.10: Percentage of positive polarity of each magnetic component of IMF, Eureka (EUA) and Resolute Bay (RES) for every case in each event type during a specified 3-hour period (except on Event Type $K_p > 4$) for $0.2 \text{ TECU/min} < \text{ROT} < -0.2 \text{ TECU/min}$	159
Table 4.11: Percentage of positive polarity of each magnetic component of IMF, Eureka (EUA) and Resolute Bay (RES) for every case in each event type during a specified 3-hour period (except on Event Type $K_p > 4$) for $\sigma_\phi > 0.15 \text{ rad}$	160
Table 5.1: Monthly lower decile, median, and upper decile of Doppler spread (Hz) at 4.64 MHz	166
Table 5.2: Monthly lower decile, median, and upper decile of Doppler spread (Hz) at 6.95 MHz	167

Table 5.3: Monthly lower decile, median, and upper decile of Doppler spread (Hz) at 8.01 MHz	168
Table 5.4: Monthly lower decile, median, and upper decile of Doppler spread (Hz) at 10.39 MHz	169
Table 5.5: Monthly lower decile, median, and upper decile of Doppler spread (Hz) at 11.12 MHz	170
Table 5.6: Monthly lower decile, median, and upper decile of Doppler spread (Hz) at 14.36 MHz	171
Table 5.7: Percentage of Doppler spreads $3 > \text{Hz}$ on each frequency	183
Table 5.8: Summary of geomagnetic activity where $K_p \geq 5$ from 14 March 2009 to February 2011	184
Table 5.9: Daily upper decile Doppler spread for each frequency during the days where $K_p \geq 5$ from 14 March 2009 to February 2011. Data was not available on 2 and 3 May 2010. Number of cases per day is in the brackets	186
Table 5.10: No. of Doppler spread data, the maximum Doppler spread during a specified 6-hour period for every case of $K_p > 4$	195
Table 5.11: Minimum value of each magnetic component of IMF, Eureka (EUA) and Resolute Bay (RES) for every case of $K_p > 4$ during a specified 6-hour period	196
Table 5.12: Maximum value of each magnetic component of IMF, Eureka (EUA) and Resolute Bay (RES) for every case of $K_p > 4$ during a specified 6-hour period	196
Table 5.13: Percentage of positive polarity of each magnetic component of IMF, Eureka (EUA) and Resolute Bay (RES) for every case of $K_p > 4$ during a specified 6-hour period	196
Table 6.1: Description of each event type	197
Table 6.2: Sunspot number (SSN), maximum geomagnetic index (K_p) and maximum polar cap index (PC(N)) for every case in each event type	262
Table 6.3: No. of patches, minimum and maximum ROT, maximum σ_ϕ , and maximum Doppler spread for every case in each event type during a specified 1-hr period except on 4 February 2011. The Number of data for the satellites(s) in the specified period and the number of data of Doppler spread on a particular frequency are also included	264
Table 6.4: Minimum values of each magnetic component of IMF, Eureka (EUA) and Resolute Bay (RES) for every case in each event type during a specified period. Different time frame was applied for each case, but mean value for each component at Eureka and Resolute Bay was calculated for 1-day period	266

Table 6.5: As in Table 6.5 but for maximum values of each component.....266

Table 6.6: Percentage of positive polarity of each magnetic component of IMF, Eureka (EUA) and Resolute Bay (RES) for every case in each event type during a specified period.....267

Abbreviations

HF	High Frequency
GPS	Global Positioning System
TEC	Total Electron Content
EISCAT	Incoherent-scatter Radar
MLT	Magnetic Local Time
IMF	Interplanetary Magnetic Field
IGS	International GNSS Service
GISTM	GPS Ionospheric Scintillation and TEC Monitor
DISS	Digital Ionospheric Sounding Systems
MSP	Meridian-scanning Photometer
ROT	Rate of change of TEC
ROTI	Rate of TEC Index
CGM	Corrected Geomagnetic
MLat	Magnetic Latitude
CHAIN	High Arctic Ionospheric Network
DAMSON	Doppler and Multipath Sounding Network
TOF	Time of Flight
PRI	Pulse Repetition Interval
SSN	Sunspot Number
ISACCO	Ionospheric Scintillations Arctic Campaign Coordinated Observation
eSW	electronic Space Weather
INGV	Istituto Nazionale di Geofisica e Vulcanologia
SNR	Signal-to-Noise Ratio

Chapter One: Introduction

The ionosphere is an ionised region of the upper atmosphere produced by solar radiation and high-energy particles from the sun. The ionised electron concentrations change with, among others, height above earth's surface, geographic and geomagnetic location, time of day, season, solar activity, and solar disturbances. This will affect to a greater or lesser extent all radio signals which pass through or travel via it, including high frequency (HF) sky-wave signals and transionospheric signals, for example, those of the Global Positioning System (GPS). Satellite transmissions traverse the ionised space plasma and are subject to changes due to the amount of ionisation along the ray path (i.e., the line integral of the electron density known as the Total Electron Content (TEC)). At high latitude region where geosynchronous satellites are not available to be used for communication, HF radio is used instead. HF communication is also widely used elsewhere. Disruption to the quiet ionosphere may affect the performance of the HF signals.

Perturbations to the ionosphere's quiet condition may adversely affect satellite systems (positioning error, weakened signal), affect communication systems in general, and cause disruption of power transmission [*Jayachandran et al., 2009*]. Several cases have been documented due to severe space weather conditions, for example a series of geomagnetic storms in October-November 2003. This storm caused several casualties including a power blackout in Southern Sweden and effects on the Scottish power grid, degrading of GPS signals, a variety of satellite anomalies including orientation problem, disruption on HF radio causing polar route flights to

be re-routed, and also forced astronauts on the ISS to remain in the most shielded part (*Eastwood [2008]* and the references therein).

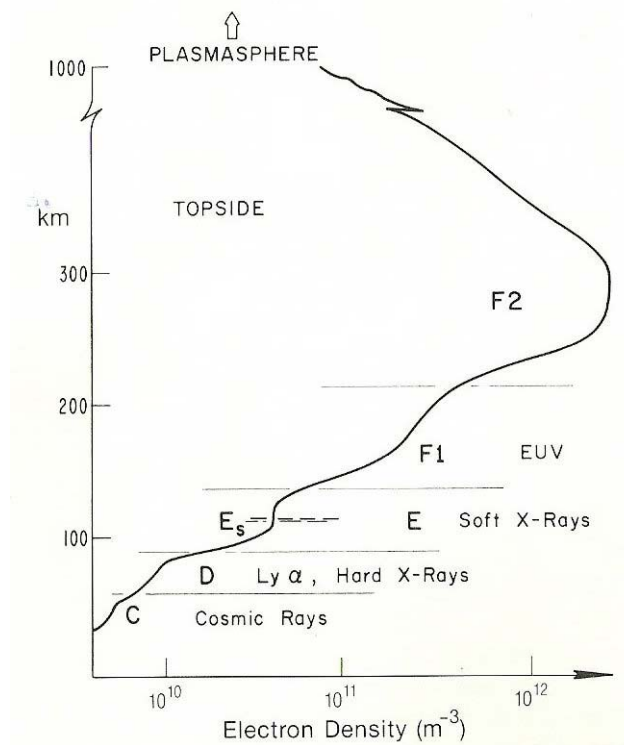


Figure 1.1: Ionospheric regions (Source: Davies [1990]. Reproduced by permission of Institution of Engineering and Technology)

The ionosphere can be divided into several regions, namely the D region, E region and F region. The boundaries between these regions are defined by the minima in electron density between the various peaks. According to *Davies [1990]*, the D region is located around 50 km to 90 km. Above the D region is the E region, which is up to 140 km. This is followed by the most ionised region, which is the F region where the peak electron density usually occurs. Above the F region is the topside, and followed by the plasmasphere. The F region can be further divided into

F1 and F2 layers during the day. Both layers combine at night becoming the F region. Meanwhile the D region vanishes at night and the E region becomes much weaker [Davies, 1990]. Figure 1.1 illustrates the ionospheric regions on a summer day in a mid latitude region.

The ionosphere can also be categorised into three regions based on the latitude; which are low, mid and high. The low latitude region is within about 20° to 30° of the magnetic equator. The high latitude region extends poleward from about 60° geomagnetic, and the mid latitude is between these two regions. The mid latitude ionosphere is the most explored and understood. The high latitude ionosphere can be further sub-divided into two; which are the auroral region (approximately 60° to 70° magnetic) and the polar cap (from the auroral region poleward). The high latitude ionosphere is the most variable compared to the low and mid latitudes.

According to *Hunsucker and Hargreaves* [2003], the winter anomaly can be seen at sunspot maximum but not at sunspot minimum. The electron density is also larger in the months before and after the winter solstice. This is an indication of the presence of a semi-annual anomaly [*Hunsucker and Hargreaves*, 2003]. The high latitude ionosphere behaves differently from the low and middle latitude ionospheres since the geomagnetic field at high latitudes runs nearly vertical (as opposed to the horizontal magnetic field at low latitudes near to the magnetic equator) and connecting this area to the outer part of the magnetosphere, which is controlled by the solar wind.

In comparison, the mid latitude ionosphere is connected to the inner magnetosphere which rotates with the earth and therefore is less sensitive to the external influence. Therefore, at high latitudes, any particle from the sun has the possibility of penetrating the ionospheric layer, and hence, perturbing the normal (quiet) condition of the ionosphere. These make the high latitude ionosphere an interesting area to study.

Recent studies on various topics regarding the high latitudes are conducted by many researchers, for example *Skone et al.* [2001], *Breed et al.* [2002], *Dandekar* [2002]; *Rogers et al.* [2003], *Mitchell et al.* [2005], *Stolle et al.* [2005], *Zaalov et al.* [2005], *Krankowski et al.* [2006], *Shagimuratov et al.* [2006], *MacDougall and Jayachandran* [2007], *De Franceschi et al.* [2008], *Li et al.* [2010], and *Gwal and Jain* [2011]. Some of the findings of these studies will be reviewed in the next chapter. Most of the studies focused at the auroral region and research on the area of polar cap ionosphere is still lacking.

The research work focuses on the study of high latitudes ionosphere variability. Our area of interest is at a polar cap station in Alert, Canada, located at 82.48° N, 297.75° E, corresponding to around 86.95° N, 155.77° E of the geomagnetic coordinate. Magnetic Local Time (MLT) midnight is ~ 2216 UT. Figure 1.2 shows the location of Alert superposed on the map illustrating the auroral oval location. The map is generated for 24 May 2008 at 1340 UT during the period of low geomagnetic activity. Alert is located far from the auroral oval and very near to the geomagnetic pole, making it an interesting place to study the ionospheric variability.

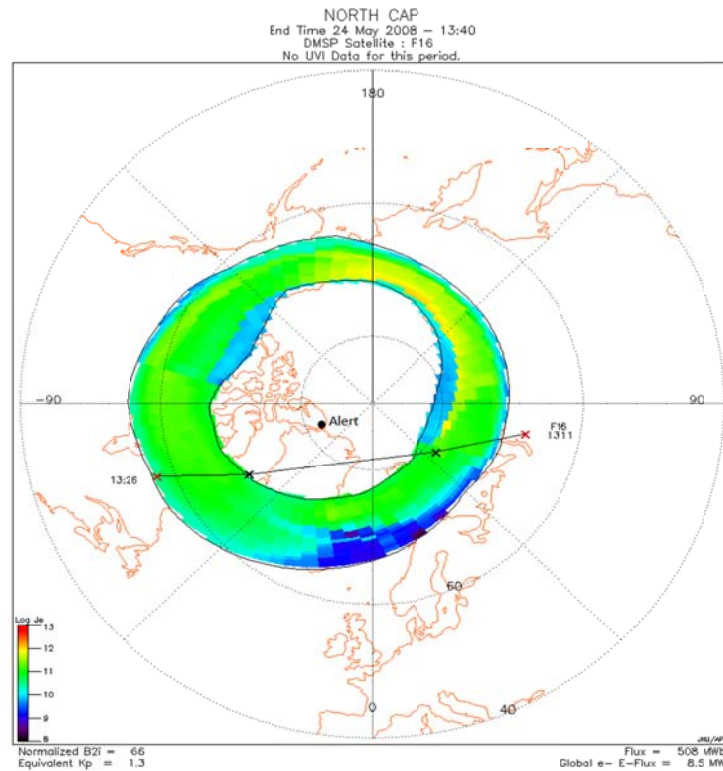


Figure 1.2: Auroral oval on 24 May 2008. Location of Alert is superposed on the map (Source: <http://sd-www.jhuapl.edu>)

Furthermore, a HF link between Qaanaaq, Greenland (77.5° N, 291.3° E, geomagnetic coordinate: 87.59° N, 16.31° E) and Ny-Ålesund, Svalbard (78.9° N, 11.9° E, geomagnetic coordinate: 75.74° N, 128.59° E) has been in operation since 14 March 2009. The distance between the transmitter and the receiver is ~ 1700 km. Figure 1.3 shows the location of HF transmitter and receiver, HF path midpoint, and GPS receiver at Alert.

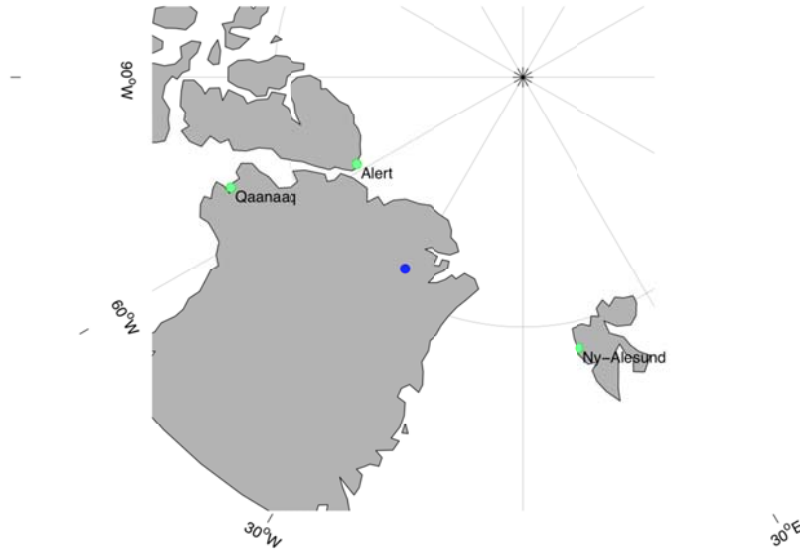


Figure 1.3: Location of HF transmitter (Qaanaaq) and receiver (Ny-Ålesund), HF midpoint (indicated by the blue circle), and GPS receiver (Alert)

It is the aim of this study to develop a better understanding of the propagation effects of the polar cap ionosphere. The total periods of observations were from May 2008 until February 2011, which were during the period of very low solar activity. Extensive experimental measurements, including incorporating HF and transionospheric data, were undertaken in order to observe the TEC enhancements and scintillation effects and also Doppler spreads at the polar cap ionosphere. This will improve understanding of the propagation effects associated with the irregularities within the polar cap ionosphere, and their influence on radio systems.

Knowledge of the space weather conditions is important so that adverse effects on human and assets can be reduced. Sufficient knowledge of the behaviour of polar cap ionosphere will benefit operators, for example the commercial airlines. Re-routing flights in the polar region costs a huge sum of money, reported as \$100,000 per flight [Eastwood, 2008]. Airlines rely on HF communications for polar routing.

They are not allowed to go on these routes if they expect the communications to fail due to ionospheric conditions.

Furthermore, exposure to cosmic radiation is also a possibility [*Jones et al.*, 2005]. Therefore, knowledge of the polar ionosphere behaviour is definitely important and valuable for further usage, for example, warning, mitigating and/or predicting the effect of the space weather conditions at this region.

Chapter Two: Review of Previous Works

Many of the problems that affect communication at high latitudes are due to the fact that the magnetic field is nearly vertical there. Particles from the sun can penetrate into the earth's atmosphere and collide with the components here, hence, causing ionisation to increase, and consequently perturbing the quiet condition of the ionosphere. There are two main irregularities that have impact on the high latitude ionosphere: large-scale fluctuation known as patches and arcs, and small-scale fluctuations that lead to scintillations in the signal.

2.1 Patches and Arcs

Patches are enhanced plasma density structures in the F layer that flow across the polar cap during periods of high magnetic activity ($K_p > 4$) in a generally antisunward direction with sizes of 100-1000 km and speed of 300-1000 m/s (e.g., *Buchau et al.* [1983], *Breed et al.* [2002]). Observations using ionosondes and all-sky imaging photometers by *Buchau et al.* [1983] revealed that the patches have a diffuse and cloudlike structure. The patches also show great variability in size and shape, with small scale structures within. There is no universal agreement on the patches formation mechanism, but researchers tend to agree that the source of ionisation for patch formation is the enhanced ridge of plasma called the 'tongue of ionisation' created by the polar convection dragging sunlit plasma from equatorward of the cusp into the polar cap [*Breed et al.*, 2002].

Patches are generally observed when the Interplanetary Magnetic Field (IMF) is southward ($B_z < 0$) and they move with the general plasma drift. *McEwen et al.* [2004] conducted an experiment using a photometer and an ionosonde at Eureka, Nunavut, Canada (80° N, 274° E) and concluded that the F-region patches are frequently present when B_z is southward. This is in agreement with measurements reported by *Krankowski et al.* [2006] where the intensity of the patches and their occurrences in four Antarctic stations (McMurdo (-78° N, 167° E), Casey (-66° N, 110° E), Mawson (-68° N, 63° E), and Davis (-69° N, 78° E)) was the highest when B_z is negative. However, *MacDougall and Jayachandran* [2007] pointed out the patches only show correlation with the IMF B_z for atypical days (i.e. when there are very large swings of IMF B_z), with only weak correlation for typical days.

Hunsucker and Hargreaves [2003] concluded based on a number of observations that patches occur during all seasons but more frequently during the winter night under disturbed condition. At these times, the F layer electron density may be increased by as much as a factor of ten above the background. They tend to be stronger at times of high sunspot number [*Hunsucker and Hargreaves*, 2003].

Another phenomenon called arcs is seen when the IMF is northward ($B_z > 0$) and also when the geomagnetic conditions are less disturbed. These are produced by soft (several hundreds eV average energy) particle precipitation. The arcs are normally sun-aligned, tend to drift slowly at the speed of 100-250 m/s from dawn to dusk (perpendicular to their alignment) [*Carlson et al.*, 1984], although the opposite direction is also observed [*Buchau et al.*, 1983]. They appear as elongated thin strips ~ 100 km in size. These features can persist for more than one hour [*Carlson et al.*,

1984]. During the period of an arcs existence, the electron density is enhanced by a factor of 5-8 above the background density at sunspot maximum, but only by a factor of 2 around sunspot minimum [Hunsucker and Hargreaves, 2003]. Krankowski et al. [2006] observed strong TEC fluctuation when B_z was positive and under the weak magnetically disturbed conditions at four stations in Antarctic.

The polar ionosphere is said to alternate between these two phenomena, with patches present during the periods when the IMF is southward, and arcs present at other times when the IMF is northward [Carlson, 1994]. However, both patches and arcs may exist simultaneously. This could be indicated when B_z switches polarities often [Prikryl et al., 2010]. Small patches were observed moving at much higher speed in the anti sunward direction, in between arcs [Buchau et al., 1983]. At these times when both irregularities co-exist, the ionograms are dominated by the signatures of the arcs, which is a spread oblique echo traces [Buchau et al., 1983]. All these irregularities are illustrated in Figure 2.1.

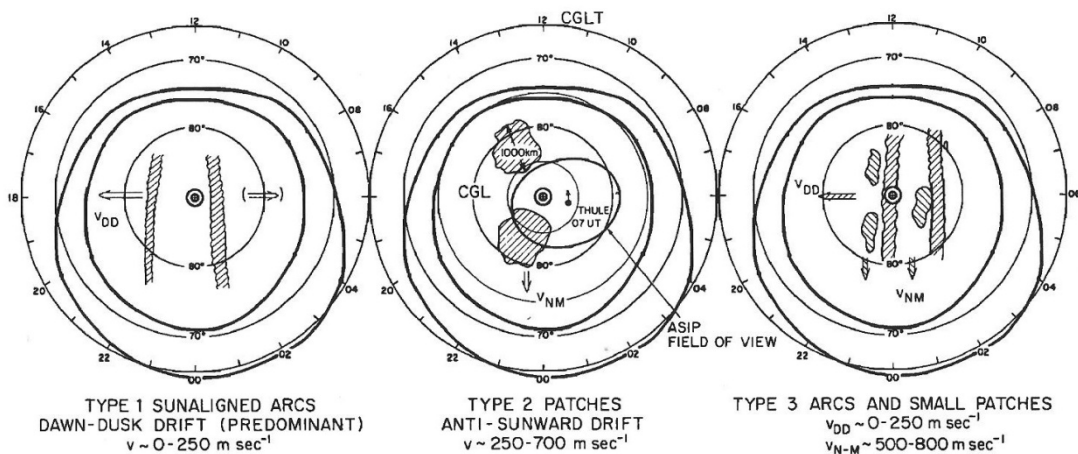


Figure 2.1: Polar cap F region structures (Source: Buchau et al. [1983])

Signatures of patches and/or arcs can be observed using a variety of equipment and they have been studied for a number of years. Recent researchers, for example *Breed et al.* [2002], *Dandekar* [2002], *Rogers et al.* [2003] and *MacDougall and Jayachandran* [2007] used ionosondes to detect the existence of patches and/or arcs. Meanwhile, the International GNSS Service (IGS) network (e.g., *Mitchell et al.* [2005], *Stolle et al.* [2005], *Krankowski et al.* [2006], *Shagimuratov et al.* [2006]), GPS Ionospheric Scintillation and TEC Monitor (GISTM) receivers (e.g., *Mitchell et al.* [2005], *Gwal and Jain* [2011]), a photometer (e.g., *McEwen et al.* [2004]), an incoherent scatter radar (e.g., *Pedersen et al.* [2000], *Friedrich et al.* [2006]), and satellites (e.g., *Crowley et al.* [2000], *Cumnock et al.* [2006]) were also used as the detection equipment.

The existence of the patches is normally determined by looking at the changes in critical frequency, electron content, and/or electron density. The most obvious effect of the patches is an increase in the critical frequency since it is related to the increase of electron density. For any irregularities to be called a patch, the electron density must be at least twice the background value, equivalent to an increase of at least 40% of the critical frequency [*MacDougall and Jayachandran*, 2007].

James and MacDougall [1997] developed a model that shows the effects of the electron density structures and the appearance of U-shaped or hyperbolic traces in the ionograms and in the virtual height versus time at a constant frequency. The U-shaped traces are formed because the echoes from the ionosonde do not necessarily come from overhead. When the patches approach a station, the ranges of the echoes decrease, and inversely, the patches go away from the station, the ranges

will increase, thus forming U-shaped traces. *Breed et al.* [2002] employed this method and observed the U-shaped traces plotted for a specific frequency. Observations conducted by *Breed et al.* [2002] at Casey, Antarctic (66.3°S, 110.5°E) using a Lowell Digital Ionosonde during 1997-1999 revealed that patches occurrence correspond to the peaks of the critical frequency (Figure 2.2). Smaller patches are usually indicated by a number of closely spaced peaks of the critical frequency.

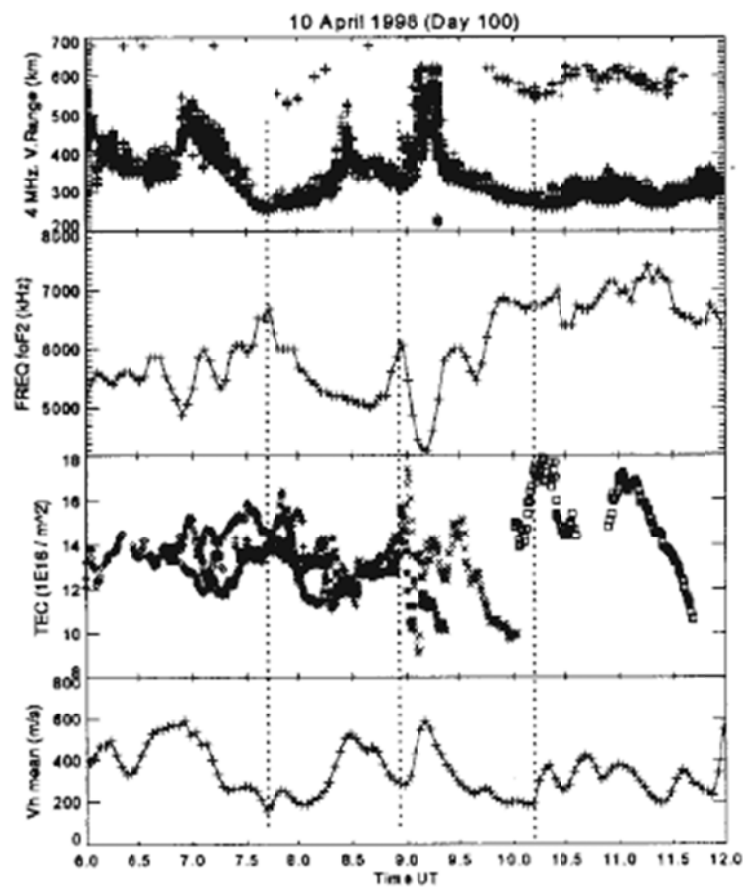


Figure 2.2: Patches identified on the virtual height plot at 4 MHz, critical frequencies, TEC measurements and horizontal drift velocity on 10 April 1998 (Source: Breed et al. [2002])

Breed et al. [2002] then compared the U-shaped traces with the critical frequency, the TEC measurement (from a co-located GPS receiver), and the horizontal drift velocity (from the digisonde drift measurement). They found out that there is a correlation between the U-shaped traces in the virtual height plot, peaks in the critical frequency and TEC, and minimum in horizontal drift velocity. Meanwhile, the surges of the horizontal drift velocity are found to be associated with the patch edges. However, *Breed et al.* [2002] suggested that this should be further investigated as it may be caused by the turbulence or instabilities at the patch edges. In addition, digisonde can also be used to produce skymaps of the echo sources. Although the signature of the patches using skymaps is still under investigation, it is expected that larger patches edges would appear as ‘fronts’ of echoes crossing the filed-of-view, while smaller patches may be seen entirely [*Breed et al.*, 2002].

Dandekar [2002] used the critical frequency, f_oF_2 from two Digital Ionospheric Sounding Systems (DISS) in Greenland, Sondrestromjford (67° N, 50.6° W, 75.16° N CGM) and Qaanaaq (77.5° N, 68.7° W, 86.71° N CGM), for 4 years (1989-1990, 1991-1992, 1993-1994, 1996-1997) that include 4 different levels of solar activity (annual averaged sunspot number (SSN) with standard deviation of 150 ± 50 , 125 ± 50 , 40 ± 20 , and 10 ± 10 , respectively) to study the dependency of the occurrence and intensity of the patches on solar cycle activity. Sondrestromjford is located at auroral latitudes during daytime and at polar latitudes during nighttime, whereas Qaanaaq is always a polar station. Refer to Figure 2.3 for the locations of these stations.

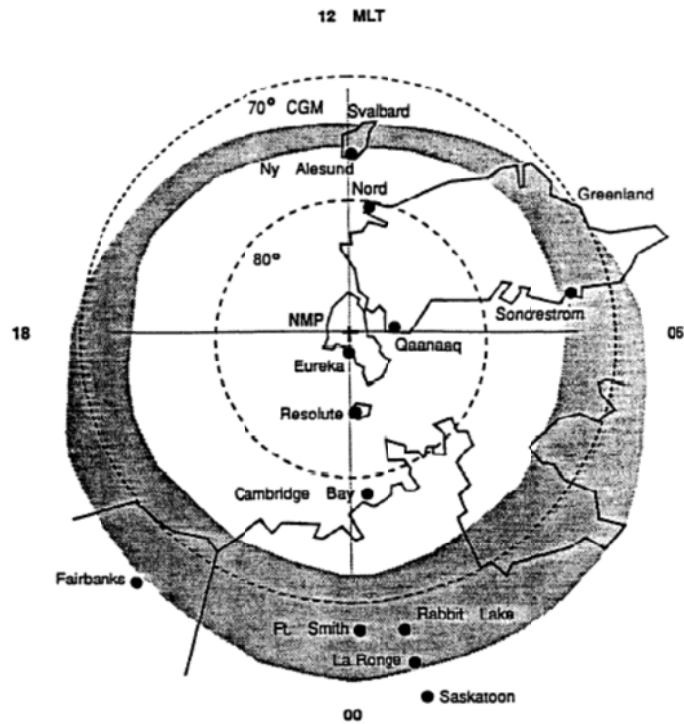


Figure 2.3: A polar map in magnetic coordinate and local time, centred at north magnetic pole. Locations of some polar stations are shown. An auroral oval at 0600 UT and $K_p = 4$ is also shown (Source: McEwen and Harris [1996])

In Dandekar [2002], a patch structure is measured by subtracting a baseline from the observed electron density (obtained from f_oF_2 measurement). The baseline is the monthly standard deviation of the electron density. Although the patch strength is actually in electron density, it is more convenient to use the megahertz scale by manipulating the relationship $N(\text{cm}^{-3}) = 1.24 \times 10^4 f_oF_2^2 \text{ MHz}$. Therefore, for example, a patch with electron density of 10^6 el cm^{-3} corresponds to a 9-MHz patch. An example of determining polar patches is illustrated in Figure 2.4.

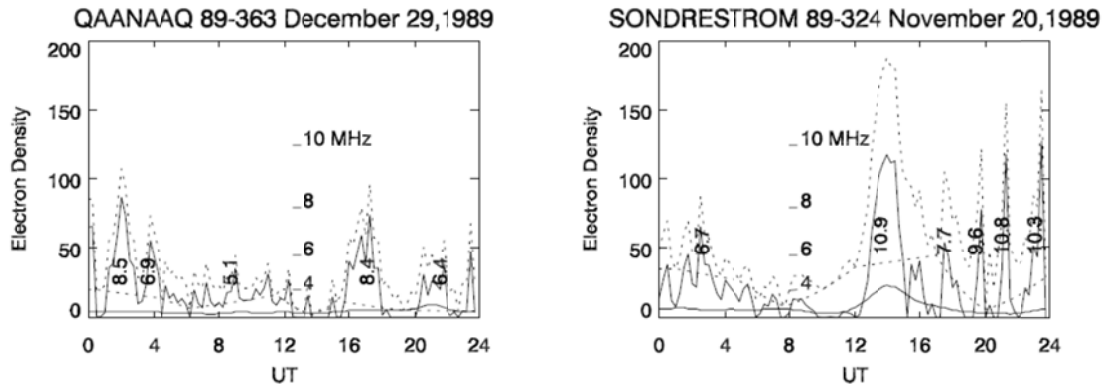


Figure 2.4: Appearance of polar cap patches at Qaanaaq on 29 December 1989 and Sondrestromfjord on 20 November 1989. The scale for y-axis extends from 0 to 200×10^4 electron cm^{-3} (Source: Dandekar [2002]).

The example shows patches determined using both the old baseline [Dandekar and Bullett, 1999], indicated by dashed curve and the new baseline

Dandekar [2002] concluded that there was a significant reduction in both patch strength and in the number of patches per day corresponding to reduced sunspot activity. The number of polar patches exceeding a given strength was counted for each day. At patch strengths ≥ 3 MHz and with declining sunspot number, the number of patches reduced from six per day to three per day at Sondrestromfjord, and from eight per day to four per day and Qaanaaq. This number reduces to half for patches ≥ 7 MHz with declining sunspot number. More patches occur in Qaanaaq than in Sondrestromfjord because the former is closer to the geomagnetic pole than the latter. In terms of diurnal behaviour, the maximum patch occurrence is around magnetic noon.

The seasonal behaviour of the patches with respect to the daily occurrence is shown in Figure 2.5. A weak seasonal dependence is observed at high sunspot activity (1989–1992) where the patch occurrence at both stations is $> 90\%$ from September to March for patch strengths ≥ 5 MHz. Meanwhile, at higher patch strengths, the

seasonal behaviour is at its highest of 40% occurrence for patch strength of 9 MHz during the winter months. At medium to low sunspot activity there is no systematic seasonal dependence, but the level of occurrence reduces with declining sunspot activity. At low solar activity, strong patches (≥ 7 MHz) are rare at both stations. In term of diurnal variations, patch activity peaks around 1800 UT and is at minimum around 1200 UT. Thus, the peak activity occurs a few hours after magnetic noon. At specific patch strength, the occurrence level reduces with the decreasing of solar activity. *Dandekar* [2002] concluded that diurnal, seasonal and solar cycle dependence of polar patch occurrence is predominant and dependence on magnetic activity is secondary.

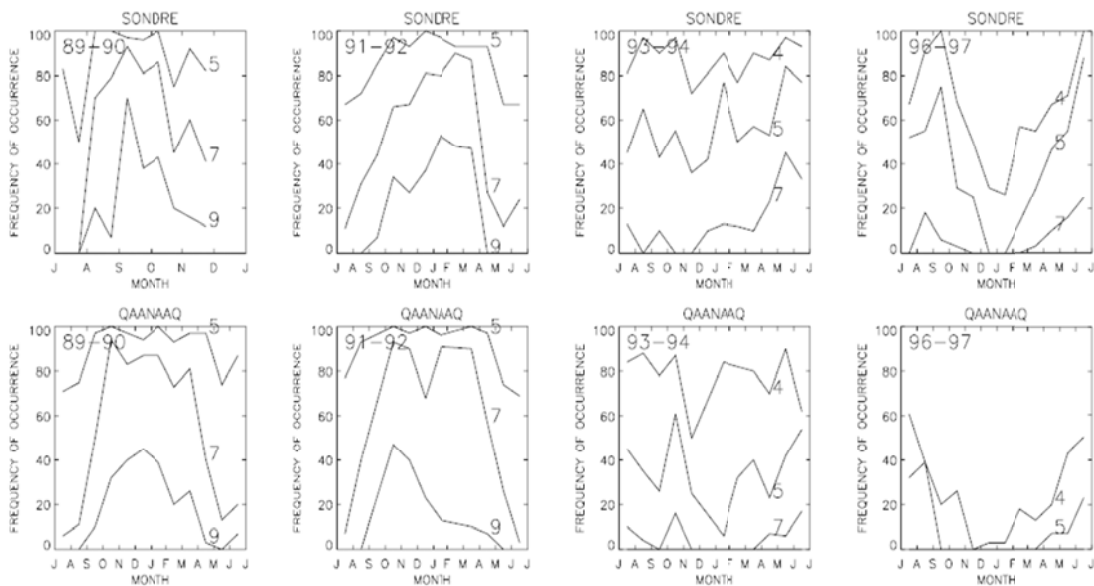


Figure 2.5: Seasonal behaviour of polar cap patches at Sondrestromfjord and Qaanaaq with respect to daily occurrence. The labels of the curves in each graph refer to levels exceeding the patch strengths. From left to right, the annual average SSN is 150, 125, 40, and 10, respectively (Source: Dandekar [2002])

In another observation using a meridian-scanning photometer (MSP), *McEwen and Harris* [1996] observed about 6 to 8 patches exist per day in the winter months at Eureka, Canada (refer to Figure 2.3 for location of this station) during the duration of four years (1990-1994). This observation is conducted during high to medium sunspot activity. In this study, the existence of patches is clearly seen as the enhancements above airglow in both 630 and 558 channels of the MSP. Patches are observed about 25 % of the time and at all hours but more frequent during local evening hours.

Signature of patches can also be observed on GPS data. *Krankowski et al.* [2006] used GPS data from the IGS network of four Antarctic stations during 2001 (refer Figure 2.6 for the locations of these stations). The enhancement of the vertical TEC is used as an indication of the existence of patches. The numbers of patches were evaluated by counting the peaks of TEC enhancement along individual satellite path. This study also used Rate of change of TEC (ROT) to estimate TEC fluctuations [*Krankowski et al.*, 2006]:

$$\text{ROT} = 9.53((\varphi_1 - \varphi_2)_{t_j} - (\varphi_1 - \varphi_2)_{t_i}) \quad (2.1)$$

where $\Delta t = t_j - t_i = 1$ min, φ_1 and φ_2 [m] are differential carrier phase observed at L1 and L2.

ROTI (Rate of TEC Index) also used based on work done by *Pi et al.* [1997] where

$$\text{ROTI} = \sqrt{\langle \text{ROT}^2 \rangle - \langle \text{ROT} \rangle^2} \quad (2.2)$$

ROTI is used as the indication of the intensity of the patches. ROTI over 5 minutes were suggested in *Pi et al.* [1997], but *Krankowski et al.* [2006] used ROTI over 30 minute interval to look at large scale irregularities. ROTI > 0.5 is classified as moderate and high intensity, where $0.2 < \text{ROTI} < 0.5$ as low intensity.

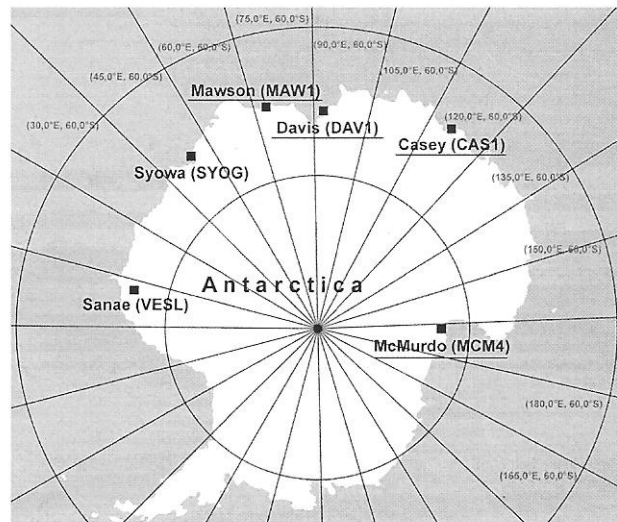


Figure 2.6: Map of southern high-latitude GPS stations. The underlined names of stations indicated the station used in the study (Source: Krankowski et al. [2006])

Krankowski et al. [2006] concluded that the maximum patch activity occurred in the winter between 0300 UT and 1100 UT at four stations, where these activities can also be observed all day at equinox. TEC fluctuation reached 10 to 40 TECU during geomagnetic disturbances in June and September 2001. TEC also increased by 10 to 50 TECU in about 5–10 min. This is about 2 to 8 times the background value.

The McMurdo station, which is the highest latitude station showed the most intense TEC fluctuation while the lowest latitude of these four stations, the Mawson station revealed the least intense TEC fluctuation. Meanwhile, *Shagimuratov et al.* [2006] reported TEC fluctuation up to 10 TECU and the TEC enhancement exceeding 2-4 times of the background value. This occurred during the magnetic storm day in July 2004 as observed at the same Antarctic stations. *Krankowski et al.* [2006] concluded that the intensity of the patches increased during geomagnetic disturbances. However, observation at these stations shows only a low degree of dependency of patch occurrence on the daily geomagnetic index. Control of UT on occurrence of patches during storm time can be seen on 18 June and 23 September 2001 (refer Figure 2.7) where TEC fluctuation took place at the same UT time regardless of location of all four stations.

At the northern hemisphere, *Gwal and Jain* [2011] conducted a study of TEC fluctuation using a GISTM receiver located at Ny-Ålesund during March 2008. Large patches of low to moderate intensity around 4 to 8 patches with ~3-8 TECU enhancement were observed on disturbed days. Patches were also found likely to exist when $B_z < 0$ and/or $K_p > 4$. *Gwal and Jain* [2011] used the same technique as *Krankowski et al.* [2006] in order to determine the number of patches. Size of the patches varied from 180 to 540 km determined based on *Basu et al.* [1998]. Plasma horizontal drift of 600 m/s was measured using digisonde at Ny-Ålesund during low solar activity during 10-11 January 1997. Patches with TEC increase of ~2 TECU were detected with duration of ~30 minutes. By combining the horizontal drift and the duration, *Basu et al.* [1998] obtained the horizontal size of the patch of ~1080 km.

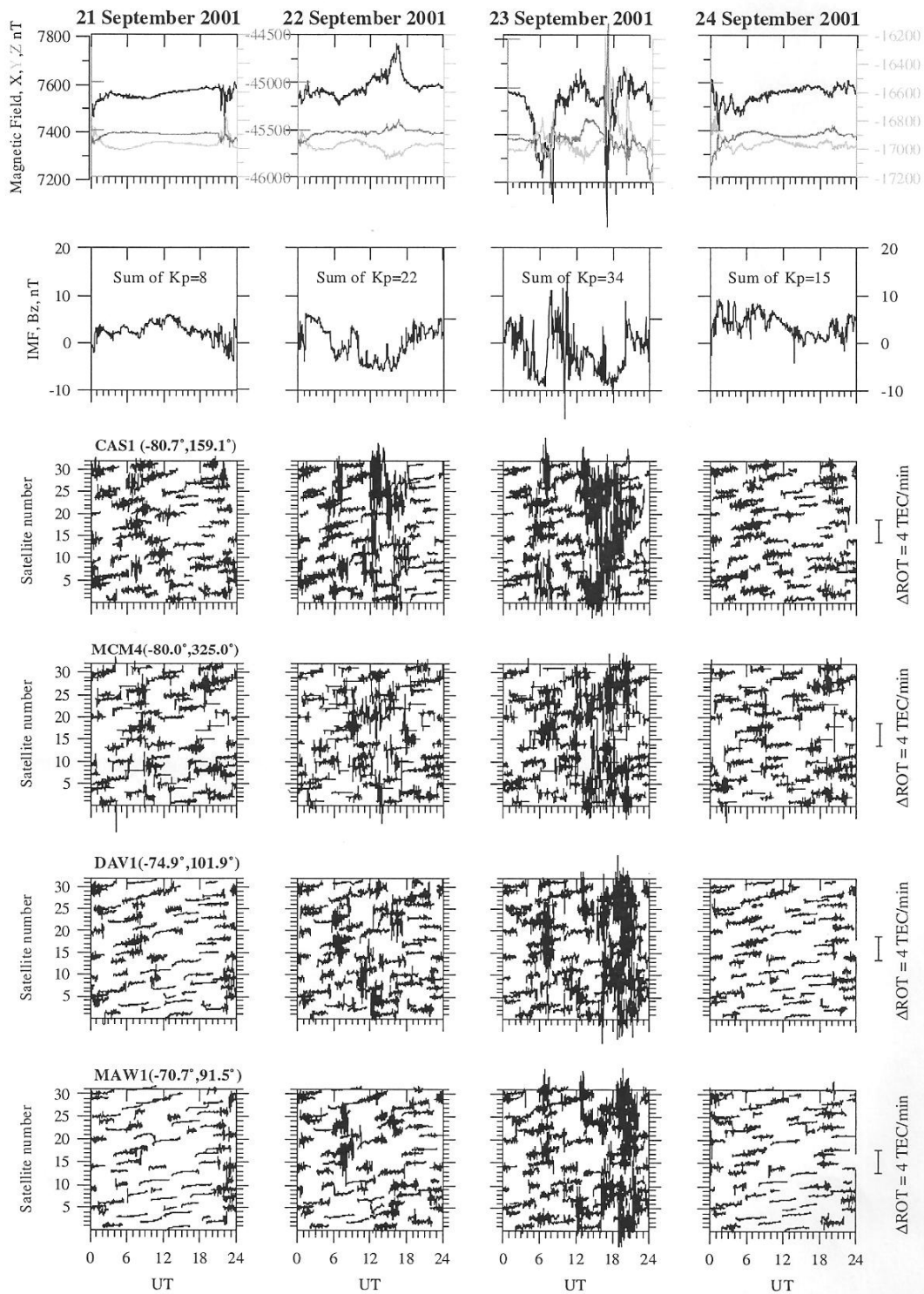
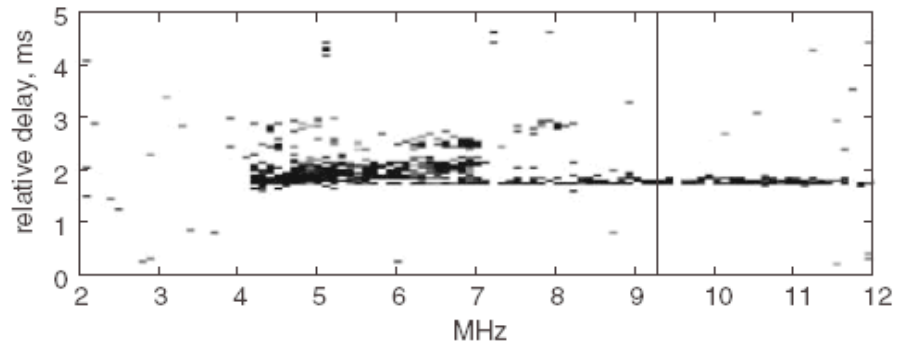


Figure 2.7: The magnetic activity at Mawson (the top panel) and the ROT occurrence (the lower panels) at different stations on 21–24 September 2001 for all individual satellite passes (Source: Krankowski et al. [2006])

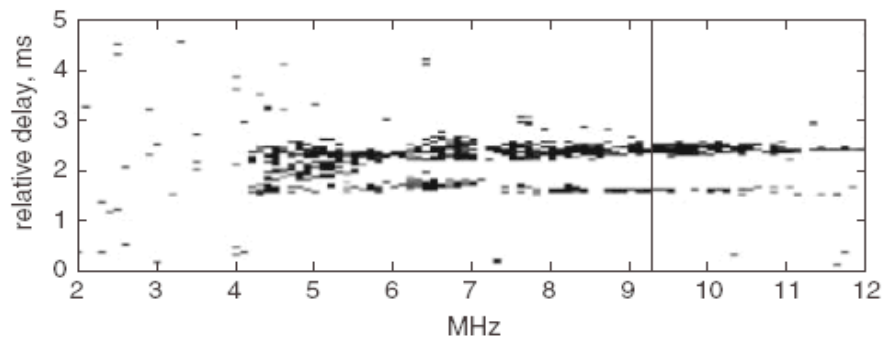
Experimental works investigating off-great-circle propagation mechanisms over the polar cap path from Iqaluit (63.7° N, 291.5° E) to Alert (82.5° N, 297.7° E) by *Rogers et al.* [2003] identified signatures on the oblique ionograms associated with the presence of the patches and arcs. Observation during a geomagnetically quiet period on 23 January 1996 (Figure 2.8) generally produced ionograms with a single or multiple thin, intense and unstructured horizontal lines, high maximum observed frequency, lack of an adjoining high angle trace, and low delay spread.

These features are observed when there is a deviation in bearing from the great-circle propagation, indicating that the reflections on the ionograms come from thin, dense ionospheric structures that drift transverse to the propagation path, which sources are most likely arcs [*Rogers et al.*, 2003]. The existence of multiple lines on the ionograms is further suggested as a result from reflections of multiple arcs.

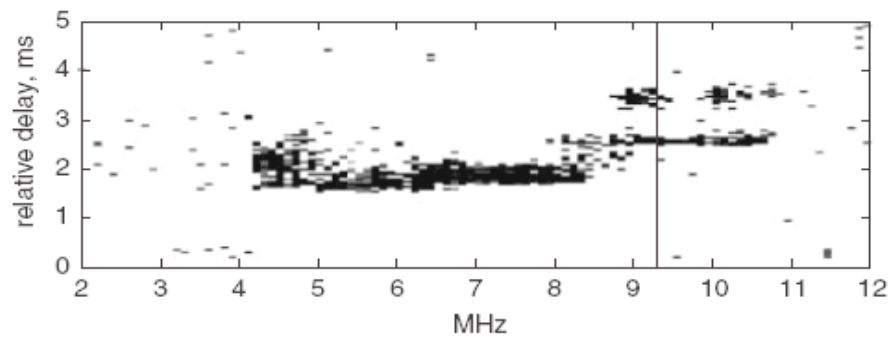
Other ionogram observation on 24 February 1996 during a geomagnetically active period shows a detached ‘nose-extension’ with spreading and slanted features, and considerable frequency and delay spread [*Rogers et al.*, 2003]. An example of these can be seen in Figure 2.9. These features indicate large scale, horizontal gradients in the electron density near the great circle path. The high geomagnetic activity during that period suggests the presence of patches, therefore these patches are most likely to be the sources of the observed features on the ionograms.



(a) 0415 UT



(b) 0515 UT



(c) 0945 UT

Figure 2.8: Oblique ionogram recorded at Alert on 23 January 1996 (Source: Rogers et al. [2003] © IEE 2003)

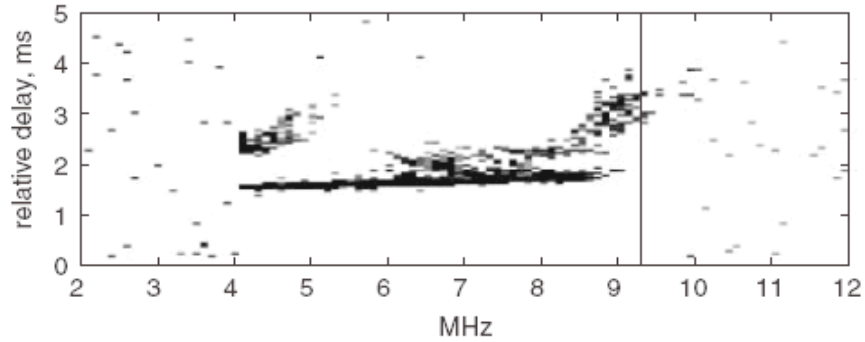


Figure 2.9: Oblique ionogram recorded at Alert at 0115 UT on 24 February 1996
(Source: Rogers et al. [2003] © IEE 2003)

Besides the experimental measurements undertaken to investigate the properties of the high latitude ionosphere, modelling studies have also been undertaken to serve this purpose. A three-dimensional ray tracing model of the polar cap features related to the HF systems has been developed by *Zaalov et al.* [2005] where a quasi-statistical approach in modelling F layer patches and arcs is adopted. Large scale features and their temporal development are modelled using ray-tracing techniques. In this model, although it is not possible to predict individual events as the precise position of polar patches and arcs is unpredictable, it is possible to predict the periods during which the large deviations in propagation from the great-circle path are likely to occur, their magnitudes and directions [*Warrington et al.*, 2006]. At present, there are no reliable self-consistent models of F layer patches and arcs of enhanced electron density in the polar ionosphere [*Zaalov et al.*, 2005].

This model includes the background ionosphere and the enhanced electron density structures due to polar patches and arcs. The model is able to reproduce the main features of the experimental data. However, many other parameters have to be considered in order to reproduce an identical match of this simulation model to the

actual measurement. Examples of the simulated oblique ionograms using this model of a polar cap path between Iqaluit and Alert in February 1994 can be seen in Figure 2.10 and Figure 2.11. The presence of patches is shown in Figure 2.10 where a detached feature with large spreading delay is evident in every ionogram. A ‘nose extension’ can also be seen in 0400 UT ionogram.

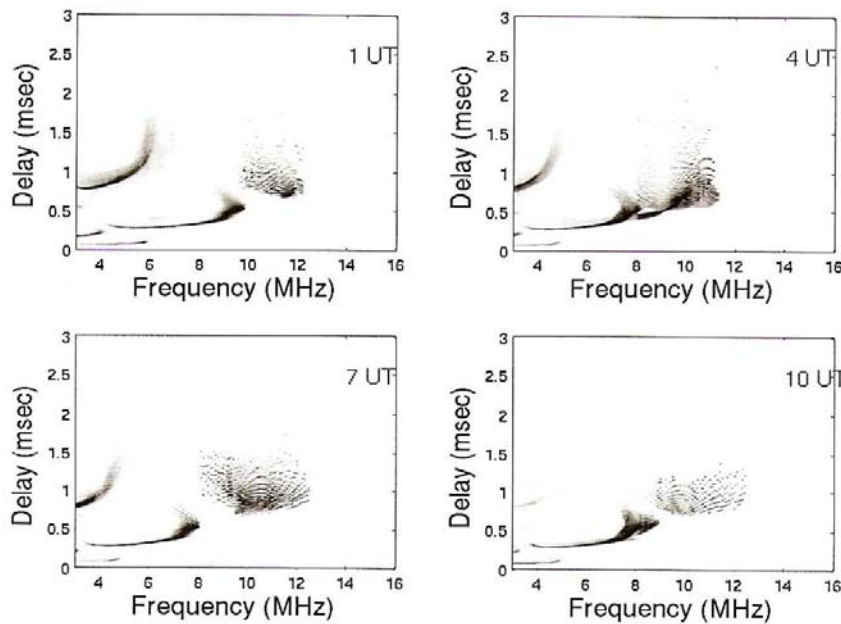


Figure 2.10: Simulated ionograms through the ionosphere containing patches (Source: Zaalov [2004])

Meanwhile, the existence of arcs is shown as the ‘nose extension’ as in Figure 2.11. Thin flat horizontal traces are a common feature on the ionogram to indicate the presence of the arcs on the path. The detached features (like on the patches-dominant ionogram) are less pronounced here, but sometimes they do exist. These features are in agreement with those normally observed in the experimental ionograms as discussed in previous works, for example in *Rogers et al.* [2003].

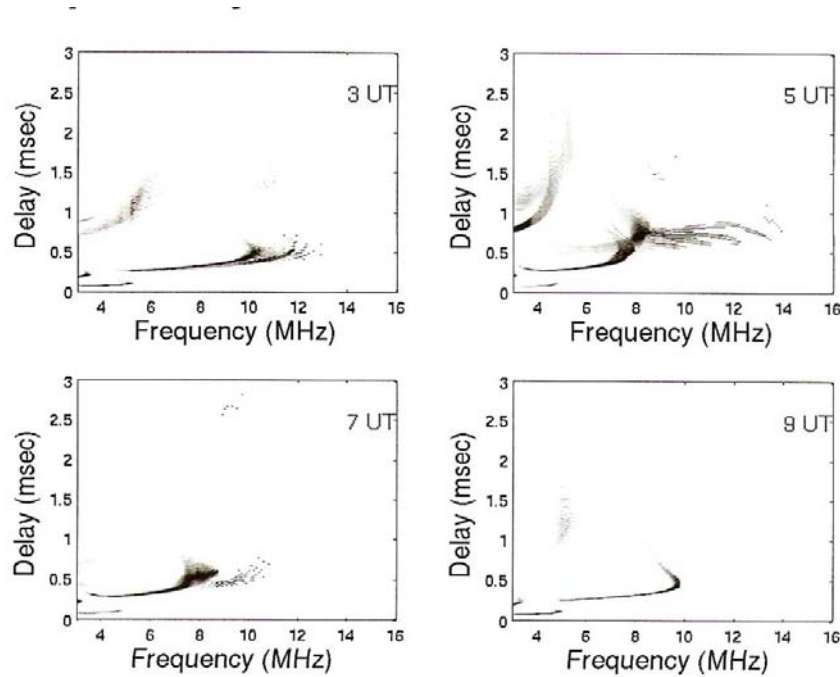


Figure 2.11: Simulated ionograms through the ionosphere containing arcs
(Source: Zaalov [2004])

2.2 Phase and Amplitude Scintillations

In addition to the association of patches and arcs with TEC enhancements, studies have also been undertaken associated with the intermediate scale irregularities (tens of metres to tens of kilometres) in the ionosphere causing rapid fluctuations in the amplitude and phase of a radio signal. These fluctuations are known as scintillations. Irregularities smaller than about 1 km produce both amplitude and phase scintillations, and irregularities larger than that produce phase scintillations only. Amplitude scintillations are caused by irregularities of scale size smaller than the Fresnel radius [Hunsucker and Hargreaves, 2003]. Phase scintillation can cause Doppler spread in the signal and may affect the phase lock of the signal within GPS receivers. The loss of lock in the GPS signals occurred when the Doppler shift

caused by rapid phase variations exceeds the bandwidth of the phase lock loop (PLL) of both L1 and L2, which are ~ 15 Hz and ~ 1 Hz, respectively [Skone, 2001]. Meanwhile, amplitude scintillation may deteriorate the signal-to-noise ratio (SNR) [Skone et al., 2001].

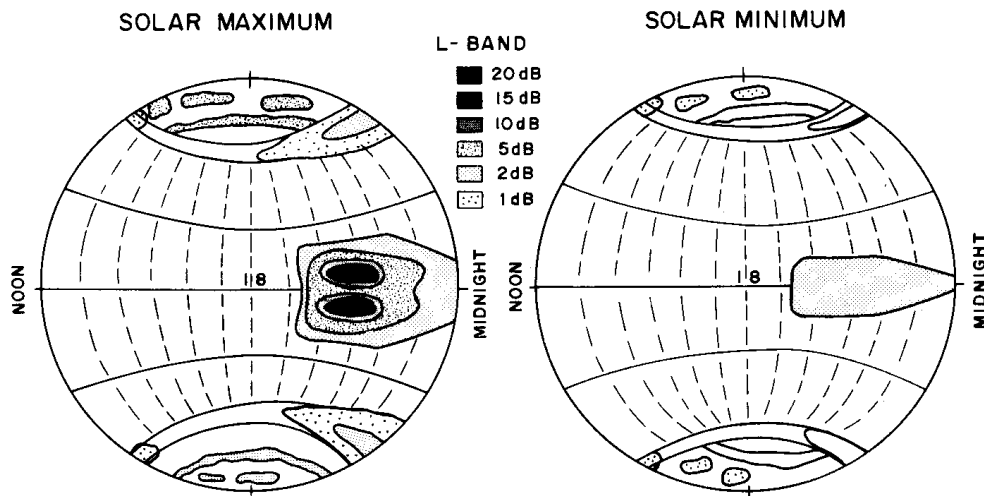


Figure 2.12: Worst-case fading depths of scintillation at L-band during solar maximum and minimum (Source: Davies [1990]. Reproduced by permission of the Institution of Engineering and Technology)

Scintillation effects on transionospheric signals have been observed on frequencies ranging from 20 MHz to about 10 GHz [Davies, 1990]. Both amplitude and phase scintillation are strongest in the equatorial, auroral and polar cap regions as illustrated in Figure 2.12. Energetic electron precipitation and current systems are the dominant factors in producing irregularities in the auroral and polar regions, where the scintillations are stronger in auroral zone [Davies, 1990]. High latitude scintillations have been widely studied using GPS receivers [Ngwira et al., 2010]. Phase scintillations in the polar cap are often associated with large-scale structures

such as patches and arcs [Spogli *et al.*, 2009]. In general, the high latitude scintillations are associated with geomagnetic storms [Skone *et al.*, 2001].

Aarons *et al.* [1981] used satellite beacon at ~250 MHz to measure amplitude scintillation at Thule, Greenland (76.537° N, 68.825° W) during April-October 1975 (period of low solar activity) and November 1978-March 1980 (high solar activity). The effects of seasonal and diurnal variations, and also solar and geomagnetic activity were investigated and the results are presented in Figure 2.13.

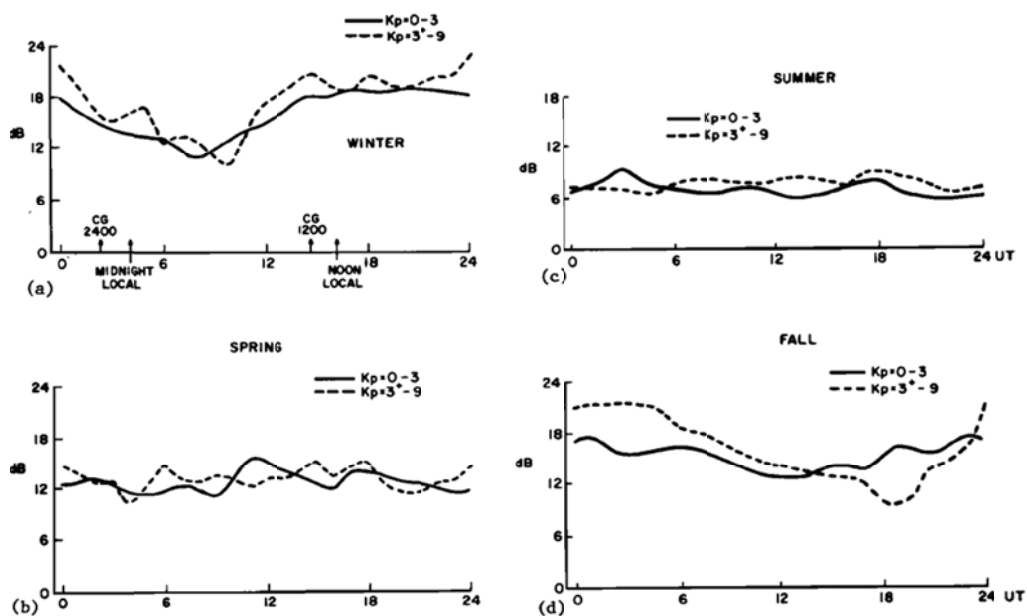


Figure 2.13 Mean value of scintillation (in dB) observed at Thule for both quiet and disturbed magnetic activity periods in (a) winter (November-January), (b) spring (February-April), (c) summer (May-July), (d) fall (August-October) (Source: Aarons *et al.* [1981])

In general, the lowest scintillations occur in summer and the largest in autumn and winter. Meanwhile, there are only slight differences in average scintillation levels for low and high geomagnetic activity, and also little diurnal variations in any season. In addition, even with low magnetic activity, the year of high solar flux (i.e. 1979) clearly shows increases in the intensity and in the occurrence of ionospheric irregularities which produce scintillations on a satellite (Figure 2.14).

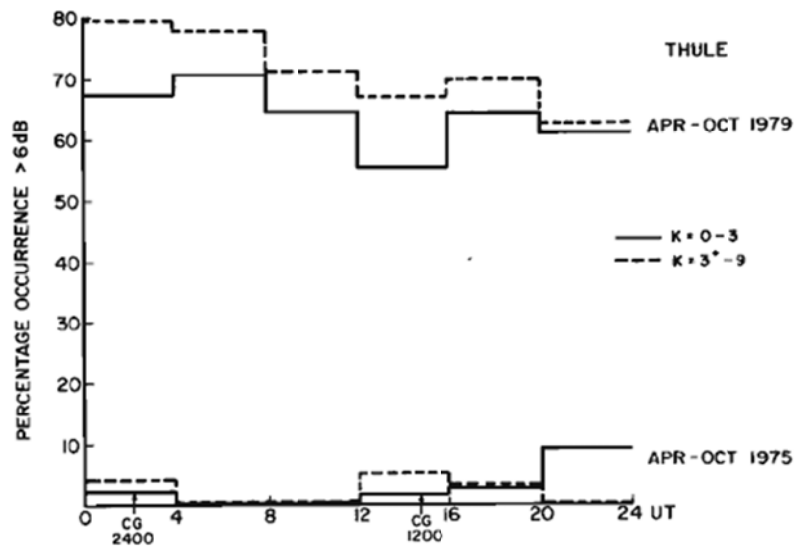


Figure 2.14: Percentage occurrence of scintillation greater than 6 dB for April-October 1975 (10.7 cm flux of ~45) and April-October 1979 (10.7 cm flux of ~150-225) for both quiet and disturbed magnetic conditions (Source: Aarons et al. [1981])

In more recent work by *Aarons and Lin* [1999] using GPS data also indicates a low level of phase scintillation at Thule even during severe magnetic storms in January, April and May 1997. In terms of solar dependency, the scintillations are high in the period of high solar activity even when the geomagnetic activity is low.

Recent work by *Li et al.* [2010] over the period of solar minimum (2007-2008) at two polar region stations at Ny-Ålesund, Svalbard (78.9°N, 11.9°E) and Larsemann Hill, East Antarctic (69.4°S, 76.4°E) concluded that phase scintillation and irregularities observed from GISTM receivers mainly takes place in October, November and December at Ny-Ålesund, and in May and June at Larsemann Hill. This is in agreement with the finding by *Aarons et al.* [1981].

Basu et al. [1987] reported that the median of the amplitude scintillation index, S4 is 0.5 at 250 MHz at a polar cap location (Thule), which is slightly higher than that recorded in an auroral oval area (Goose Bay). There is also an absence of diurnal variation of scintillation level. In addition, the long-term morphology (1979-1984) of amplitude scintillations in the polar cap (Figure 2.15) shows that, besides the presence of an annual variation with minimum scintillations during summer, there exists a pronounced solar control of scintillation activity, where it decreases when solar activity falls.

Spogli et al. [2009] conducted a study for the period from October to December 2003 using four GISTM receivers at different mid to high latitude stations from 52.9° N to 78.9° N. The period of observation was subjected to two intense geomagnetic storms that were investigated by others, for example *Mitchell et al.* [2005] and *Momani et al.* [2008]. By assuming a quiet day if when every K_p value is less than 5 and if 50% of values in that day is less than or equal to 4, *Spogli et al.* [2009] concluded that half of the days in each month is geomagnetically disturbed.

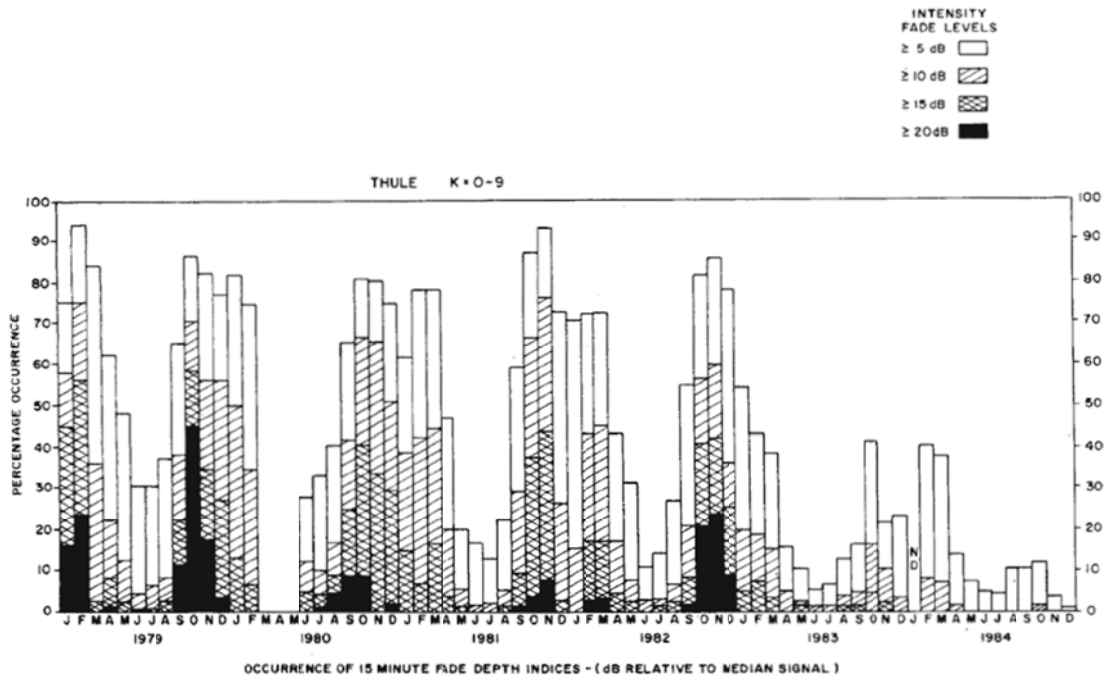


Figure 2.15: Thule scintillation intensity statistics at 250 MHz during 1979-1984
 (Source: Basu et al. [1987] © 1987 IEEE)

Percentage of occurrence for phase scintillation, $\sigma_\phi > 0.25$ rad and $S_4 > 0.25$ of 3-hour duration (in MLT) and 2° -step of magnetic latitude for the whole period of observations were computed. The authors chose to use vertically projected scintillation values to account for the effect of varying geometric conditions when using different elevation angles. Using all data for all four stations, the polar area is found to be more sensitive to the phase scintillation ($\sim 2.8\%$) than amplitude scintillation ($\sim 0.16\%$).

This is consistent with the finding by *Li et al.* [2010] using regular scintillation indices (i.e. non-vertically converted). The study conducted at Ny-Ålesund for a longer period and at solar minimum from August 2007 to July 2008 also demonstrated that phase scintillations were more significant than amplitude scintillation. This is also true at a southern polar region station at Larsemann Hills

(March to November 2007). Note that *Li et al.* [2010] used CGM Latitude for analysis while *Spogli et al.* [2009] employed Altitude Adjusted CGM Latitude.

Spogli et al. [2009] also highlighted that increased phase scintillation around magnetic local noon can be seen mainly in Ny-Ålesund station (Figure 2.16, top left) while during midnight, the enhancements are evident in Hammerfest (top right) and Brønnøysund (bottom left). Both stations are in auroral region. Only weak scintillations were observed in Nottingham (bottom right), a mid-latitude station.

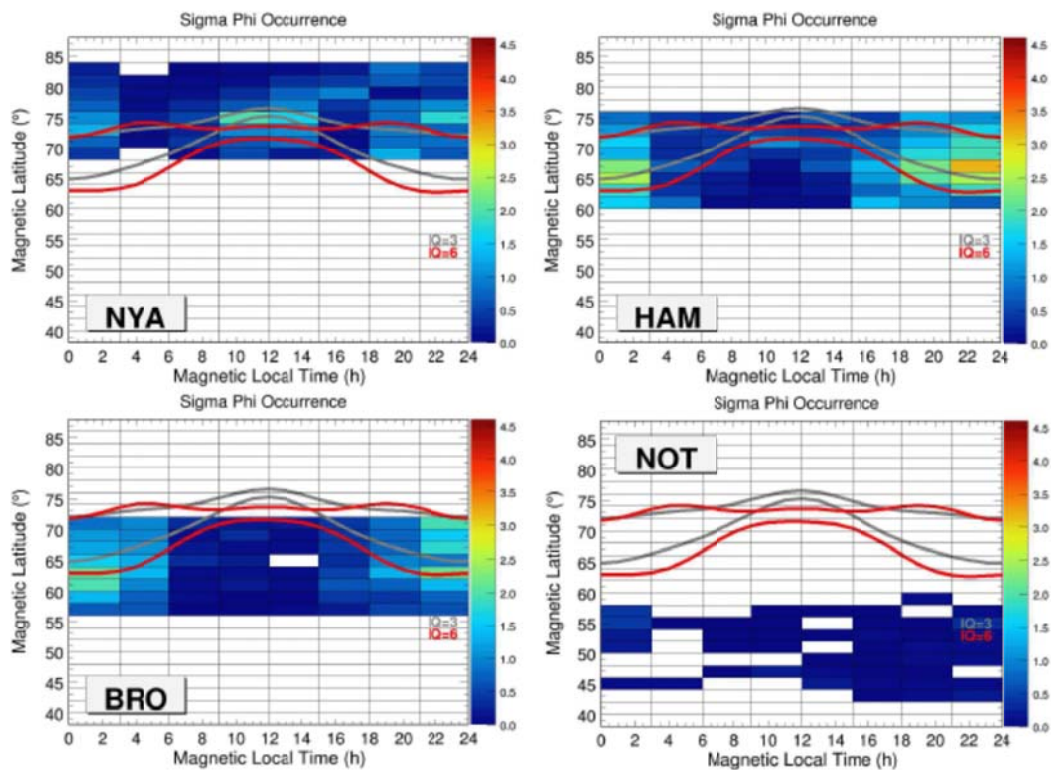


Figure 2.16: Phase scintillation maps of all days (disturbed and quiet) and for each station separately. In grey is the quiet Feldstein oval (i.e. auroral activity, $IQ=3$), while in red is the disturbed oval (i.e. $IQ=6$) (Source: *Spogli et al.* [2009])

Contour plots of percentage of occurrence of $S4 > 0.25$ and $\sigma_\phi > 15^\circ$ (i.e. 0.26 rad) and 10° (i.e. 0.17 rad) presented by *Li et al.* [2010] are reproduced in Figure 2.17. Since it involved a longer period of observations, significant phase scintillations were observed to be more frequent in local winter months. With reference to magnetic local time, high occurrence of $\sigma_\phi > 15^\circ$ is found during 0800-1300, 1600-1800 and 2300-0200 MLT at Ny-Ålesund and between 0500-1100 and 1900-2200 MLT at Larsemann Hills (Figure 2.18). Using lower threshold of $\sigma_\phi > 10^\circ$ yields that the maximum occurrence at Ny-Ålesund is centred around magnetic noon.

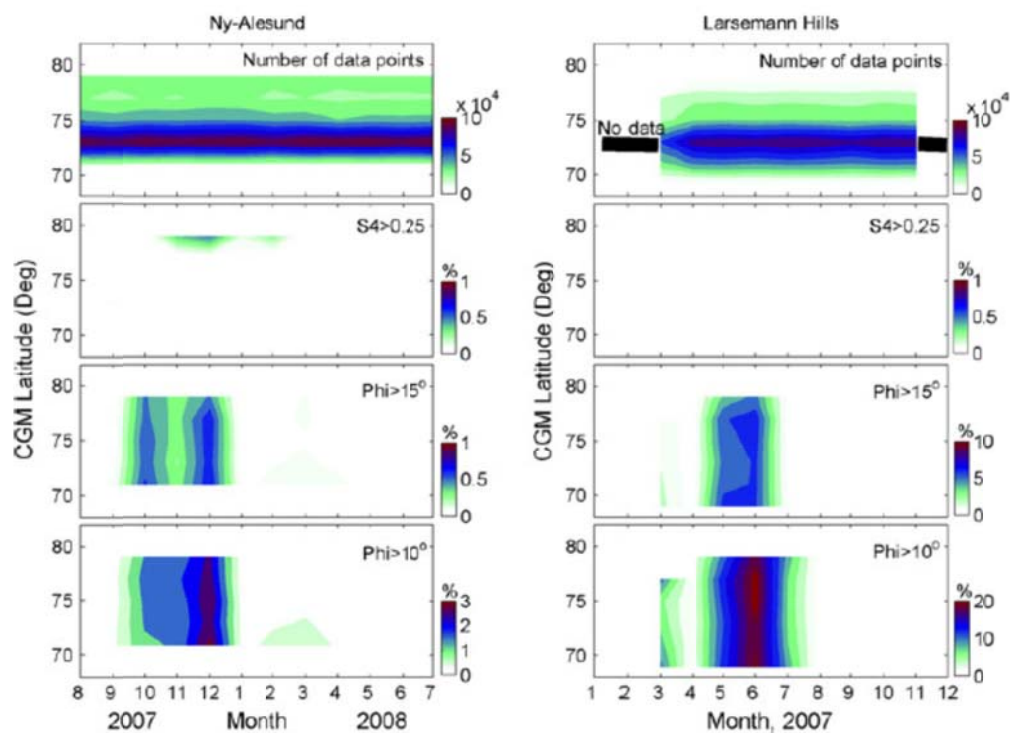


Figure 2.17: Contour plots of percentage occurrence of amplitude ($S4 > 0.25$) and phase scintillation ($\sigma_\phi > 15^\circ$ (i.e. 0.26 rad) and 10° (0.17 rad)) as a function of corrected geomagnetic latitude and month for observations made at Ny-Ålesund and Larsemann Hills (Source: Li et al. [2010])

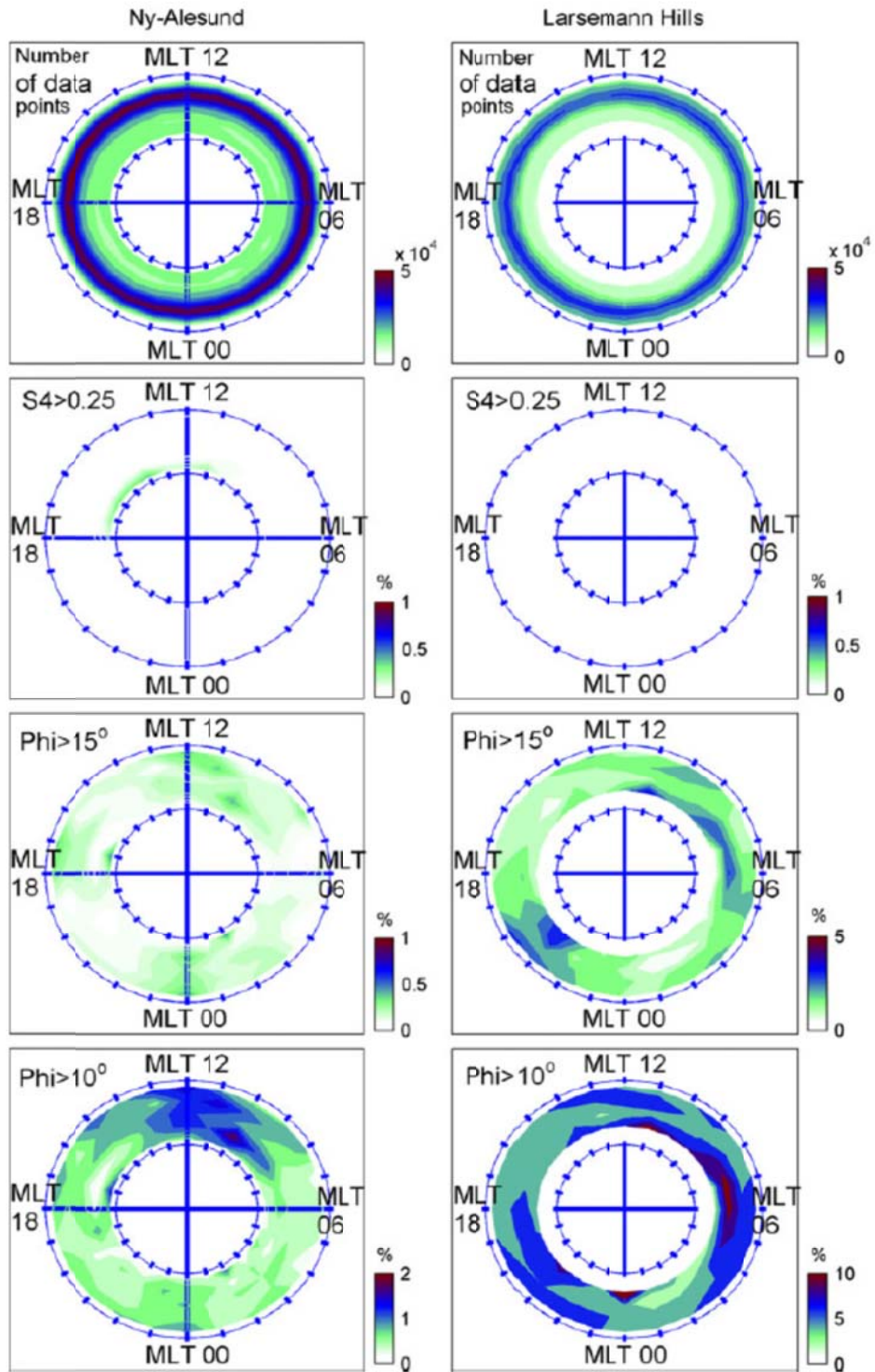


Figure 2.18: Percentage occurrence of amplitude ($S_4 > 0.25$) and phase scintillation ($\sigma_\phi > 15^\circ$ (i.e. 0.26 rad) and 10° (0.17 rad)) as a function of corrected geomagnetic (CGM) latitude and MLT observations made at Ny-Ålesund and Larsemann Hills
Source: Li et al. [2010]

This is in agreement with finding by *Spogli et al.* [2009] but at different scintillation intensity scale. *Li et al.* [2010] also studied the dependence of phase scintillation on B_y and B_z and concluded that the dependence appeared to be associated with magnetic local time at both stations. Phase scintillation occurrence level is higher from late afternoon to sunset (1600-1900 MLT) at Ny-Ålesund, and from sunset to pre-midnight (1800-2300 MLT) at Larsemann Hills.

Gwal and Jain [2011] studied the irregularities at Ny-Ålesund in March 2008 and applied similar method as *Spogli et al.* [2009] but used a threshold of $S4 > 0.25$ and $\sigma_\phi > 0.2$ rad, and the percentage of occurrence is calculated for each day for every 2° magnetic latitude, MLat and 2-h MLT. Result indicated phase scintillations occurred more frequent ($\sim 7\%$) than amplitude scintillations ($\sim 0.25\%$) and S4 seems confined to well-defined regions due to the influences of small scale irregularities, while σ_ϕ is characterised by MLat and MLT. These finding are consistent with previous works at the same location conducted by *Spogli et al.* [2009] and *Li et al.* [2010]. *Spogli et al.* [2009] and *Gwal and Jain* [2011] agreed that both phase and phase scintillation occurrence at Ny-Ålesund increased during disturbed days compared with quiet days.

Data from Canadian High Arctic Ionospheric Network (CHAIN) were used in *Prikryl et al.* [2010] to study ionospheric variability over few high latitude locations including at a polar cap station at Resolute Bay (74.7° N, 265.1° E) using GPS data from 2008 to 2009. *Prikryl et al.* [2010] found that amplitude scintillation was very low, but phase scintillation was still observed, consistent with findings by *Spogli et al.* [2009], *Li et al.* [2010] and *Gwal and Jain* [2011] at Ny-Ålesund. Phase

scintillation is low when the plasma density is expected to be low, particularly in winter before about 1200 UT. However, mean σ_ϕ is higher than average around local magnetic noon from April to November (Figure 2.19).

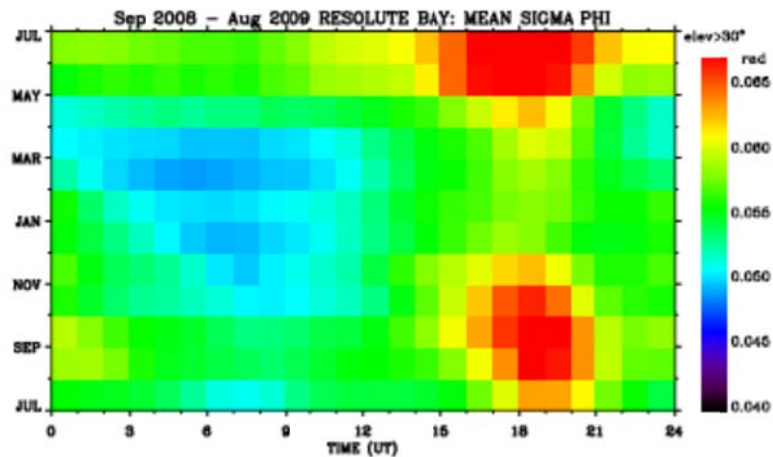


Figure 2.19: Mean σ_ϕ for Resolute Bay from September 2008 to August 2009. Magnetic local midnight and noon at Resolute Bay is around 0710 and 1940 UT, respectively (Source: Prikryl et al. [2010])

Prikryl et al. [2010] also studied mean TEC variations at Resolute Bay for the same period as scintillation observations. The mean TEC shows the expected seasonal and UT variation of electron density of high latitude. The value is high in summer due to longer daylight and low in winter corresponding to prolonged darkness. Diurnal variations were observed and they maximised around winter solstice due to the offset of the magnetic and geographic poles.

Several authors have discussed the co-existence of TEC fluctuations and amplitude and/or phase scintillations, with more emphasis given to storm events. Mitchell et al. [2005] highlighted the coincidence of increased vertical TEC values and both the amplitude and phase scintillations during a geomagnetic event on 30 October 2003.

These are observed from a GISTM located at Ny-Ålesund. The scintillations were observed around the edge of TEC increase. The authors suggested that the scintillations on the edge were likely generated by the gradient-drift instability mechanism. In addition, ionospheric images produced by the multi-instrument data analysis system (MIDAS) indicate that the high TEC values over Svalbard during this period have originated from the convection of plasma from the North America region [De Franceschi *et al.*, 2008].

The effects of geomagnetic storms on October 2003, November 2003 and July 2004 were investigated at quasi-conjugate locations at Scott Base, Antarctic (77.85°S, 327.23°E) and Resolute Cornwallis Island, Canada (74.69°N, 265.12°E) using Trimble 5700 and Ashtect UZ-12 dual-frequency receivers, respectively [Momani *et al.*, 2008]. Pronounced phase scintillations were observed at the nightside hemisphere while only weak scintillations were detected at the conjugate dayside hemisphere. Enhanced TEC and severe phase scintillations also coincided with the long duration of southward IMF. However, both stations responded differently to the IMF. At the nightside hemisphere, strong phase scintillations and enhanced TEC occurred almost simultaneously with the timing of southward B_z . Meanwhile, at the dayside hemisphere, the response lagged about 2 to 6 hours.

Besides the experimental works, scintillation modelling has also been developed. For example, a numerical and analytical model characterizing the transionospheric propagation channel has been developed by Gherm *et al.* [2000]. It is an extension of their previous work on the HF ionospheric fluctuating channel of propagation using complex phase method. In Gherm *et al.* [2000], several parameters, for example the

effect of Earth's magnetic field and the dependence of the curved path of propagation on transmission frequency are taken into account. This model is able to describe a variety of propagation conditions, including different models of the background ionosphere, ionospheric fluctuating parameters, and geometry and orientation of the propagation path.

Meanwhile, a hybrid (a combination of the complex phase method and the technique of a random screen) model has been developed by *Gherm et al.* [2005]. In addition, a high-latitude climatological scintillation model was developed by *Wernik et al.* [2007] using Dynamics Explorer 2 retarding potential analyser plasma density data, IRI ionosphere model, and the phase screen propagation model. The results from this model were able to reproduce the measured data.

2.3 HF Channel Characteristics at High Latitude

HF channel characteristics such as Doppler and multipath spreads, Doppler shift, and signal to noise ratio, are normally subjected to investigation for a better understanding of the ionospheric condition. Studies have been conducted focusing on the HF channel characteristics over high latitudes by several authors including *Cannon et al.* [1995], *Broms et al.* [1997], *Warrington* [1998], *Jacobsen et al.* [2000], *Warrington et al.* [2006], and *Vilella et al.* [2008]. Doppler and multipath effects are more prevalent at high and equatorial latitudes than at mid latitudes [*Angling et al.*, 1998].

A channel sounder network known as DAMSON (Doppler and Multipath Sounding Network) has been used extensively to develop better understanding of HF channel characteristics. DAMSON employed a number of sounding waveforms at a set of pre-determined frequencies ranging from 2 to 30 MHz. It quantifies the characteristics of HF channel by measuring frequency dispersion of Doppler spread and shift, and also multipath dispersion. The GPS system was used to synchronise transmitter and receiver, and also to allow Time of Flight (TOF) to be determined [Angling *et al.*, 1998].

DAMSON operates using several modes including a noise measurement period lasting 2.8 s and 4 s of CW transmission [Cannon *et al.*, 1992]. Another mode is using 13-bit Barker coded BPSK modulated at 2400 baud. This configuration was employed by Cannon *et al.* [1995], Broms *et al.* [1997], Angling *et al.* [1998], Warrington [1998] and Warrington *et al.* [2006]. The difference in the output lies in the different period of code length and the Pulse Repetition Interval (PRI) that will give different Doppler frequency range and the frequency resolution.

Several high latitude paths have been studied by several authors, e.g. Cannon *et al.*, [1995], Broms *et al.* [1997], and Angling *et al.* [1998] for different periods and geomagnetic conditions. Those paths are summarised in Table 2.1. Several campaigns were conducted from 1994 to 1995 over these paths. Geographic coordinates for these stations and the locations on the map is shown in Figure 2.20.

Table 2.1: Path lengths of high latitude campaigns observing HF channel characteristics using DAMSON (Source: Angling et al. [1998])

Path	Length (km)
Isjford-Tuentangen	2019
Isjford-Kiruna	1158
Harstad-Tuentangen	1019
Harstad-Kiruna	194

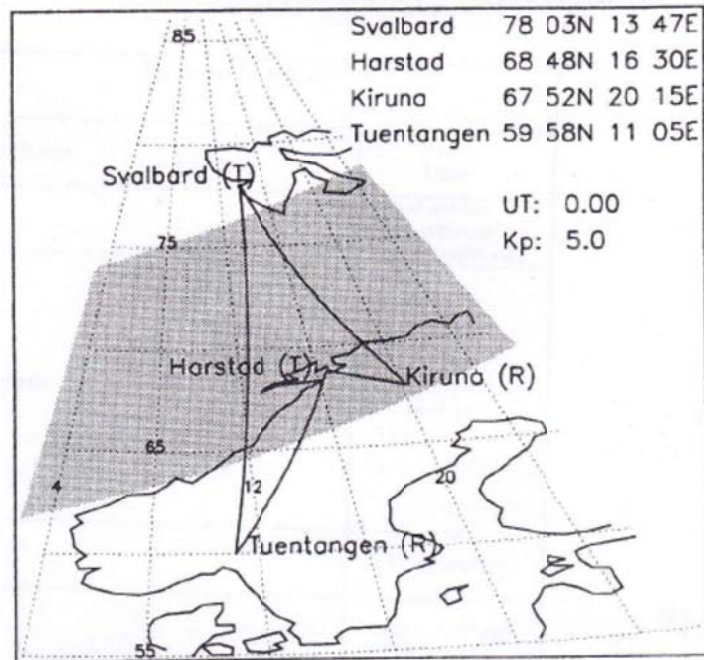


Figure 2.20: Map showing the location of four Scandinavian stations. Approximate location of auroral oval during high geomagnetic activity is also illustrated in grey (Source: Angling et al. [1998])

Cannon et al. [1995] conducted a study from 23 August to 1 September 1994 over the path from Isjford to Tuentangen. The measurements show that even though the Doppler spread can reach up to ~ 20 Hz, the spreads were actually much less than this with a mean value of 4.7 Hz. The spreads were also found to be very much higher on the lower frequencies than on the higher frequencies, particularly for all frequencies above 5 MHz. This is in contrast with the Doppler equation where a bigger Doppler

shift/spread is expected at higher frequency. In addition, higher mean Doppler spread of ~ 7 - 7.5 Hz is registered during pre- (1800-2400 UT) and post-midnight (0000-0600 UT), in contrast with the mean of only ~ 1.9 to 3.1 Hz at other time windows.

Angling et al. [1998] conducted observations during 1995 on all four high latitude paths described in Table 2.1. Doppler spreads range from ~ 2 to ~ 55 Hz at 95% of the times and generally increased with the increasing frequency, with noticeable exception over Isjford to Tuentangen (i.e. the longest link) where the Doppler spread is the highest (~ 13 Hz) in the lowest frequency band (2.8-4.7 MHz), and the lowest (~ 8 Hz) in the highest band (14.4-21.9 MHz).

Broms et al. [1997] utilised the DAMSON system studying the channel characteristics from 16 to 22 October 1995, which is the period of several ionospheric disturbances. The path of interest is over auroral zone from Harstad to Kiruna (194 km) and from Harstad to Tuentangen (1019 km). Doppler spreads and shifts were reported to be in general, correlated with the level of ionospheric disturbances. Observations made by *Jacobsen et al.* [2000] using ground-based magnetometers during magnetic disturbances concluded that although several cases of good correspondence between increases on Doppler spread and magnetic variation occurred, this was not apparent at all times.

Measurements for signals received over the transauroral path from Isjford, Svalbard to Cricklade, UK (3073 km path length – see Figure 2.21) were conducted on 7 days in late 1995 and early 1996 by *Warrington* [1998] where variety of signal

characteristics were observed. At times the signal did not exhibit significant Doppler spread, whereas at other times large spreads were occasionally observed. Measurements on a polar path from Isfjord to Alert, Canada (1383 km) on 22 and 25 January 1996 showed greater spreads than those observed on Isfjord-Cricklade transauroral path.

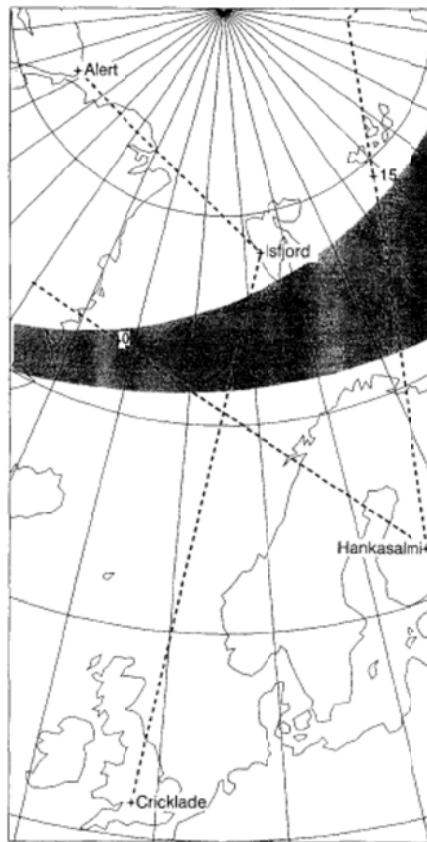


Figure 2.21: Map showing the path from Isfjord to Cricklade and from Isfjord to Alert. Auroral oval location is also illustrated at 1500 UT with $K_p=3$ (Source: Warrington et al. [2006])

Another measurement of HF channel spread characteristics has been done by Warrington et al. [2006] from 2003 to 2005 on eight different frequencies. Observations were conducted over two paths to Kiruna (in northern Sweden) from

Adventdalen, Svalbard (1152 km path length) and also from Bjørnsund near to Kirkenes in northern Norway (430 km).

Results yield complex characteristics of the received signals. Composite Doppler spreads at the 95% level (for peak-to-mean power ratio greater than 3.5) tends to increase with increasing frequencies for Kirkenes-Kiruna (i.e. the shorter path). In addition, a model incorporating channel scattering characteristics has been developed by *Warrington et al.* [2006]. A number of test cases that are representative from the observation of individual soundings are identified. The model is capable to reproduce the nature of test soundings.

In another instance, a very long distance HF link from Antarctica to Spain (~12700 km) is established from December 2006 to February 2007 covering both hemispheres [*Vilella et al.*, 2008]. The channel is sounded hourly on 25 frequencies from 5 to 17 MHz. The maximum Doppler spread is around 1.5 Hz under different conditions, and the minimum is around 0.5 Hz at higher frequencies at sunrise. Two time intervals are observed. Firstly, from 2300 UT to 0400-0500 UT, the composite multipath spread decreases with increasing frequency whereas the composite Doppler spread is unchanged. This coincides with the absence of solar radiation along the link. Typical spread values during this period are 1.5 ms and 1 Hz. Secondly, from 1800 UT to 2300 UT and from 0500-0600 UT to 1100 UT, the multipath and Doppler spread are strongly varying. This is partially due to the variability in the ionosphere during sunrise and sunset.

Chapter Three: Experimental Configuration

A transionospheric link via GPS signals detected at Alert, Canada is used to observe TEC fluctuations and also both amplitude and phase scintillations over this area. In addition, a HF link from Qaanaaq, Greenland to Ny-Ålesund, Svalbard has been established in order to study the scattering characteristics.

The aim of the investigation is to look at the relationship between the irregularities the polar ionosphere (i.e. polar patches and arcs, scintillations), and the HF channel signalling characteristics. We are also interested in the behaviour of the transionospheric signals, in particular near the HF path midpoint, to see if there is any relation to the HF link characteristics.

This study covers a total period of time of 33 months from end of May 2008 to February 2011 where this period mostly within the period of the minimum state of solar activity. Figure 3.1 illustrates the daily sunspot number (SSN) for the whole period of observations. SSN mostly did not exceed 10 during 2008. This value slightly increased to ~30 at the end of 2009. In 2010, SSN reached up to ~48 and increased up to ~53 at the end of observation period in February 2011. In addition, this solar cycle reached the lowest minimum in the last five cycles as illustrated in Figure 3.2. Therefore, it will be interesting to study the ionospheric variability at the polar cap area as not only it was during the increasing sunspot number from the minimum state, this period also the at the lowest SSN minimum in the last five cycles.

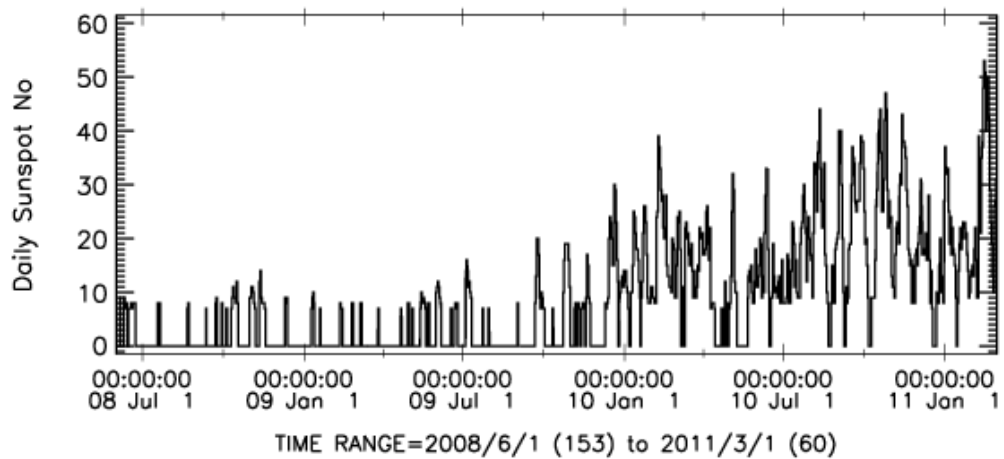


Figure 3.1: Daily Sunspot Number, SSN from June 2008 to February 2011
(Source: <http://cdaweb.gsfc.nasa.gov>)

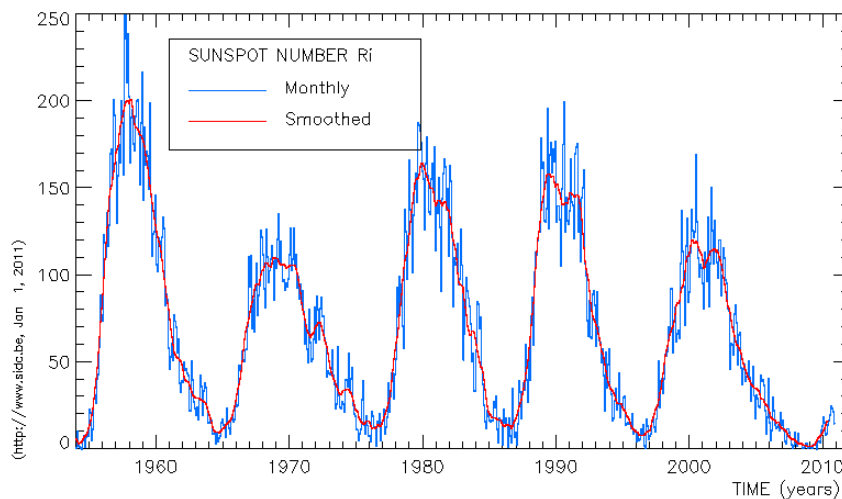


Figure 3.2: Illustration of sunspot number for the last five cycles
(Source: <http://www.sidc.be>)

During the period where data were not overlapping from both sources, observations were done by looking at the TEC variations and both phase and amplitude scintillation at Alert, Canada from the GISTM receiver. On the other hand, data from HF link transmitted from Qaanaaq to Ny-Ålesund were used to analyse channel

characteristics. GPS data from GISTM receivers at Ny-Ålesund and Longyearbyen, Svalbard were also used in addition to the HF data.

During the period of where both GPS (at Alert) and HF data were available (i.e. from March 2009 to July 2010), data from HF and transionospheric links are compared to see any relation between these two. Area of interest is around the midpoint of HF link between Qaanaaq and Ny-Ålesund. Doppler spreads are compared with TEC and scintillations information from GPS receivers at Alert and also at Svalbard.

At all times, data were used together with the information of geomagnetic conditions to help establish any relation to the observed parameters. The IMF data were obtained from the Space Physics Data Facility of Goddard Space Flight Center website (<http://cdaweb.gsfc.nasa.gov>). In addition, geomagnetic data from two polar stations at Eureka (80.0°N, 274.1°E) and Resolute Bay (74.7°N, 265.1°E) were also utilised. Data from these stations were obtained from Natural Resources Canada website (<http://www.geomag.nrcan.gc.ca>). The locations of all stations are depicted in Figure 3.3. Note that the magnetic observatory at Eureka is closer to the geomagnetic pole compared to Resolute Bay station.

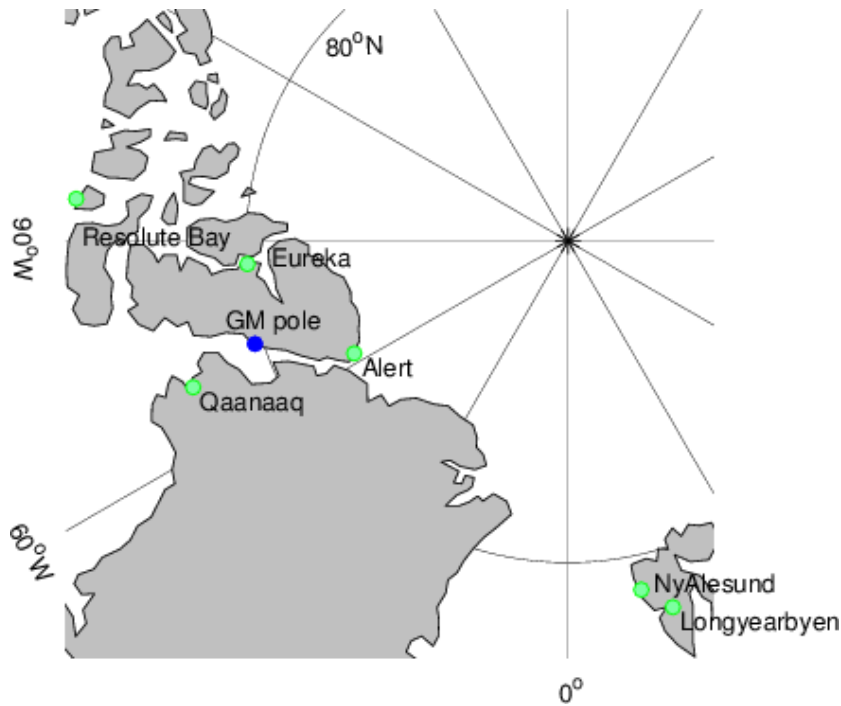


Figure 3.3: Location of HF transmitter (Qaanaaq) and receiver (Ny-Ålesund), GPS receivers at Alert, Ny-Ålesund and Longyearbyen, and magnetic observatories at Eureka and Resolute Bay. The geomagnetic pole is indicated by the blue circle.

3.1 Transionospheric Link

A dual-frequency (L1 frequency at 1575.42 MHz, and L2 frequency at 1227.6 MHz) GPS receiver, GSV4004B, has been installed at Alert, Canada since end of May 2008. For the purpose of this study, data until July 2010 is used for analysis. This GISTM receiver is specifically configured to measure amplitude and phase scintillation from the L1 frequency, and TEC from the L1 and L2 frequencies. The GISTM receiver computes the TEC, and both amplitude and phase scintillations.

The delay of the transmitted signal from a GPS satellite on L1 and L2 is used to measure the electron content along the propagation path as these delays are proportionate to each other. TEC is a measure of the number of electrons in a vertical

column with a cross-section of 1 m^2 that extends along the way from the transmitter to receiver. Using GSV4004B, the TEC (in TECU, where $1 \text{ TECU} = 1 \times 10^{16} \text{ electrons m}^{-2}$) can be determined following *GSV GPS Silicon Valley* [2007]:

$$TEC = [9.483 \times (PR_{L2} - PR_{L1} - \Delta_{C/A-P,PRN}) + TEC_{RX} + TEC_{CAL}] \quad (3.1)$$

where

PR_{L2} : L2 pseudorange (metres)

PR_{L1} : L1 pseudorange (metres)

$\Delta_{C/A-P,PRN}$: input bias between satellite C/A- and P-code chip transitions (metres)

TEC_{RX} : TEC due to internal receiver L1/L2 delay (TECU)

TEC_{CAL} : user defined TEC offset (TECU)

$\Delta_{C/A-P,PRN}$ is the bias for each individual satellite and can be included either during hardware initialization process or added later on to the recorded TEC values. These bias values are available from IGS website. However, these biases are not used in this study, therefore the TEC values presented here is a relative one rather than an absolute value. The receiver bias has already been calibrated by the manufacturer with the value of -51.12 TECU.

The value computed by the GPS receiver is the slant TEC (STEC). Conversion from slant to vertical TEC (VTEC), can be achieved by assuming a thin-shell model and a horizontally uniform ionosphere [*Nava et al.*, 2007]:

$$VTEC = STEC \cos(\chi) \quad (3.2)$$

where $\cos(\chi)$ is the mapping function:

$$\cos(\chi) = \sqrt{1 - \left(\frac{R_E}{R_E + h_{pp}} \cos(E)\right)^2} \quad (3.3)$$

where χ is the satellite zenith angle at the sub-ionospheric pierce point, R_E is the radius of the earth, E is the satellite elevation angle, h_{pp} is the height of the sub-ionospheric pierce point (refer Figure 3.4).

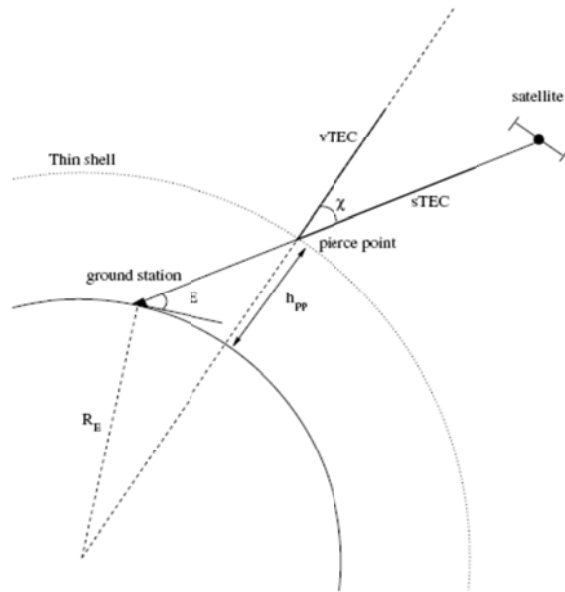


Figure 3.4: Geometry for the conversion from slant to vertical TEC
(Source: Nava [2007])

Other important parameters are Rate of TEC (ROT), and its index, ROTI. The Rate of TEC (ROT (in TECU)) is already computed by the GSV4004B based on the carrier phase measurement at L1 and L2 [*GSV GPS Silicon Valley, 2007*]:

$$\text{ROT} = 1.1723\Delta PR_{L1,carrier} \quad (3.4)$$

measured over 1-sec interval, where

$$\Delta PR_{L1,carrier} = 1.54573(\Delta ADR_{L1} - \Delta ADR_{L2}) \quad [\text{cycles}] \quad (3.5)$$

measured over 15-sec interval, where ΔADR_{L1} and ΔADR_{L2} are the phase measurement for L1 and L2, respectively.

ROT Index (ROTI) is used as an indication of the intensity of the patches. Two different values of ROTI (refer Equation 2.2) are computed, which are over 5-minute interval and also 30-minute interval as suggested by *Pi et al. [1997]* and *Krankowski et al. [2006]*, respectively. Larger interval is used to look at large scale irregularities. *Basu et al. [1998]* measured the horizontal drift of plasma of 600 m/s using digisonde at Ny-Ålesund during low solar activity during 10-11 January 1997 and K_p index up to 6. However, observation over long period from 1989 to 1997 shows that geomagnetic storm only has secondary effect on patch formation [*Dandekar, 2002*].

By applying the ionospheric drift of ~ 600 m/s, and using the size of the patches normally varies from 100 to 1000 km, the duration of the patch is between 3 min to 28 min. Therefore, both intervals are suitable to observe the existence of small and

also large patches. The classification of patches used throughout this study is summarised in Table 3.1.

Table 3.1: Summary of patches classification

ROTI ₅ (small patches)	0.2 < ROTI ₅ < 0.5 (low intensity patches)
	ROTI ₅ > 0.5 (moderate to high intensity patches)
ROTI ₃₀ (large patches)	0.2 < ROTI ₃₀ < 0.5 (low intensity patches)
	ROTI ₃₀ > 0.5 (moderate to high intensity patches)

The GPS receiver also collects phase measurements and then detrended with a 6th-order Butterworth high-pass filter with the cut-off frequency of 0.1 Hz. Next, the standard deviations, σ_ϕ of the phase over 1-second, 3-second, 10-second, 30-second and 60-second intervals are produced. All these standard deviation values are computed by the receiver. The 60-second σ_ϕ is normally used as the phase scintillation indicator, and hence will be used in this study.

The receiver is also capable of measuring amplitude scintillation, which normally represented by its index, S4. The raw amplitude measurements are normalized by averaging the measurements over the 60-second interval. This produces the total S4, S_{4T} which includes the effects of ambient noise and multipath [Dubey *et al.*, 2006]:

$$S_{4T} = \sqrt{\frac{\langle P^2 \rangle - \langle P \rangle^2}{\langle P \rangle^2}} \quad (3.6)$$

where P is the signal intensity, which is actually the received signal power.

As mentioned earlier, S_{4T} contains ambient noise that causes a relatively high S4 at lower frequencies, such as at VHF and UHF. The effects of ambient noise can be removed by estimating the average of the signal-to-noise density, S/N_0 over the same 60-second interval. The correction to the total S4 due to ambient noise, S_{4N_0} is [Zou, 2011]:

$$S_{4N_0} = \sqrt{\frac{100}{\overline{S/N_0}} \left(1 + \frac{500}{19\overline{S/N_0}} \right)} \quad (3.7)$$

where $\overline{S/N_0}$ denotes the 60-second average of S/N_0 .

The corrected S4 can then be computed as follows [Zou, 2011]:

$$S4 = \sqrt{S_{4T}^2 - S_{4N_0}^2} \quad (3.8)$$

Both S_{4T} and S_{4N_0} values are provided by the software of the GPS receiver. The corrected S4 can then be determined and were used throughout this study. However, the corrected S4 still contains the effect of multipath, especially when the elevation angle is low. The GPS receiver can distinguish between S4 that is due to multipath (and noise) and S4 due to scintillation [GSV GPS Silicon Valley, 2007]. This can be achieved by looking at the difference between code and carrier pseudorange, which is recorded by the receiver as code/carrier divergence. This is based on the fact that

in the presence of multipath, the divergence of the code/carrier is faster than the divergence due to the ionosphere [Aquino *et al.*, 2009].

A plot of the standard deviation of the code/carrier divergence, $\sigma_{\text{CCD}_{\text{iv}}}$ versus corrected S4 (from Equation 3.8) can be used to detect the multipath effect as there is no (or very little) code/carrier divergence due to scintillation [GSV GPS Silicon Valley, 2007]. An example of this plot is shown in Figure 3.5 for the data observed on 24 May 2008. The dividing line (as suggested from the receiver's manual) separates the points due to multipath and non-multipath. Every point above the line is most likely due to multipath fading and noise, and below the line indicates scintillation.

The line is only an approximation to distinguish multipath and scintillation, and is chosen by considering both the environmental multipath and the probability of scintillation occurrence [Aquino *et al.*, 2009]. In this study, the dividing line used is following what is suggested by the receiver's manual where it is based on the experience of a challenging multipath case [Aquino *et al.*, 2009]. In the example shown in Figure 3.5, all S4 indices are categorised as multipath. The single S4 point under the dividing line is not considered as significant scintillation.

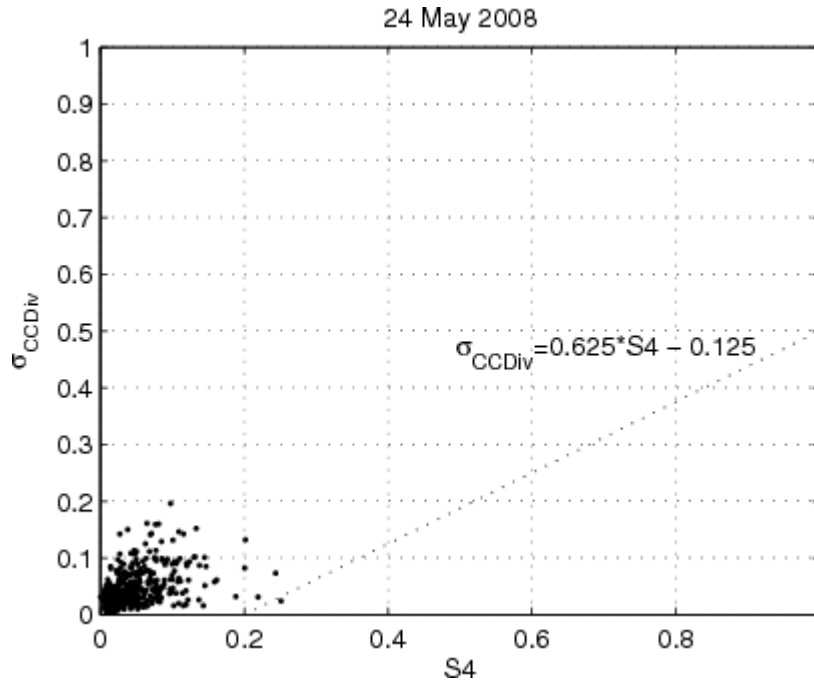


Figure 3.5: σ_{ϕ} of code/carrier divergence versus corrected S4 for 24 May 2008

An offline program, Parseismr.exe is used to extract the data recorded by GSV4004B receiver. The data can be converted into a text file and then called in Microsoft Excel to further editing. These are the processes involved in the unwanted data elimination [GSV GPS Silicon Valley, 2007]:

1. The phase scintillation data collected before the phase detrending filter has converged is eliminated by deleting the lock time data for L1 and L2 that is less than 240 seconds, where convergence is obviously has not yet happened. The convergence is not a problem to amplitude scintillation when using averaging technique. Therefore, a lower lock time value can be used. In all our cases, lock time threshold for amplitude and phase scintillation are 60 seconds and 240 seconds, respectively.

2. Other non-converging value that is the 60-second phase scintillation data that is very large is deleted to avoid confusion with legitimate scintillation events. All values greater than 2 radians are eliminated.

3. Low-to-moderate amplitude scintillation at lower elevation angles can be due to multipath. The elevation angle should be considered carefully because the multipath effect is more frequent at low elevation. An elevation angle of more than 15° is used by *Spogli et al.* [2009], while *Krankowski et al.* [2006], *Gwal and Jain* [2011] and *Warnant and Pottiaux* [2000] opted to use an elevation angle of more than 20° . Meanwhile, *Prikryl et al.* [2010] and *Breed et al.* [2002] chose a cut off elevation angle of 30° and 50° , respectively. Even though the cut off elevation angle for the GPS receiver is set to 5° , only data with the elevation angle greater than 25° are considered as meaningful. This is to make sure that multipath effect is minimised.

Transionospheric link via GPS satellites provides information regarding the TEC, and also both amplitude and phase scintillations. We utilise data from GPS receiver installed at Alert, Canada, and also from the Ionospheric Scintillations Arctic Campaign Coordinated Observation (ISACCO) database where GPS receivers are installed in Svalbard.

The GPS receivers' network of ISACCO also employs GSV4004B. There are two receivers in Ny-Ålesund, NYA0 (78.923°N , 11.925°E) and NYA1 (78.929°N , 11.864°E), installed in 2003 and 2004, respectively. Another station (LYB0; 78.169°N , 15.992°E) is located at Longyearbyen (125 km from the other two

stations), which has been in operation since 2006. Data are available for any station since the date of installation (except on few occasions) from electronic Space Weather (eSW) database, maintained by Istituto Nazionale di Geofisica e Vulcanologia (INGV), Italy. Data can be retrieved from <http://www.eswua.ingv.it>

3.2 HF Link

A HF link between Qaanaaq, Greenland and Ny-Ålesund, Svalbard has been in operation since 14 March 2009. BPSK signals using 13-bit Barker code are transmitted on six frequencies from 4.64 MHz to 14.36 MHz for two-second every 20 seconds. This results an observation for every two minutes on each frequency. Several parameters are measured at the receiver, including the time-of-flight (TOF), signal-to-noise ratio (SNR), Doppler frequency, Doppler spread, and delay spread. The GPS is used to ensure synchronisation between transmitter and receiver.

Doppler spread is measured from the Doppler power profile as the 80% power spread *Angling et al.* [1998]. In order to determine Doppler spread, each mode is assumed to have a Gaussian power spectrum, which is defined by its measured mean (Doppler shift) and standard deviation (Doppler spread). These spectra are weighted by their relative powers and then summed [*Angling et al.*, 1998].

For i modes, the composite Doppler profile is defined as [*Angling et al.*, 1998]:

$$P(x) = \sum_i \frac{h_i}{\sigma_i \sqrt{2\pi}} \exp \left[-\frac{1}{2} \left(\frac{x - \mu_i}{\sigma_i} \right)^2 \right] \quad (3.7)$$

where:

x frequency (Hz)

h_i power of mode peak

μ_i mean (Hz)

σ_i standard deviation (Hz)

As the resultant of Doppler spectrum generally may not be Gaussian, the Doppler spread is taken to be the central 80% power region of the composite spectrum [Angling *et al.*, 1998]. In this study, the channel characteristics to be considered are the Doppler spread, and also the corresponding delay-Doppler spectrum. Multipath spreads were found to be very low throughout the observation periods and were not discussed in detail.

Data from 14 March 2009 to 28 February 2011 were used in this study. This covers a complete 2-year data on each frequency used, thus allows observations of the channel characteristics (i.e. the Doppler spread) over different seasons and years, with increasing solar activity. The delay-Doppler spectrum was checked manually for each frame to remove outliers. Extra attention was given to the spectrum where Doppler spread returned too high value. This normally corresponds to signals with too many interference, thus will be deleted from the statistical analysis.

SNR for the received signals can be as low as ~ -11 dB. In order to manually eliminate erroneous Doppler spread values, SNR threshold was set to 0 dB. Signals weaker than 0 dB normally returned erroneous value of Doppler spreads. The choice of threshold of SNR > 0 dB is based on observations of many delay-Doppler spectra.

During this process of elimination of erroneous Doppler spreads, only Doppler spreads greater than 10 Hz were checked. This threshold is again chosen based on observations on delay-Doppler spectrum where very large Doppler spread values should be treated with caution.

After the elimination process, statistics of the Doppler spreads can be presented. Only signals with SNR > 0 dB were considered since signals weaker than that tend to give erroneous Doppler spreads value. This is illustrated in Figure 3.6 for 8.01 MHz for various SNR thresholds. Doppler spreads demonstrated similar behaviour for other frequencies too. SNR threshold is fixed at 0 dB to account for as many meaningful data as possible. However, this may include large Doppler spread that may be erroneous, as shown in Figure 3.6. These large spreads normally corresponds to low SNR very close to 0 dB and only involved a very small amount of data. Therefore, it will not affect the statistics. These outliers will be manually removed later.

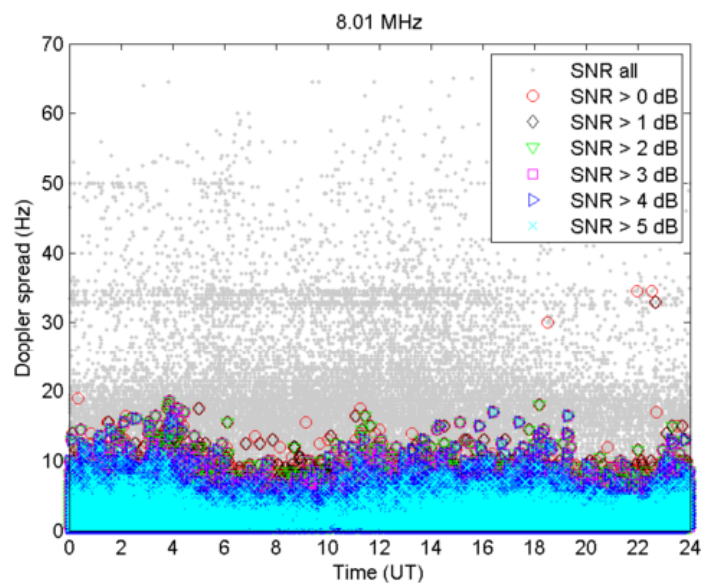


Figure 3.6: Plot of Doppler spreads on 8.01 MHz from 14 March 2009 to 28 February 2011 for various SNR

Chapter Four: Variations of TEC and Scintillations at Alert, Canada

Data from the Alert GPS receiver are collected starting at the end of May 2008. Data from 1 June 2008 to 31 July 2010 are used for statistical analysis. Data are available each day during that period, except on 2 June 2008, from 31 August to 19 September 2008, and from 30 November 2009 to 7 February 2010. Data are collected every 60 seconds.

4.1 TEC Variations

Vertical TEC (VTEC) is used here to observe the temporal variations to eliminate dependence of TEC values on the elevation angles of the satellites. However, this of course will introduce errors to the TEC values. Converting slant TEC into vertical TEC involves various assumptions, including a uniform ionosphere. Therefore, care is needed in interpreting the vertical TEC values. Figure 4.1 shows mean VTEC computed for each hour averaged for each month from June 2008 to July 2010. Since the GPS satellite is around 4 minutes earlier on the next day over a same location, the elevation angle of the satellite will also change. This will affect conversion from slant to vertical TEC and causing increase/decrease effect on the hourly/monthly vertical TEC.

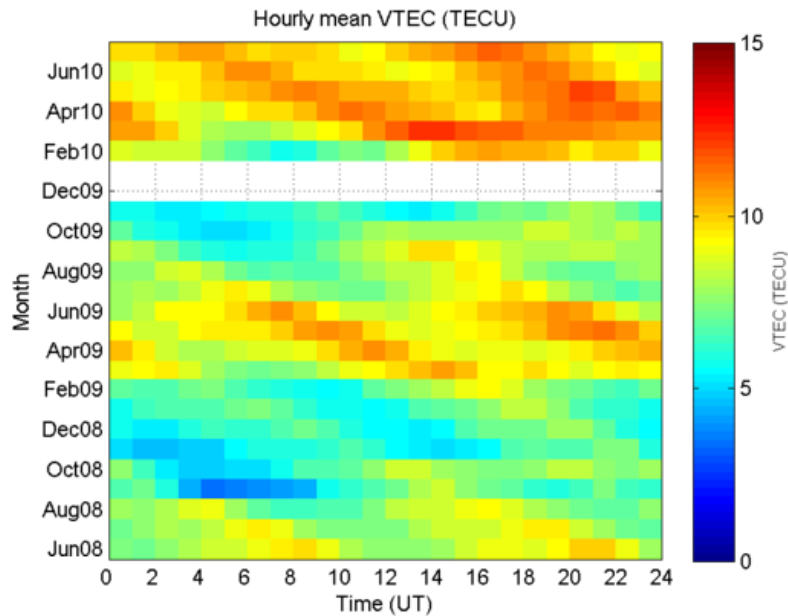


Figure 4.1: Hourly mean VTEC for every month from June 2008 to July 2010

Lowest mean vertical TEC was observed from September 2008 to February 2009 varying from a minimum of ~ 3 TECU to a maximum of ~ 10 - 11 TECU (Table 4.1) (except in October 2008). February 2009 started to show increase in mean TEC where higher TEC than those observed in winter months can be seen for a few hours. With an exception of February 2010, the following year also showed the same pattern of low mean vertical TEC, with slight increase only. Unfortunately, data for December 2009 and January 2010 are not available. June-October 2009 exhibited similar behaviour as in June-October 2008. Characteristics of vertical TEC for March to June in 2009 and 2010 were similar for both years. However, TEC variability in 2010 was more apparent and TEC gave higher values than in 2009.

Based on the observations on all months, monthly and yearly pattern can be seen. Winter months showed lower mean vertical TEC than summer and equinox months. This is expected as longer daytime is experienced. This is in agreement with the

work done by *Prikryl et al.* [2010] when observing the TEC changes at high latitudes during September 2008 to August 2009. Furthermore, March to June exhibited higher TEC for longer time than in July and August. All observed months in 2010 showed higher mean TEC than in 2008 and 2009, with an exception of February (Figure 4.2). However, mean VTEC in February 2010 was still higher than in the previous year.

Table 4.1: Minimum, lower decile, median, upper decile and maximum values of hourly mean VTEC from June 2008 to July 2010

Month	Hourly mean VTEC (TECU)				
	Min	10%	50%	90%	Max
Jun 08	5.4	7.1	8.5	9.9	11.9
Jul 08	5.1	6.8	8.2	9.6	11.5
Aug 08	4.5	6.3	7.7	9.4	11.3
Sep 08	2.7	3.7	6.3	8.0	9.7
Oct 08	3.2	4.7	7.0	9.0	14.3
Nov 08	3.1	4.3	5.8	7.4	10.8
Dec 08	3.5	4.9	6.3	8.0	10.5
Jan 09	3.0	5.2	6.6	8.1	10.2
Feb 09	3.7	5.3	7.0	9.1	11.8
Mar 09	5.8	7.3	9.0	10.5	12.7
Apr 09	6.9	8.0	9.4	10.7	12.5
May 09	7.1	8.5	9.8	11.3	13.6
Jun 09	6.5	7.9	9.3	11.0	12.8
Jul 09	5.2	6.8	8.1	9.7	11.6
Aug 09	4.0	6.4	7.7	9.3	11.1
Sep 09	3.6	5.8	7.9	9.6	11.6
Oct 09	3.8	4.9	7.1	9.0	12.8
Nov 09	3.2	4.8	6.2	8.1	11.4
Dec 09	-	-	-	-	-
Jan 10	-	-	-	-	-
Feb 10	3.8	6.1	8.4	11.5	14.6
Mar 10	4.9	7.6	10.4	12.8	16.1
Apr 10	6.6	8.7	10.4	12.1	14.0
May 10	6.8	8.8	10.5	12.0	15.4
Jun 10	6.7	8.5	10.0	11.3	12.9
Jul 10	7.1	8.7	10.1	11.7	13.9

Even the conversion to vertical TEC was considering only the elevation angle of greater than 25° , the effect of low elevation angle can still be seen on the mean vertical TEC plot. Therefore, this plot only effectively show that TEC values increase with the increasing of sunspot number. Diurnal variation and particularly UT dependence should not be concluded from this plot.

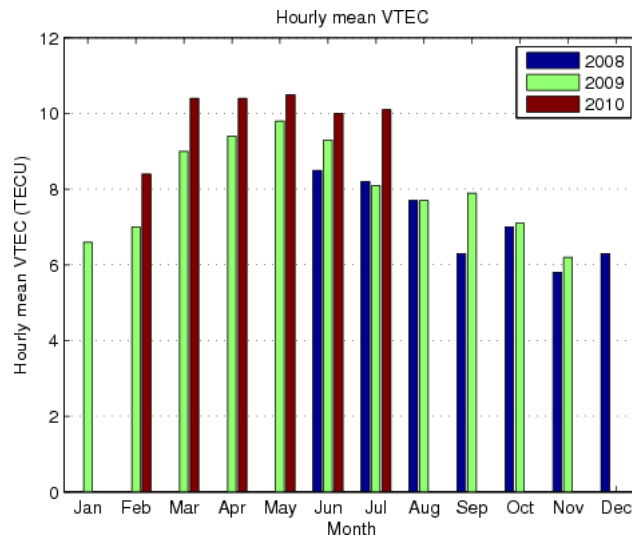


Figure 4.2: Hourly mean vertical TEC values for each year

Figure 4.3 shows the number of occurrence of smaller scale patches for each month from June 2008 to July 2010 in every UT hour. The levels of patches intensity are classified as low (i.e. weak patches) if ROTI is between 0.2 and 0.5, and moderate and high if ROTI is greater than 0.5. Weak patches, both small and large in size were observed at all time during the period of observations, with small patches were more frequently formed.

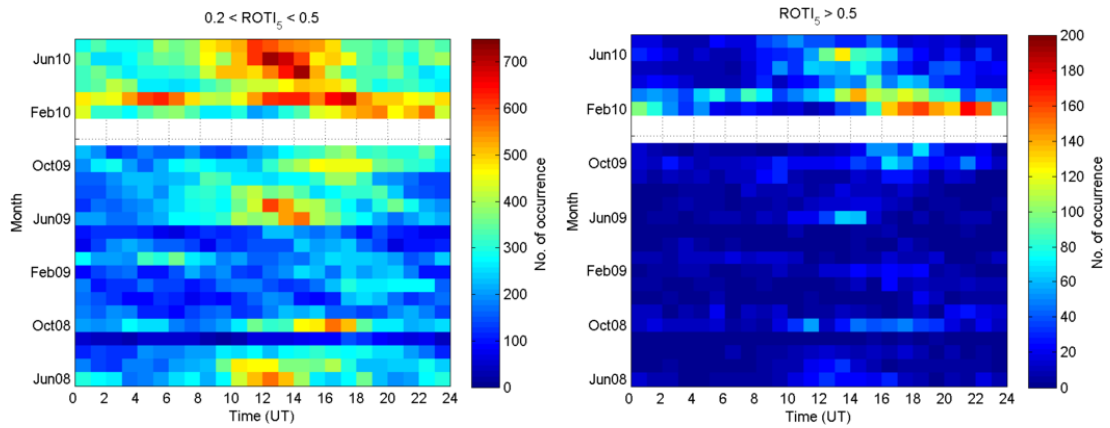


Figure 4.3: The number of occurrence of small patches ($0.2 < ROTI_5 < 0.5$ (left) and $ROTI_5 > 0.5$ (right)) in 5-minute interval

Figure 4.4 illustrates the number of occurrence of large size patches for the same period of observations. Both small and large patches showed similar UT dependence where ~ 80 large and ~ 300 small patches were identified around 1000 to 2000 UT from June to October in both 2008 and 2009. These numbers increased about twice in 2010 during the same UT hour. In addition, the number of all patches increased in 2010 for all UT hours compared to previous years. Even though it maximised around 1200 to 1800 UT, but a large number of weak patches were distributed all day in 2010. This may correspond to the slight increase of solar activity and in agreement with the finding in *Dandekar* [2002] where the number of patches is found to be dependent on sunspot activity.

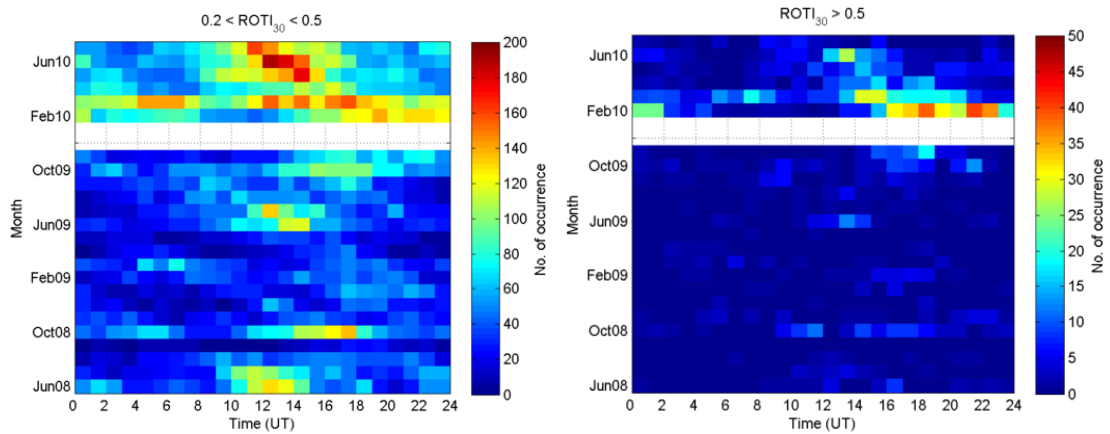


Figure 4.4: The number of occurrence of large patches ($0.2 < ROTI < 0.5$ (left) and $ROTI > 0.5$ (right)) in 30-minute interval

In contrast with the weak patches, occurrences of moderate to high intensity patches in 2010 were more confined to a range on UT hours only where it maximised from ~ 1800 to 2400 UT in February and March with about 30 moderate to high intensity large patches were observed as opposed to around 80-120 weak and smaller patches. In general, only a small number of moderate to high intensity patches were recognised during the whole period of observation as compared to the low intensity patches. The occurrence of large moderate to high intensity patches showed similar pattern of small weak patches in terms of UT dependence. The number of patches, however, can be overestimated as ROTI is calculated based on individual satellite and added up, and the same patch could be seen by different satellite(s) over or near the same path.

The percentage of patches occurrence is illustrated in Figure 4.5 and Figure 4.6. Patches were observed more in 2010 in any month, regardless of its size and intensity. The occurrence of small patches of moderate to high intensity were found to be more than twice at $\sim 17\%$ of the times in February and March 2010 than in the

other months of the same year for ~5-8% only. In addition, the percentage of occurrence of moderate to high intensity of small patches in February-March 2010 was also found to be twice than the low intensity patches in February-March 2009. There was not much difference of both low and moderate to high intensity for the same months in 2008 and 2009, namely in January-February and October to December. However, for the rest of the year, less moderate to high patches were formed than the low intensity patches.

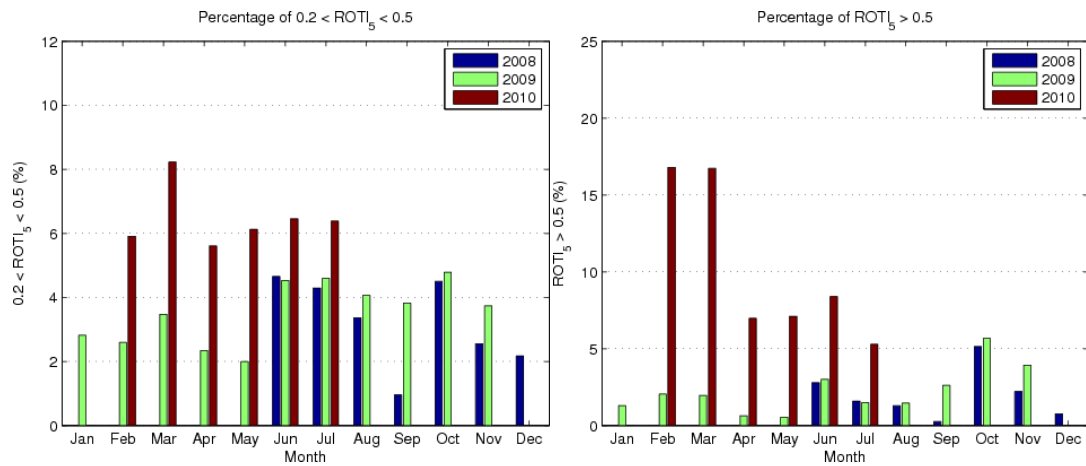


Figure 4.5: The percentage of occurrence of small patches ($0.2 < ROTI < 0.5$ (left) and $ROTI > 0.5$ (right)) in 5-minute interval

Similar to small patches observations, the number of moderate to high intensity of large patches increased significantly in February and March 2010 for about twice as much compared to previous years and even more when compared to other months of the same year. Moderate to high intensity patches in February 2010 were three times as much than the low intensity patches, while in March 2010 the difference was about twice. The seasonal pattern of low intensity patches was not clear where patches were recognised all year regardless of the size. However, with the exception

of 2010, moderate to high intensity patches tended to occur more frequent in October and November, both for small and large patches.

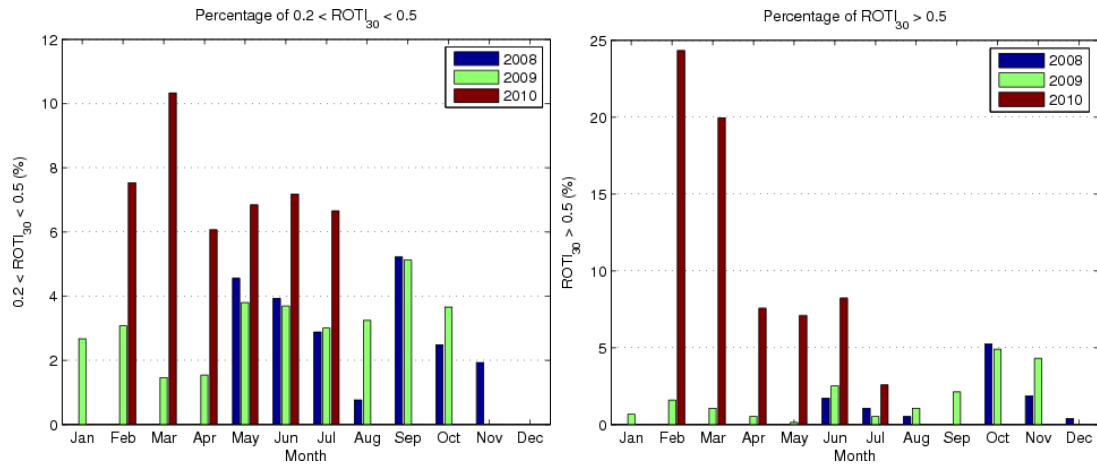


Figure 4.6: The percentage of occurrence of large patches ($0.2 < ROTI < 0.5$ (left) and $ROTI > 0.5$ (right)) in 30-minute interval

Dandekar [2002] summed up that at medium to low sunspot activity there is no systematic seasonal dependence, and only weak seasonal dependence at high sunspot activity. Meanwhile, Krankowski *et al.* [2006] concluded that the maximum patch activity occurred in the winter between 0300 and 1100 UT at four Antarctic stations during 2001 (period of high sunspot activity), and all day at equinox.

Figure 4.7 illustrates the ROTI in 5-minute interval as a function of geomagnetic latitudes and observation months. The top panel consists of all data of $ROTI_5$ for each month from June 2008 to July 2010 that has been categorised based on the geomagnetic latitudes from 81° to 90° using 1-degree bin size. The distribution was almost equal on each month except on September 2008 and February 2010. This is due to less number of data in these two months.

The middle panel represents the percentage of weak patches of small size for each month. The percentage is calculated as the ratio between the number of ROTI between 0.2 and 0.5 in 1-degree bin, and the total of ROTI in that bin. The weak patches for each month were registered at all geomagnetic latitudes from 81° to 90°. Distribution of weak patches between November 2008 and April 2009 showed the least variability for each geomagnetic latitude bin. Most weak patches were observed in February 2010 from 85° to 90° of geomagnetic latitudes and maximised at 85-87°, followed by March 2010 but distributed at larger range of geomagnetic latitudes.

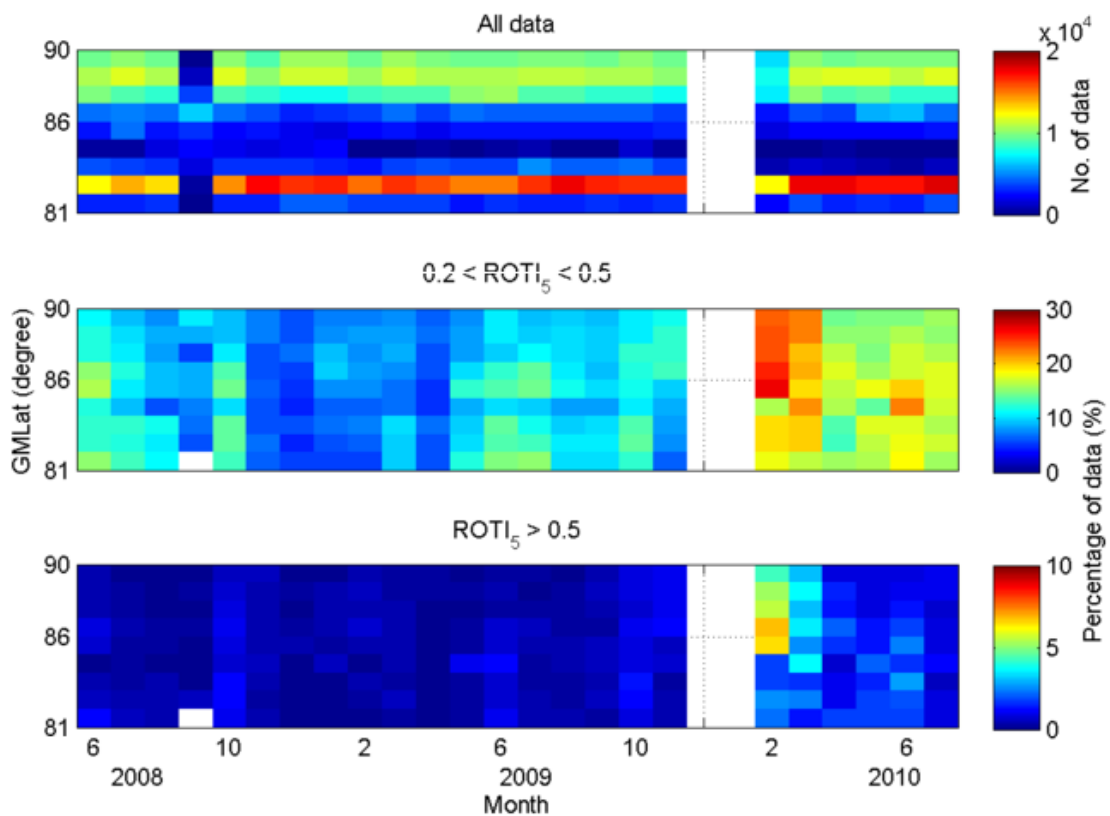


Figure 4.7: Number of 5-minute ROTI data for each month and degree of magnetic latitude (top), and the percentage of these data for which $0.2 < ROTI < 0.5$ (middle) and $ROTI > 0.5$ (bottom)

Moderate to high intensity of small size patches were observed less frequent compared to the weak ones. The percentage of occurrence was low in mostly all months at any geomagnetic latitude bin, with exceptions in February and March 2010 where relatively higher percentage of moderate to high intensity of small patches were observed from 84° to 90° geomagnetic latitude.

Similar pattern of dependence on geomagnetic latitude was observed for large patches as illustrated in Figure 4.8. However, the percentage of occurrence of low intensity of large size patches was sometimes higher than the small size patches especially between February and July 2010, with difference up to ~7% occurrence. On the other hand, the percentage of occurrence of moderate to high intensity of large size patches was mostly slightly lower than the small size patches.

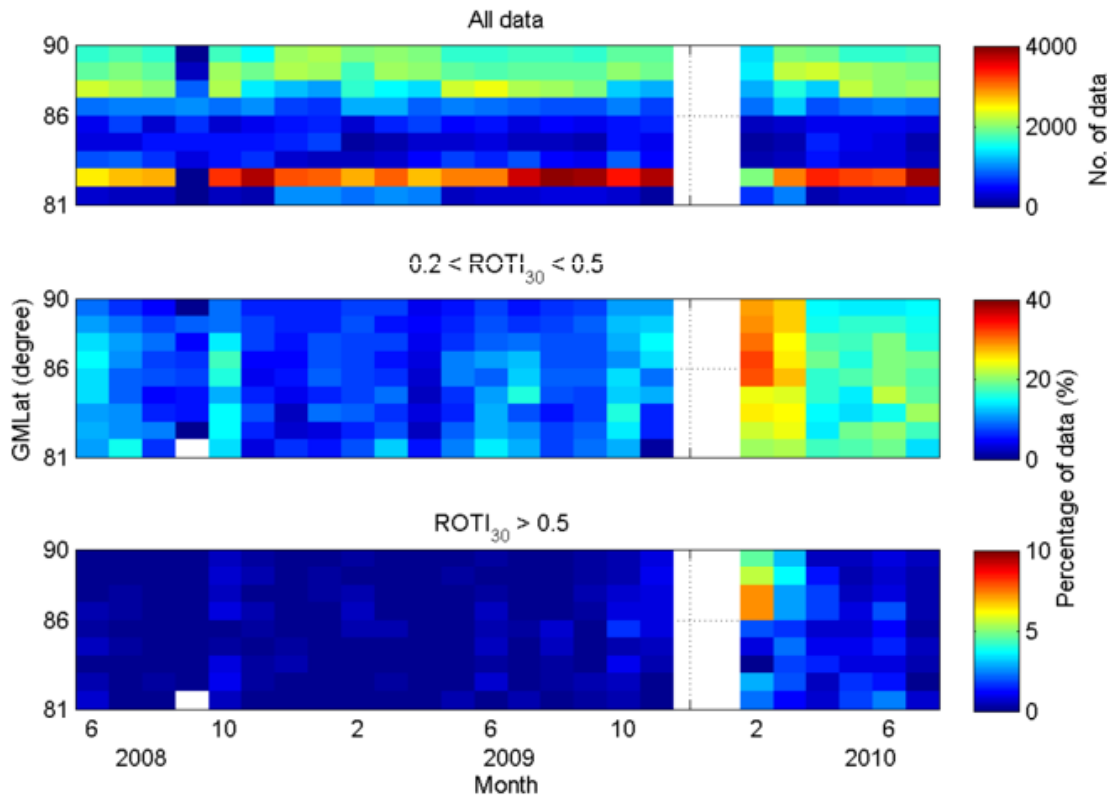


Figure 4.8: Number of 30-minute ROTI data for each month and degree of magnetic latitude (top), and the percentage of these data for which $0.2 < ROTI_{30} < 0.5$ (middle) and $ROTI_{30} > 0.5$ (bottom)

4.2 Amplitude Scintillations

Table 4.2 shows the occurrence of the amplitude scintillations index, S4 for every observed month for all data exceeding the elevation angle of 25° . S4 were very low in all months where at least $\sim 99\%$ were in the range of 0 and 0.1, and the remaining 1% mostly never exceeded 0.3, with only 0.01% of the scintillations were between 0.2 and 0.3. S4 between 0 and 0.2 are usually considered as insignificant.

Table 4.2: Number of occurrence of amplitude scintillation index, S4 for every month from June 2008 to July 2010

Month	Total cases	S4					
		0-0.05	0.05-0.1	0.1-0.15	0.15-0.2	0.2-0.25	0.25-0.3
Jun 08	279118	230197	45601	3112	198	10	0
Jul 08	298710	243223	52126	3211	146	4	0
Aug 08	278647	229253	47185	2129	79	1	0
Sep 08	96291	84365	11760	158	6	2	0
Oct 08	297785	252218	43263	2055	224	25	0
Nov 08	290433	243763	43720	2602	325	23	0
Dec 08	299399	251509	45818	1936	131	5	0
Jan 09	300525	243763	53593	2965	189	15	0
Feb 09	272762	226405	44943	1372	41	1	0
Mar 09	302642	243098	57221	2122	199	2	0
Apr 09	287983	235774	50706	1403	97	3	0
May 09	300911	245645	53622	1589	55	0	0
Jun 09	291550	239531	48566	3137	282	30	4
Jul 09	302206	247531	51164	3210	284	16	1
Aug 09	301387	242265	54872	3899	330	21	0
Sep 09	293577	239786	50527	3053	202	9	0
Oct 09	297380	251064	44825	1435	53	3	0
Nov 09	278881	226496	49468	2731	182	4	0
Dec 09	0						
Jan 10	0						
Feb 10	203157	158385	43157	1508	99	8	0
Mar 10	299692	245481	52791	1356	63	1	0
Apr 10	285368	236932	46659	1660	103	14	0
May 10	295010	243887	47870	3097	148	8	0
Jun 10	285645	232961	49859	2653	160	12	0
Jul 10	294893	236620	54423	3566	267	17	0

Amplitude scintillation between 0.2 and 0.3 are dismissed as insignificant too as they occurred individually and not in sequence, and therefore considered as outliers. Furthermore, these indices were mostly at low elevation angle (refer Figure 4.9) and could possibly due to multipath. This can be seen in Figure 4.10 where the plot of standard deviation of carrier/code divergence versus S4 showed that most of the data were above the dividing line, which is referring to potential multipath cases and not the scintillation ones.

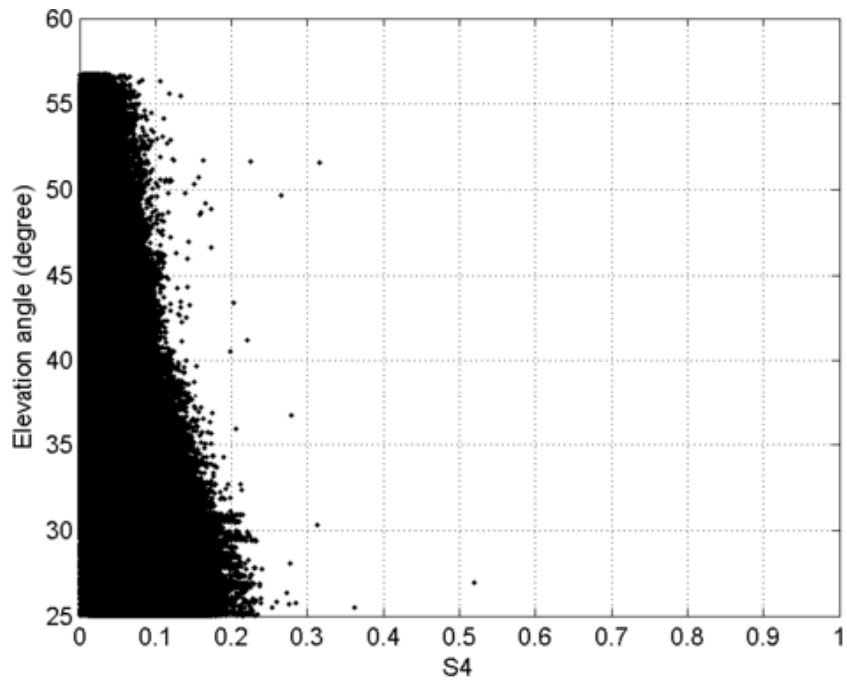


Figure 4.9: Plot of elevation angle versus $S4$ for all data $> 25^\circ$

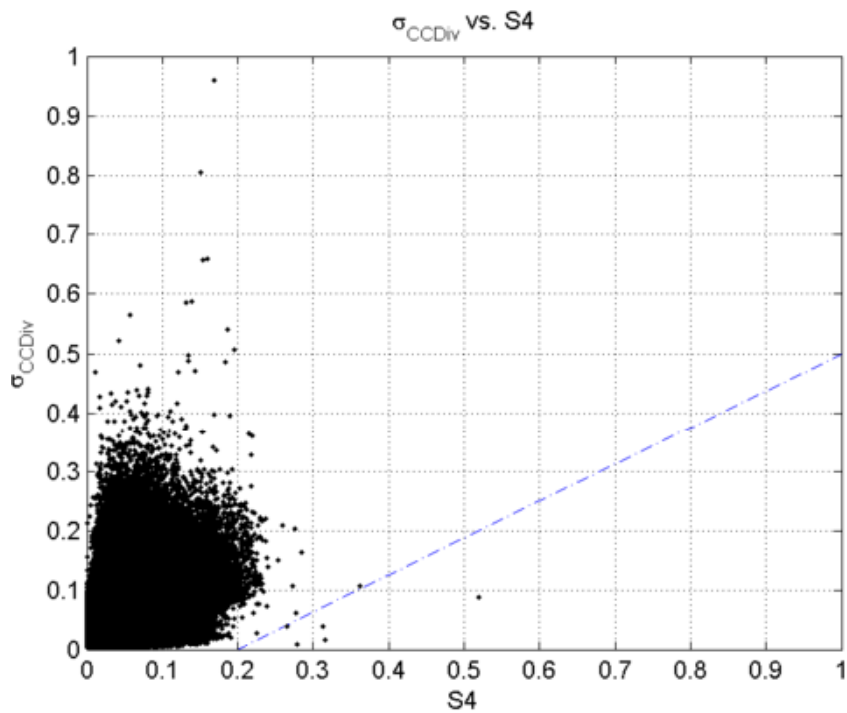
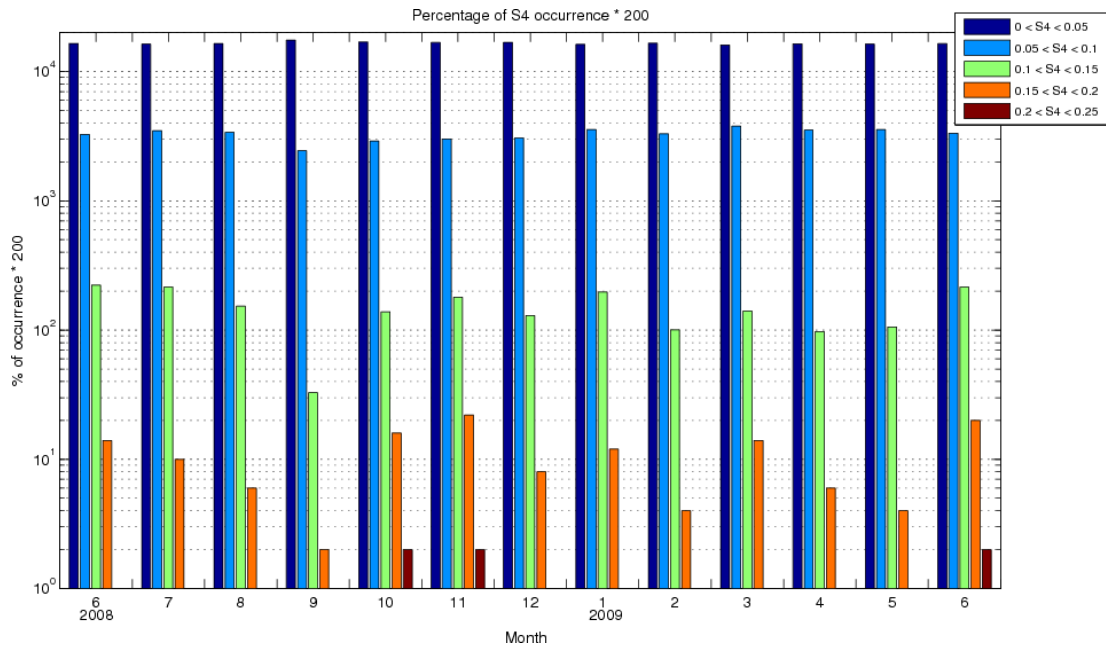
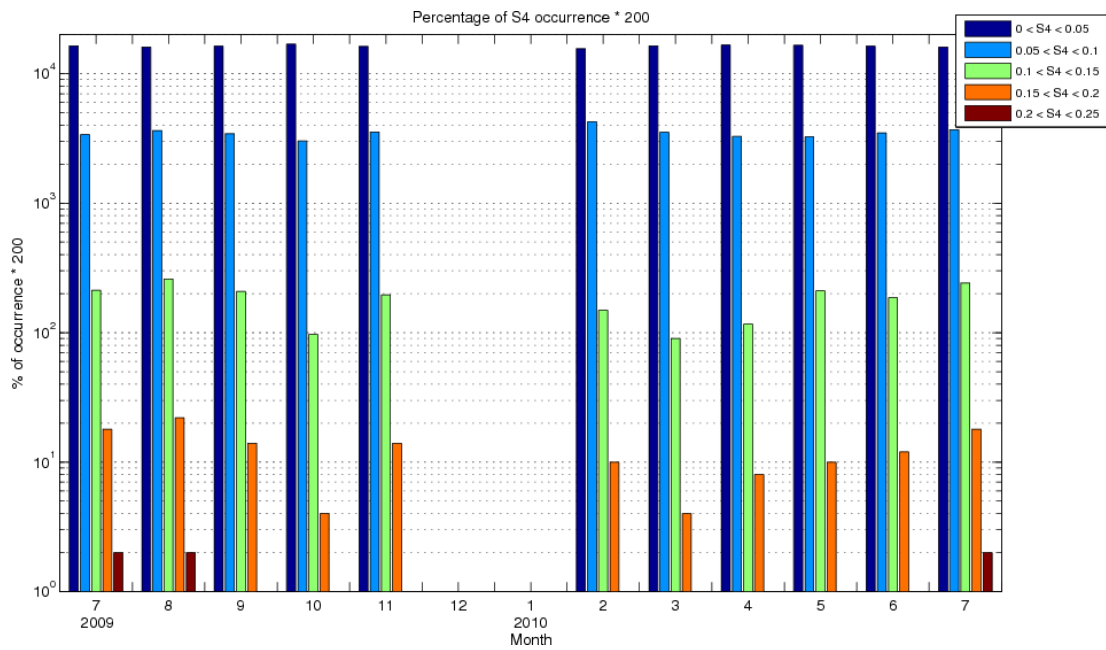


Figure 4.10: Plot of the standard deviation of carrier/code divergence versus $S4$ for all data $> 25^\circ$



(a)



(b)

Figure 4.11: Percentage of occurrence of S4 for every month (a) June 2008 – June 2009 and (b) July 2009 - July 2010

The low occurrence of significant scintillations is in agreement with the work done by Li *et al.* [2010] where only < 1% of $S4 > 0.25$ observed at Ny-Ålesund during 2007 and 2008. Observations from September 2008 to August 2009 over a polar cap

station at Resolute Bay, Canada also revealed that amplitude scintillations were very low during this period [Prikryl *et al.*, 2010]. The percentage of occurrence of amplitude scintillation in each range (up to $S4 < 0.25$) for every month is illustrated in Figure 4.11. Only October and November 2008, June – August 2009, and July 2010 experienced amplitude scintillation up to $S4 = 0.25$, but for only 0.1% of the times.

Although it is mentioned above that all $S4$ during the period of observations are considered as insignificant, the percentage of considerably high amplitude scintillations are presented here in order to examine the effect of increasing solar activity. Figure 4.12 shows the percentage of occurrence of $S4 > 0.15$ for all available months for each year, which demonstrated no dependence on the increasing of solar activity. For example, the percentage of $S4 > 0.15$ was higher in May 2008 than in May 2010.

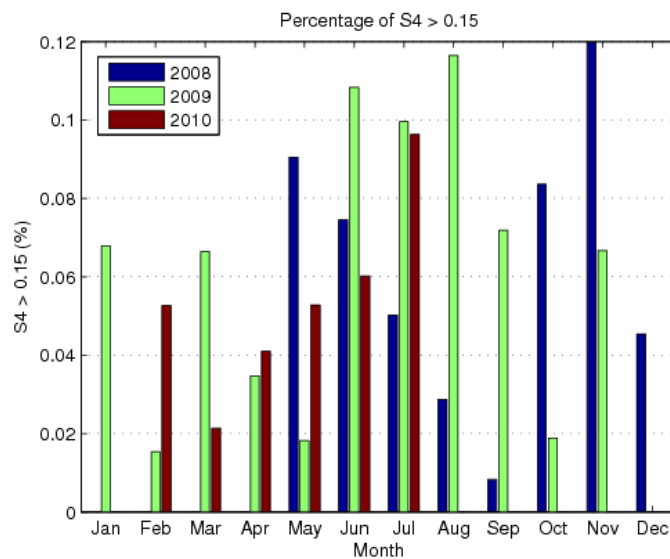


Figure 4.12: Percentage of $S4$ values greater than 0.15 for every available month from June 2008 to July 2010

Similarly, the percentage was higher in June 2009 than in June 2010. However, in this instance, the conclusion is drawn based on S4 values that are normally considered as insignificant. Long-term investigation (1979-1984) of amplitude scintillations in the polar cap conducted by *Basu et al.* [1987] shows the presence of an annual variation with minimum scintillations during summer, and also a pronounced solar control of scintillation activity, where it decreases when solar activity falls. However, investigation by *Basu et al.* [1987] was done at 250 MHz.

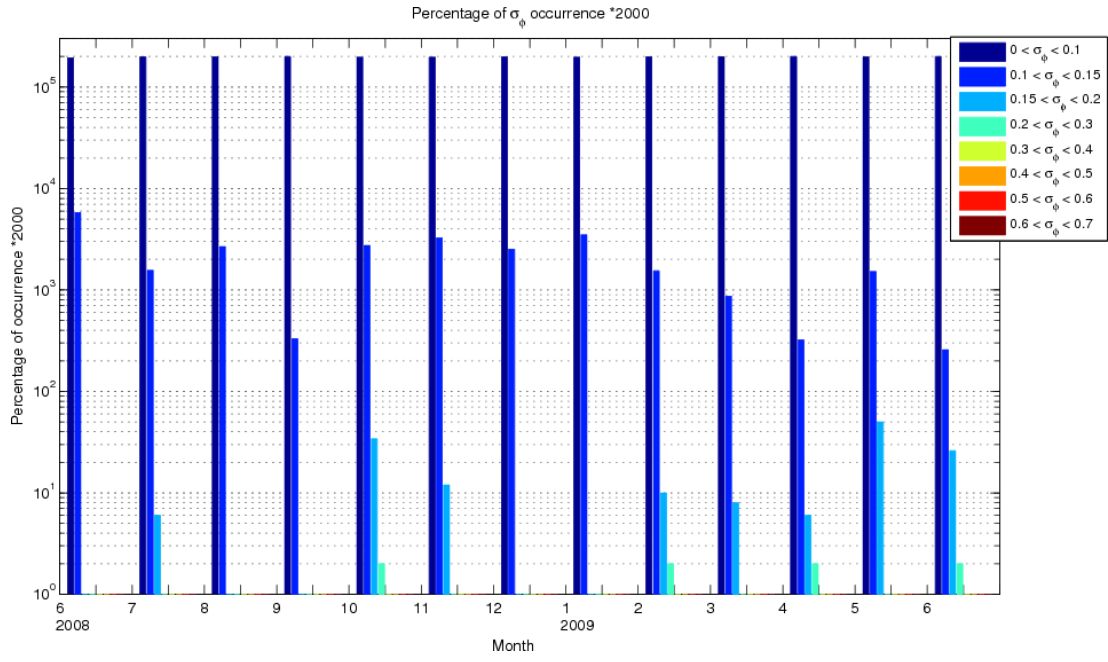
4.3 Phase Scintillations

Table 4.3 shows the occurrences of phase scintillations index, σ_ϕ at Alert for every observed month. Similar to amplitude scintillations, phase scintillations were also in the range of 0 to 0.1 rad for at least 93% of the time and can reach up to ~100% in certain months. The remaining 7% varied from 0.1 to 0.7 rad, where it mostly never exceeded 0.2 rad. About up to 0.2% of the phase scintillations were in 0.15 to 0.2 rad.

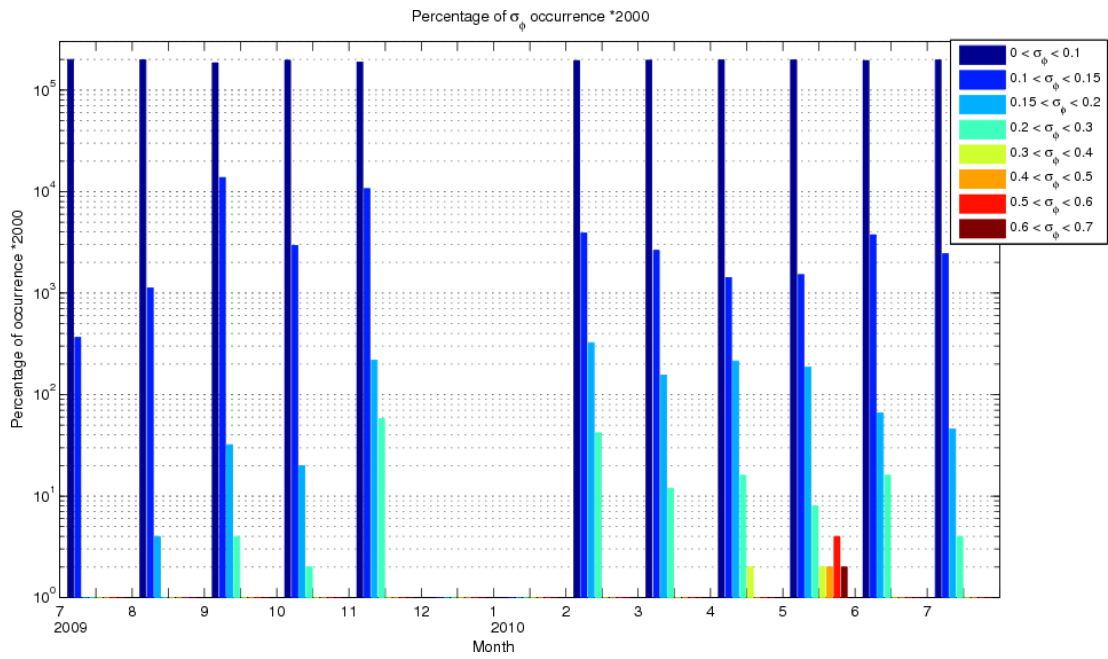
The percentage of occurrence of phase scintillation in each range for every month is illustrated in Figure 4.13. The maximum phase scintillation for most months was only up to 0.3 rad, except for April and May 2010. Phase scintillation in April 2010 reached up to 0.4 rad (but only for about 0.001% of the times) and up to 0.7 rad in May 2010 (for a maximum of 0.002% only). Most of the $\sigma_\phi > 0.4$ rad were observed on PRN 11 on 12 May 2010. This occurrence will be explained further in Section 4.5.

Table 4.3: Number of occurrence of σ_ϕ for every month from June 2008 to July 2010 in 0.1-rad step, except between 0.1 rad and 0.2 rad

Month	Total cases	σ_ϕ (rad)							
		0-0.1	0.1-0.15	0.15-0.2	0.2-0.3	0.3-0.4	0.4-0.5	0.5-0.6	0.6-0.7
Jun 08	274622	266679	7943	0	0	0	0	0	0
Jul 08	276862	274700	2153	8	1	0	0	0	0
Aug 08	272372	268725	3647	0	0	0	0	0	0
Sep 08	95665	95507	158	0	0	0	0	0	0
Oct 08	295350	291235	4063	49	3	0	0	0	0
Nov 08	284933	280295	4620	18	0	0	0	0	0
Dec 08	294951	291241	3710	0	0	0	0	0	0
Jan 09	289661	284619	5042	0	0	0	0	0	0
Feb 09	269596	267499	2081	14	2	0	0	0	0
Mar 09	300299	298985	1300	13	1	0	0	0	0
Apr 09	286256	285784	459	10	3	0	0	0	0
May 09	297716	295380	2261	74	1	0	0	0	0
Jun 09	290424	290008	376	37	3	0	0	0	0
Jul-09	301142	300590	552	0	0	0	0	0	0
Aug 09	300239	298541	1692	6	0	0	0	0	0
Sep 09	289604	269540	20010	47	6	1	0	0	0
Oct 09	295597	291219	4346	29	3	0	0	0	0
Nov 09	275645	260577	14688	301	79	0	0	0	0
Dec 09	0								
Jan 10	0								
Feb 10	202397	198092	3935	327	42	1	0	0	0
Mar 10	297562	293392	3920	233	17	0	0	0	0
Apr 10	284165	281815	2021	305	22	2	0	0	0
May 10	293618	291085	2234	273	12	2	4	6	2
Jun 10	283223	277782	5325	93	22	1	0	0	0
Jul 10	293045	289389	3580	68	7	1	0	0	0



(a)



(b)

Figure 4.13: Percentage of occurrence of phase scintillations for every month
 (a) June 2008 – June 2009 and (b) July 2009 - July 2010

Figure 4.14 shows the mean σ_ϕ computed for every UT hour for each month. The mean values were particularly low since most of the σ_ϕ concentrated around 0 to 0.1 rad only. Comparatively high σ_ϕ can be observed in September and October 2009

for the whole day, and for various hours from November 2008 to January 2009, and from February to July 2010. February to August 2009 showed little variations of phase scintillations. Dependence on the increase of solar activity can be seen where mean of phase scintillations were all higher in 2010 compared to the both previous years. However, no dependence on UT hour can be registered.

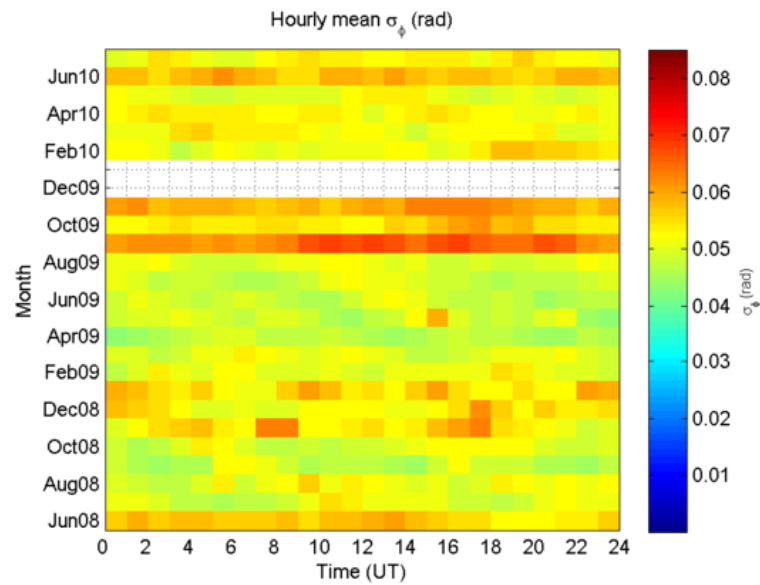


Figure 4.14: Hourly mean σ_ϕ for every month from June 2008 to July 2010

This is in contrast with the study conducted by *Prikryl et al.* [2010] where enhancement of phase scintillations was observed at Resolute Bay and the values were distinctively low when the plasma density is expected to be low, particularly in winter before about 1200 UT. The mean was higher near magnetic noon, particularly from April to November. In other instance, our finding is consistent with *Li et al.* [2010] where scintillations are observed to occur at all time in the polar cap region.

Further analysis is done by selecting relatively high σ_ϕ of greater than 0.15 rad and computing its percentage in each month. Phase scintillations were found to be high with the increasing of solar activity where most of the cases of $\sigma_\phi > 0.15$ rad were detected in 2010 (see Figure 4.15). $\sigma_\phi > 0.15$ rad was the highest in February 2010 and followed by in November 2009. As comparison, recent finding by *Li et al.* [2010] during 2007 and 2008 at Ny-Ålesund and Larsemann Hill revealed that phase scintillation mainly takes place in October, November and December at Ny-Ålesund, and in May and June at Larsemann Hill, which is around the local winter months. Selective cases of relatively high phase scintillations will be discussed in the next section.

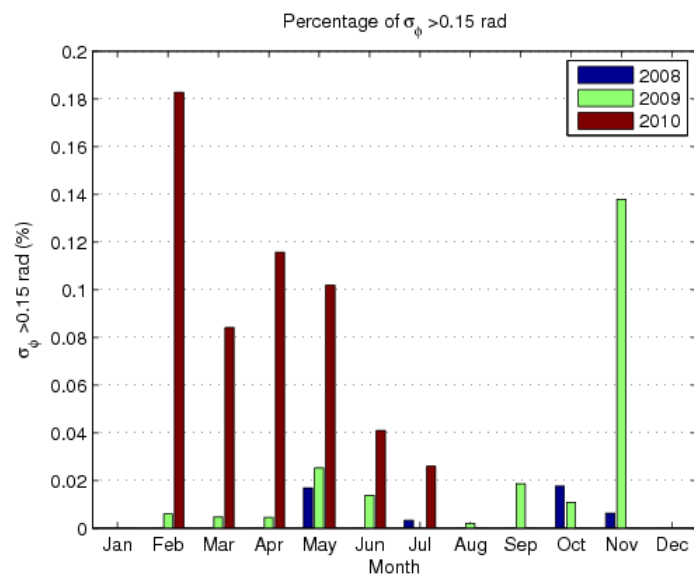


Figure 4.15: Percentage of σ_ϕ greater than 0.15 rad for every available month from June 2008 to July 2010

Figure 4.16 illustrates the total number of data (top panel) and the percentage of $\sigma_\phi > 0.15$ rad (bottom panel) for every month in 1-degree step of geomagnetic latitudes. As mentioned earlier, the number of data in September 2008 and February 2010 is less than the rest of the months due to the lack of data in these months. $\sigma_\phi > 0.15$ rad were very limited where the maximum occurrence was only $\sim 0.3\%$. Most of the $\sigma_\phi > 0.15$ rad occurred in November 2009, and from February to March 2010. It maximised at $86-87^\circ$ geomagnetic latitude in November 2009 and at $84-85^\circ$ in April 2010. Meanwhile, $\sigma_\phi > 0.15$ rad was relatively high in February 2010 from 81° to 86° .

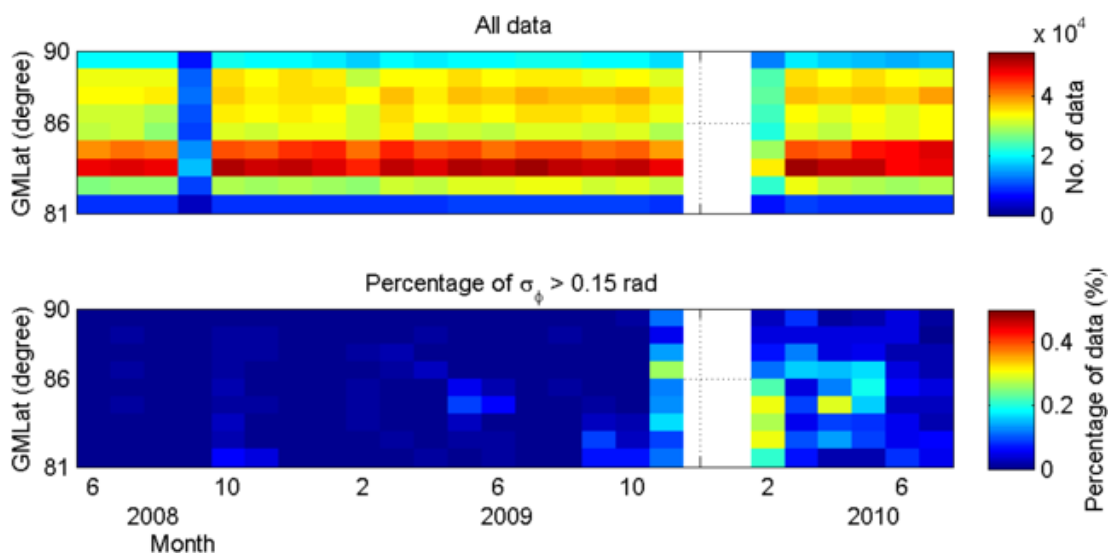


Figure 4.16: Number of all data (top) and percentage of $\sigma_\phi > 0.15$ rad (bottom) as a function of geomagnetic latitude and observed months

4.4 Geomagnetic Activity Dependence

There are a total of 36 cases where the 3-hour K_p indices are considered as active geomagnetic activity, starting from $K_p = 5-$. These cases were distributed in 18 days; covering 5 days in 2008, 4 in 2009 and 9 in 2010. In addition, 27 cases were recognised as unsettled geomagnetic activities where $K_p = 4$ during these days. Table 4.4 lists out the geomagnetic activity level on the days where $K_p \geq 5-$ from June 2008 to July 2010.

Table 4.4: Summary of geomagnetic activity where $K_p \geq 5-$ from June 2008 to July 2010

Date	3-hour K_p indices							
14 Jun 2008	1-	0+	1-	0+	2-	3+	5-	6-
9 Aug 2008	2+	3+	2+	2	2+	4-	5-	5+
18 Aug 2008	2+	3+	3-	3+	5-	4-	3+	3
4 Sep 2008	6-	6	4-	3+	4-	3+	2+	2+
11 Oct 2008	1+	2+	4	3+	5+	6+	5	3-
13 Mar 2009	5-	4	3+	3	3-	3-	2	2+
24 Jun 2009	2+	3	4	2-	2-	2+	5+	3-
22 Jul 2009	3	6-	5	4+	2-	2-	2+	1+
30 Aug 2009	2	1+	3-	2	3	6-	4+	3+
5 Apr 2010	3	3+	5+	8-	6-	5	4+	4-
6 Apr 2010	5	5+	5-	5-	4+	5+	5-	5-
12 Apr 2010	6-	4	3+	1+	1+	3	3-	1
14 Apr 2010	2-	1	0+	1	1-	1+	2+	5
2 May 2010	1	1	1+	4	6	5	6-	5+
3 May 2010	5	4	4-	3+	4-	3	3+	4-
29 May 2010	3-	4-	5+	4-	4+	4+	4+	3
30 May 2010	3-	2+	4	3-	2	4	5	4
4 June 2010	5-	4	2	3+	2-	1	1+	2-

The largest geomagnetic index observed was $K_p = 8-$ was which occurred once only during the period of observations on 5 April 2010. This largest index is categorised

as major storm and was accompanied by minor/moderate storm (i.e. K_p between 5 and 6-) for a few hours before and after that. The events where $K_p > 4$ lasted for 9 hours which were from 0600 to 1800 UT. Figure 4.17 shows the σ_ϕ , slant TEC, and Rate of TEC Index (ROTI) for 5- and 30-min intervals on each visible satellite from 0600 to 1200 UT. This is only the first half part where $K_p > 4$ (refer Table 4.4). The purpose of ROTI is to measure the intensity of patches as described in *Krankowski et al.* [2006]. The 5-min interval gives an indication of the presence of small size patches while 30-min interval implying the presence of large scale patches.

Slant TEC variations can be observed on several satellites through the course of these 6 hours (Figure 4.17 (i-iii) (b)). PRN26 and PRN27 showed increase of ~ 5 TECU from ~ 0630 to 0730 UT where no other satellite showed similar increase. Interestingly, the paths of these two satellites were close to each other and no other nearby satellite (refer Figure 4.18). However these variations on both satellites were mostly only registered as small and large size patches with low intensity, except at ~ 0730 UT where moderate intensity patches was observed on PRN27 (Figure 4.17 (iii) (c)).

TEC variations were also observed from ~ 0830 to ~ 1130 UT on several satellites at various intervals paths. Alternate increase and decrease of TEC signifies that patches were transiting across a satellite path [*Basu et al.*, 1998]. Rate of TEC change per minute for the satellites was high when the respective TEC on a particular satellite shows variations in its value. TEC variations led to formation of patches of small and large sizes with different intensity. Overall, small size patches were more frequently observed during this period of observation than the larger ones.

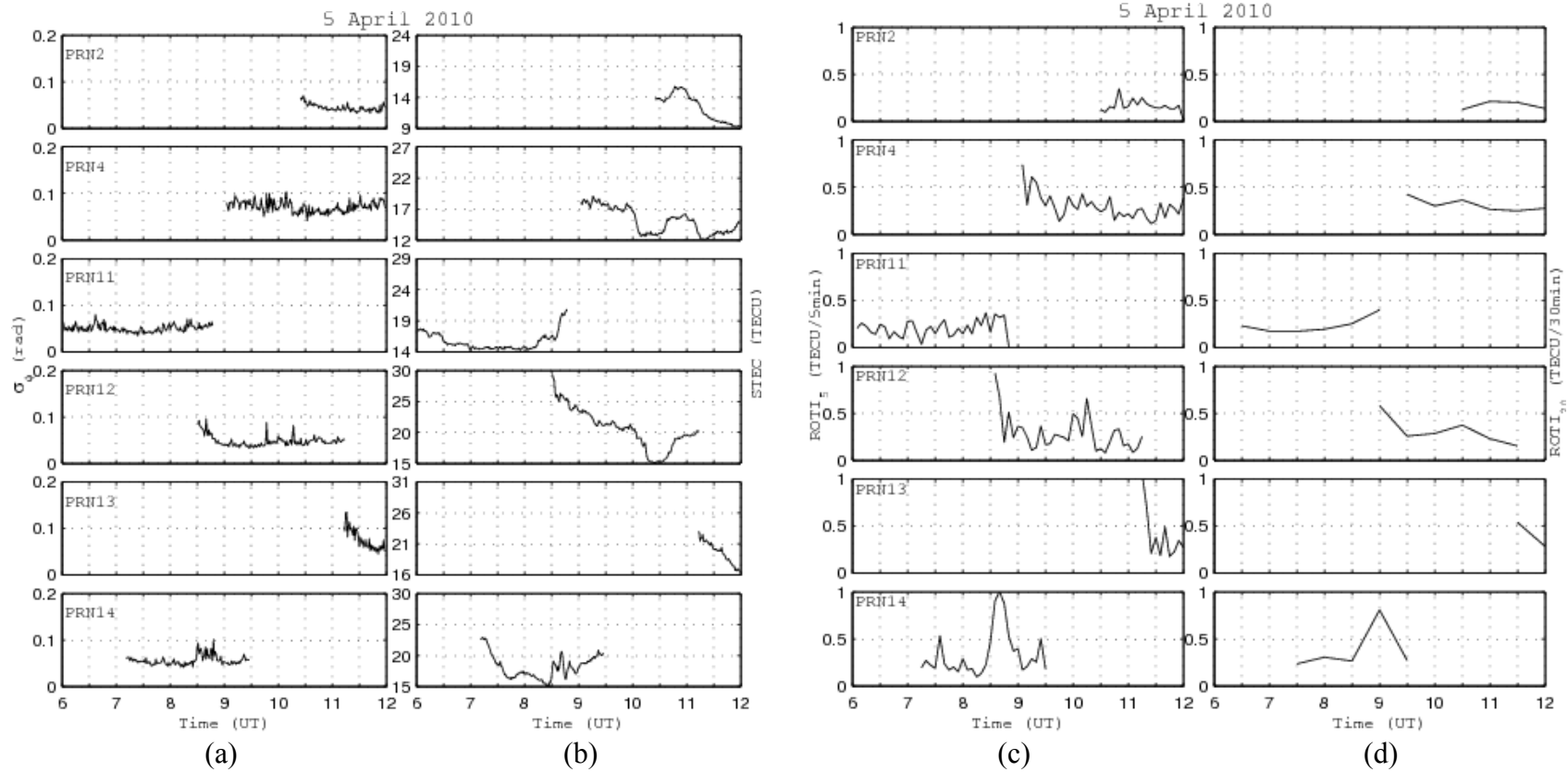


Figure 4.17 (i): (a) σ_ϕ , (b) STEC, (c) ROTI₅ and (d) ROTI₃₀ observed on each visible satellite on 5 April 2010 from 0600 to 1200 UT. Note the different values on y-axis for STEC, but grid scale is equal

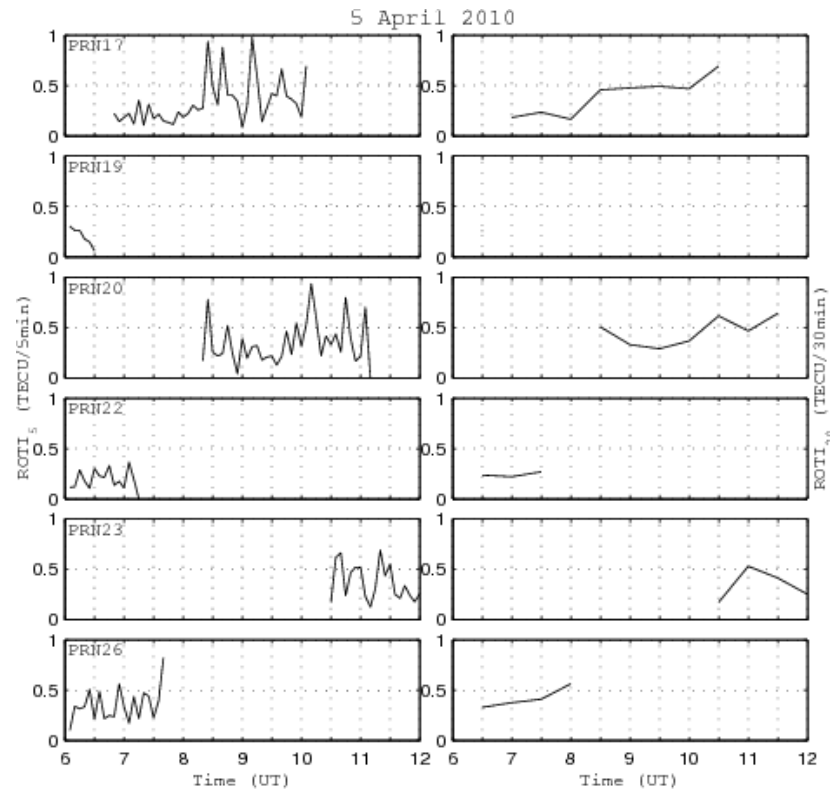
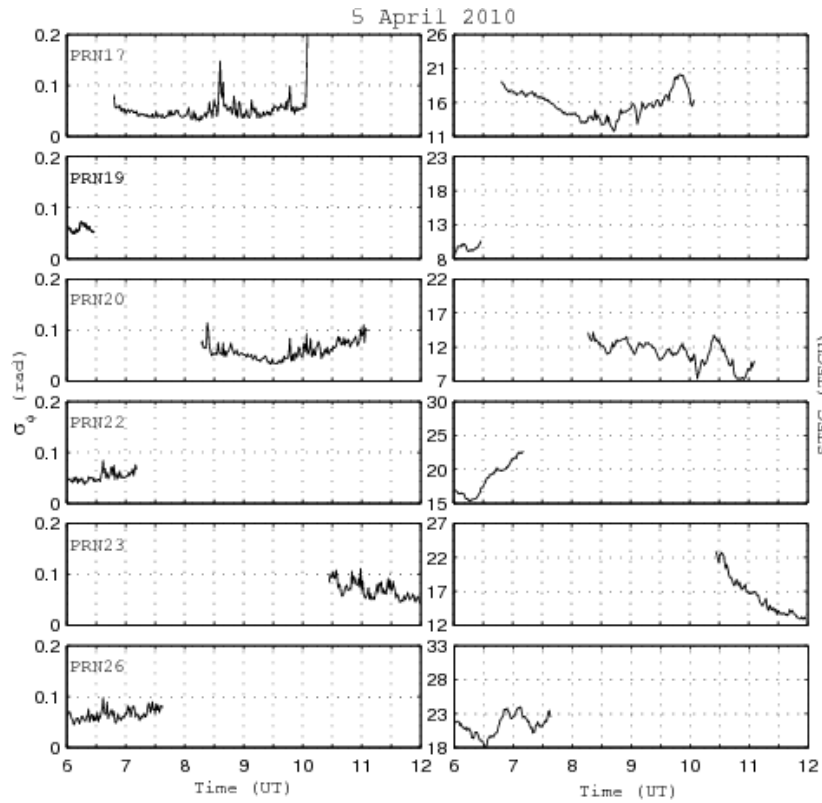


Figure 4.17 (ii): As of (i) but for different satellites

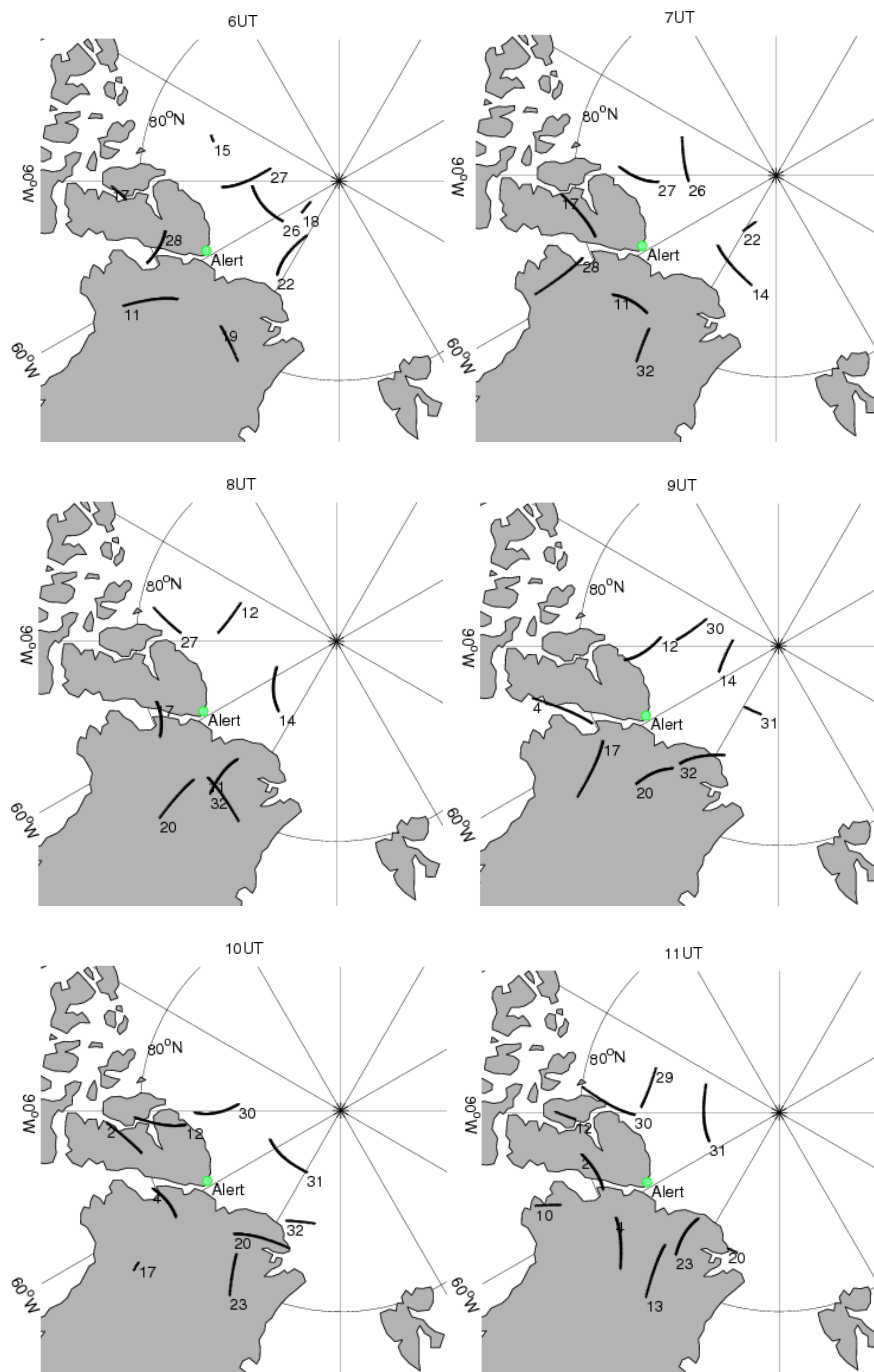


Figure 4.18: Path of all visible satellites for every hour at 350 km ionospheric pierce point on 5 April 2010 from 0600 to 1200 UT. Number on the map refers to satellite number and also marks the start of the path for the period of observation

Existence of moderate to high intensity of small patches were evident from ~0930 to ~1100 UT on PRN20, 30, 31 and 32. The path of these satellites were scattered all above Alert (projected at ~350 km of ionospheric pierce point). Another series of moderate to high intensity and small size patches were observed between ~0815 and ~0930 UT on PRN17. Meanwhile, one large size patches was detected on PRN14 between ~0830 UT to ~0900 UT (Figure 4.17 (i) (d)). Since TEC were fluctuating quite frequent in short period time consecutively, these small size patches will accumulate and registered as large patches.

Regarding the phase scintillations, increased σ_ϕ were observed on PRN17 at ~0830 UT (Figure 4.17 (ii) (a)), and on PRN30 and PRN31 from ~0945 to 1030 UT (Figure 4.17 (iii) (a)). Paths of PRN30 and PRN31 were not nearby during this period. Overall, ionospheric behaviour during this period of active geomagnetic activity varies from observation of one satellite to another, regardless of the intensity of the geomagnetic index and the path of the satellites. Only a few satellites demonstrated significant variations of TEC and phase scintillations during this period.

IMF B_z component was mainly southward between ~0700 to ~0900 UT up to ~-15 nT, then fluctuating between both polarities until ~1000 UT before settled on northward direction up to ~15 nT until ~1300 UT. Then the values decreased but predominantly northward until end of the day (see Figure 4.19). B_x and B_y components also demonstrates similar behaviour with B_z where fluctuations from background values were observed from ~0800 to ~1300 UT. All IMF data were obtained from <http://cdaweb.gsfc.nasa.gov> unless stated otherwise.

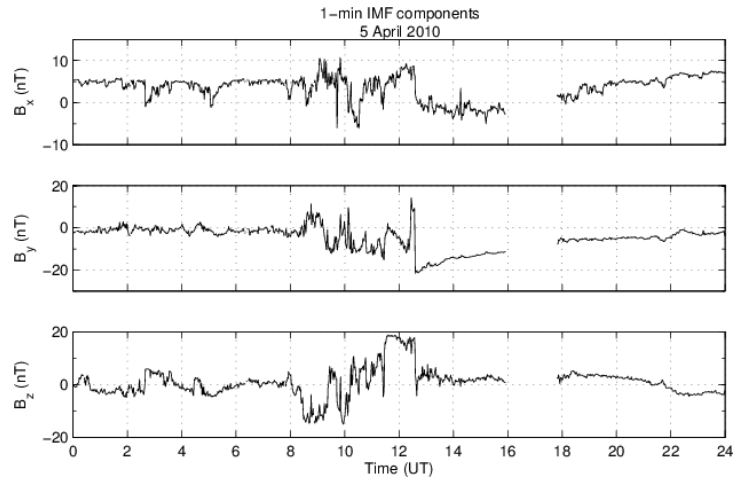
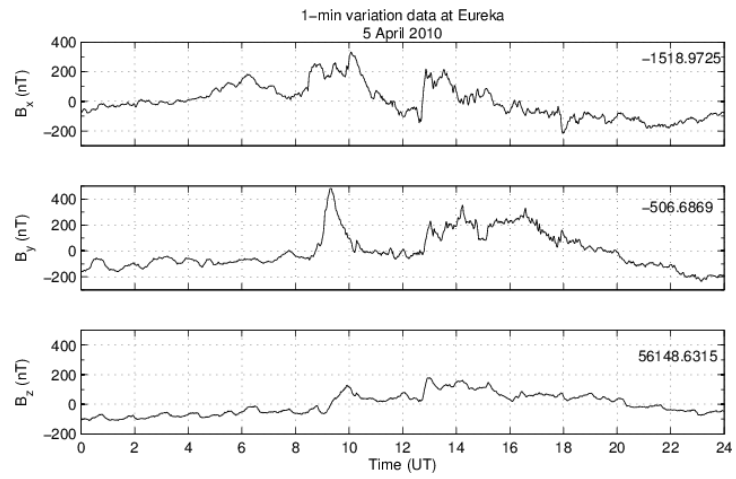
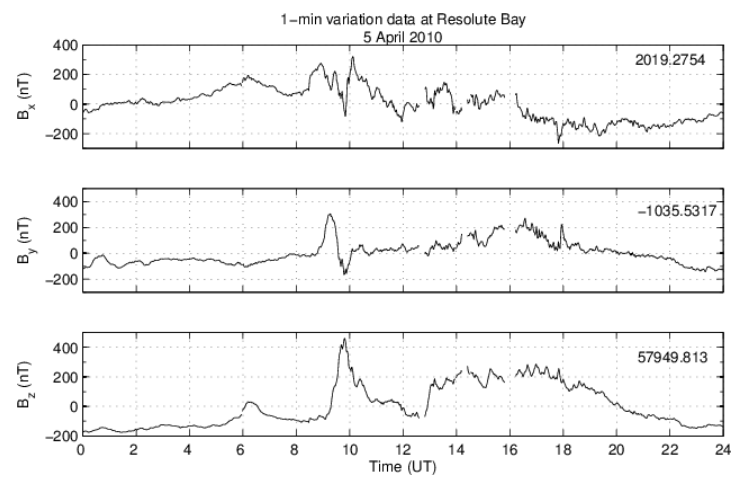


Figure 4.19: 1-minute IMF components on 5 April 2010



(a)



(b)

Figure 4.20: 1-minute variation data at (a) Eureka, and (b) Resolute Bay on 5 April 2010. The number at the top right of each frame is the mean of its respective component

Magnetic data (Figure 4.20) at two polar cap stations at Eureka and Resolute Bay are utilised in order to observe the behaviour of ground magnetic field at the polar region. Eureka is closer to the geomagnetic pole compared to Resolute Bay. Each component of magnetic fields demonstrates large variation from its respective mean between 0500 and 1400 UT (for B_x), and between 0830 and 1800 UT (B_y) at both stations. Meanwhile, B_z component at Resolute Bay shows large variation from its mean between 0900 and 1800 UT. These periods were where $K_p > 4$. B_z component at Eureka are relatively low compared to Resolute Bay but still reached up to ~ 180 nT.

Overall, only 3.2% of all cases where $\sigma_\phi \geq 0.15$ rad occurred during all events where $K_p \geq 5$. This shows that geomagnetic activity has a very small effect of on the phase scintillations during the period of observations. Largest contribution of $\sigma_\phi \geq 0.15$ rad was from 11 October 2008 and 2 May 2010 where 26 and 22 cases, respectively, were observed from total of 2149 cases. Only 6 cases of $\sigma_\phi \geq 0.15$ rad were observed on 5 April 2010 where K_p index showed the highest of 8-. Although amplitude scintillations during the period of observations are all dismissed as insignificant, for comparison, $S4 > 0.1$ during $K_p \geq 5$ are only 0.5 % of the total occurrences.

Figure 4.21 shows σ_ϕ , STEC and both ROTI for 5- and 30-min intervals observed on all visible satellites on 11 October 2008 from 1200 to 1800 UT where $K_p > 4$. Generally, variations of phase scintillations (Figure 4.21 (i-iii) (a)) and TEC (Figure 4.21 (i-iii) (b)) on this day were more frequently observed than on 5 April 2010 (where K_p was higher). Similar to the previous case, the plots are shown only partly where $K_p > 4$.

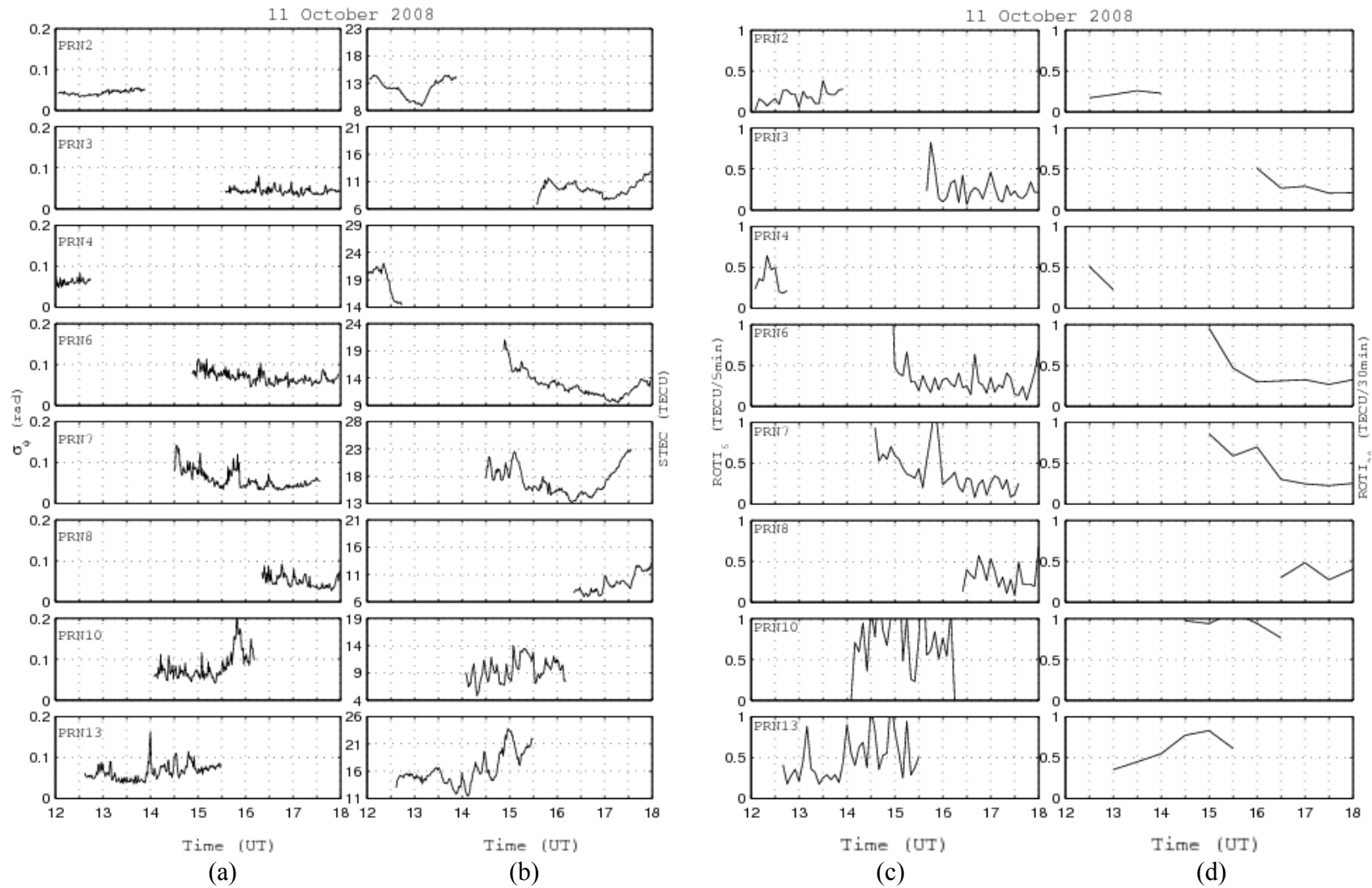
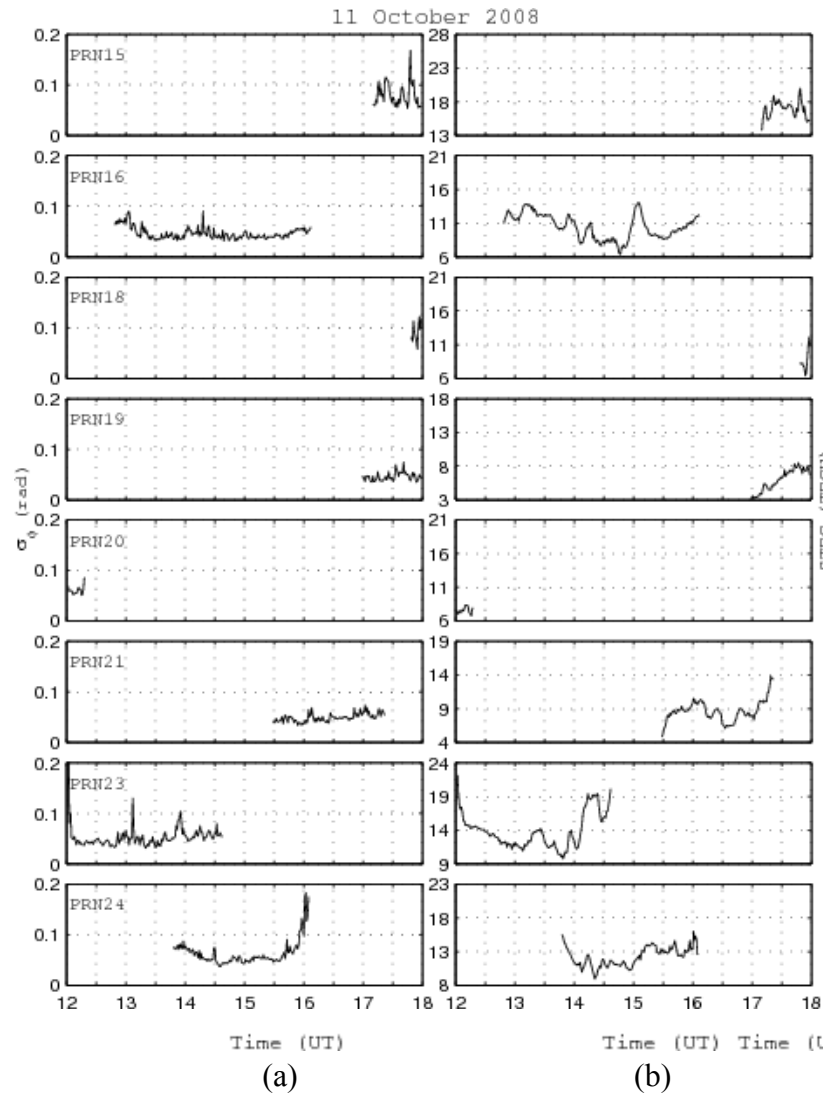
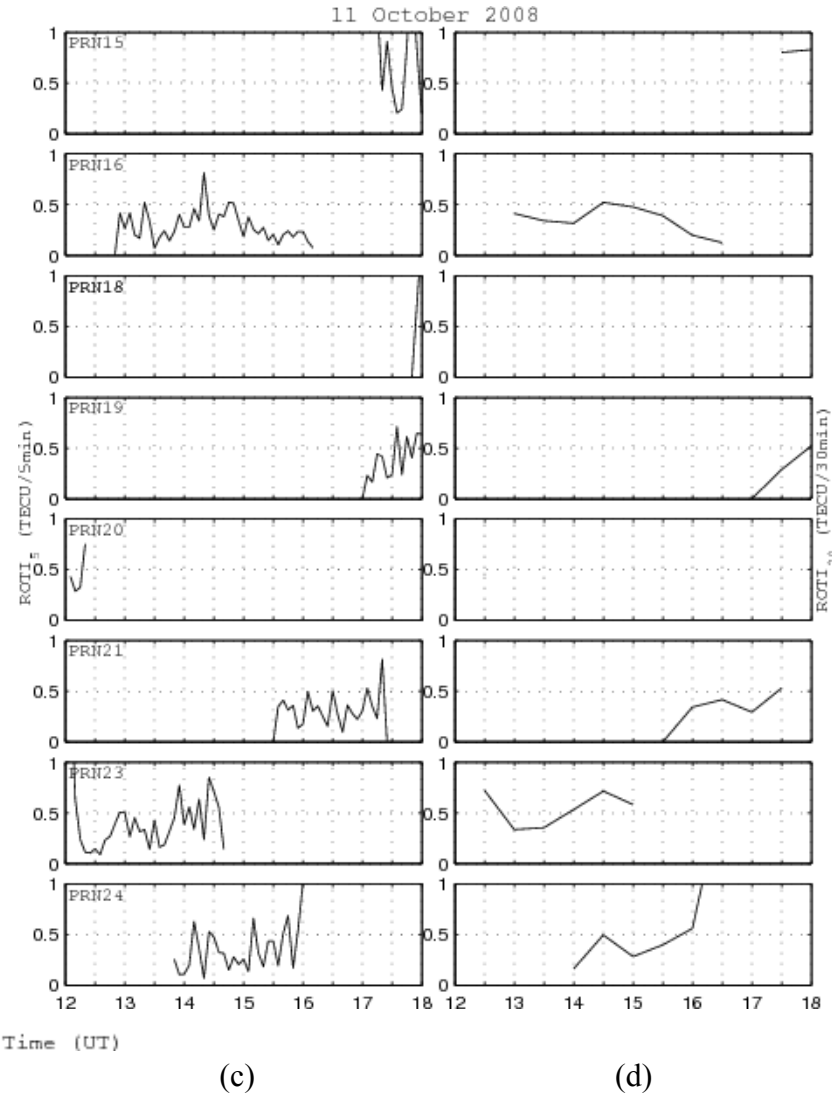


Figure 4.21 (i): (a) σ_ϕ , (b) STEC, (c) $ROTI_5$ and (d) $ROTI_{30}$ observed on each visible satellite on 11 October 2008 from 1200 to 1800 UT



(b)



(d)

Figure 4.21(ii): As of (i) but for different satellites

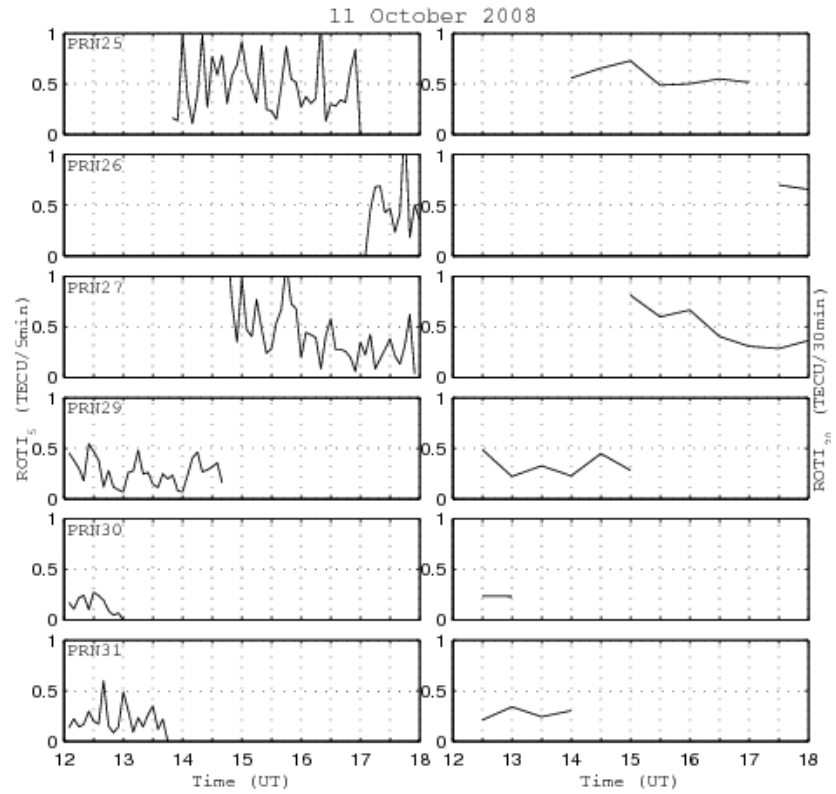
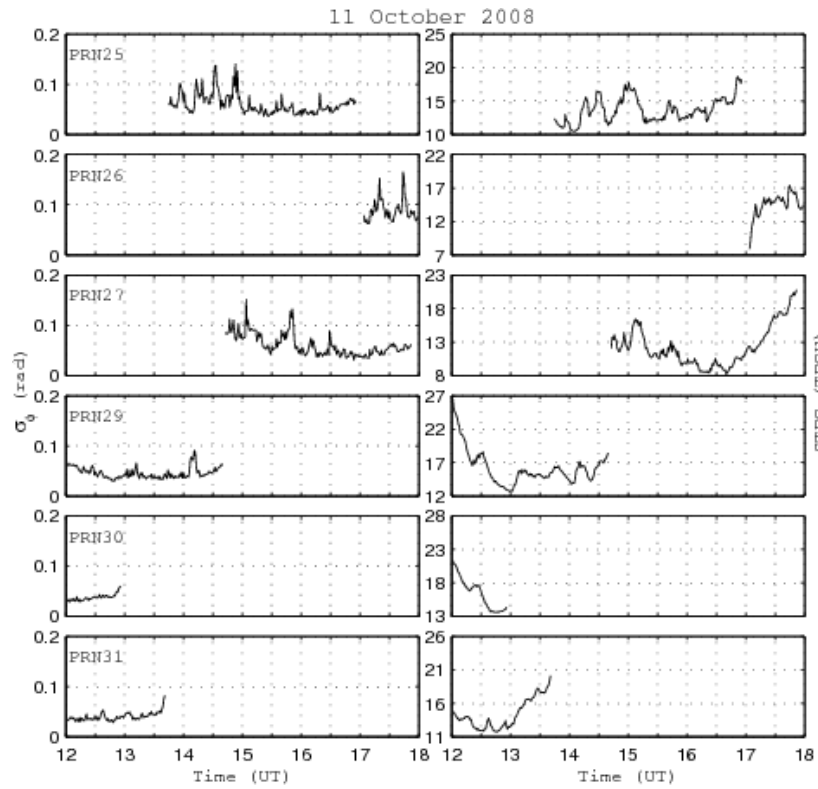


Figure 4.21 (iii): As of (i) but for different satellites

Series of moderate to high intensity of small patches were apparent on many satellites at various paths from ~1400 to ~1600 UT, and from ~1400 to ~1700 UT on PRN25. Less small patches of moderate to high intensity were observed between ~1700 to ~1800 UT. Meanwhile, one large patch was observed on PRN17 from ~1530 to ~1600 UT. Series of small size patches can be seen as one larger patch, for example on PRN10 and PRN13. Path of all these satellites at 350 km ionospheric pierce point is illustrated in Figure 4.22.

IMF B_z component was southward until ~1100 UT when it changed its polarity and stayed ~10 nT before returning southward at ~1300 UT and then fluctuating between positive and negative polarities until ~1800 UT when it stayed northward until end of the day (see Figure 4.23). B_x component at Eureka varied from -230 to 160 nT between 0730 and 1830 UT. This is similar of what were recorded at Resolute Bay during the same periods. B_y varied from -100 to 200 nT at both stations (but slightly smaller at Resolute Bay) between 0800 and 22 UT. B_z at Eureka for the same durations were only half of the values recorded at Resolute Bay. The period where $K_p > 4$ was between 1200 and 2100 UT, but magnetic components at both stations varied largely from their respective means starting from few hours earlier. In comparison with the previous case, the magnetic components on 11 October 2008 were smaller than 5 April 2010 where K_p was lower on the former day.

Direct comparison may not be suitable as these two days are in different month and year, thus the dissimilarity in behaviour. This is supported by finding of *Dandekar* [2002] where diurnal, seasonal and solar cycle dependence of polar patch occurrence is predominant and dependence on geomagnetic activity is secondary.

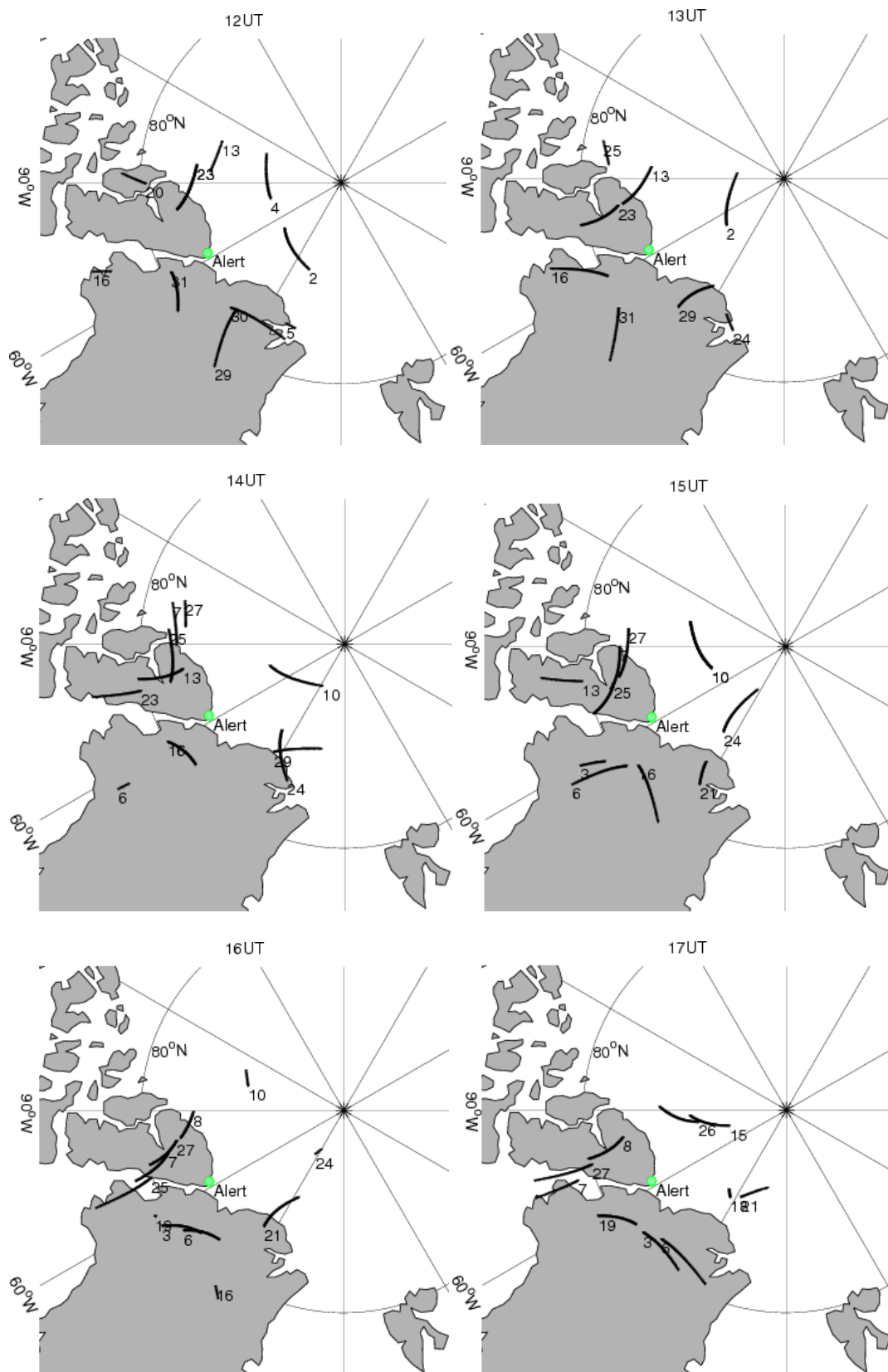


Figure 4.22: Path of all visible satellites for every hour at 350 km ionospheric pierce point on 11 October 2008 from 1200 to 1800 UT

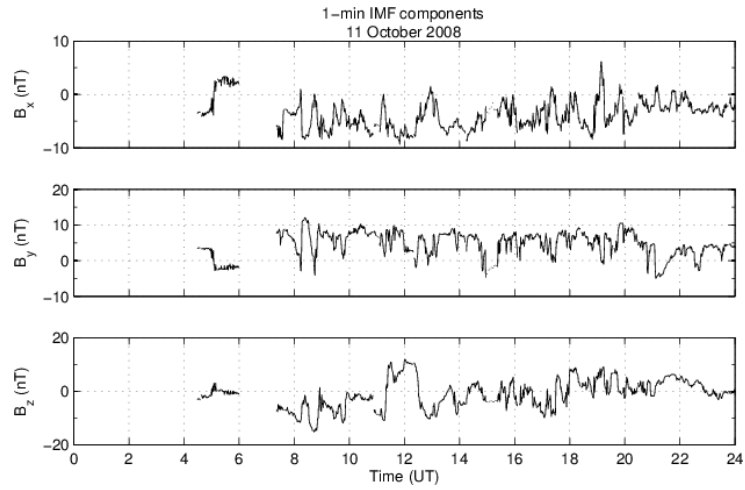
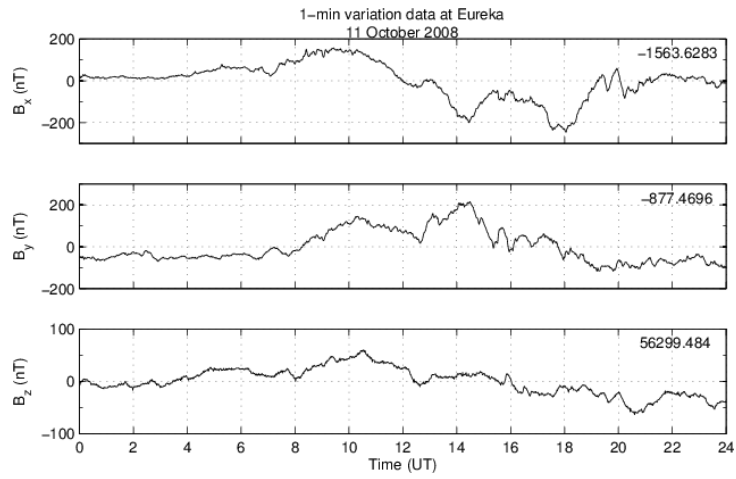
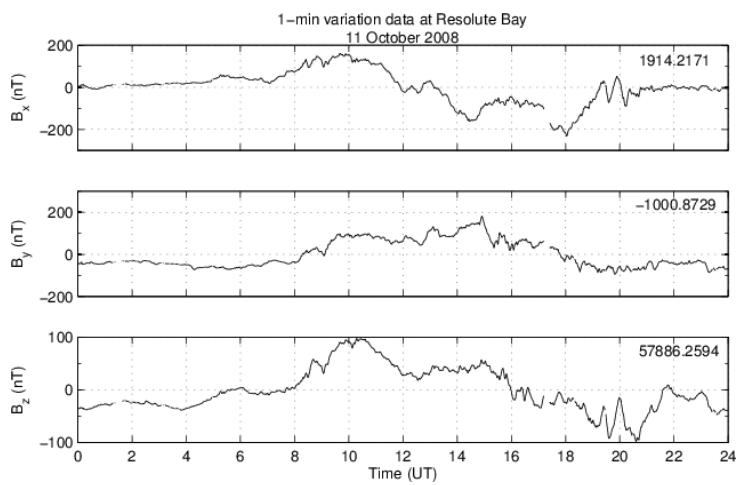


Figure 4.23: 1-minute IMF components on 11 October 2008



(a)



(b)

Figure 4.24: : 1-minute variation data at (a) Eureka, and (b) Resolute Bay on 11 October 2008

In the storm event on 30 November 2003, regions on both amplitude and phase scintillations occurred in coincidence with increasing vertical TEC values, where scintillations were observed around the edges of TEC. The parameters are observed on a GISTM receiver located at Ny-Ålesund [Mitchell *et al.*, 2005]. However, direct comparison with this storm event should not be made as series of severe and strong storm were recorded in October 2003 while only once occurrence of $K_p = 8-$ in April 2010, followed by short series of minor storms (refer Figure 4.25 and Figure 4.26). Polar cap index at Thule, PC(N) shows similar pattern with K_p index where maximum PC(N) of 16 was recorded during October 2003 storm but only ~ 5 in April 2010.

Hourly value of B_z reached ~ 30 nT in October 2003 and only ~ 7 nT in April 2010 event. In addition, D_{st} index also shows huge differences on these two events. Daily SSN reached ~ 170 during October 2003 event but only < 30 during April 2010 event. Different time of the year could also affect the severity of TEC and/or scintillation variations as weak phase scintillations observed at Resolute station, Canada in July 2004 storm event compared to October and November 2003 storms as concluded in Momani *et al.* [2008].

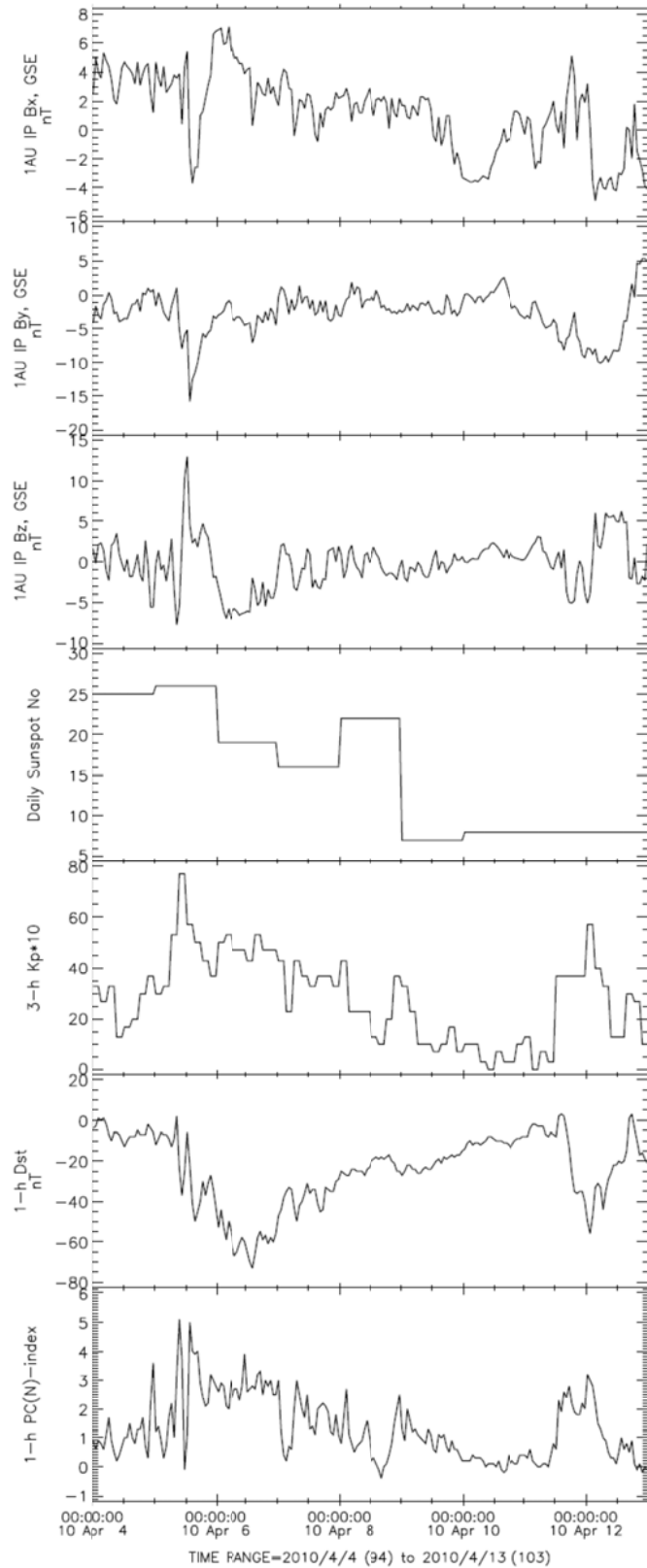


Figure 4.25: Hourly IMF components, D_{st} and $PC(N)$ indices, 3-hour K_p index, and daily SSN from 4 April to 12 April 2010 (Source: <http://cdaweb.gsfc.nasa.gov>)

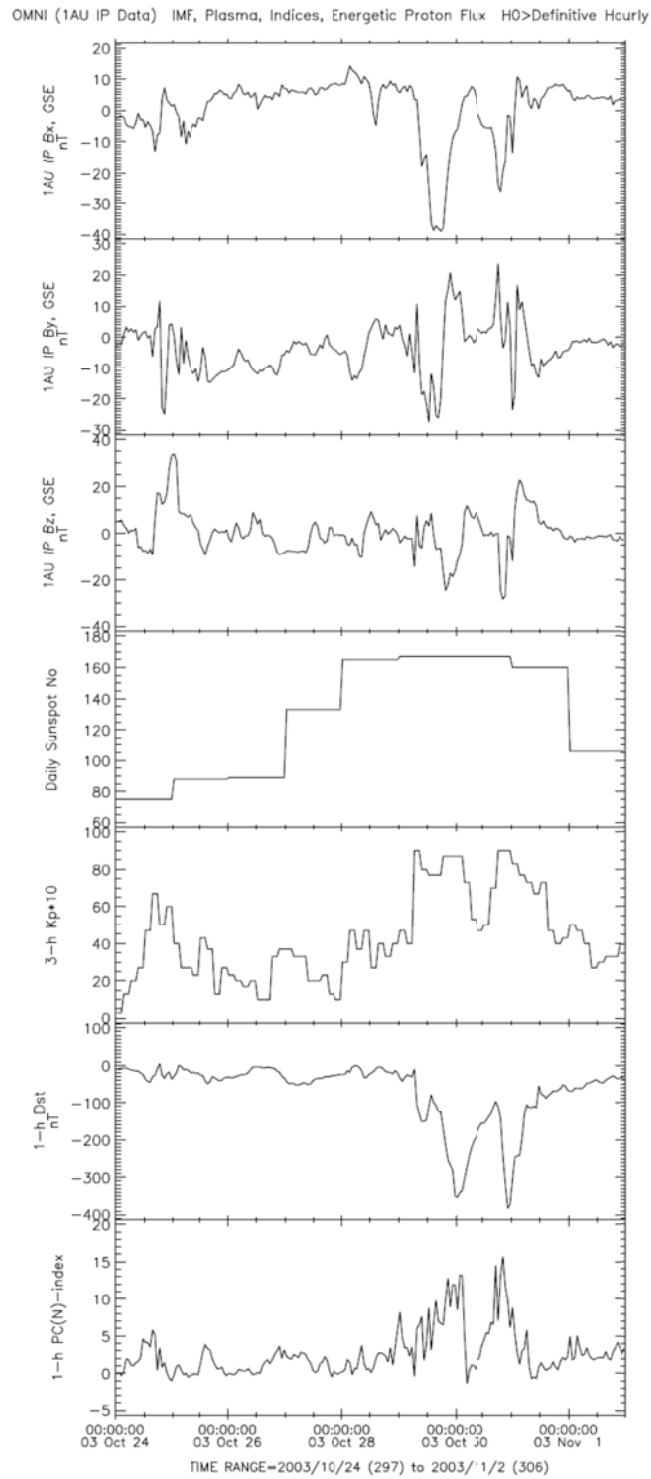


Figure 4.26: Hourly IMF components, D_{st} and $PC(N)$ indices, 3-hour K_p index, and daily SSN from 24 October to 3 November 2003
(Source: <http://cdaweb.gsfc.nasa.gov>)

4.5 Selected Events

Ionospheric variability at high latitude area is very complex, making it difficult to categorise the changes. Here, several events of significant phase scintillations and TEC variations are presented. Event types are labelled as A1, A2, A3 and so on in order to differentiate with the event types discussed later in Chapter Six, labelled as B1, B2, B3 and so on.

The alphabet refers to the detection method used to observe the polar ionosphere irregularities; A is the transionospheric link as seen by the dual-frequency GPS receiver at Alert, Canada, and B is the HF link between Qaanaaq and Ny-Ålesund. The number of the event types does not correspond to the same irregularity observed in A and B, but rather just a categorisation of different event types seen using each detection method. Table 4.5 gives the description for each event type used in this section.

Table 4.5: Description of each event type

Event Type	Description
A1	σ_ϕ increase, no TEC changes
A2	TEC fluctuation, σ_ϕ increase
A3	TEC fluctuation, no σ_ϕ increase
A4	TEC increase, and/or small σ_ϕ increase
A5	TEC increase, σ_ϕ increase at edges
A6	Longer TEC increase, no σ_ϕ increase

Event Type A1

Event Type A1 represents selected events of which experienced medium phase scintillations. In this study, phase scintillations greater than 0.15 rad is used as threshold. Different σ_ϕ threshold was used in other works by several authors including 0.25 rad in *Spogli et al.* [2009], 0.17 and 0.25 rad in *Li et al.* [2010], and 0.2 rad in *Gwal and Jain* [2011].

Figure 4.27 (a) shows σ_ϕ occurrence on 4 February 2009 between 0200 and 0400 UT. Medium σ_ϕ were recorded on PRN12 (0.24 rad) and PRN30 (0.22 rad) at 0313 UT and 0318 UT, respectively. Relatively lower σ_ϕ of ~ 0.16 to 0.17 rad can be seen few minutes later on these two satellites and also on PRN5. Paths of these satellites are close to each other and having similar orientations as shown in Figure 4.28.

Slant TEC (Figure 4.27 (b)) on satellites which experienced medium phase fluctuations (i.e. PRN5, 12, 30) showed small fluctuation that leads to formation of small size of mostly weak patches, and also occasionally moderate to high intensity patches as indicated by the ROTI (Figure 4.27 (c)). However, moderate to high intensity of large patches do not exist (Figure 4.27 (d)). A clearer example of TEC small fluctuation of ~ 1 -2 TECU is illustrated in Figure 4.29, Figure 4.30 and Figure 4.31 for PRN30, 12 and 5, respectively. This figure also demonstrates that ROT (i.e. the rate of TEC fluctuations) can reach up to $\sim \pm 1$ TECU on few occasions for these satellites.

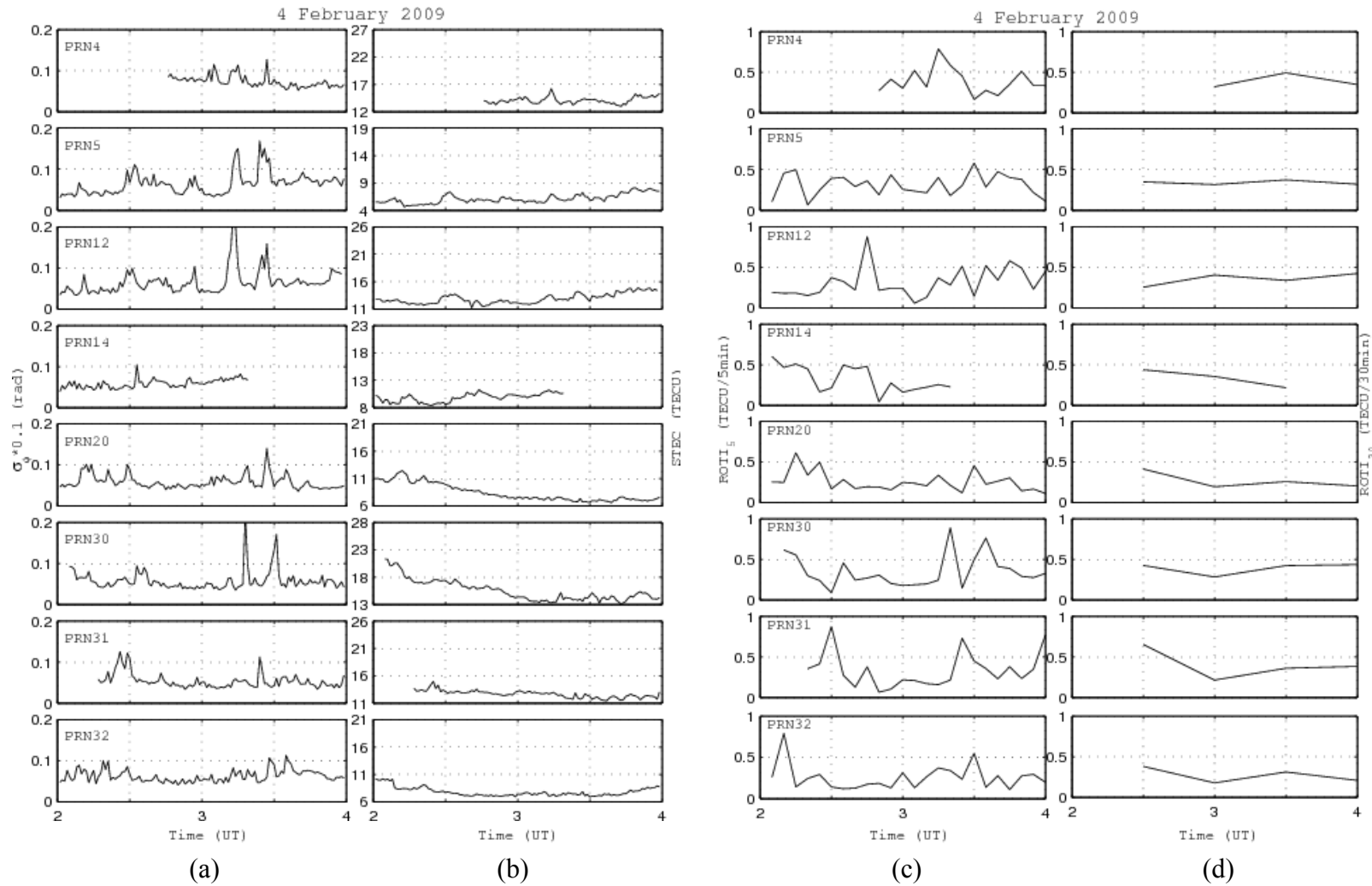


Figure 4.27: (a) σ_{ϕ} , (b) STEC, (c) ROTI₅ and (d) ROTI₃₀ observed on each visible satellite on 4 February 2009 from 0200 to 0400 UT. Short-period observations on any satellite from 0300 to 0400 UT are not shown

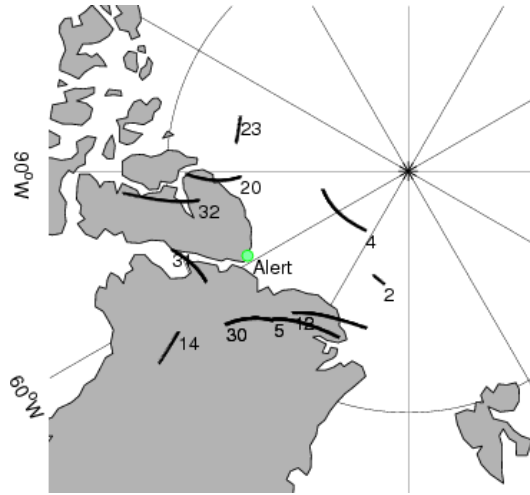


Figure 4.28: Path of all visible satellites for every hour between 0300 to 0400 UT on 4 February 2009

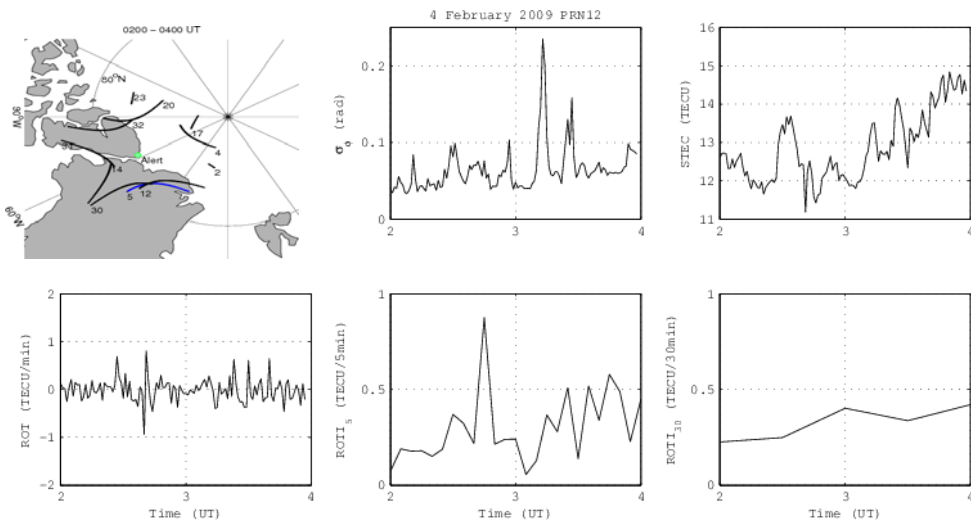


Figure 4.29: σ_ϕ , STEC, ROT, and ROTI for 5- and 30-min interval of PRN12 on 4 February 2009 from 0200 to 0400 UT. Paths of all visible satellites at 350 km are also shown

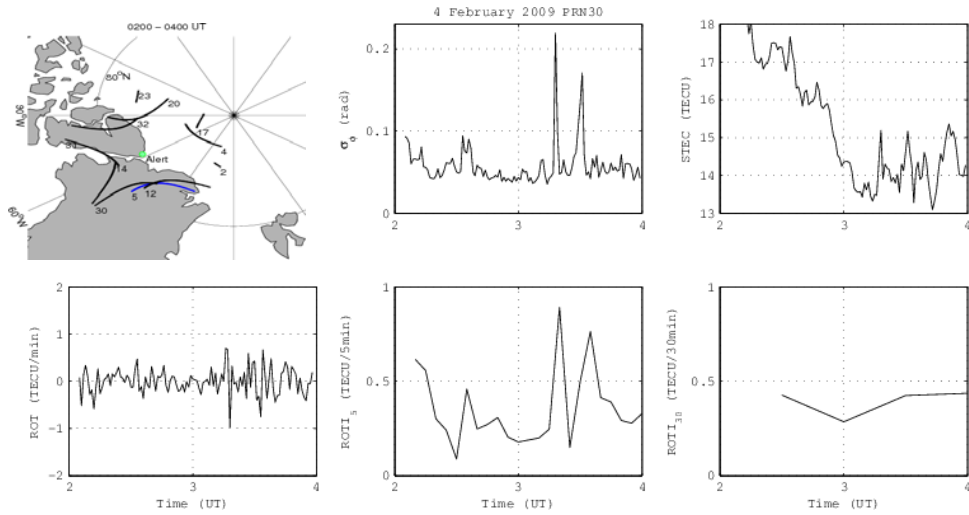


Figure 4.30: σ_ϕ , STEC, ROT, and ROTI for 5- and 30-min interval of PRN30 on 4 February 2009 from 0200 to 0400 UT. Paths of all visible satellites at 350 km are also shown

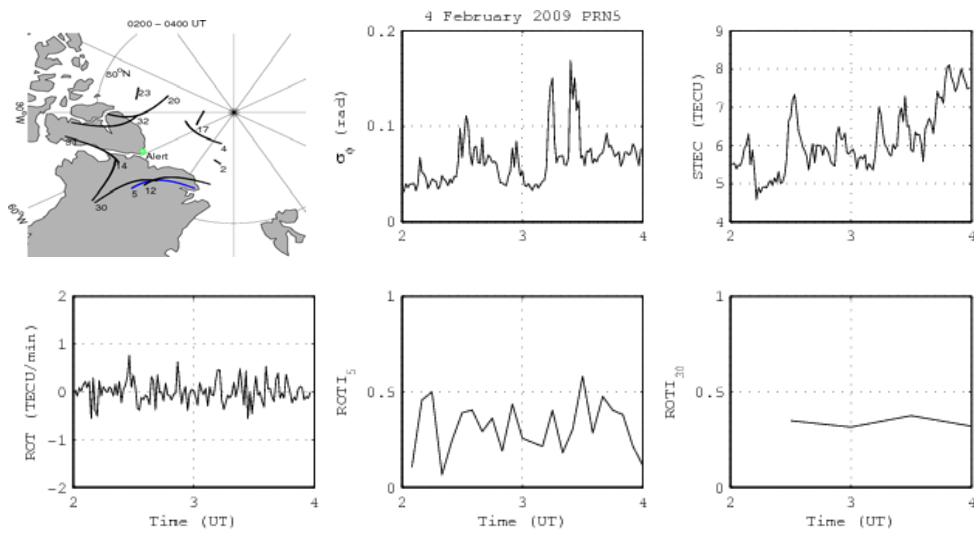


Figure 4.31: σ_ϕ , STEC, ROT, and ROTI for 5- and 30-min interval of PRN5 on 4 February 2009 from 0200 to 0400 UT. Paths of all visible satellites at 350 km are also shown

In addition, all other visible satellites also showed small phase scintillations increase between 0.1 and 0.14 rad during the same time of the medium phase scintillations detected on PRN5, 12 and 30, but at various locations above Alert. K_p on this day was low, which was between 3- and 4-. IMF B_y and B_z (see Figure 4.32) were from -7 to 10 nT and mostly northward during the period of observation (0200 to 0400 UT). The 1-minute magnetic field variation data at Eureka and Resolute Bay stations showed not much variation from their respective means during the period of interest between 0200 and 0400 UT (Figure 4.33). However, outside the period of observations, magnetic components can reach up to ± 100 nT (and even higher on B_y at Eureka) between ~ 1000 and 1900 UT. B_z component at Eureka was still the least variable compared to all other components.

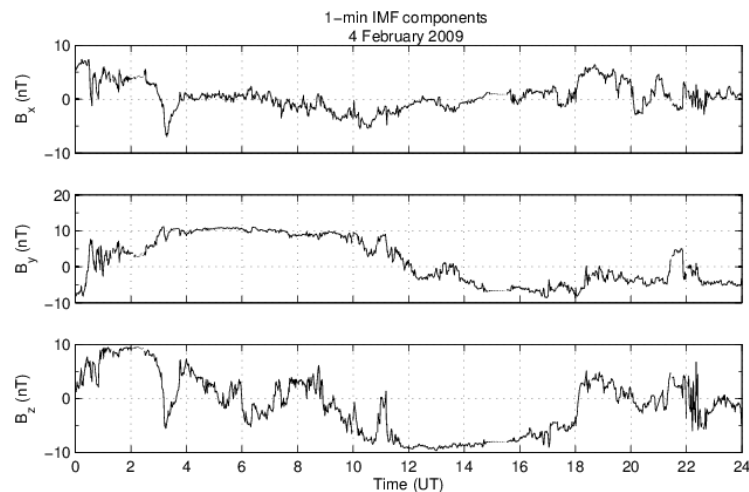


Figure 4.32: 1-minute IMF components from 1200 UT on 4 February 2009

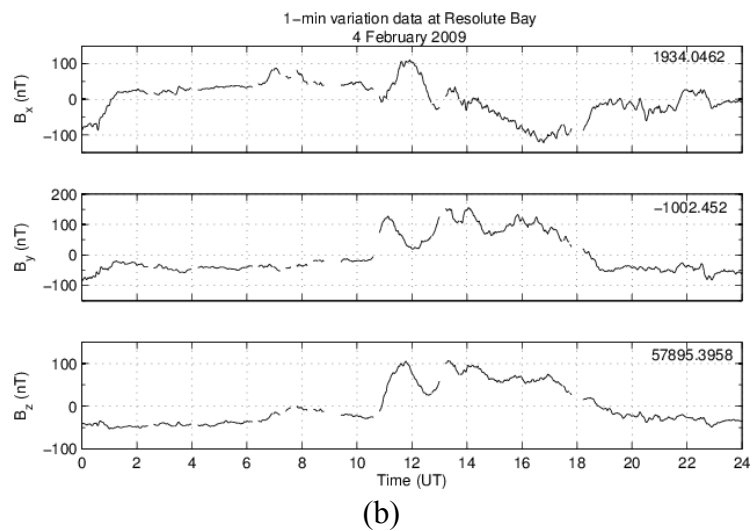
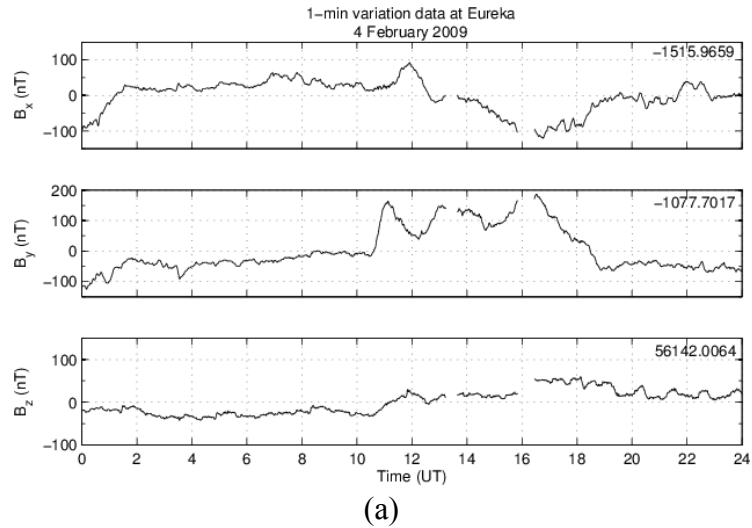


Figure 4.33: 1-minute variation data at (a) Eureka, and (b) Resolute Bay on 4 February 2009

Figure 4.34 shows an event of σ_{ϕ} occurrence on 8 April 2009 where a peak of 0.19 rad can be seen at 1120 UT on PRN4 that lasted for 4 minutes only. A higher and longer σ_{ϕ} up to 0.22 rad occurred from 1211 UT to 1229 UT. Slant TEC on PRN4 showed very little variation as illustrated in the rate of TEC plot. No patch was registered for this satellite during this period.

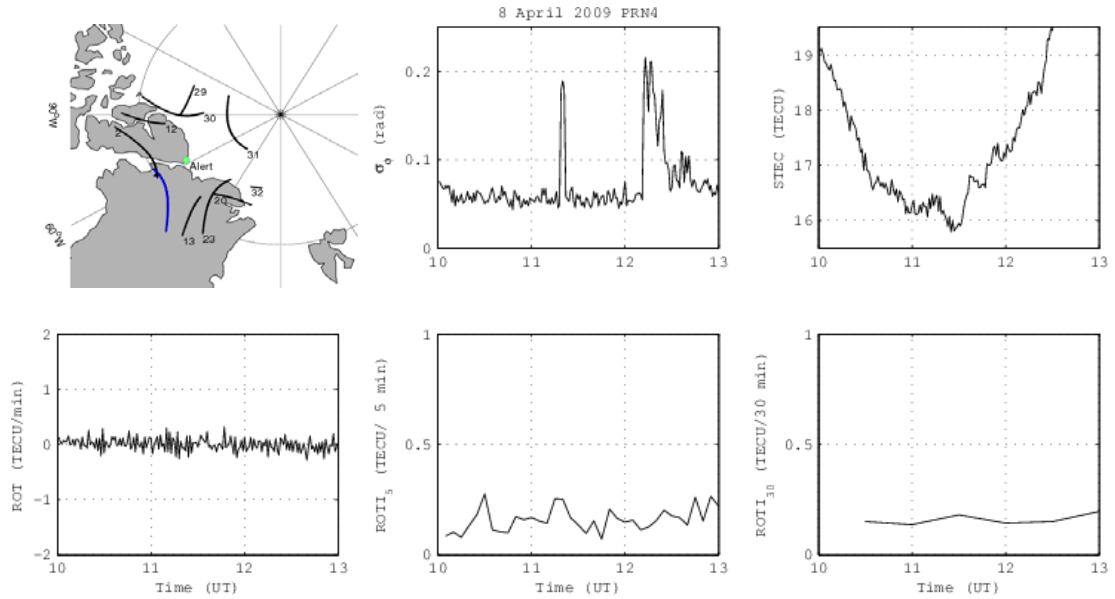


Figure 4.34: σ_ϕ , STEC, ROT, and ROTI for 5- and 30-min interval of PRN4 on 8 April 2009 from 1000 to 1300 UT. Paths of all visible satellites from 1100 to 1300 UT at 350 km are also shown

In general, nothing significant detected on slant TEC for this day on any satellite (Figure 4.35 (b)), and no moderate to high intensity of patches detected either for small or large size (Figure 4.35 (c)-(d)). This could be an event of a small scale irregularity of localised phase scintillations. No other satellite was orbiting nearby (PRN2 reached the same location of the scintillation event but at a different time). K_p was low between 0+ and 3+, and data for IMF components were not available during the time of observations. However, the following data shows low B_z of $< \pm 2$ nT only (see Figure 4.36).

All components at both Eureka and Resolute Bay stations showed no significant variations from their mean values during the period of observations (1100-1300 UT) as illustrated in Figure 4.37.

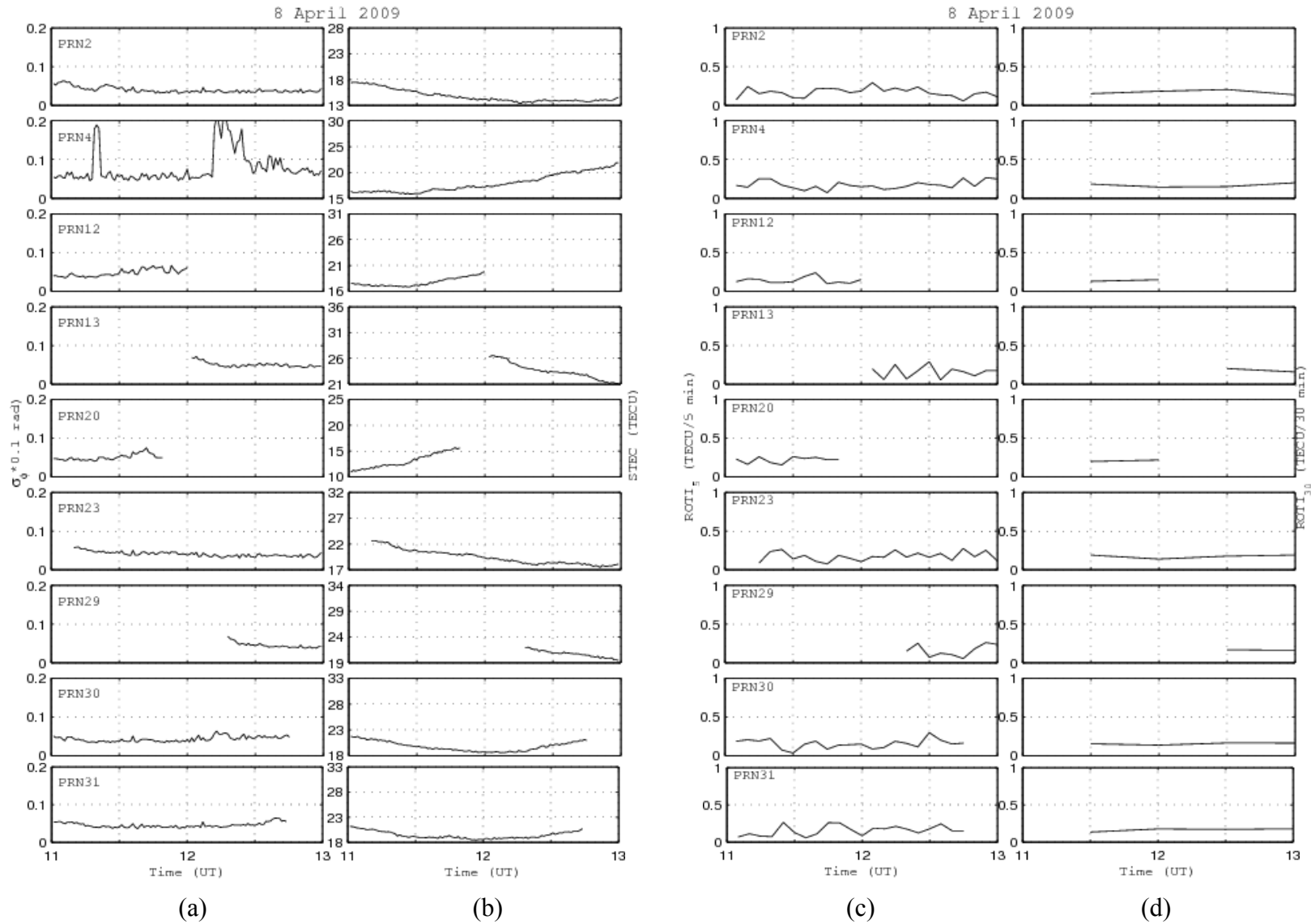


Figure 4.35: (a) σ_{ϕ} , (b) STEC, (c) ROTI₅ and (d) ROTI₃₀ observed on each visible satellite on 8 April 2009 from 1100 to 1300 UT. Short-period observations on any satellite are not shown

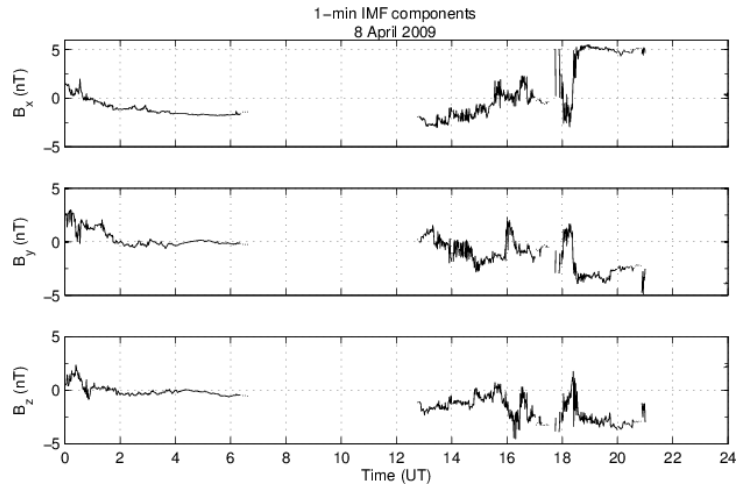
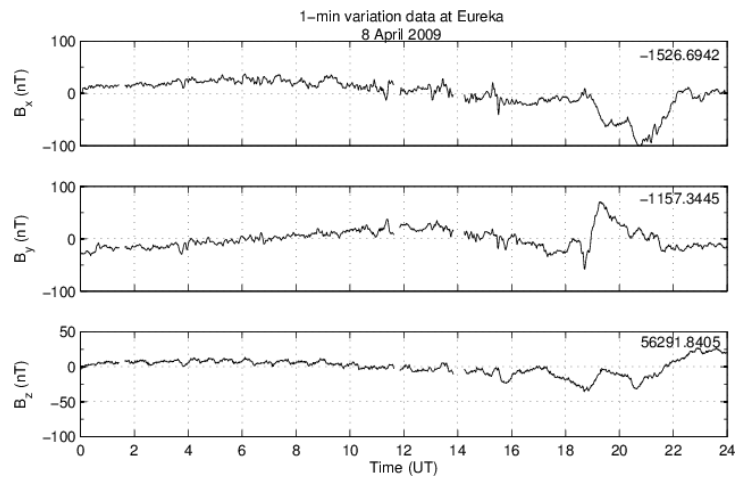
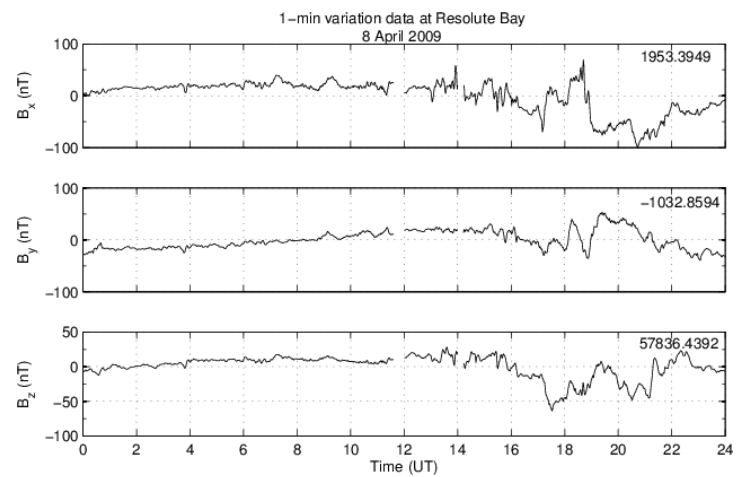


Figure 4.36: 1-minute IMF components on 8 April 2009



(a)



(b)

Figure 4.37: 1-minute variation data at (a) Eureka, and (b) Resolute Bay on 8 April 2009

A similar case was also observed on PRN11 on 12 May 2010 at ~0500-0515 UT where no other satellite experienced phase scintillations that reached up to ~0.6 rad (refer Table 4.3). Most of the $\sigma_\phi > 0.4$ rad was observed on this satellite alone. However, PRN11 on 12 May 2010 recorded slightly more TEC fluctuations in comparison to PRN4 on 8 April 2009.

Event Type A2

Event Type A2 refers to the events where medium to large TEC fluctuations and/or increases were detected on some satellites and they were accompanied by increased phase scintillations. Several events have been highlighted in Section 4.4 on 11 October 2008 and 5 April 2010 where K_p is greater than 4. Details of two of the events on 11 October 2008 are illustrated in Figure 4.38 and Figure 4.39. It is evident from these figures that increased phase scintillations occurred during the time of fluctuating TEC as illustrated on STEC and also Rate of TEC (ROT) plots. Large TEC variations were observed, sometimes up to ~8 TECU. TEC fluctuation indicator, that is the ROT also reached up to ± 2.5 TECU/min especially on PRN10. This is well above the average value of $\sim \pm 0.15$ TECU/min.

Phase scintillations were observed for a few times on each satellite during the period of observations, varying from ~0.16 rad to ~0.23 rad. Existence of series of moderate to high intensity of small patches can also be seen from the figures. Large patches of moderate to high intensity were also observed on both satellites. Geomagnetic indices on this day were categorised as active.

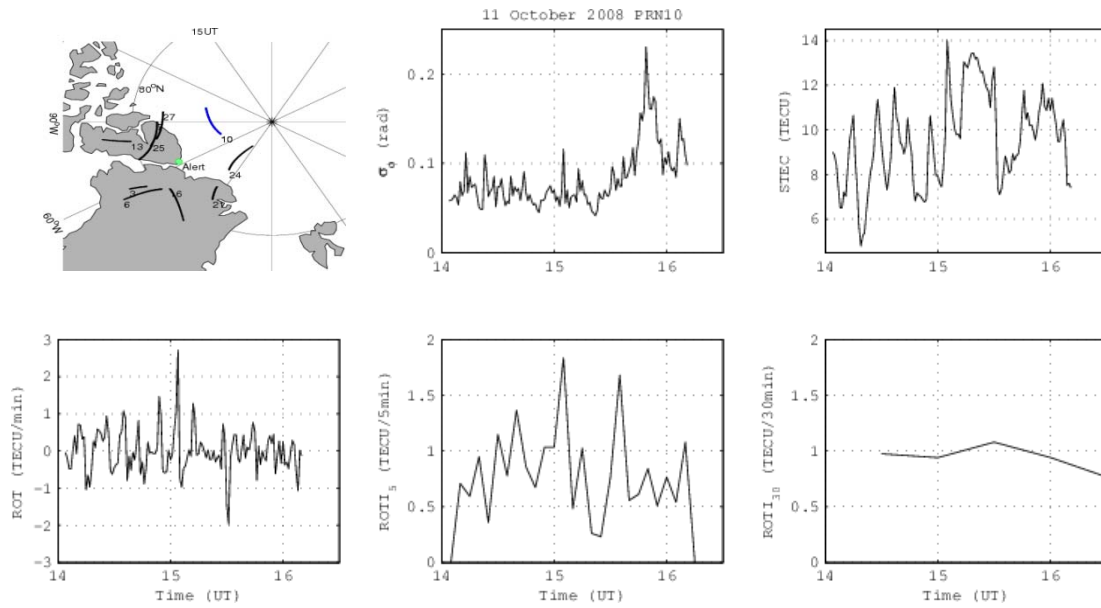


Figure 4.38: σ_ϕ , STEC, ROT, and ROTI for 5- and 30-min interval of PRN10 on 11 October 2008 from 1400 to 1630 UT. Paths of all visible satellites from 1500 to 1600 UT at 350 km are also shown

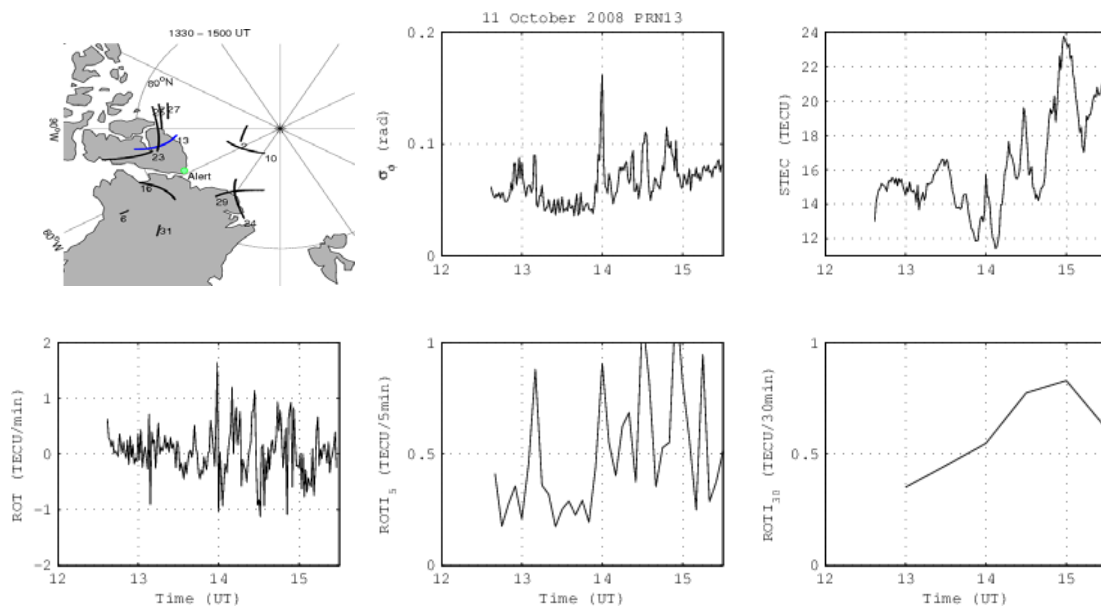


Figure 4.39: σ_ϕ , STEC, ROT, and ROTI for 5- and 30-min interval of PRN13 on 11 October 2008 from 1200 to 1530 UT. Paths of all visible satellites from 1330 to 1500 UT at 350 km are also shown

Another example of similar event is presented in Figure 4.40 between 1600 and 2000 UT on 15 February 2010. Increased phased scintillations of 0.17 rad was observed on PRN24 between ~1810 to ~1825 UT where slant TEC was also increased ~7TECU during this time. However, TEC increases and/or fluctuations were also observed on most visible satellites at the same time. Relatively smaller σ_ϕ increase of ~0.16 rad was also apparent on PRN8 together with smaller TEC fluctuation. Paths of PRN8 and PRN24 were not close to each other during this period (see Figure 4.41).

Meanwhile, PRN7 observed phase scintillations of ~0.17 and ~0.16 rad earlier which peaked at ~1700 UT and ~1746 UT, respectively. TEC increases on PRN7 were also evident at these times. Small size patches with moderate to high intensity were observed on all visible satellites corresponding to unsettling TEC behaviour. Since small scale TEC fluctuations occurred continuously, they can also be interpreted as large patches. Details of the σ_ϕ , slant TEC, ROTI for both 5- and 30-minute interval for PRN24, PRN7 and PRN8 were illustrated in Figure 4.42, Figure 4.43 and Figure 4.44, respectively.

Event Type A2 was commonly observed on many days throughout the whole 2-year observation periods. Whenever large TEC fluctuations occurred, they would normally followed by increase of σ_ϕ . However, the phase scintillations were normally less than the threshold which is set to 0.15 rad. Phase scintillations also normally did not occur continuously but rather in chaotic and random manner.

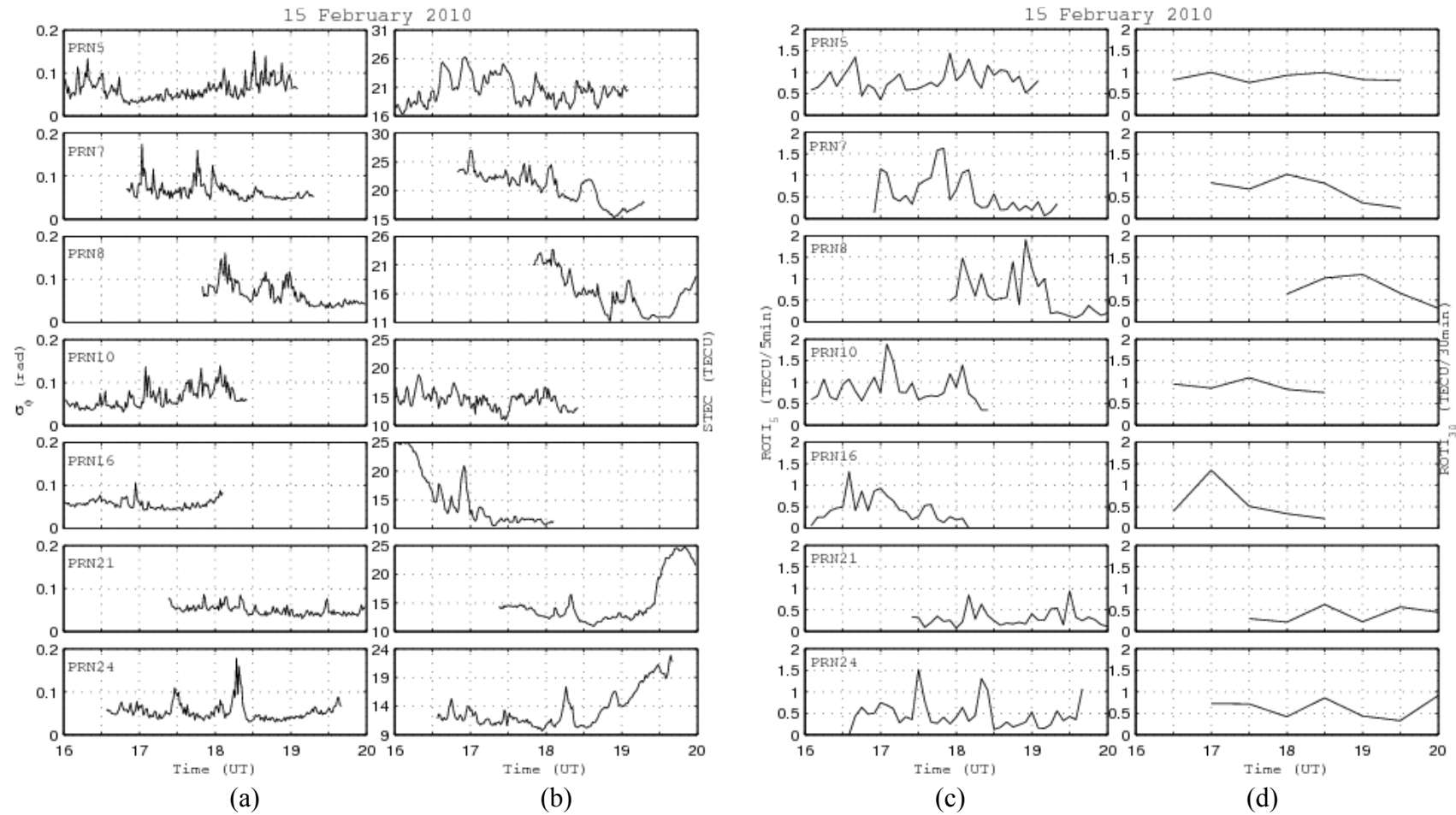


Figure 4.40: (a) σ_ϕ , (b) STEC, (c) $ROTI_5$ and (d) $ROTI_{30}$ observed on each visible satellite on 15 February 2010 from 1600 to 2000 UT

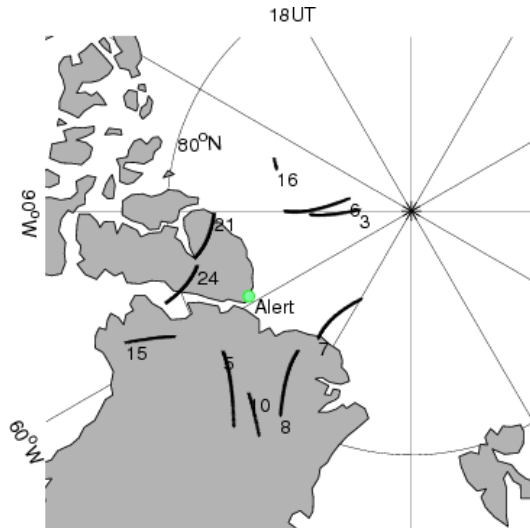


Figure 4.41: Path of all visible satellites from 1800 to 1900 UT on 15 February 2010

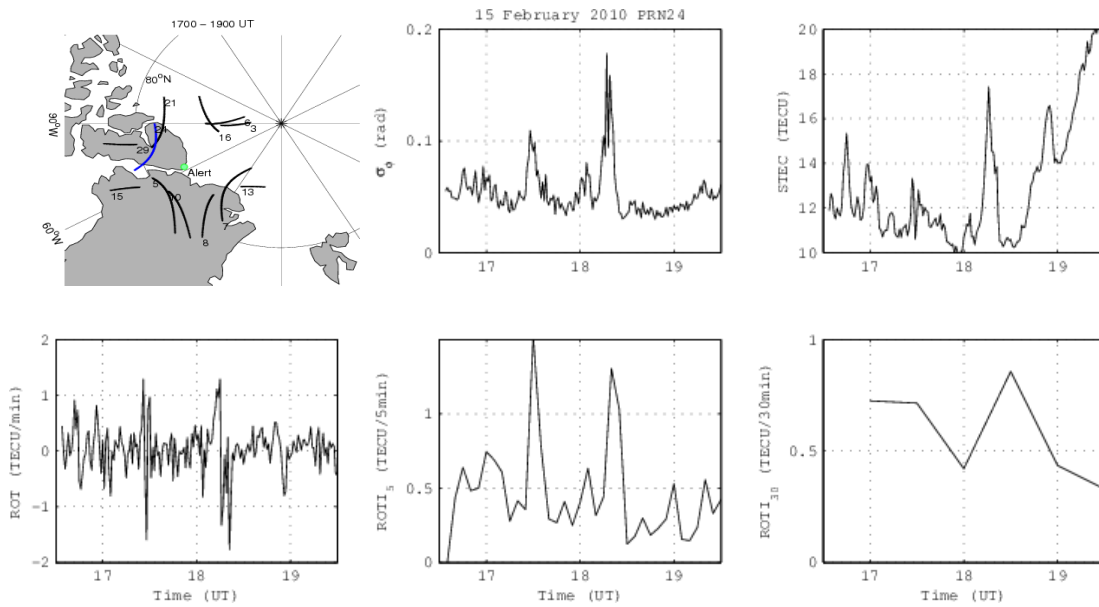


Figure 4.42: σ_ϕ , STEC, ROT, and ROTI for 5- and 30-min interval of PRN24 on 15 February 2010 from 1630 to 1930 UT. Paths of all visible satellites from 1700 to 1900 UT at 350 km are also shown

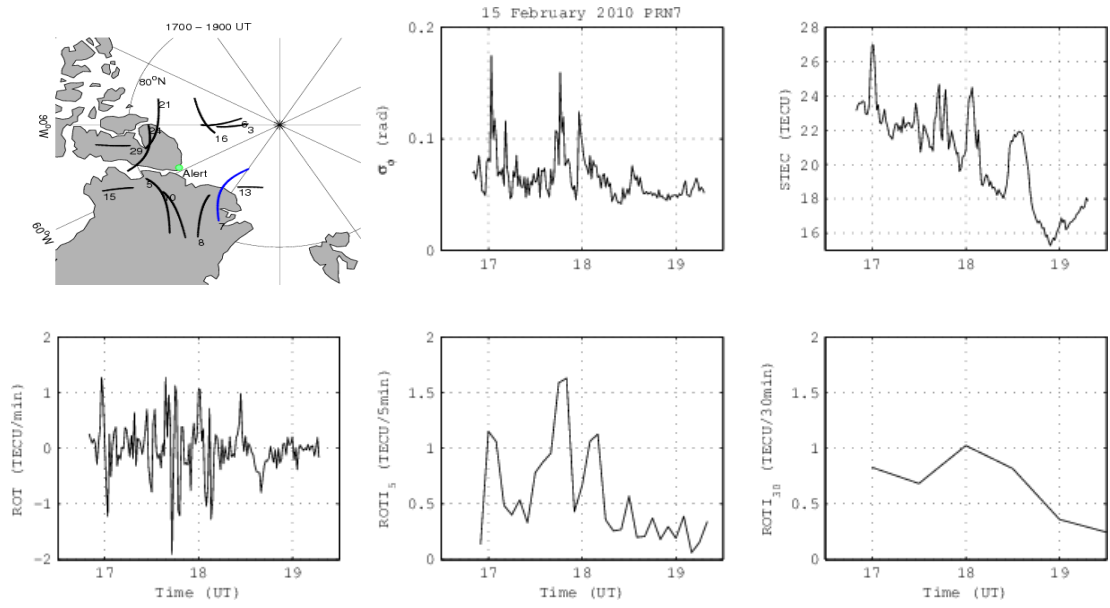


Figure 4.43: σ_ϕ , STEC, ROT, and ROTI for 5- and 30-min interval of PRN7 on 15 February 2010 from 1630 to 1930 UT. Paths of all visible satellites from 1700 to 1900 UT at 350 km are also shown

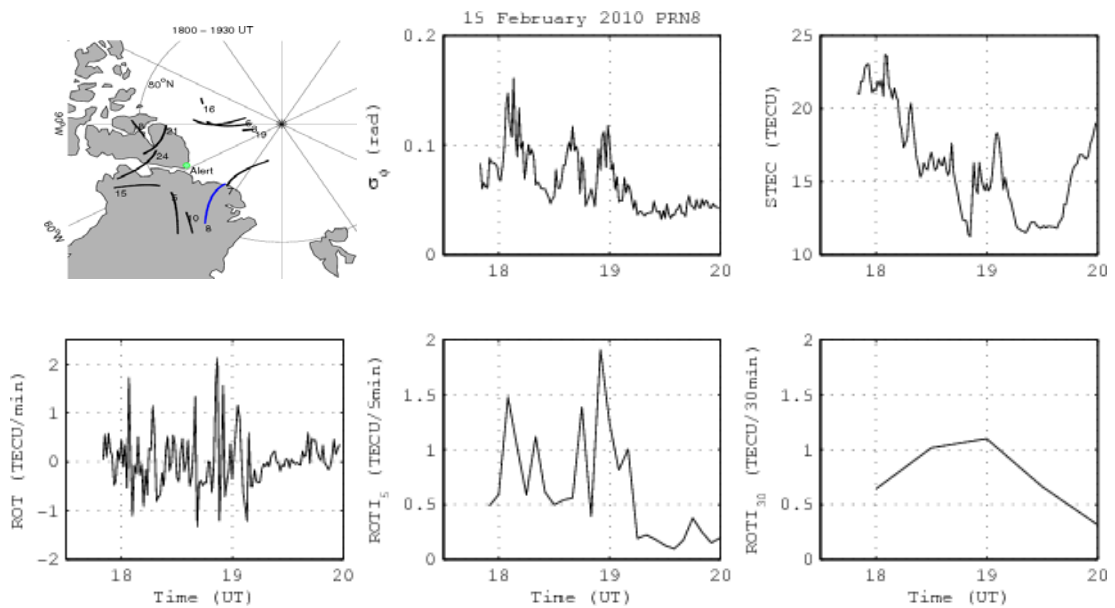


Figure 4.44: σ_ϕ , STEC, ROT, and ROTI for 5- and 30-min interval of PRN8 on 15 February 2010 from 1730 to 2000 UT. Paths of all visible satellites from 1800 to 1930 UT at 350 km are also shown

Geomagnetic indices on 15 February 2010 were between 1+ and 4+ (i.e. low to unsettled) and IMF B_z component was predominantly southwards (see Figure 4.45). Events discussed from 15 February 2010 (1600 to 2000 UT) are in contrast with the events extracted from both 11 October 2008 and 5 April 2010, where the former were observed during low geomagnetic condition. All components of magnetic field at Eureka and Resolute Bay demonstrated changes from their background values starting from ~ 1700 UT until ~ 2200 UT (Figure 4.46). This was around the same time as the observations period of TEC fluctuations and relatively smaller σ_ϕ increases on many satellites.

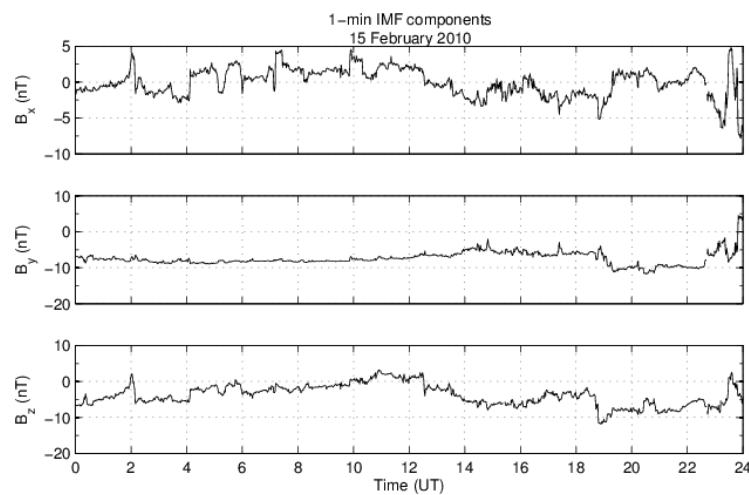


Figure 4.45: 1-minute IMF components on 15 February 2010

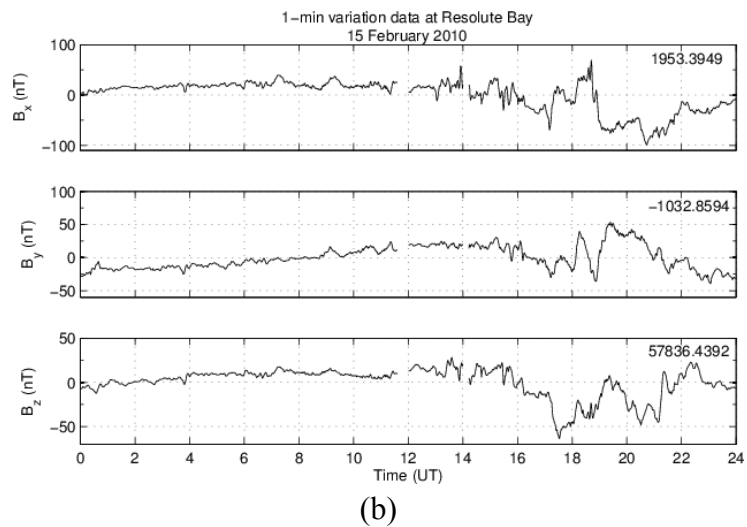
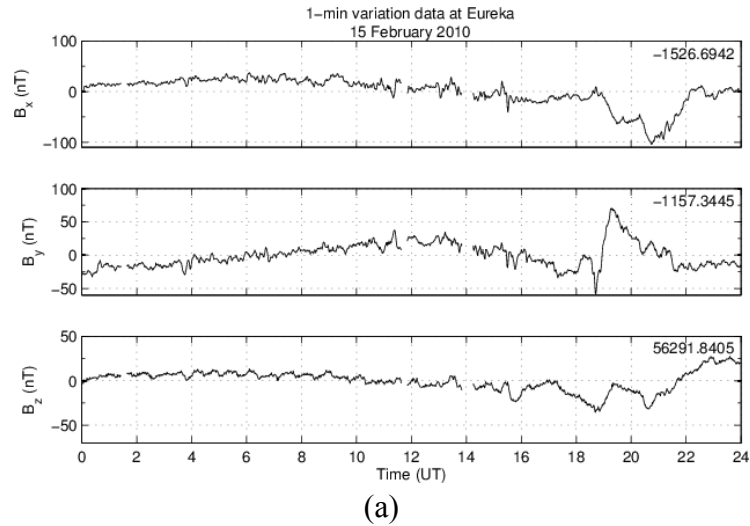


Figure 4.46: 1-minute variation data at (a) Eureka, and (b) Resolute Bay on 15 February 2010

Event Type A3

Examples shown in Event Type A2 so far demonstrated cases where phase scintillations were found to be increased or fluctuated during the same period of TEC fluctuations. However, this is not always true. Figure 4.47 shows an example on 24 February 2010 for PRN27 where large TEC fluctuations were observed between ~ 2000 and ~ 2300 UT but σ_ϕ was maintained at low values except a small increase of ~ 0.06 rad at ~ 2035 UT.

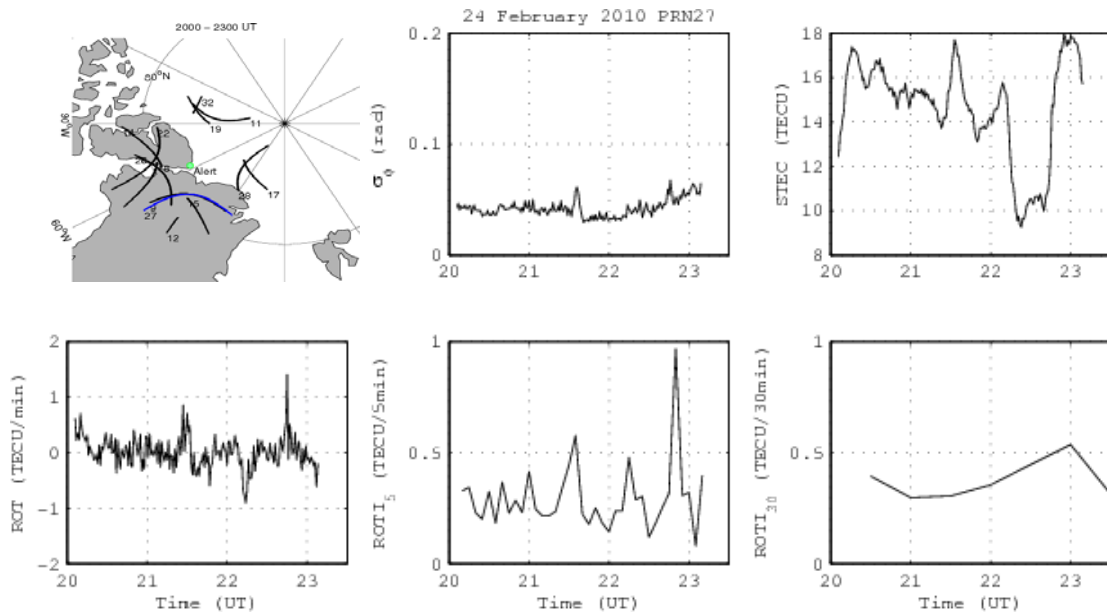


Figure 4.47: σ_ϕ , STEC, ROT, and ROTI for 5- and 30-min interval of PRN27 on 24 February 2010 from 2000 to 2330 UT. Paths of all visible satellites from 2000 to 2300 UT at 350 km are also shown

It is interesting to note that large TEC fluctuations were also observed on other satellites as illustrated in Figure 4.48, for example on PRN17 and PRN26. However, large σ_ϕ of ~ 0.2 rad were also detected on these satellites. These are the cases that fall under the category of Event Type A2.

Similar example as PRN27 is shown in Figure 4.49 for PRN28 on 11 March 2010 between 0600 and 1000 UT. While large TEC fluctuations were observed on PRN28, σ_ϕ remained at low levels except at ~ 0930 UT where it increased up to ~ 0.1 rad only. Several cases of large TEC fluctuations were also detected on other satellites (Figure 4.50), together with no significant increases of σ_ϕ .

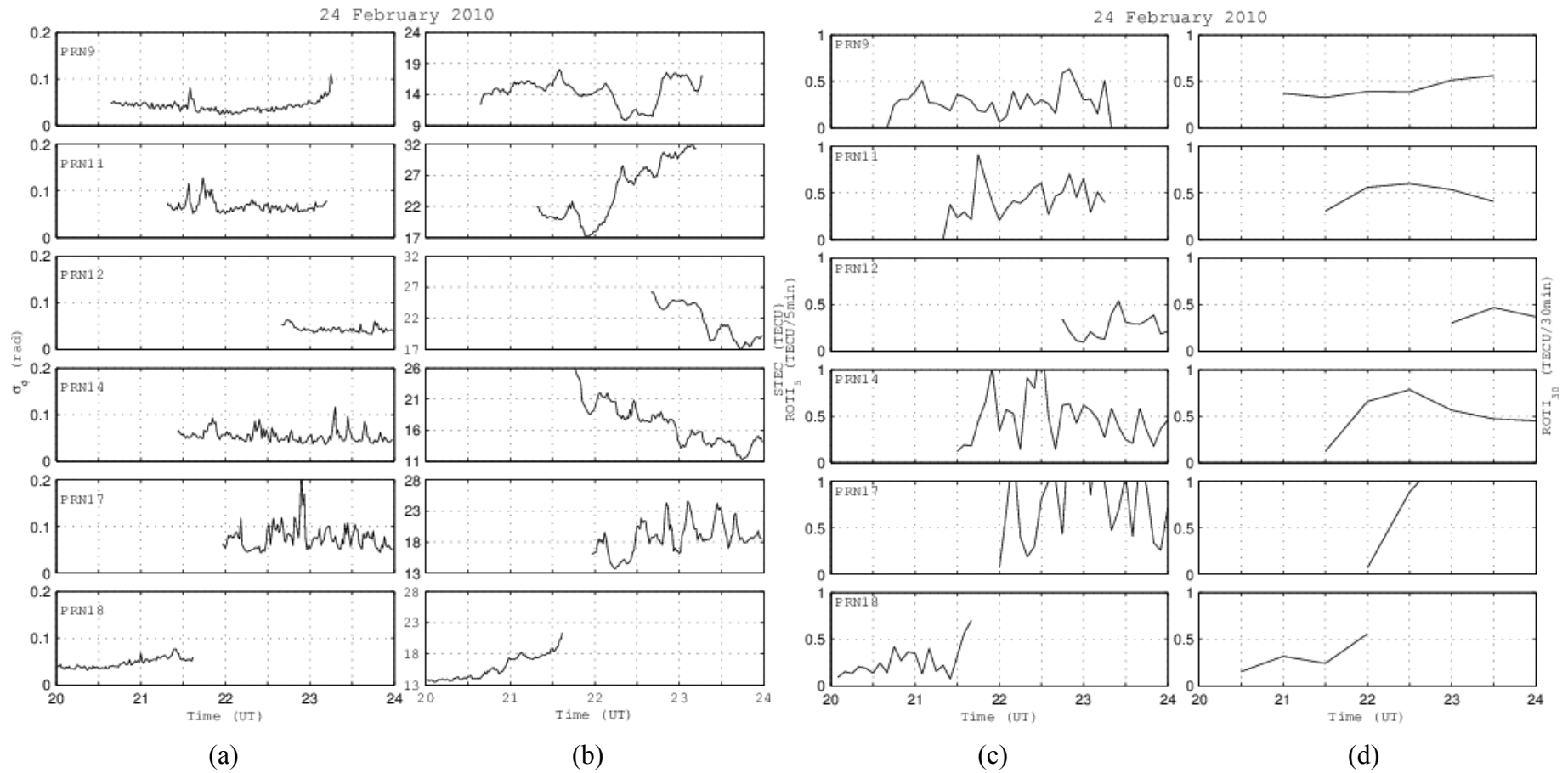


Figure 4.48 (i): (a) σ_ϕ , (b) STEC, (c) $ROTI_5$ and (d) $ROTI_{30}$ observed on each visible satellite on 24 February 2010 from 2000 to 2400 UT

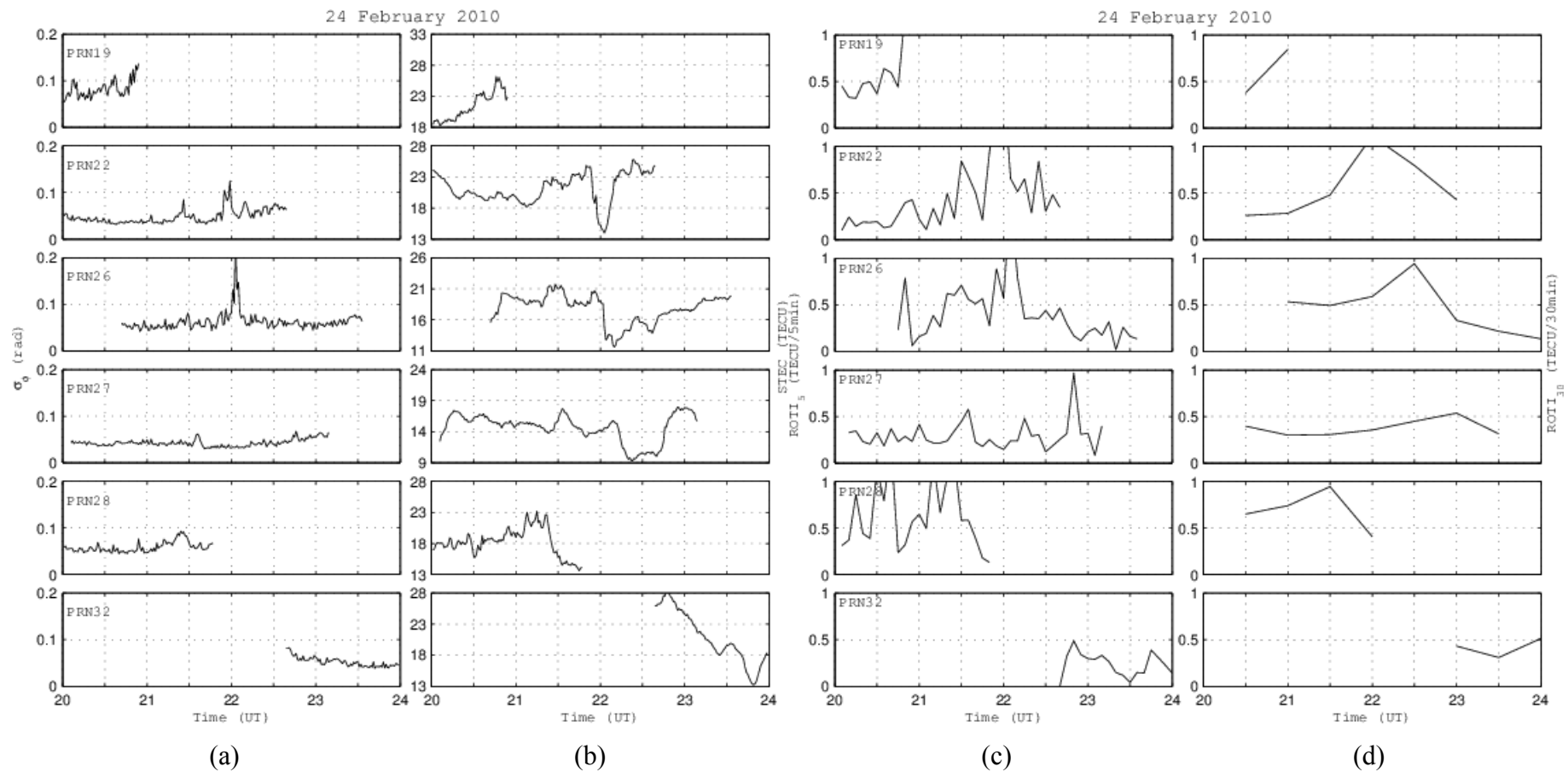


Figure 4.48 (ii): As of (i) but for different satellites

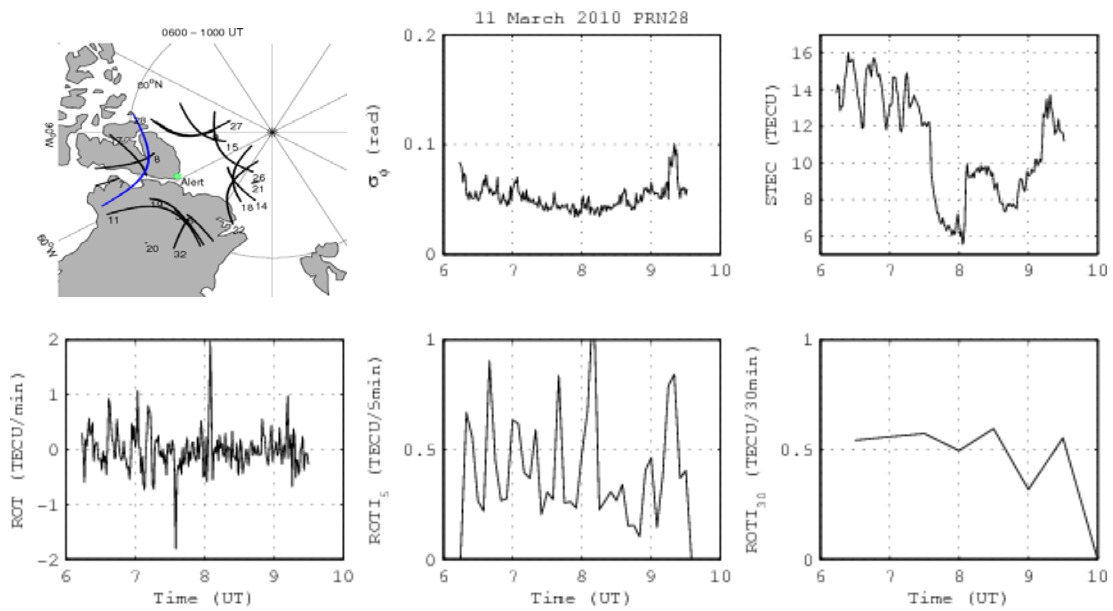


Figure 4.49: σ_{ϕ} , STEC, ROT, and ROTI for 5- and 30-min interval of PRN28 on 11 March 2010 from 0600 to 1000 UT. Paths of all visible satellites at 350 km are also shown

Cases presented in Event Type A2 and A3 indicate that large TEC fluctuations were not necessarily existed together with increases in phase scintillations. Both types of events were observed on many days during the whole 2-year period of observations. The formation of TEC fluctuations are not correlated to the increases of phase scintillations.

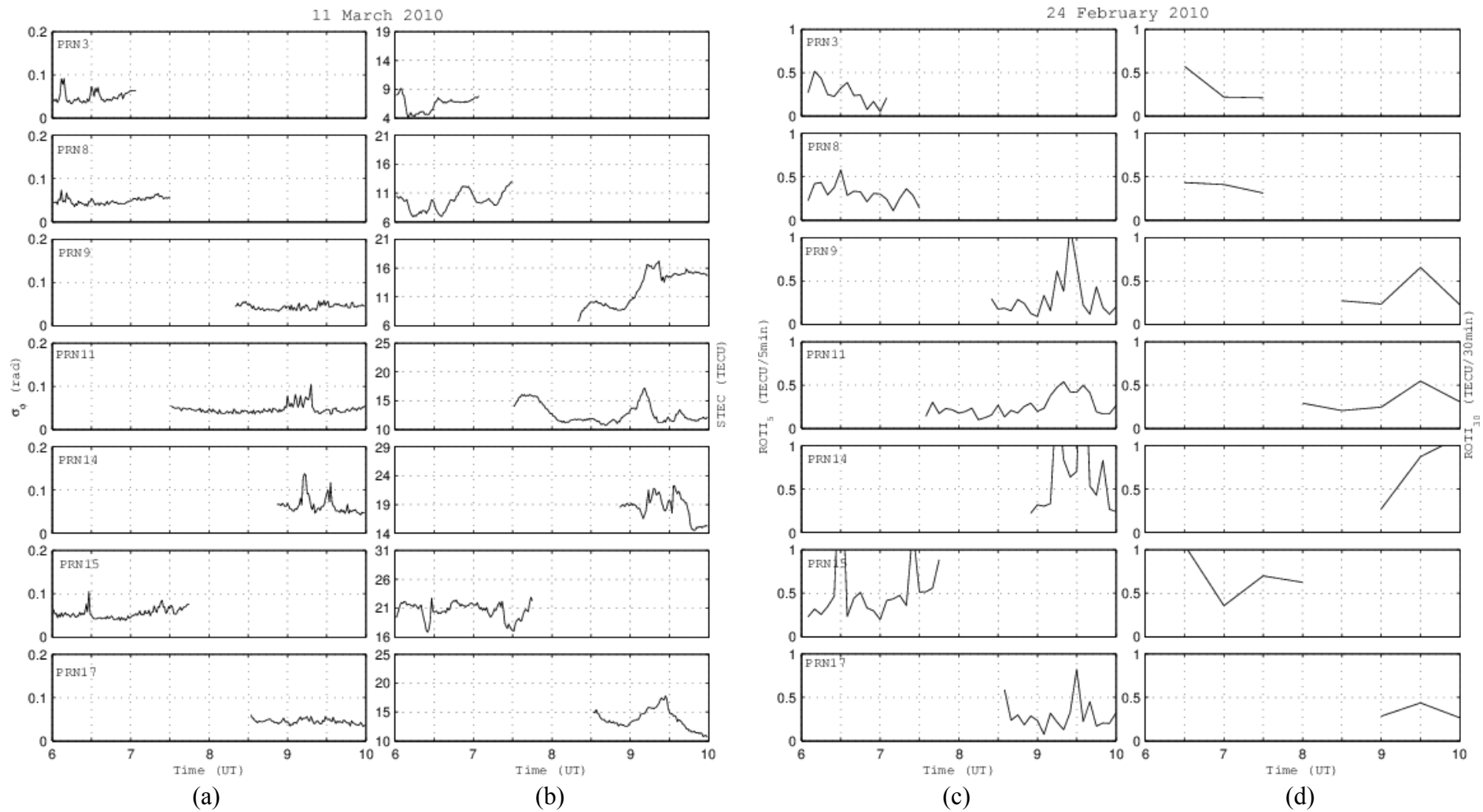
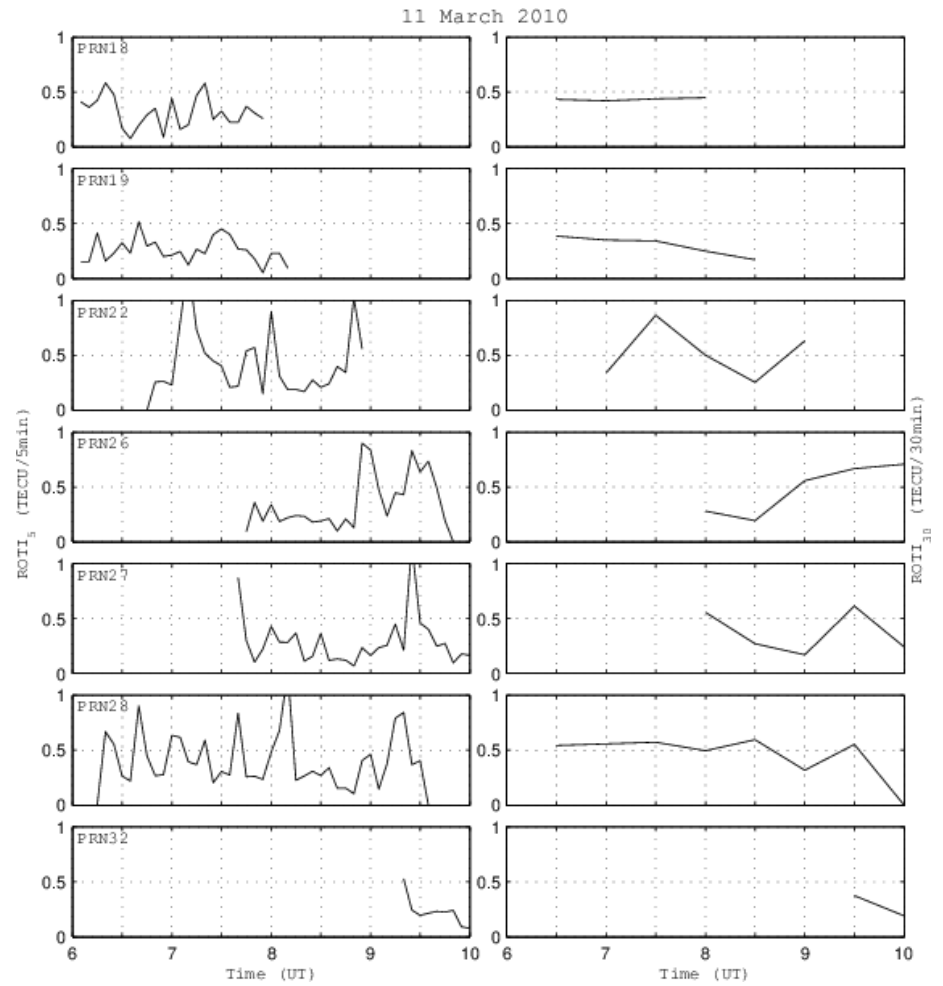
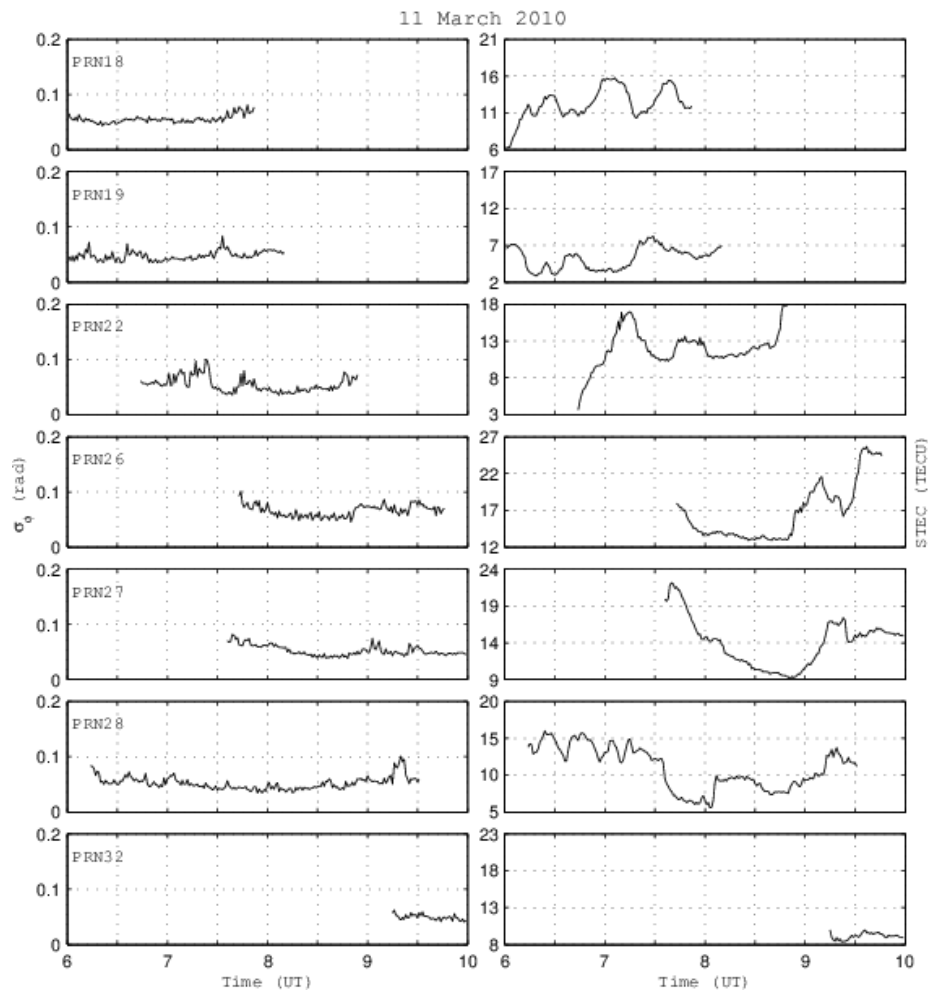


Figure 4.50 (i): (a) σ_ϕ , (b) STEC, (c) $ROTI_5$ and (d) $ROTI_{30}$ observed on each visible satellite on 11 March 2010 from 0600 to 1000 UT



(a)

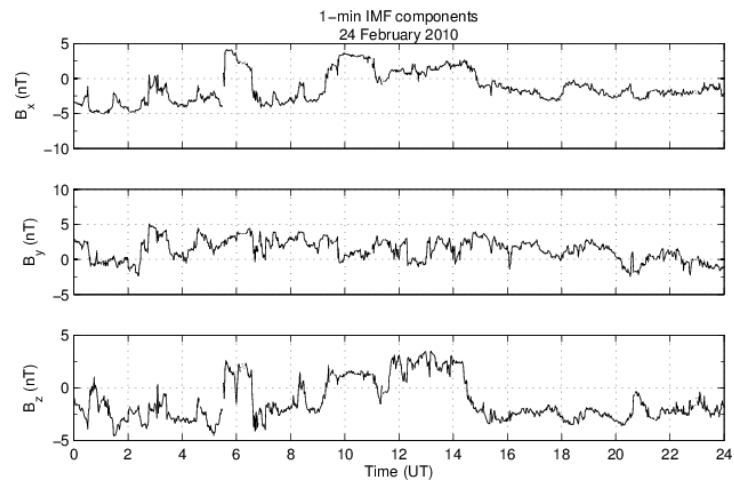
(b)

(c)

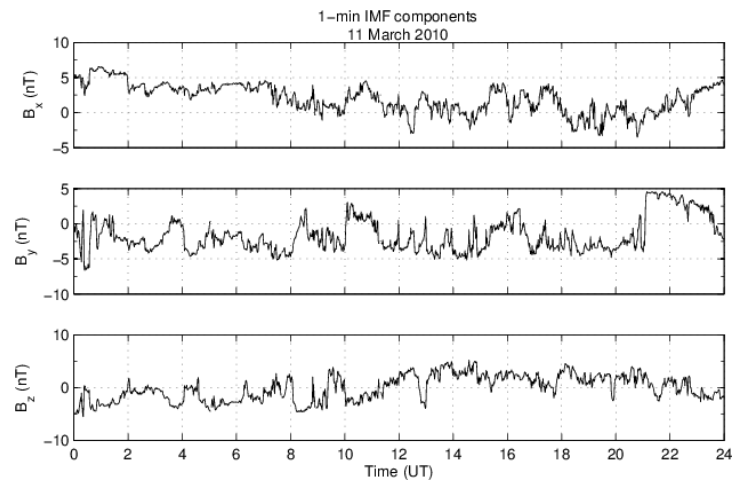
(d)

Figure 4.50 (ii): As of (i) but for different satellites

K_p for both days during the period of observations were low between 0+ and 2+ (24 February 2010), and between 2+ and 3 (11 March 2010). IMF B_z components was predominantly northward up to ~ 3 nT on 24 February 2010 between 2000 to 2359 UT, and was southward mostly ~ -5 nT on 11 March 2010 between 0600 to 1000 UT as illustrated in Figure 4.51.



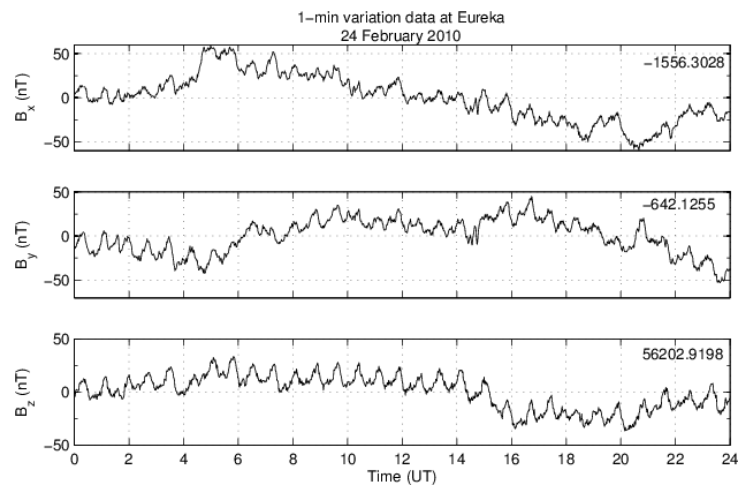
(a)



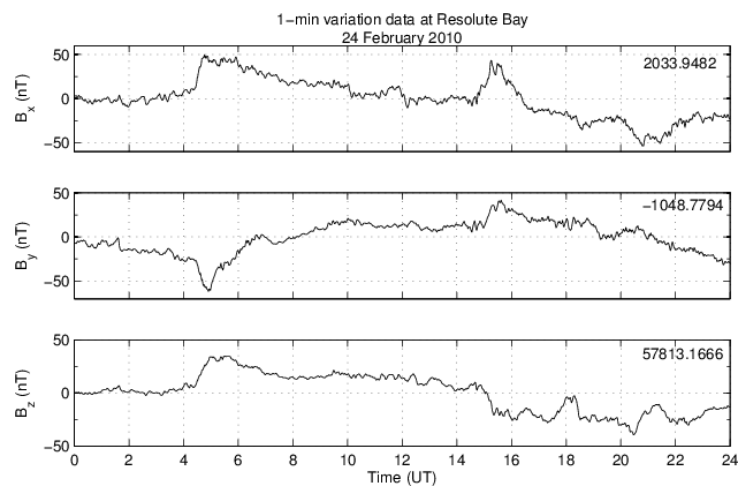
(b)

Figure 4.51: 1-minute IMF components on (a) 24 February 2010 and (b) 11 March 2010

Magnetic fields at both Eureka and Resolute Bay on 24 February 2010 during the period of observations (2000 to 2400 UT) showed variations up to $\sim\pm 50$ nT from their respective means on all components (Figure 4.52). Meanwhile, magnetic fields at both stations on 11 March 2010 reached up to $\sim\pm 50$ nT for all components during the period of observations (0600 to 1000 UT), with an exception on B_z component at Eureka where it demonstrated very little variations from the mean value (Figure 4.53).



(a)



(b)

Figure 4.52: 1-minute variation data at (a) Eureka, and (b) Resolute Bay on 24 February 2010

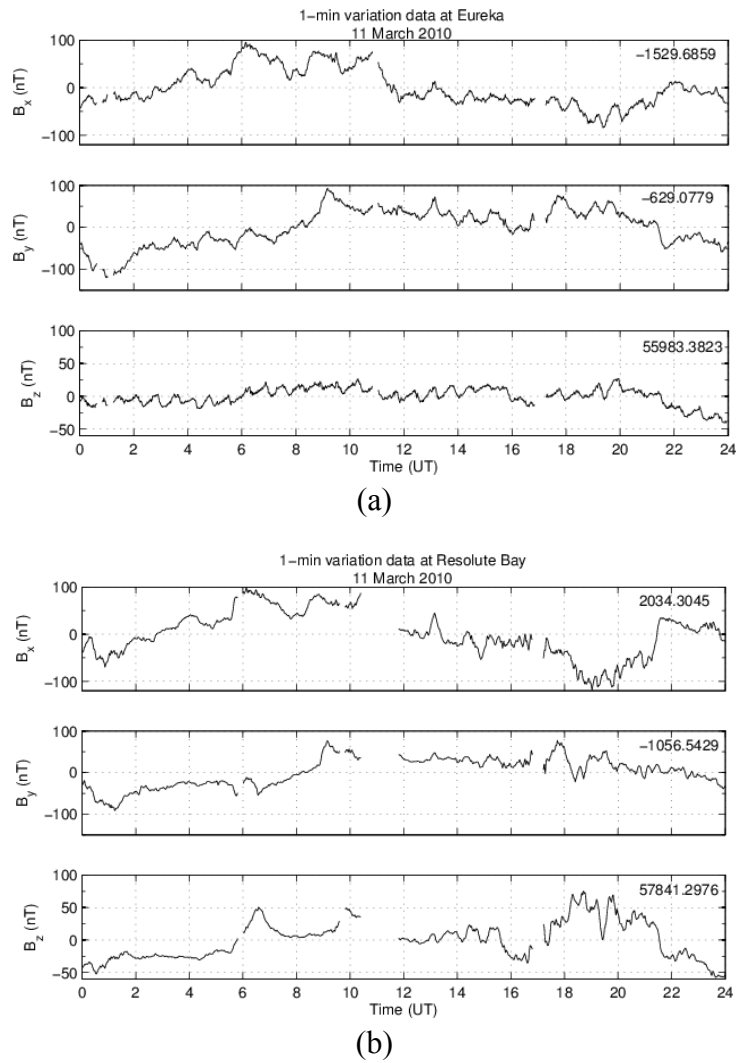


Figure 4.53: 1-minute variation data at (a) Eureka, and (b) Resolute Bay on 11 March 2010

Event Type A4

Figure 4.54 (b) shows STEC variations on all visible satellites between 1600 and 1800 UT on 26 January 2009. TEC increase smoothly with one and two peaks between ~ 4 and ~ 8 TECU were observed on PRN2, 5, 12, 29, 30 and 31. This is in contrast with the examples discussed in Event Type A3, where TEC variations were in a form of fluctuations during most of the observation time. However, TEC

fluctuations were recorded on the rest of the visible satellites (with an exception of PRN32 where data is very short during the period of observations).

The path of all visible satellites above Alert between 1600 and 1800 UT is illustrated in Figure 4.55. The satellites experienced TEC increases and the ones experienced TEC fluctuations were separated into two areas. PRN2, 5, 12 and 30 were all in the nearby area between 1600 and 1700 UT. PRN31, although separated, was still close by. Meanwhile, satellites experienced TEC fluctuations were concentrated at another area (i.e. PRN20 and 23 were nearby, but PRN4 was isolated). Similar trait was also observed during the following hour where satellites experienced TEC increases (i.e. PRN29 and PRN30) were nearby, and PRN2 and PRN31 were individually isolated. At the other side, PRN4, 13 and 23 were quite close to each other.

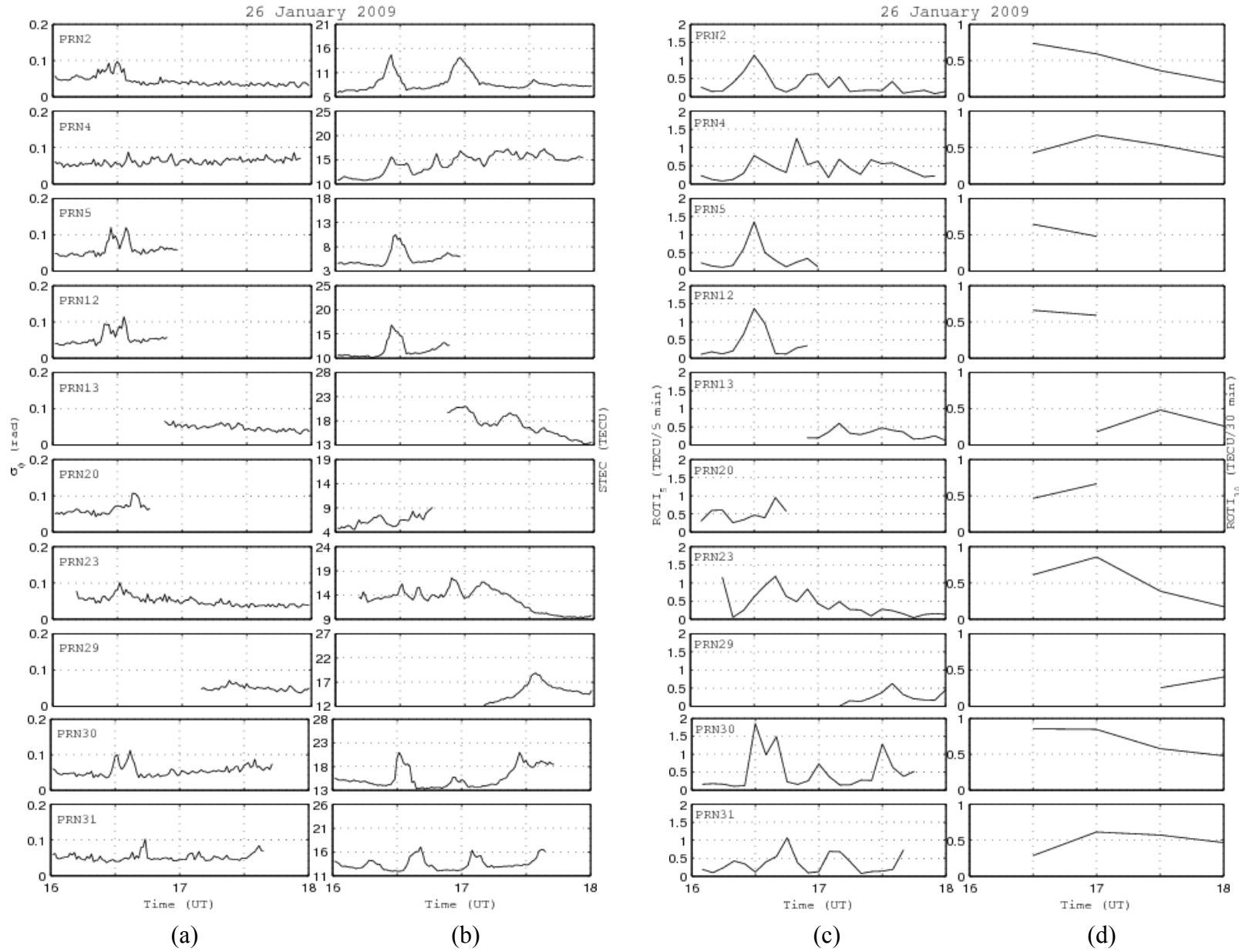


Figure 4.54: (a) σ_ϕ , (b) STEC, (c) $ROTI_5$ and (d) $ROTI_{30}$ observed on each visible satellite on 26 January 2009 from 1600 to 1800 UT

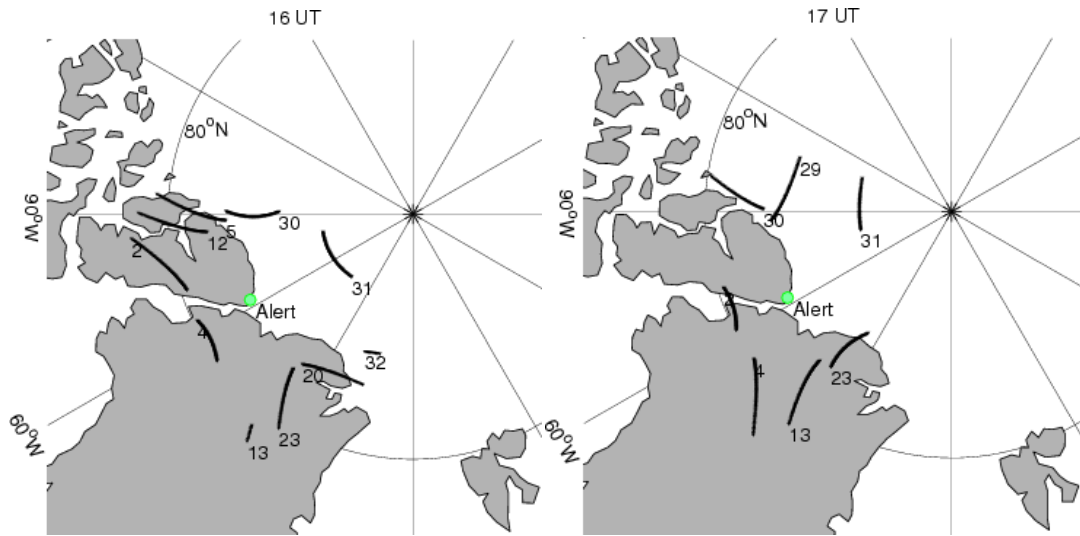


Figure 4.55: Path for all visible satellites for every hour between 1600 and 1800 UT on 26 January 2009

Figure 4.56 illustrates the details of σ_ϕ , slant TEC, and rate of TEC Index (ROTI) for PRN5 from 1600 to 1700 UT. Using 600 m/s as the speed of a patch, the size of the irregularities observed on PRN5 was determined as 540 km. Phase scintillations also increased up to ~ 0.12 rad during the same time as TEC increase. Meanwhile, for PRN12 (Figure 4.57), the size of the irregularities was around 583 km lasting from ~ 1617 until ~ 1633 UT (i.e. for 16 minutes).

Similar to PRN5, phase scintillations on PRN12 was observed around the same time as TEC increase. Following the σ_ϕ threshold which is set at 0.15 rad throughout this section, the phase scintillations observed on PRN5 and PRN12 are categorised as weak scintillations. One small patch of high intensity was clearly observed on both satellites. Based on the size of TEC increase, the irregularities can also be interpreted as one large patch.

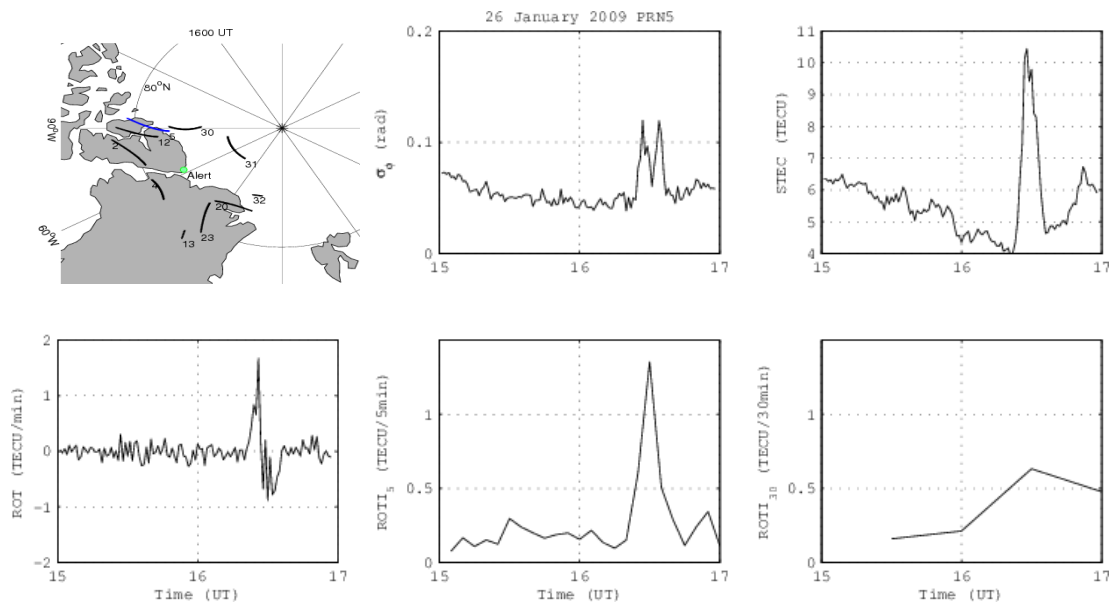


Figure 4.56: σ_ϕ , STEC, ROT, and ROTI for 5- and 30-min interval of PRN5 on 26 January 2009 from 1500 to 1700 UT. Paths of all visible satellites between 1600 and 1700 UT at 350 km are also shown

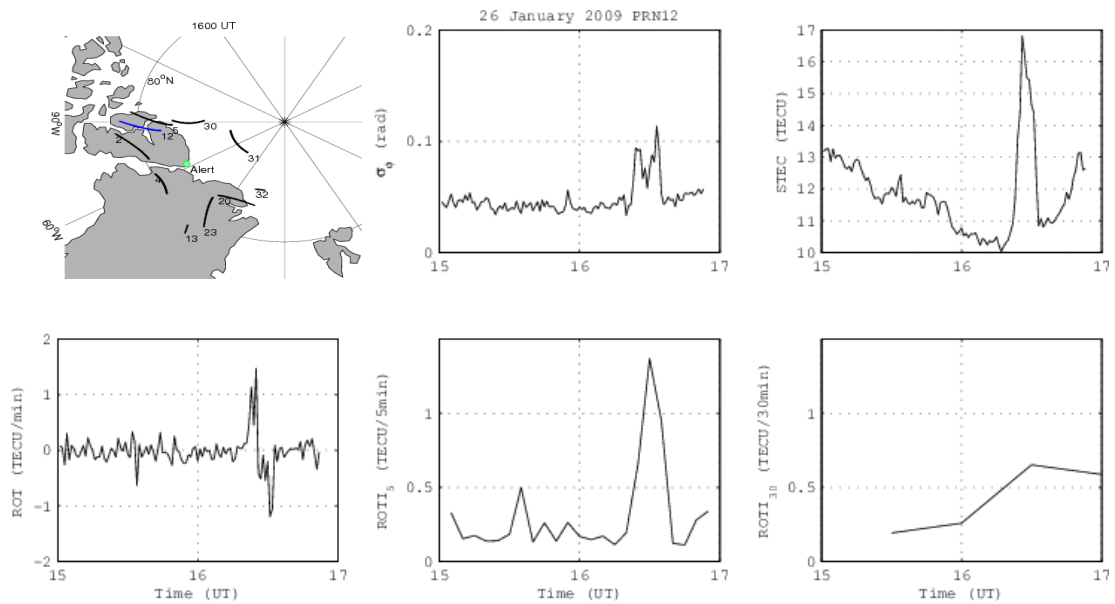


Figure 4.57: σ_ϕ , STEC, ROT, and ROTI for 5- and 30-min interval of PRN12 on 26 January 2009 from 1500 to 1700 UT. Paths of all visible satellites between 1600 and 1700 UT at 350 km are also shown

Looking at the path for these two satellites, other than located nearby at 350 km above Alert, they both also had the same orientation of movement. Therefore, the irregularities observed on both satellites could probably were the same one as both satellites were showing similar behaviour of TEC variations and phase scintillations.

K_p was low between 0+ and 1+ during the period of observations, and IMF B_z component was southward up to ~ 8 nT from ~ 1100 UT until ~ 1700 UT and then changed polarity (Figure 4.58). All magnetic components at Eureka showed little variations from each respective mean. Meanwhile, at Resolute Bay, B_x reached up to 100 nT and -100 nT for B_y during the period of observations where the values peaked at ~ 1700 UT and ~ 1600 UT, respectively. B_z reached its maximum value of 75 nT at ~ 1400 UT and around 50 nT during the period of observations (Figure 4.59).

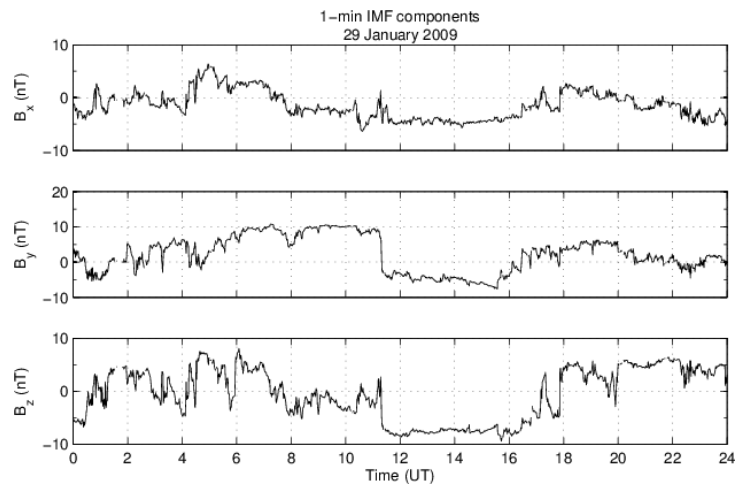
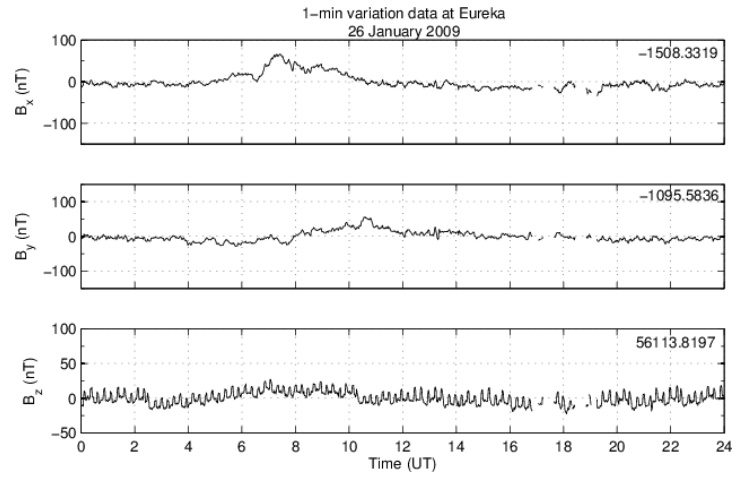
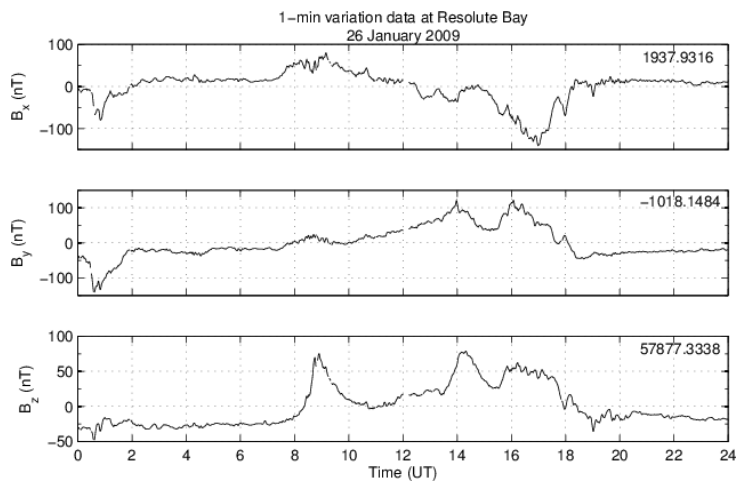


Figure 4.58: 1-minute IMF components on 26 January 2009



(a)



(b)

Figure 4.59 : 1-minute variation data at (a) Eureka, and (b) Resolute Bay on 26 January 2009

Figure 4.60 and Figure 4.61 show details of σ_{ϕ} , slant TEC, ROT, and ROTI for both 5- and 30-minute interval for PRN3 and PRN6, respectively, on 3 December 2008. The map illustrates that PRN3 and PRN6 were close to each other during the period of observations from 1230 to 1330 UT. Although the increase in slant TEC was not as smooth as discussed in previous case, an increase of slant TEC was evident on PRN3 and PRN6. However, these increases were not accompanied by an increase of σ_{ϕ} .

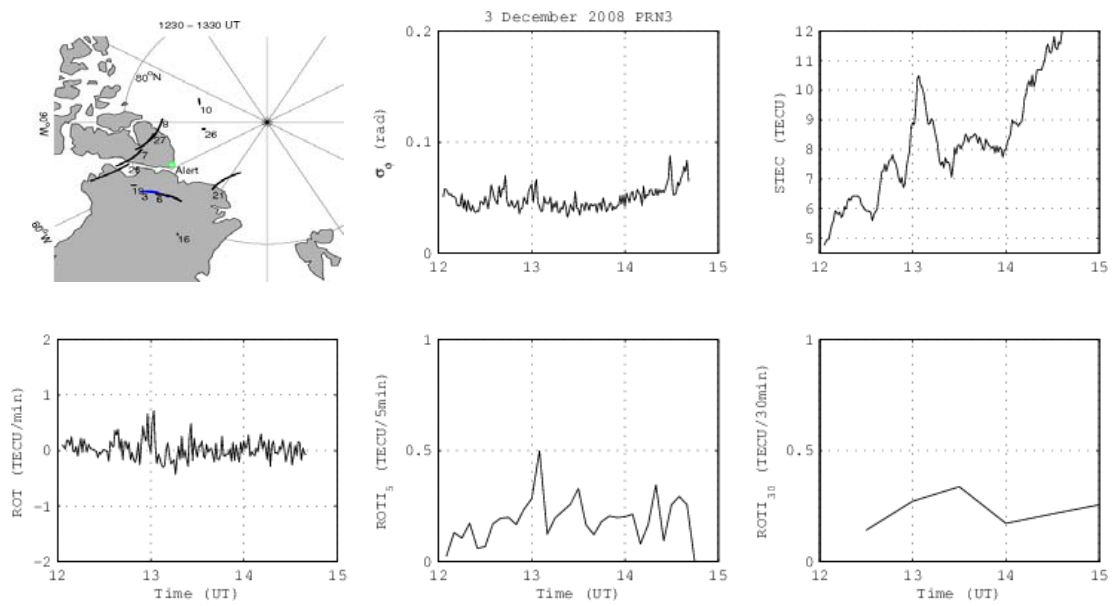


Figure 4.60: σ_ϕ , STEC, ROT, and ROTI for 5- and 30-min interval of PRN3 on 3 December 2008 from 1200 to 1500 UT. Paths of all visible satellites between 1230 and 1330 UT at 350 km are also shown

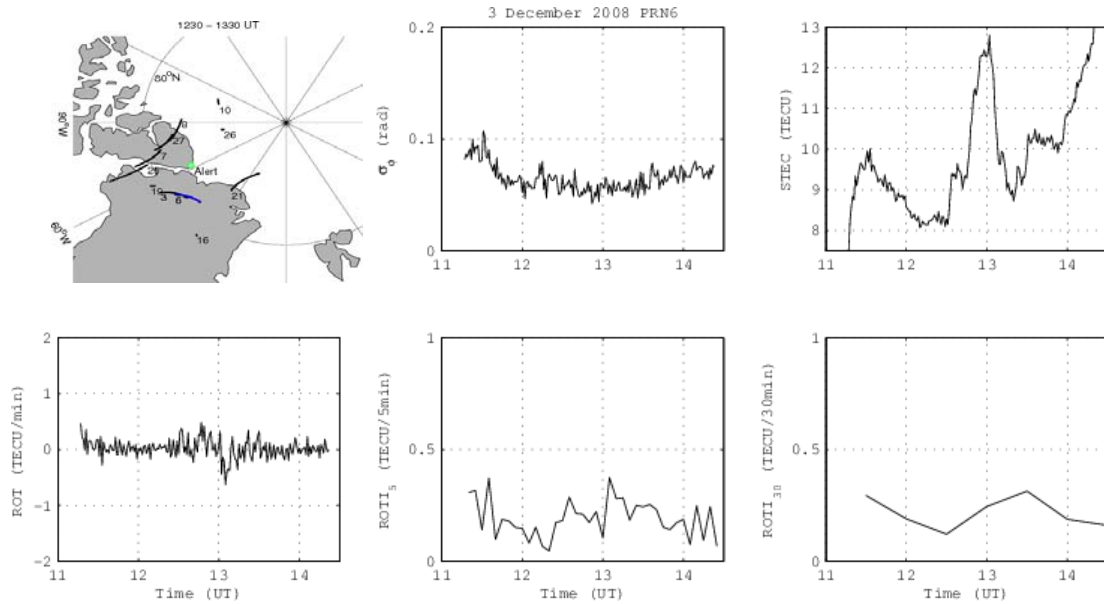


Figure 4.61: σ_ϕ , STEC, ROT, and ROTI for 5- and 30-min interval of PRN6 on 3 December 2008 from 1100 to 1430 UT. Paths of all visible satellites between 1230 and 1330 UT at 350 km are also shown

There were ~ 3 TECU increase from 1243 to 1309 UT on PRN6, and also similar increase few minutes later from 1254 to 1318 UT on PRN3. The size of the irregularity observed on PRN3 was ~ 936 km and registered as weak patches. Meanwhile, the irregularity on PRN6 is ~ 864 km in size and also considered as weak patches. No other satellites during this period observed similar increase in TEC (Figure 4.62 (b)), except the expected small TEC fluctuation, and also TEC increase on PRN7. However, this increase occurred when the increases on PRN3 and PRN6 almost ceased, and also at different location. Therefore, this event will not be discussed here.

Figure 4.63 shows TEC variations of PRN3 and PRN6 (both in red) together with the comparison with the previous (blue) and following (black) days. The time of previous and following days were corrected so that the satellites were at the same position. No TEC increase was detected on these two days as opposed to the observed day. K_p was low on 3 December between 1- and 3. Meanwhile, IMF B_z component was dominantly northward (up to ~ 8 nT) until ~ 1200 UT, and then switch polarity and remains southward (up to ~ -7 nT) until ~ 1600 UT (Figure 4.64).

Variations of up to -50 nT and 50 nT were observed on B_x and B_y components, respectively at both Eureka and Resolute Bay (Figure 4.65). However, these did not occur during the period of observations but rather after that. B_z component on both stations experienced only little variations from the mean.

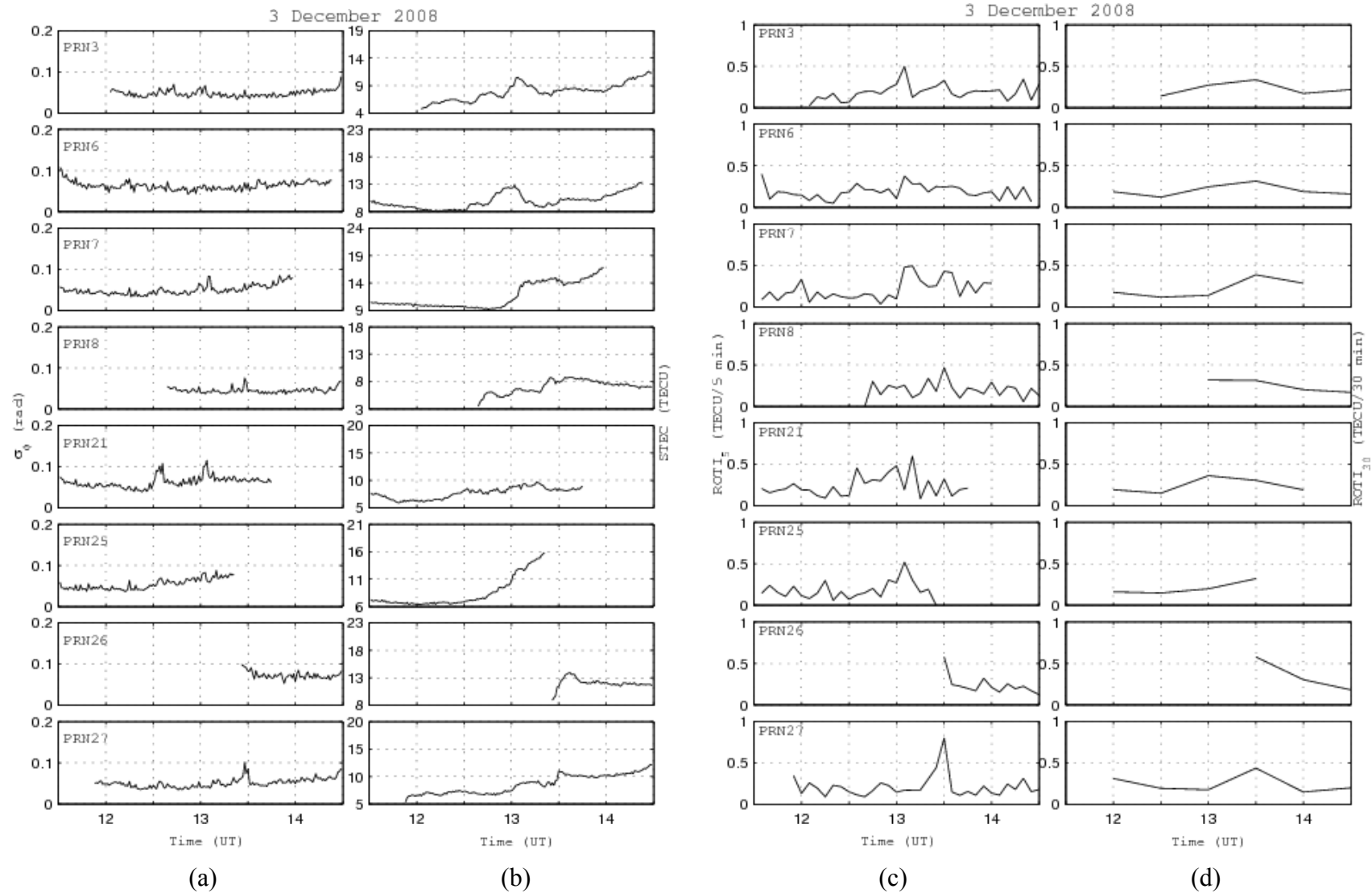


Figure 4.62: (a) σ_ϕ , (b) STEC, (c) ROTI₅ and (d) ROTI₃₀ observed on each visible satellite on 3 December 2008 from 1130 to 1430 UT

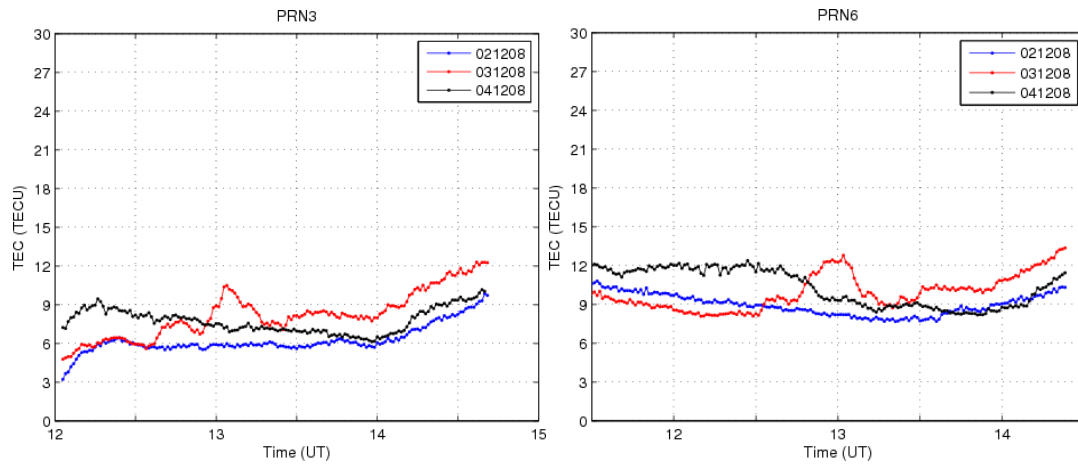


Figure 4.63: Comparison of TEC variations for PRN3 (left) and PRN6 (right) on 3 December 2008 (red curve) with previous and following days

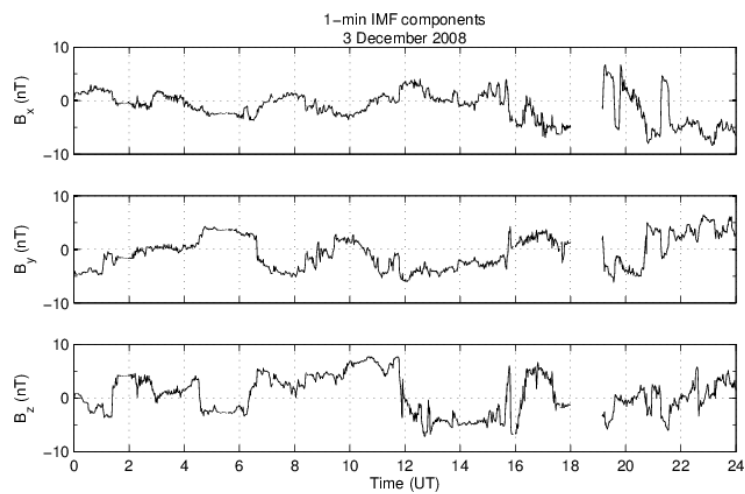


Figure 4.64: 1-minute IMF components on 3 December 2008

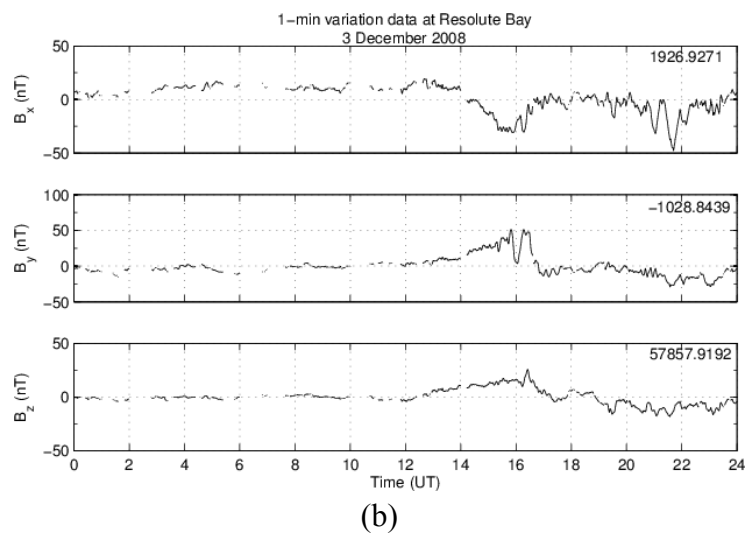
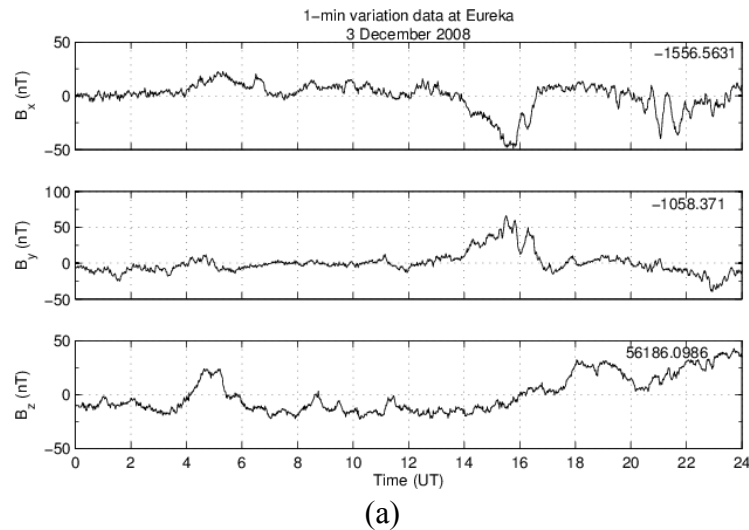


Figure 4.65: 1-minute variation data at (a) Eureka, and (b) Resolute Bay on 3 December 2008

Event Type A5

Figure 4.66 shows the σ_{ϕ} , slant TEC, and ROTI for both 5- and 30- minute interval observed on each visible satellite on 24 May 2008 from 1100 to 1400 UT. Paths for these satellites are illustrated in Figure 4.67. Increased phase scintillations were observed on several satellites during this period. These increases occurred at the edges of TEC increase, either at the leading or trailing edge.

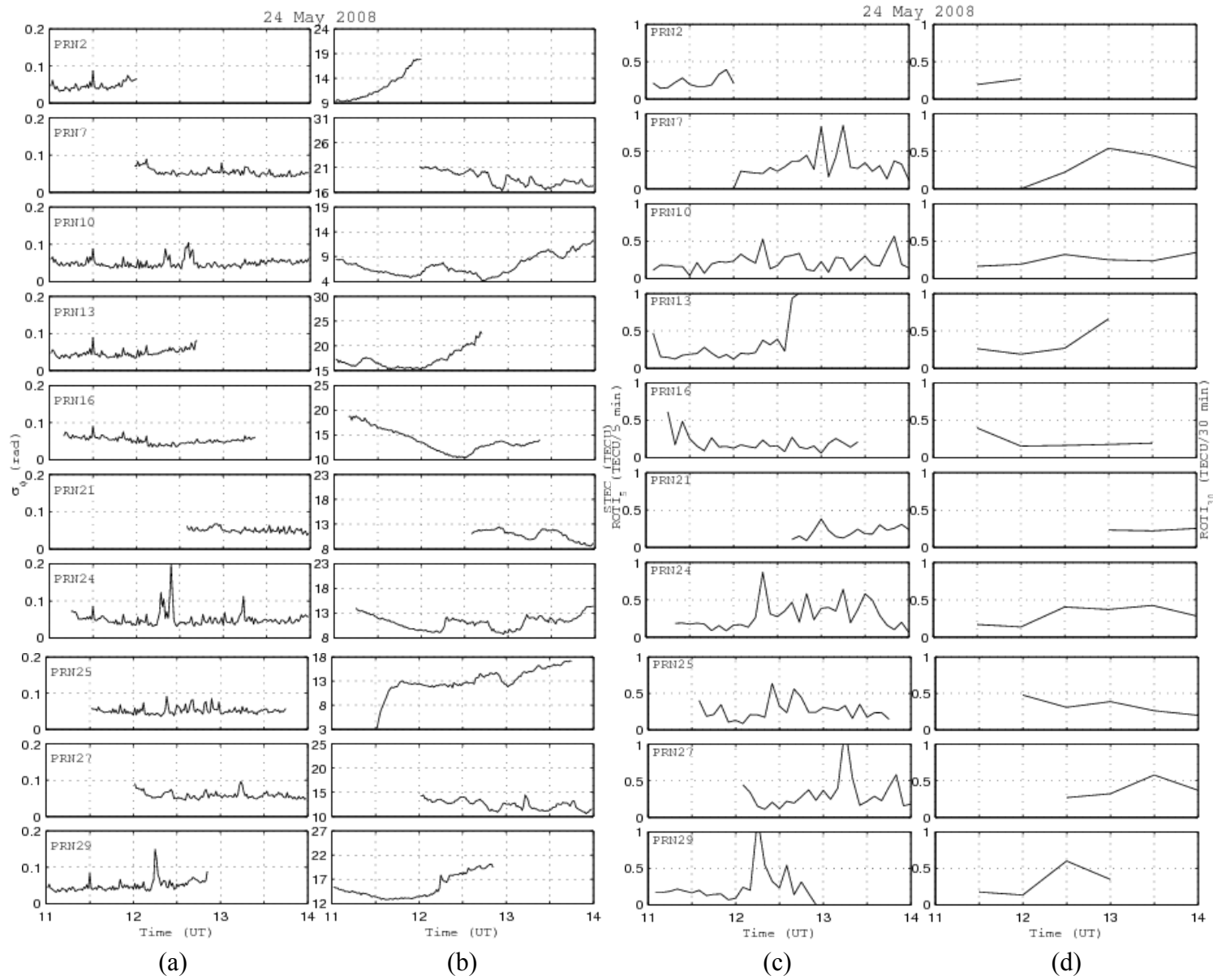


Figure 4.66: (a) σ_ϕ , (b) STEC, (c) ROTI₅ and (d) ROTI₃₀ observed on each visible satellite on 24 May 2008 from 1100 to 1400 UT

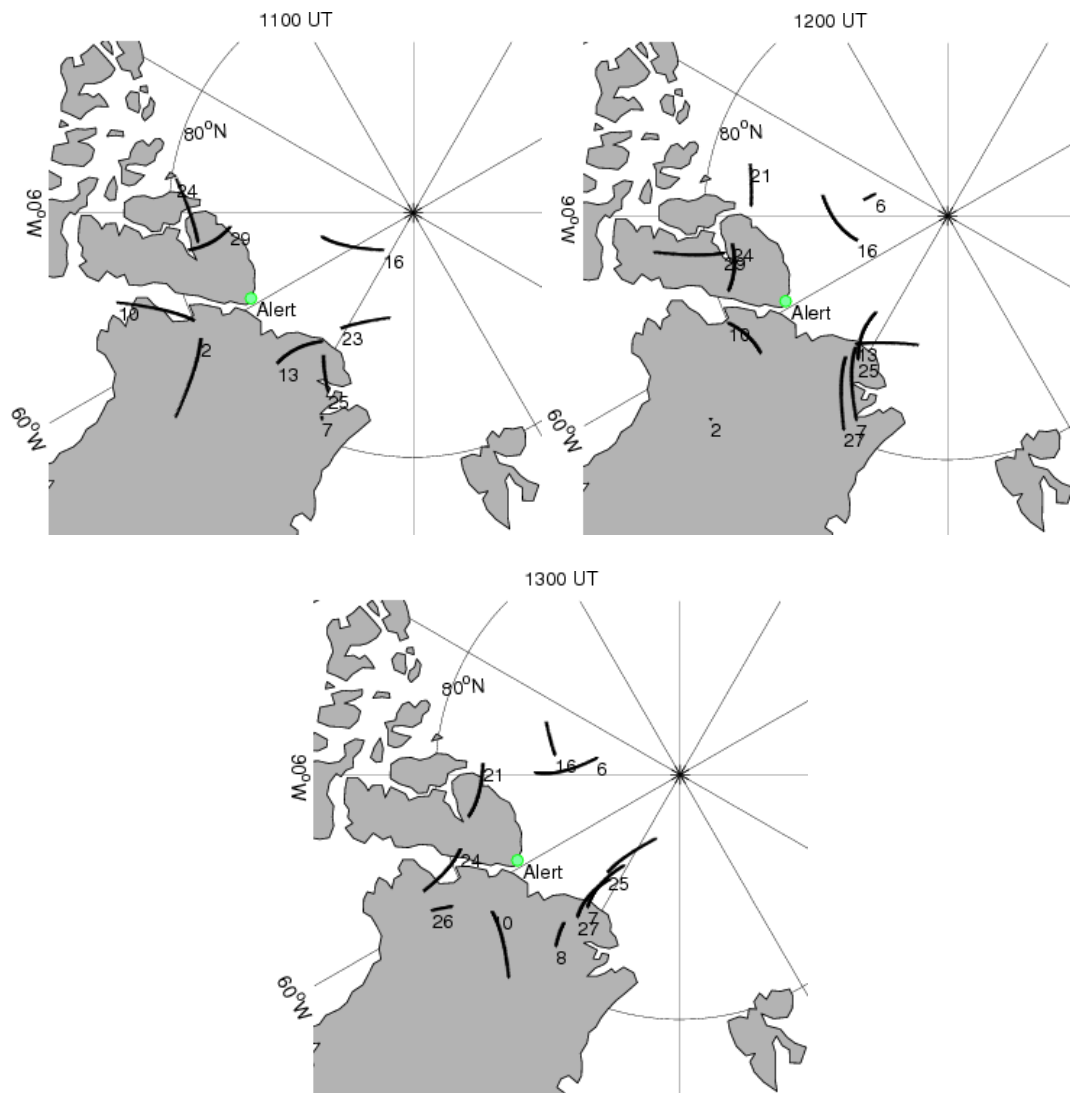


Figure 4.67: Path for all visible satellites for every hour between 1100 and 1400 UT on 24 May 2008

The increases of σ_ϕ were different from the examples discussed in Event Type A3 where increases of σ_ϕ were observed at any time during the whole duration as the increases in slant TEC. In addition, these increases occurred around the same time and also at nearby locations. Fluctuations of σ_ϕ were observed on PRN24 (Figure 4.68) and PRN29 (Figure 4.69) between 1200 to 1230 UT, where σ_ϕ was slightly higher than the former. The TEC on PRN24 not only showed increases but also

fluctuations in between. These bring to the existence of small patches of moderate to high intensity and also large patches of low intensity. Fewer patches were registered on PRN29 where less TEC variations were observed.

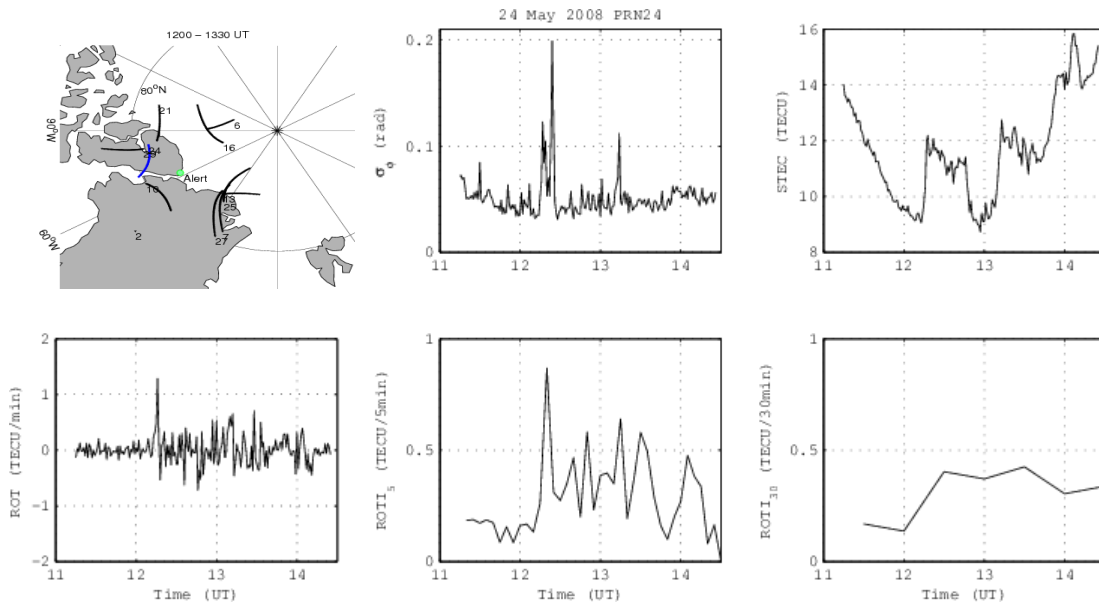


Figure 4.68: σ_ϕ , STEC, ROT, and ROTI for 5- and 30-min interval of PRN24 on 24 May 2008 from 1100 to 1430 UT. Paths of all visible satellites between 1200 and 1330 UT at 350 km are also shown

The paths of both satellites were close to each other at this time (see Figure 4.70). However, another nearby satellite, PRN21 did not exhibit any significant fluctuations, although it should be noted that the observations for PRN21 started after the fluctuations seen by PRN24 and PRN29 had ceased. PRN10 (see Figure 4.71) had relatively smaller scintillations around 1230 UT although the path was somewhat separated from the others. However, the path of PRN10 at this time nearly coincided with the path of PRN24 where smaller scintillations were observed between 1300 and 1330 UT.

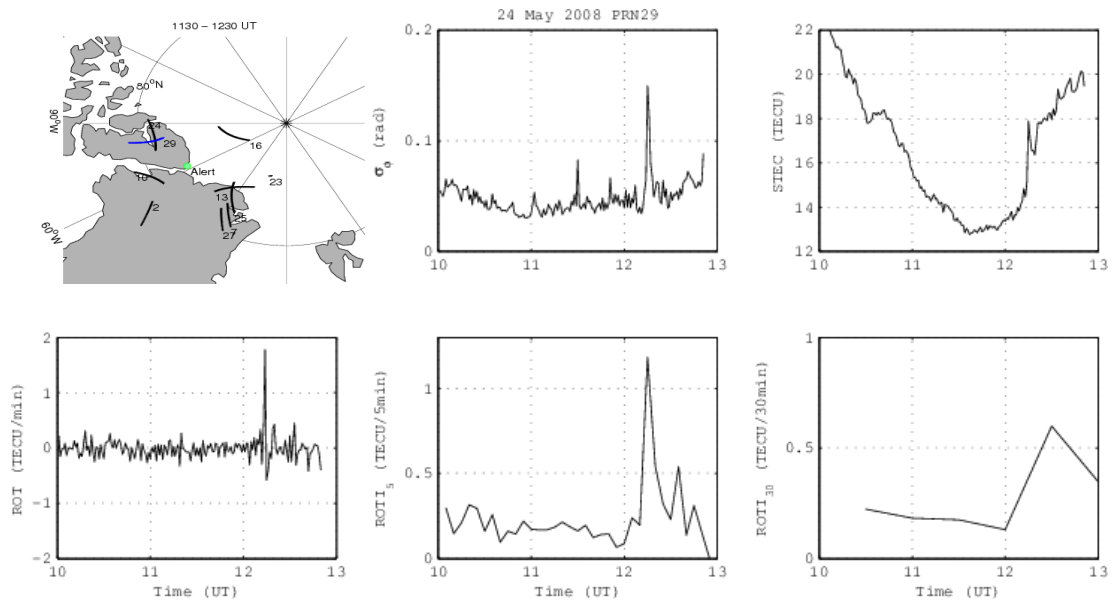


Figure 4.69: σ_ϕ , STEC, ROT, and ROTI for 5- and 30-min interval of PRN29 on 24 May 2008 from 1000 to 1300 UT. Paths of all visible satellites between 1130 and 1230 UT at 350 km are also shown

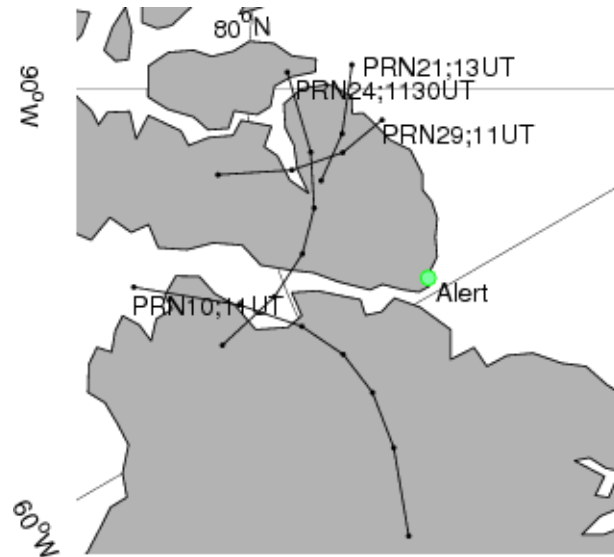


Figure 4.70: Paths of selected visible satellites (i.e. PRN10, PRN21, PRN24 and PRN29) observed at Alert between 1100 and 1400 UT on 24 May 2008, at the ionospheric pierce point of 350 km. The movement of the satellite is indicated by the satellite's PRN number, where the starting time of the track is also denoted. The dots represent the 30-minute interval of the satellite movement

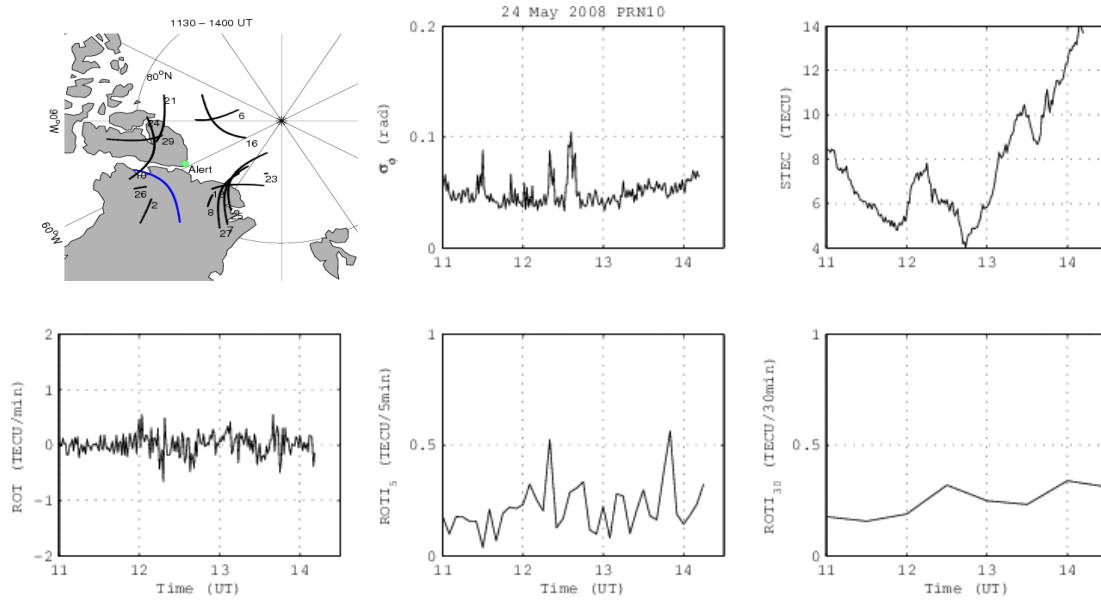


Figure 4.71: σ_ϕ , STEC, ROT, and ROTI for 5- and 30-min interval of PRN10 on 24 May 2008 from 1100 to 1430 UT. Paths of all visible satellites between 1130 and 1400 UT at 350 km are also shown

The slant TEC showed marked increase on all four satellites. This is consistent with the presence of polar patches. The relatively higher phase scintillations on PRN24 and PRN29 corresponded to the leading edge (in time) of the slant TEC increase, while the smaller phase scintillations on PRN10 corresponded to the trailing edge (in time) of the slant TEC. An increase of slant TEC was also observed on PRN21 (see Figure 4.66 (b)), where phase scintillations did not occur. This is an example of the existence of large-scale irregularities but not the relatively smaller-scale irregularities.

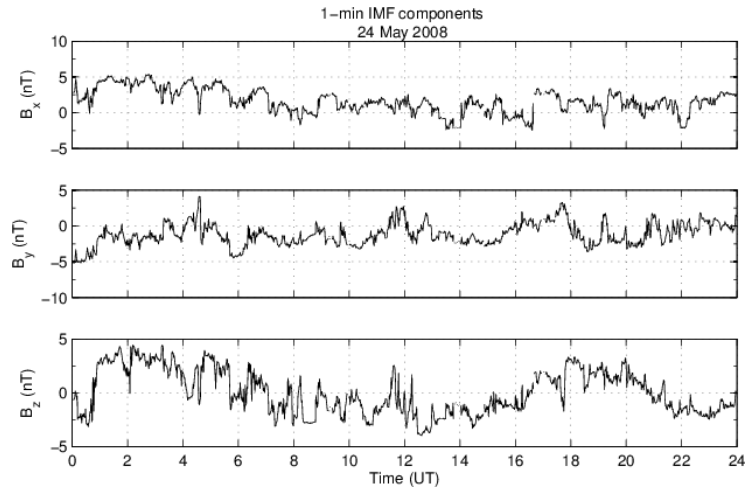
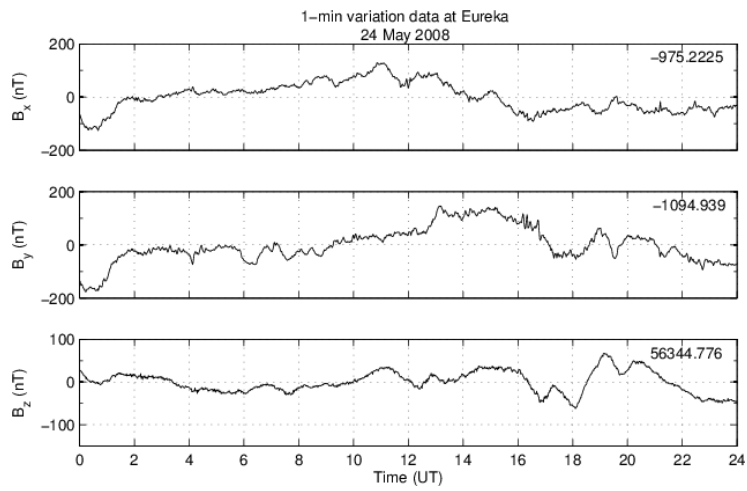
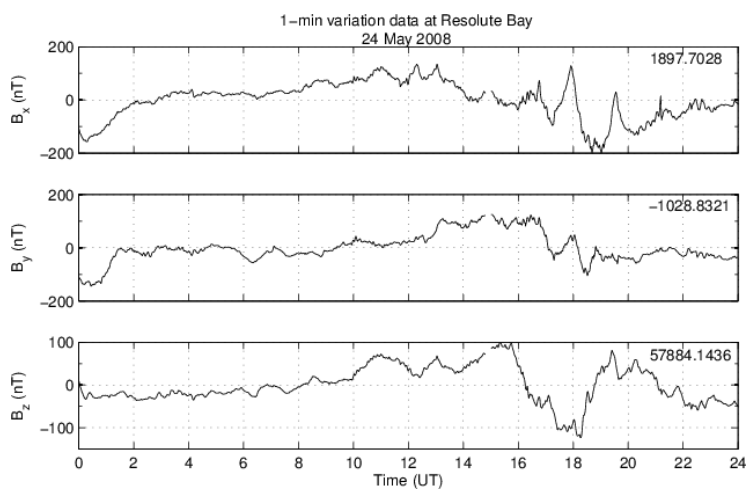


Figure 4.72: 1-minute IMF components on 24 May 2008



(a)



(b)

Figure 4.73: 1-minute variation data at (a) Eureka, and (b) Resolute Bay on 24 May 2008

K_p was low (i.e. 2+) during the period of observation, and IMF B_z component was ~ -3 nT at 1100 UT, then changes to ~ -2 nT around 1200 UT before becoming southward (up to ~ -3.5 nT) until ~ 1600 UT (Figure 4.72). B_x at both Eureka and Resolute Bay was ~ 100 nT during the period of observation (i.e. 1100-1300 UT). B_y also around the same value but slightly offset in time. B_z component reached ~ 75 nT at Resolute Bay but was slightly lower at Eureka. The magnetic components at these stations are shown in Figure 4.73.

Event Type A6

Event Type A6 represents cases of smooth TEC variations, which are at a longer time than what is normally considered as patches. A longer TEC increase can be seen in Figure 4.74 (b) where ~ 6 TECU increase occurred for about ~ 90 minutes from ~ 1710 to 1840 UT on PRN17 on 18 November 2009. No other significant TEC changes were observed on other satellites during this time. TEC rate was low that corresponded to smooth TEC variations, and both ROTI indicate weak irregularities (Figure 4.75).

This smooth TEC increase is registered as a weak and large irregularity of 3240 km in size, which is a lot larger than the normally acceptable patches size. PRN17 also did not show any apparent changes of TEC on the previous (17 November) and the following day (19 November) as illustrated in Figure 4.76. In addition, no significant phase scintillations were observed.

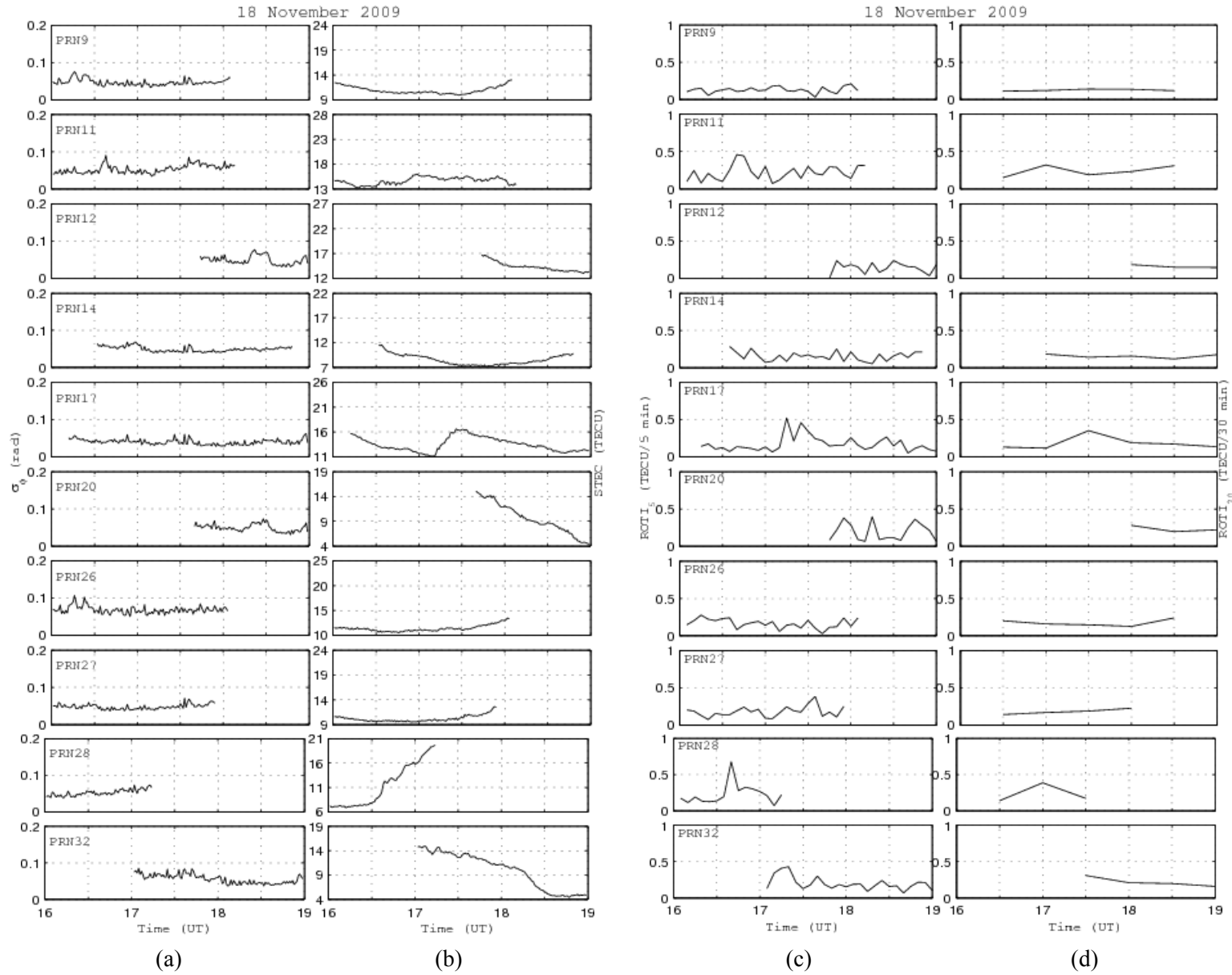


Figure 4.74: (a) σ_ϕ , (b) STEC, (c) ROTI₅ and (d) ROTI₃₀ observed on each visible satellite on 18 November 2009 from 1600 to 1900 UT

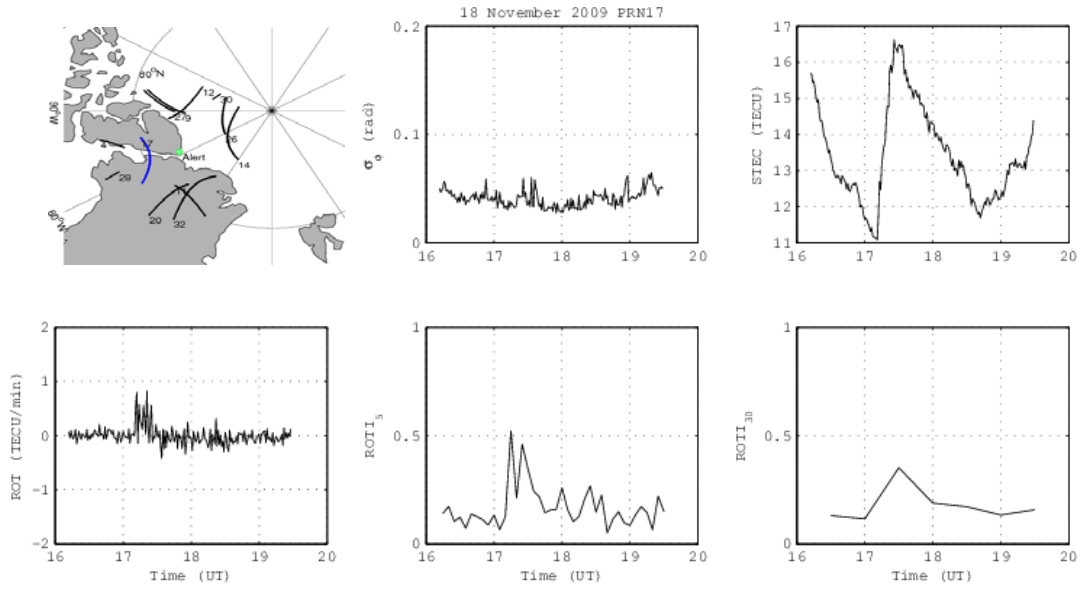


Figure 4.75: STEC, σ_ϕ , ROT, and ROTI of PRN17 on 18 November 2009. Paths of all visible satellites from 1700 to 1900 UT at 350 km are also shown

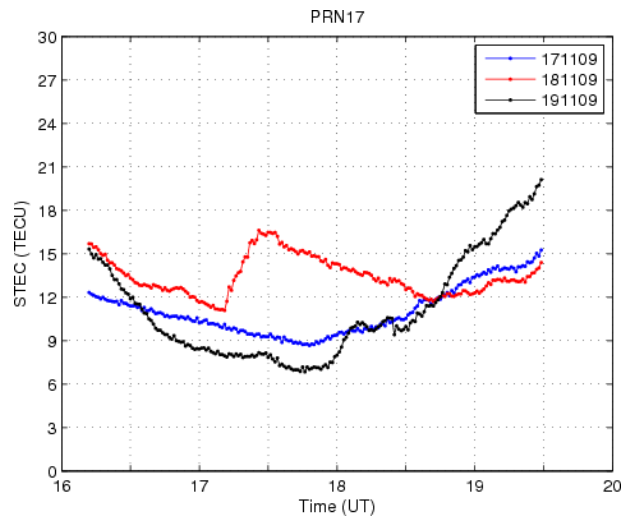


Figure 4.76: Comparison of TEC variations for PRN17 on 18 November 2009 (red curve) with previous and following days

K_p index was low between 0 and 1, and IMF B_z component was northward, up to ~ 2 nT from 1600 to 2000 UT (Figure 4.77). All magnetic components at both stations demonstrated little variations from each respective mean as shown in Figure 4.78).

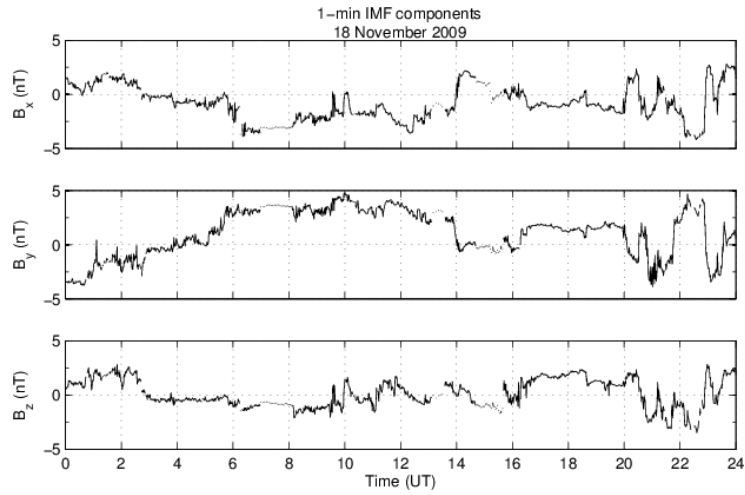


Figure 4.77: 1-minute IMF components on 18 November 2009

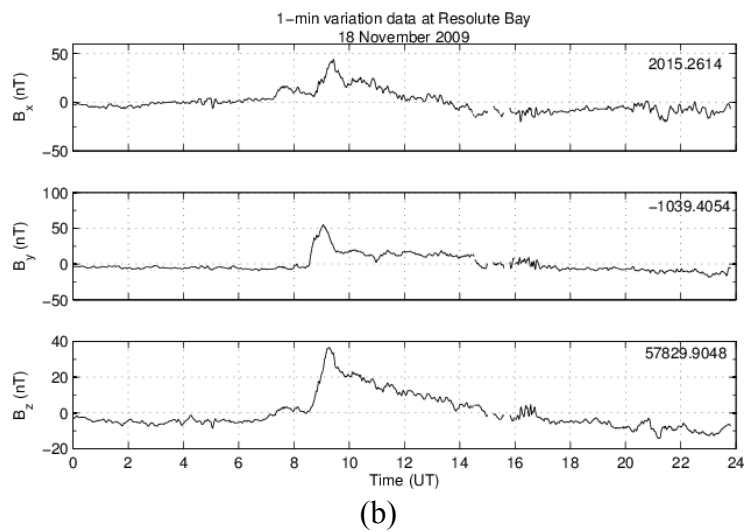
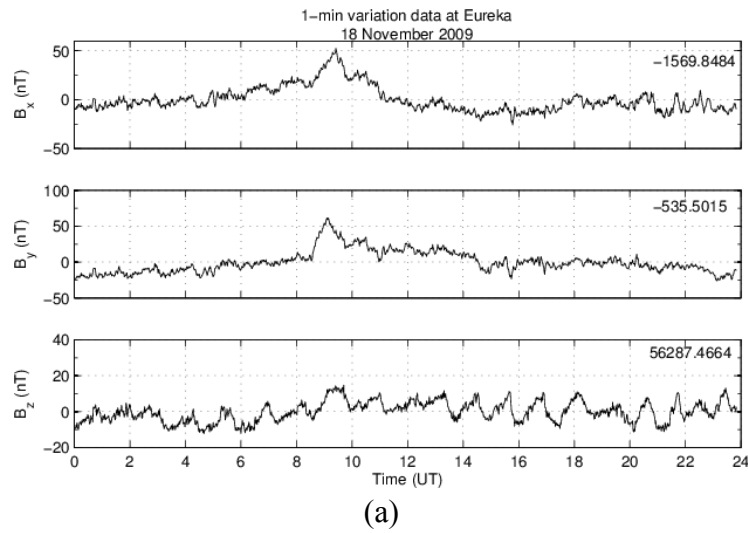


Figure 4.78: 1-minute variation data at (a) Eureka, and (b) Resolute Bay on 18 November 2009

Figure 4.79 shows an example of depletion of TEC. This type of irregularity is quite rare compared to positive enhancement of TEC. TEC observed on PRN19 on 2 October 2009 was decreasing from 1800 UT and then increased to background value starting from 1820 UT. TEC reached the background value at around 1900 UT. A decrease of ~ 4 TECU was observed for a total of almost an hour, giving the average size of the irregularity of 2160 km. Both ROTI values were low, suggesting this large irregularity is not a typical patch which has been normally looked at the changes of TEC variation per minute. No other significant TEC changes were observed on other satellites during this period (Figure 4.80 (b)).

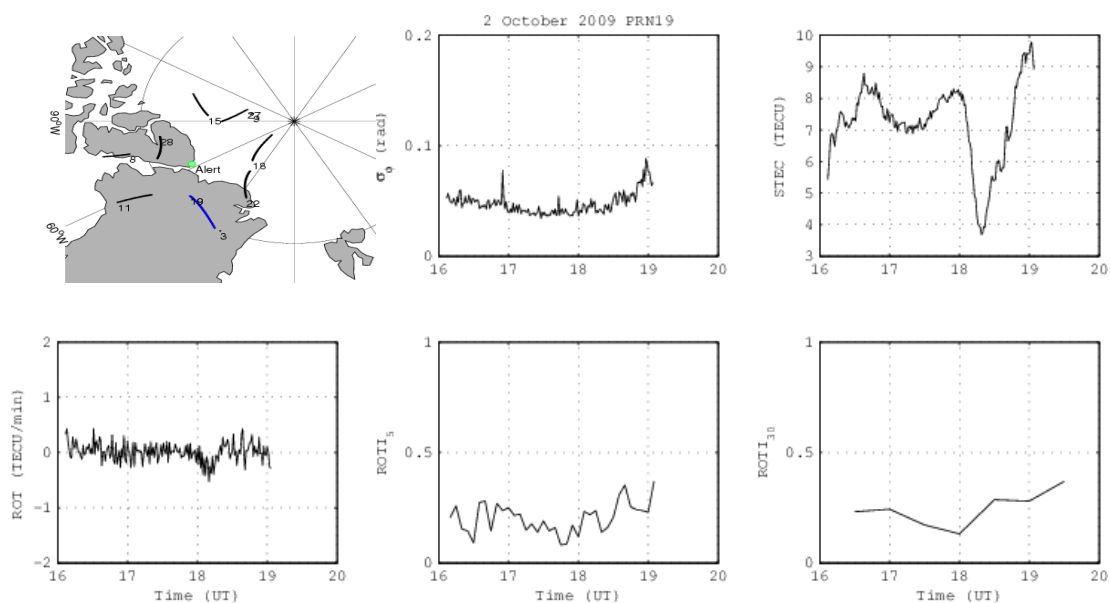


Figure 4.79: σ_ϕ , STEC, ROT, and ROTI of PRN19 on 2 October 2009. Paths of all visible satellites from 1800 to 1900 UT at 350 km are also shown

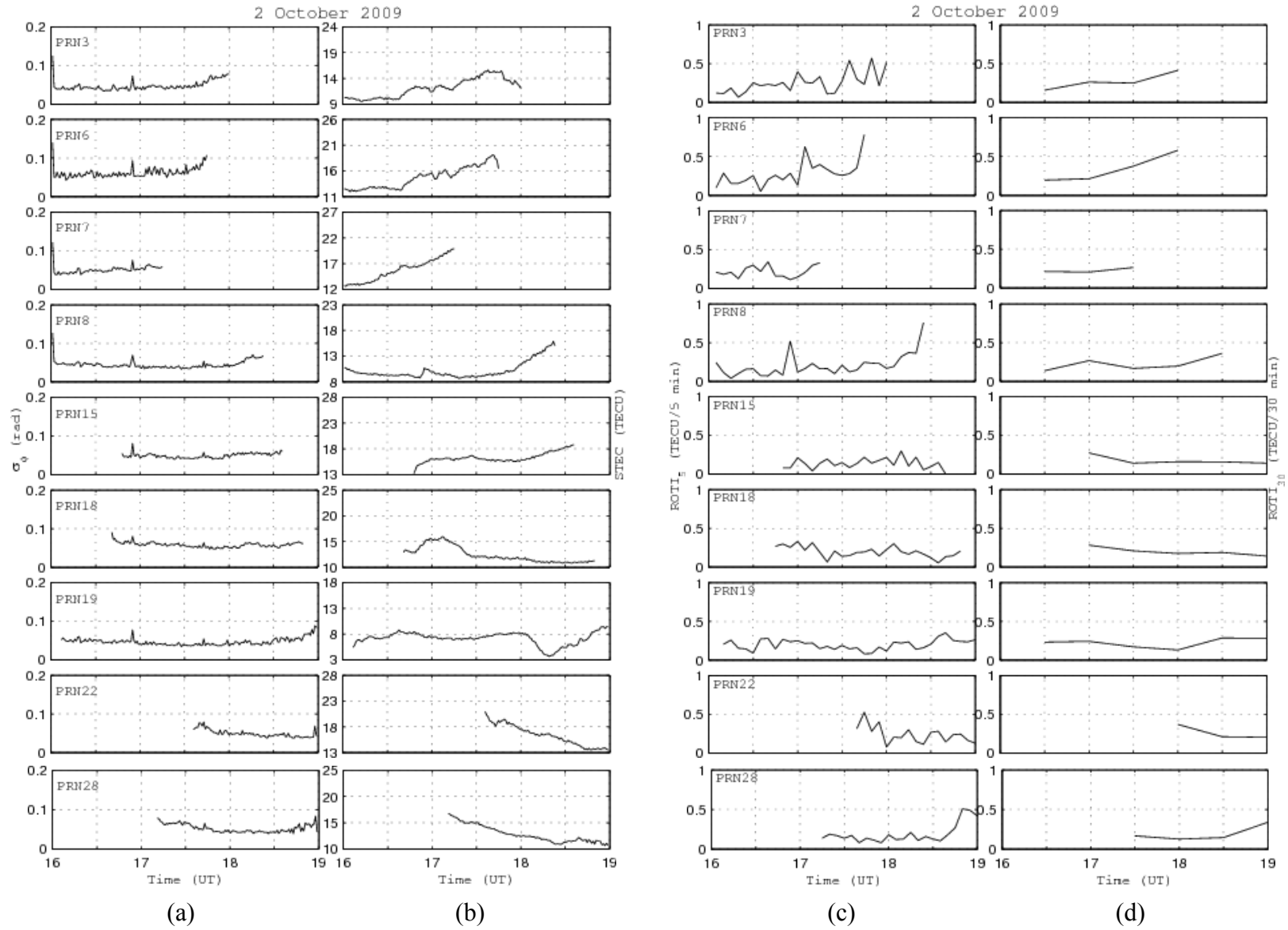


Figure 4.80: (a) σ_ϕ , (b) STEC, (c) ROTI₅ and (d) ROTI₃₀ observed on each visible satellite on 2 October 2009 from 1600 to 1900 UT

However, an increase of slant TEC, similar to previous example was observed on PRN18 between ~1650 to 1730UT. Comparison of PRN19 and PRN18 with the previous and following day is shown in Figure 4.81 and Figure 4.82, respectively. Comparison with the previous and the following days also shows no similar changes of TEC on both occasions. This occurrence was during low geomagnetic index where K_p was from 0 to 1- and B_z fluctuated between 2 to -2 nT (Figure 4.83). B_x and B_z at Eureka showed little variations from their means, while B_y fluctuated between -20 and 30 nT during the period of observations (Figure 4.84). Magnetic observations at Resolute Bay contained erroneous data and therefore is not included here.

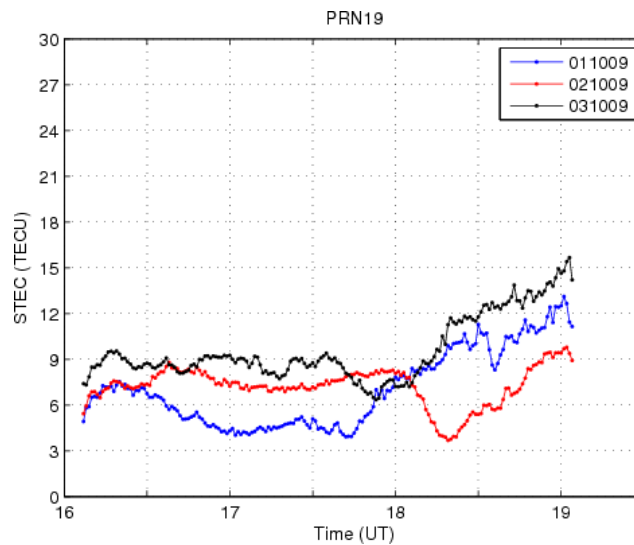


Figure 4.81: Comparison of TEC variations for PRN19 on 2 October 2009 (red curve) with previous and following days

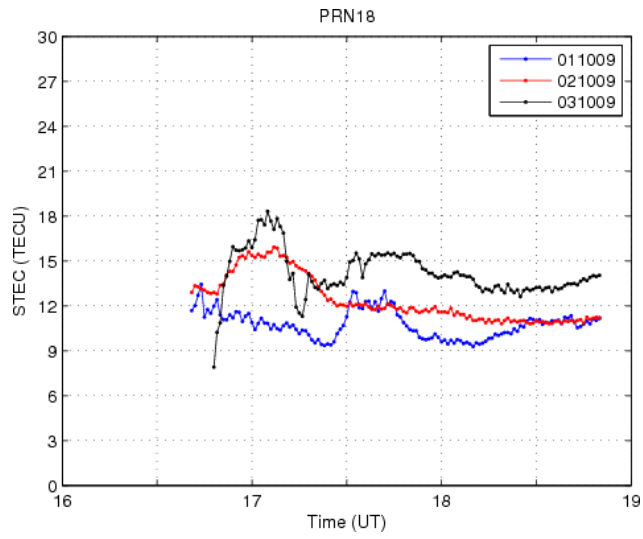


Figure 4.82: Comparison of TEC variations for PRN18 on 2 October 2009 (red curve) with previous and following days

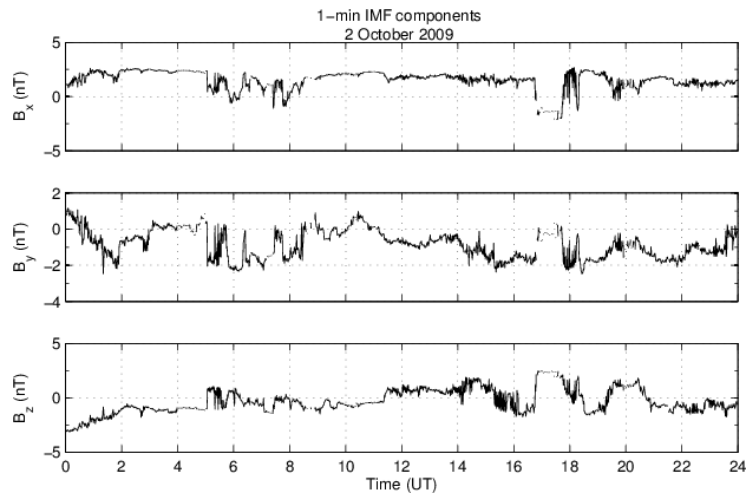


Figure 4.83: 1-minute IMF components on 2 October 2009

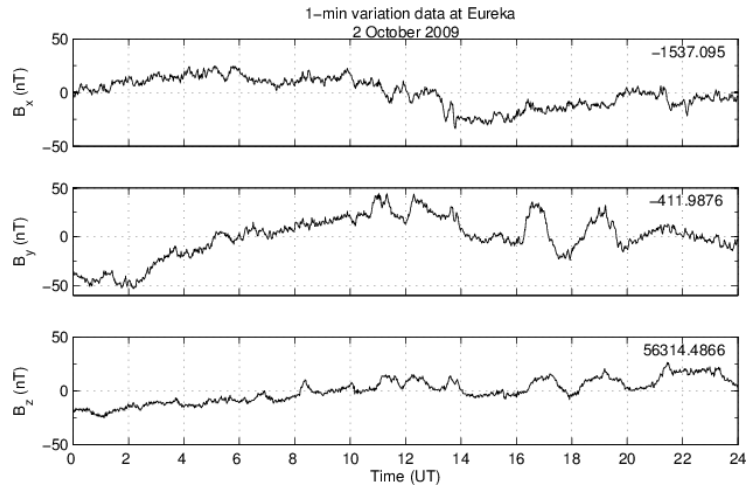


Figure 4.84: 1-minute variation data at Eureka on 2 October 2009

4.6 Concluding Remarks

This chapter discusses the finding of the TEC variations and also the amplitude and phase scintillations at Alert over the period of 2 years (from 1 June 2008 to 31 July 2010). Monthly and yearly pattern of the vertical TEC variations can be seen throughout the study. Winter months expectedly showed lower mean vertical TEC than summer and equinox months. All observed months in 2010 demonstrated higher mean TEC than in 2008 and 2009.

This in turn affects the number of patches observed where more patches were detected in 2010 than in previous years. This may be due to the slight increase of solar activity in 2010 and is in agreement with the finding in *Dandekar* [2002] where the number of patches is found to be dependent on sunspot activity.

In terms of patches formation in every UT hour, low intensity patches (both small and large in size) were observed at all time during the period of observations, with small patches were more frequently formed in an hour. Both small and large patches demonstrates similar UT dependence where ~80 large and ~300 small patches are identified around 1000 to 2000 UT from June to October in both 2008 and 2009. These numbers increase about twice in 2010 during the same UT hour.

Patches were observed more in 2010 in any month, regardless of its size and intensity. The occurrence of both small and large patches of moderate to high intensity were found to be more than twice in February and March 2010 than in the other months of the same year. The difference of occurrence of small patches in each month of the same year is about 1-2% for low intensity patches and 1-10% for moderate-high intensity patches. This difference increased for large patches of 1-4% for low intensity and 1-12% for moderate-high intensity. The large differences were mostly contributed by the occurrence in February and March 2010.

Amplitude scintillations index, S4 were very low throughout the study where at least ~99% were in the range of 0 and 0.1, and only 0.01% of the scintillations were between 0.2 and 0.3. Therefore, all S4 were considered as insignificant. This is in agreement with the work done by *Li et al.* [2010] and [*Prikryl et al.*, 2010] where observations covering the periods from 2007 to 2009 at high latitude stations discovered that amplitude scintillations were very low during those periods.

In regards to the phase scintillations, at least 93% of the data were in the range of 0 to 0.1 rad. About up to 0.2% of the phase scintillations were in 0.15 to 0.2 rad.

$\sigma_\phi < 0.15$ is considered as insignificant. Phase scintillations were found to be increased with the increasing of solar activity where most of the cases of $\sigma_\phi > 0.15$ rad were detected in 2010.

Selected events were chosen and then discussed in detail. These events cover different types of TEC variations and phase scintillations occurrences. The dependence on various geomagnetic conditions was also observed. **Table 4.6** summarises the daily sunspot number, the maximum 3-hour geomagnetic indices and also the maximum 1-hour polar cap index for a particular day in each event type. Description of each event type can be found in Table 4.5.

Table 4.6: Sunspot number (SSN), maximum geomagnetic index (K_p) and maximum polar cap index (PC(N)) for every case in each event type

Event Type	Date	SSN	Max. K_p	Max. PC(N)
A1	4 Feb 2009	0	4-	3.6
	8 Apr 2009	0	2+	1.1
A2	11 Oct 2008	9	6+	3.8
	15 Feb 2010	20	4+	3.8
A3	24 Feb 2010	20	2+	1.7
	11 Mar 2010	22	4-	2.3
A4	26 Jan 2009	0	3+	3.4
	3 Dec 2008	0	2	1.2
A5	24 May 2008	0	3+	2.6
A6	18 Nov 2009	9	1	1.1
	2 Oct 2009	0	1-	1.0
$K_p > 4$	5 Apr 2010	26	8-	5.1
	11 Oct 2008	9	6+	3.8

Table 4.6 also includes the events discussed for the dependence of geomagnetic activity (Section 4.4). Event on 11 October 2008 was discussed twice; once for the geomagnetic activity dependence, and later under the Event Type A2. All events are set to 3-hour period of observations, except on the Event Type $K_p > 4$ where the period covers the whole time of disturbed geomagnetic conditions.

Examples discussed in each event type suggest that irregularities at the high latitude ionosphere are complex. Many variations of slant TEC fluctuations/increases and phase scintillations were found. At high latitudes, ionosphere is ever variable so fluctuations of electron contents are expected; the difference is on the intensity of the irregularities to induce such fluctuations.

Certain types of irregularities are more frequent than the others. Large fluctuations of TEC were detected on many occasions at various times. Large TEC fluctuations can be observed continuously for several hours. These large fluctuations can be observed on either all or only few of the visible satellites over Alert. These fluctuations may also be accompanied by increase(s) in the phase scintillations, as presented in Event Type A2, A4 and A5. However, since fluctuations occurred continuously for a long period, the relation between these fluctuations and the occasional increases in the phase scintillations is difficult to be drawn.

Large and long-period smooth TEC increase as discussed in Event Type A6 is very rare. Similarly, there were events where phase scintillations occurred simultaneously with the increase of slant TEC, but this is also not frequent. A phase scintillation event may not be necessarily observed at the same time as patches, as discussed in

Event Type A2 and A3. Phase scintillations are smaller scale irregularity in comparison with patches. A smaller scale irregularity may cause localised phase scintillations while a strong one may cause patches of irregularities. Furthermore, nearby satellites could observe the same or even different phase scintillations, depending on their size.

Patches of small and large size with either low or moderate to high intensity were observed at various times. Table 4.7 presents the number of patches according to the sizes and intensities on all events. The number of patches may be overestimated as it is calculated based on individual satellite and added up. Therefore, different satellite(s) over or near the same path could see the same patch. Smaller patches were more likely to be formed compared to the large ones. Low intensity patches were observed more than the moderate to high intensity patches. Moderate to high intensity of small and large patches were also more frequent in Event Type A2 and A3 where large TEC fluctuations occurred. The increased total number of patches in Event Type $K_p > 4$ is expected as it covers longer period.

It is inappropriate to relate the sunspot number, SSN with the number of patches observed on each Event Type since the maximum SSN on all events was only 26. The number of patches supposedly increasing with the increasing SSN as concluded by *Dandekar* [2002] where the SSN during the observation periods varied from 10 to 150. Figure 4.85 illustrates the number of patches in each category for all Event Type A1-A6 with respect to the geomagnetic indices, K_p . The plot shows no correlation between the increasing numbers of patches with increased K_p . This is in agreement

with *Krankowski et al.* [2006] where it is concluded that there is only low dependency of patches occurrences on the geomagnetic indices.

Table 4.7: No. of patches for every case in each event type during a specified 3-hour period (except on Event Type $K_p > 4$)

Event Type	Date	Duration (UT)	No. of small patches		No. of large patches	
			Low intensity	Moderate to high intensity	Low intensity	Moderate to high intensity
A1	4 Feb 2009	0100-0400	27	1	5	0
	8 Apr 2009	1000-1300	4	0	0	0
A2	11 Oct 2008	1300-1600	18	18	2	4
	15 Feb 2010	1630-1930	5	31	0	6
A3	24 Feb 2010	2000-2300	15	21	2	4
	11 Mar 2010	0600-0900	23	12	4	2
A4	26 Jan 2009	1500-1800	21	11	4	2
	3 Dec 2008	1100-1400	19	0	3	0
A5	24 May 2008	1100-1400	33	1	6	0
A6	18 Nov 2009	1630-1930	18	0	3	0
	2 Oct 2009	1600-1900	28	0	5	0
$K_p > 4$	5 Apr 2010	0600-1800	119	11	22	2
	11 Oct 2008	1200-2100	63	45	9	9

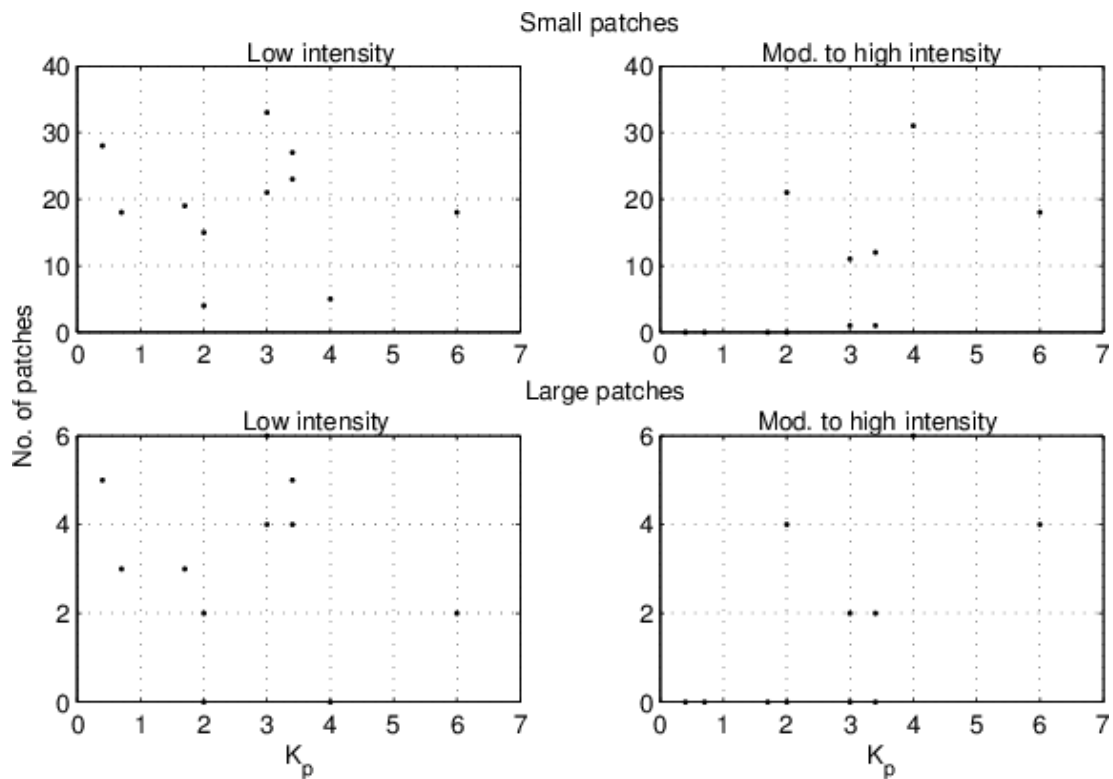


Figure 4.85: No. of patches versus K_p

Large fluctuations/increases of TEC seem independent of geomagnetic conditions where the changes in TEC can be registered during the period of both quiet and disturbed ionosphere. For example, large TEC fluctuations were observed on 24 February 2010 where maximum K_p for the day was only 2+. Similar observation can be drawn for the phase scintillations.

IMF components also do not have any particular effect on the changes in TEC (and patches formation) and phase scintillations. Similar observations can be said regarding the magnetic field effects at Eureka and Resolute Bay. The minimum and maximum values of each component did not show correlation to any event type (Table 4.8 and Table 4.9). *MacDougall and Jayachandran* [2007] emphasised that the patches only show correlation with the IMF B_z component when there are very

large swings of IMF B_z . No large value of IMF B_z was recorded in all event types. However, large swing of magnetic components were observed on both stations on 5 April 2010 where geomagnetic index was the largest (i.e. $K_p = 8-$). The magnitude of IMF B_y and B_z components on this day were also higher than any other day.

The percentage of the positive polarities of each component is presented in Table 4.10. The calculation for the percentage was only considering the ROT greater than 0.2 TECU/min and ROT less than -0.2 TECU/min. These thresholds were chosen since most considerably large TEC fluctuations correspond to $0.2 \text{ TECU/min} < \text{ROT} < -0.2 \text{ TECU/min}$. No specific pattern can be concluded on the relation between large TEC fluctuations and the polarities of the magnetic components of IMF and also of the polar cap stations. In the works done by *Gwal and Jain* [2011], it is found that patches were more likely to exist when $B_z < 0$ and/or $K_p > 4$.

Similar observation on the polarities of the magnetic components was also conducted for the phase scintillations (Table 4.11). Here, only $\sigma_\phi > 0.15$ rad was taken into consideration. Only Event Type A1, A2, A5 and also $K_p > 4$ were looked into since these are the events where phase scintillations were observed. No correlation is found between the polarities of the magnetic components and both the TEC fluctuations and phase scintillations.

Table 4.8: Minimum values of ROT and each magnetic component of IMF, Eureka (EUA) and Resolute Bay (RES) for every case in each event type during a specified 3-hour period (except on Event Type $K_p > 4$)

Event Type	Date	Period (UT)	No. of data	Min. ROT (TECU/min)	Min. IMF (nT)			Min. EUA (nT)			Min. RES (nT)		
					B_x	B_y	B_z	B_x	B_y	B_z	B_x	B_y	B_z
A1	4 Feb 2009	0100-0400	1277	-0.5	-6.9	-0.1	-5.5	-23.5	-97.6	-42.6	-14.0	-58.4	-52.9
	8 Apr 2009	1000-1300	1156	-0.2	-2.3	0.0	-2.3	-12.7	2.8	-7.4	1.3	4.7	3.7
A2	11 Oct 2008	1300-1600	1307	-0.8	-8.7	-4.8	-9.6	-200.6	-24.8	-7.3	-161.0	18.3	-7.5
	15 Feb 2010	1630-1930	1327	-0.8	-5.2	-11.2	-11.8	-101.2	36.3	-14.2	-89.7	40.2	-8.6
A3	24 Feb 2010	2000-2300	1241	-1.3	-3.1	-2.4	-3.6	-59.1	-39.4	-36.5	-53.5	-20.5	-39.6
	11 Mar 2010	0600-0900	1218	-0.6	-0.4	-5.2	-4.6	15.4	-40.1	-0.6	32.4	-54.8	3.8
A4	26 Jan 2009	1500-1800	1271	-0.8	-4.7	-7.6	-9.4	-27.2	-10.7	-19.5	-140.6	-3.0	-4.0
	3 Dec 2008	1100-1400	1395	-0.3	-1.2	-6.0	-7.2	-6.0	-13.0	-22.1	5.6	-0.2	-3.8
A5	24 May 2008	1100-1400	1362	-0.5	-2.4	-2.6	-4.0	9.2	8.0	-17.0	31.3	-0.1	17.7
A6	18 Nov 2009	1630-1930	1220	-0.3	-1.5	0.6	-0.1	-19.1	-17.3	-9.5	-15.7	-9.8	-7.8
	2 Oct 2009	1600-1900	1220	-0.3	-2.1	-2.5	-1.7	-22.0	-23.9	-8.1	n/a	n/a	n/a
$K_p > 4$	5 Apr 2010	0600-1800	4692	-0.8	-6.1	-21.6	-15.0	-215.8	-95.9	-67.2	-265.8	-164.6	-108.8
	11 Oct 2008	1200-2100	3568	-0.9	-8.7	-4.8	-10.3	-245.1	-117.6	-63.6	-231.6	-95.2	-98.2

Table 4.9: Maximum values of σ_ϕ , ROT and each magnetic component of IMF, Eureka (EUA) and Resolute Bay (RES) for every case in each event type during a 3-hour specified period (except on Event Type $K_p > 4$)

Event Type	Date	Period (UT)	No. of data	Max. σ_ϕ (rad)	Max. ROT (TECU/min)	Max. IMF (nT)			Max. EUA (nT)			Max. RES (nT)		
						B_x	B_y	B_z	B_x	B_y	B_z	B_x	B_y	B_z
A1	4 Feb 2009	0100-0400	1277	0.24	0.9	6.0	11.1	9.6	34.3	-22.3	-7.8	36.5	-19.6	-37.2
	8 Apr 2009	1000-1300	1156	0.22	0.2	-1.9	0.7	-1.1	26.7	37.4	7.0	27.6	24.1	20.4
A2	11 Oct 2008	1300-1600	1307	0.23	0.8	0.5	9.0	5.3	5.9	215.9	19.2	29.8	181.5	56.6
	15 Feb 2010	1630-1930	1327	0.18	1.5	1.6	-2.9	-1.6	-26.1	115.2	12.4	0.7	114.3	51.6
A3	24 Feb 2010	2000-2300	1241	0.23	0.8	-0.7	1.5	-0.3	-7.2	20.1	4.5	-14.9	12.6	-10.7
	11 Mar 2010	0600-0900	1218	0.17	1.2	4.6	2.2	2.7	95.7	66.5	22.5	98.5	59.2	50.4
A4	26 Jan 2009	1500-1800	1271	0.12	2.3	2.1	4.7	4.5	-7.9	12.0	15.6	-9.0	121.4	62.7
	3 Dec 2008	1100-1400	1395	0.11	0.3	4.1	-0.7	7.7	15.9	13.2	-1.0	19.4	12.5	11.1
A5	24 May 2008	1100-1400	1362	0.20	0.8	2.6	2.7	2.6	128.2	145.9	35.5	134.5	109.2	71.6
A6	18 Nov 2009	1630-1930	1220	0.09	0.4	0.4	2.1	2.4	6.1	8.7	11.0	-3.5	6.0	4.6
	2 Oct 2009	1600-1900	1220	0.14	0.4	2.7	0.3	2.5	-5.4	35.6	16.0	n/a	n/a	n/a
$K_p > 4$	5 Apr 2010	0600-1800	4692	0.21	0.8	10.7	14.2	18.9	332.3	480.9	178.6	321.3	304.7	459.4
	11 Oct 2008	1200-2100	3568	0.24	1.5	6.1	10.6	12.0	59.4	215.9	27.7	53.0	181.5	56.6

Table 4.10: Percentage of positive polarity of each magnetic component of IMF, Eureka (EUA) and Resolute Bay (RES) for every case in each event type during a specified 3-hour period (except on Event Type $K_p > 4$) for 0.2 TECU/min $<ROT < -0.2$ TECU/min

Event Type	Date	Period (UT)	No. of data	No. of data, 0.2 TECU/min $<ROT < -0.2$ TECU/min (%)	0.2 TECU/min $<ROT < -0.2$ TECU/min (%)	IMF +ve (%)			EUA +ve (%)			RES +ve (%)		
						B_x	B_y	B_z	B_x	B_y	B_z	B_x	B_y	B_z
A1	4 Feb 2009	0100-0400	1277	107	8.4	53	91	62	100	0	0	85	0	0
	8 Apr 2009	1000-1300	1156	21	1.8	0	5	0	76	81	24	81	81	81
A2	11 Oct 2008	1300-1600	1307	337	25.8	0	75	36	1	95	91	1	100	99
	15 Feb 2010	1630-1930	1327	386	29.1	5	0	0	0	100	42	2	100	93
A3	24 Feb 2010	2000-2300	1241	212	17.1	0	49	0	0	10	7	0	19	0
	11 Mar 2010	0600-0900	1218	235	19.3	97	4	23	100	21	98	100	16	100
A4	26 Jan 2009	1500-1800	1271	154	12.1	4	65	4	0	30	13	0	97	97
	3 Dec 2008	1100-1400	1395	90	6.5	72	0	26	74	68	0	74	74	59
A5	24 May 2008	1100-1400	1362	100	7.3	62	22	5	100	100	75	100	100	100
A6	18 Nov 2009	1630-1930	1220	32	2.6	3	100	100	16	38	53	0	9	16
	2 Oct 2009	1600-1900	1220	61	5.0	59	10	48	0	49	84	n/a	n/a	n/a
$K_p > 4$	5 Apr 2010	0600-1800	4692	377	8.0	62	16	58	80	53	71	80	63	67
	11 Oct 2008	1200-2100	3568	707	19.8	5	85	47	4	66	48	5	69	55

Table 4.11: Percentage of positive polarity of each magnetic component of IMF, Eureka (EUA) and Resolute Bay (RES) for every case in each event type during a specified 3-hour period (except on Event Type $K_p > 4$) for $\sigma_\phi > 0.15$ rad

Event Type	Date	Period (UT)	No. of data	No. of data, $\sigma_\phi > 0.15$ rad	$\sigma_\phi > 0.15$ rad (%)	IMF +ve (%)			EUA +ve (%)			RES +ve (%)		
						B _x	B _y	B _z	B _x	B _y	B _z	B _x	B _y	B _z
A1	4 Feb 2009	0100-0400	1277	8	0.6	0	100	0	100	0	0	100	0	0
	8 Apr 2009	1000-1300	1156	12	1.0	0	0	0	75	100	8	100	100	100
A2	11 Oct 2008	1300-1600	1307	10	0.8	0	90	70	0	90	100	0	100	100
	15 Feb 2010	1630-1930	1327	7	0.5	0	0	0	0	100	43	0	100	100
A3	24 Feb 2010	2000-2300	1241	3	0.2	0	33	0	0	0	0	0	0	0
	11 Mar 2010	0600-0900	1218	0	0.0	n/a								
A4	26 Jan 2009	1500-1800	1271	0	0.0	n/a								
	3 Dec 2008	1100-1400	1395	0	0.0	n/a								
A5	24 May 2008	1100-1400	1362	1	0.1	0	0	0	100	100	0	100	100	100
A6	18 Nov 2009	1630-1930	1220	0	0.0	n/a								
	2 Oct 2009	1600-1900	1220	0	0.0	n/a								
$K_p > 4$	5 Apr 2010	0600-1800	4692	6	0.1	67	0	33	67	67	100	67	83	83
	11 Oct 2008	1200-2100	3568	26	0.7	8	96	62	0	46	42	0	62	42

Chapter Five: Qaanaaq to Ny-Ålesund HF Link

HF channel characteristics from Qaanaaq to Ny-Ålesund have been measured since mid March 2009. Multipath spread on any frequency was small with at least 97% of the time was less than 1 ms. Therefore, only Doppler spreads are discussed here. Statistical analysis of Doppler spreads for a complete 2-year data is presented in this chapter. Dependence of Doppler spreads on geomagnetic conditions is also discussed.

5.1 Statistical Analysis of Doppler Spreads

Data from the HF link from Qaanaaq to Ny-Ålesund has been collected since 14 March 2009. Statistical analysis for data from HF link utilised a complete 2-year data from 14 March 2009 until 28 February 2011. Data were available every day except from ~1200 UT 6 July to ~1200 UT 9 July 2009, from 12 November until ~2200 UT 13 November 2009, from ~0600 UT 24 December until 30 December 2009, from 24 to 25 April 2010, from ~1300 UT 30 April to ~0900 UT 4 May 2010, from ~0400 UT 18 July to ~0900 UT 19 July 2010, and from ~1200 UT 27 October to 3 November 2010.

Figure 5.1 shows the number of all data detected in each month from March 2009 to February 2011 on each frequency. Smallest number of data was received on the highest frequency, followed by the lowest frequency. A large amount of data was

received on 6.95 MHz and 8.01 MHz, followed by on 10.39 MHz and 11.12 MHz where the number of data was fairly large with exceptions on few months, for example on December and January in both years. Data received on 11.12 MHz was generally less than on 10.39 MHz.

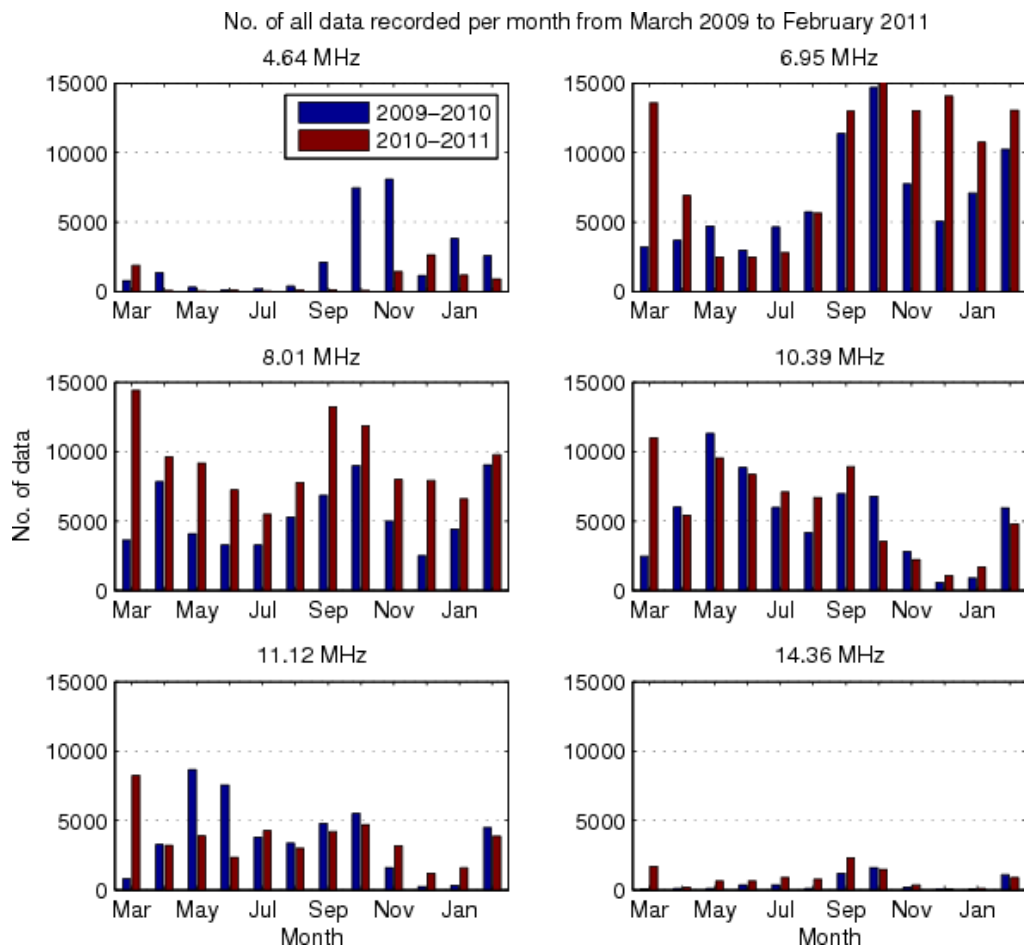


Figure 5.1: Number of all data recorded for each month from March 2009 to February 2011 on each frequency

The total number of data was then filtered in order to select the meaningful ones where the SNR of the signal is greater than 0 dB as suggested in Chapter Three. The pattern of the distribution of the data per month is similar to the untreated data.

However, the original data were significantly reduced up to ~30% (refer Figure 5.2). The figure also demonstrates that the lowest and the highest frequencies were not suitable for the communication between Qaanaaq and Ny-Ålesund. Depending on the time of the year, 6.95 MHz and 8.01 MHz could be the best frequencies to use between these locations. This is followed by 10.39 MHz.

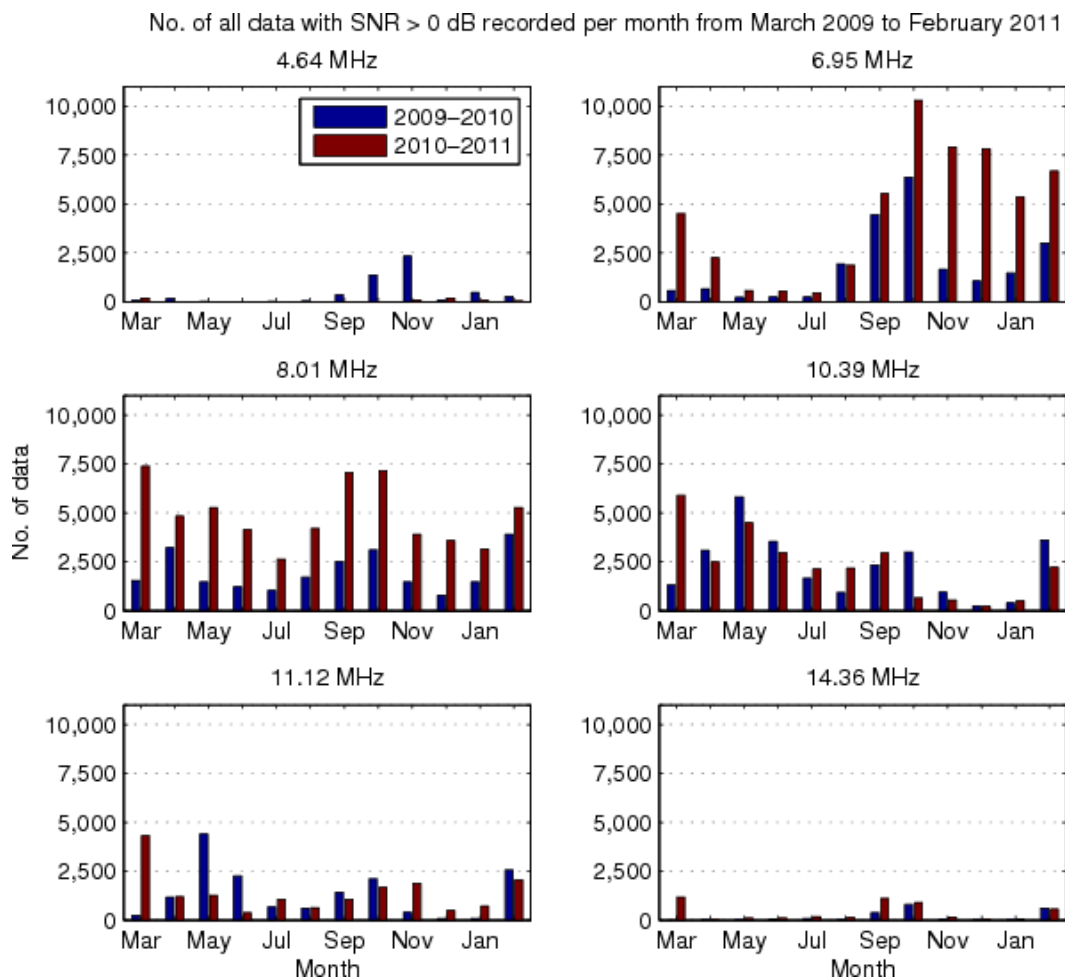


Figure 5.2: Number of all data (SNR > 0 dB) recorded for each month from March 2009 to February 2011 on each frequency

The data were then manually examined in order to eliminate erroneous Doppler spreads. Figure 5.3 shows the histogram of all Doppler spreads for signals with

SNR > 0 dB for each frequency using 0.5-Hz step. Note that the resolution of the Doppler spread in the raw measurement is 0.5 Hz. Doppler spread was mostly less than ~5 Hz and rarely exceeded 15 Hz. However, few Doppler spreads were measured up to ~35 Hz (for 8.01 MHz only, other frequencies never exceeded 20 Hz). This, however, only involved a small number of data (up to 29 data points only) and therefore will not affect the statistics. Study conducted by *Cannon et al.* [1995] from 23 August to 1 September 1994 between Isfjord and Tuentangen yielded that even though Doppler spread of 20 Hz was recorded, the mean was actually much less at only 4.7 Hz.

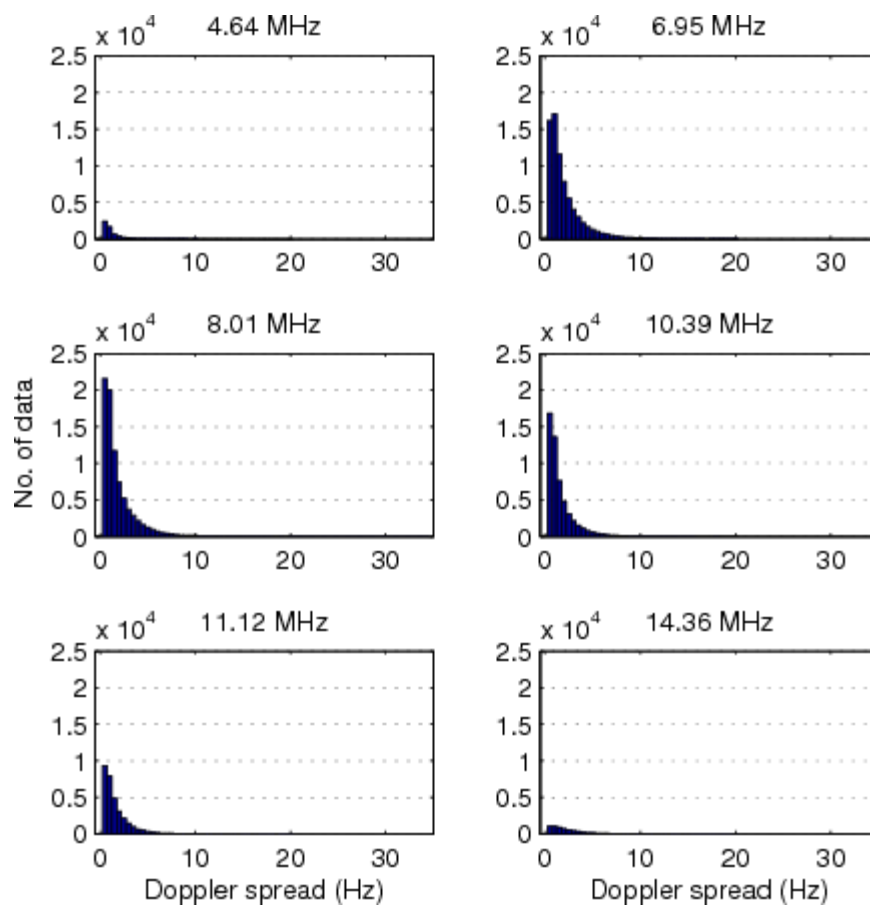


Figure 5.3: Histogram of Doppler spreads for data from March 2009 to February 2011 on each frequency

The monthly lower decile, median, and upper decile of Doppler spread for each frequency are presented in Table 5.1 to Table 5.6. Only data with more than 25 cases in a month and SNR of the received signal greater than 0 dB were considered to compute decile and median values. Lower decile on any frequency never exceeded 1 Hz with Doppler spread of 0.5 Hz was more frequently observed on most months. Median of the Doppler spread was between 0.5 to 1.5 Hz on any frequency with an exception of between 2 and 3 Hz on several months. Median of 2 Hz Doppler spread was recorded in December 2010 and January 2011 on 6.95 MHz, and in February 2010 and also from October 2010 to February 2011 at 8.01 MHz.

Slightly larger median of 2.5 Hz was measured in November 2010 on 6.95 MHz. For the next three higher frequencies, median of 2 Hz Doppler spread was observed in November 2009 and February 2010 (10.39 MHz), February, November and December 2010 (11.12 MHz), and February, March, October 2010 and also February 2011 (14.36 MHz). The largest median of 3 Hz was in October 2009 on 14.36 MHz. Doppler spread median on 4.64 MHz remained small between 0.5 and 1 Hz throughout the observation periods. In general, the median of Doppler spreads on any frequency did not demonstrate large variation from each other.

Upper decile of Doppler spreads demonstrated more variability from 1-1.5 to 5.5 Hz, except at the lowest and highest frequencies. The lowest frequencies showed the least variation of upper decile from 1 to 3 Hz only, while at 14.36 MHz it reached up to 6.5 Hz once in October 2009. There was a gap of data on 4.64 and 14.36 MHz that signifies that the lowest and highest frequencies were not suitable to be used for communication between Qaanaaq and Ny-Ålesund since signals were not detectable

on these frequencies. The signals on the lowest frequency may be absorbed by the D layer, while signals on the highest frequency passed through the ionospheric layer.

Table 5.1: Monthly lower decile, median, and upper decile of Doppler spread (Hz) at 4.64 MHz

Month	No. of data	Doppler spread (Hz)		
		10%	50%	90%
Mar 2009	63	0.5	0.5	1
Apr 2009	156	0.5	1	1.5
May 2009	9	-	-	-
Jun 2009	0	-	-	-
Jul 2009	2	-	-	-
Aug 2009	33	0.5	0.5	1
Sep 2009	346	0.5	0.5	1.5
Oct 2009	1354	0.5	0.5	1.5
Nov 2009	2330	0.5	1	3
Dec 2009	75	0.5	0.5	1.5
Jan 2010	469	0.5	1	2.5
Feb 2010	259	0.5	0.5	1.5
Mar 2010	175	0.5	0.5	1
Apr 2010	0	-	-	-
May 2010	0	-	-	-
Jun 2010	0	-	-	-
Jul 2010	0	-	-	-
Aug 2010	0	-	-	-
Sep 2010	0	-	-	-
Oct 2010	0	-	-	-
Nov 2010	74	0.5	0.5	1
Dec 2010	169	0.5	0.5	1
Jan 2011	56	0.5	0.5	1.5
Feb 2011	47	0.5	0.5	1

Table 5.2: Monthly lower decile, median, and upper decile of Doppler spread (Hz) at 6.95 MHz

Month	No. of data	Doppler spread (Hz)		
		10%	50%	90%
Mar 2009	556	0.5	1	4.5
Apr 2009	654	0.5	1	2.5
May 2009	219	0.5	1	3.5
Jun 2009	249	0.5	1	4.5
Jul 2009	240	0.5	1	3.5
Aug 2009	1939	0.5	0.5	1.5
Sep 2009	4438	0.5	1	2.5
Oct 2009	6363	0.5	1.5	3.5
Nov 2009	1651	0.5	1	3.5
Dec 2009	1054	0.5	1.5	4.5
Jan 2010	1464	0.5	1.5	3.5
Feb 2010	2980	0.5	1.5	4
Mar 2010	4495	0.5	1	3.5
Apr 2010	2244	0.5	1	2.5
May 2010	574	0.5	0.5	1.5
Jun 2010	528	0.5	0.5	1.5
Jul 2010	442	0.5	0.5	1
Aug 2010	1857	0.5	1	1.5
Sep 2010	5511	0.5	1	3
Oct 2010	10293	0.5	1.5	4.5
Nov 2010	7892	1	2.5	5.5
Dec 2010	7816	1	2	5.5
Jan 2011	5354	0.5	2	4.5
Feb 2011	6676	0.5	1.5	5

Table 5.3: Monthly lower decile, median, and upper decile of Doppler spread (Hz) at 8.01 MHz

Month	No. of data	Doppler spread (Hz)		
		10%	50%	90%
Mar 2009	1546	0.5	1	2
Apr 2009	3222	0.5	1	2
May 2009	1472	0.5	0.5	1.5
Jun 2009	1224	0.5	0.5	1.5
Jul 2009	1037	0.5	0.5	1.5
Aug 2009	1708	0.5	0.5	1
Sep 2009	2520	0.5	1	2
Oct 2009	3109	0.5	1	3
Nov 2009	1480	0.5	1.5	4.5
Dec 2009	786	0.5	1.5	4
Jan 2010	1472	0.5	1.5	4
Feb 2010	3905	0.5	2	5
Mar 2010	7376	0.5	1.5	5
Apr 2010	4838	0.5	1	3.5
May 2010	5267	0.5	1	2.5
Jun 2010	4143	0.5	1	2.5
Jul 2010	2638	0.5	1	2.5
Aug 2010	4200	0.5	1	2.5
Sep 2010	7060	0.5	1.5	4
Oct 2010	7160	0.5	2	5
Nov 2010	3902	1	2	5.5
Dec 2010	3580	0.5	2	5
Jan 2011	3156	0.5	2	4.5
Feb 2011	5282	0.5	2	5

Table 5.4: Monthly lower decile, median, and upper decile of Doppler spread (Hz) at 10.39 MHz

Month	No. of data	Doppler spread (Hz)		
		10%	50%	90%
Mar 2009	1309	0.5	1.5	3
Apr 2009	3095	0.5	1.5	3
May 2009	5824	0.5	1	3
Jun 2009	3542	0.5	1	3.5
Jul 2009	1665	0.5	1	3
Aug 2009	937	0.5	0.5	1.5
Sep 2009	2343	0.5	1	2
Oct 2009	3009	0.5	1.5	4
Nov 2009	952	0.5	2	4.5
Dec 2009	248	0.5	1.5	3.5
Jan 2010	404	0.5	1.5	3.5
Feb 2010	3603	0.5	2	5.5
Mar 2010	5895	0.5	1	4
Apr 2010	2490	0.5	1	2.5
May 2010	4496	0.5	1	3.5
Jun 2010	2972	0.5	1	3
Jul 2010	2126	0.5	0.5	2
Aug 2010	2176	0.5	0.5	2
Sep 2010	2949	0.5	1	3
Oct 2010	658	0.5	1	3
Nov 2010	549	0.5	1	3
Dec 2010	218	0.5	1.5	3
Jan 2011	514	0.5	1.5	3.5
Feb 2011	2230	0.5	1.5	3.5

Table 5.5: Monthly lower decile, median, and upper decile of Doppler spread (Hz) at 11.12 MHz

Month	No. of data	Doppler spread (Hz)		
		10%	50%	90%
Mar 2009	232	0.5	1	2.5
Apr 2009	1168	0.5	1	3
May 2009	4404	0.5	1	3.5
Jun 2009	2252	0.5	1	3
Jul 2009	667	0.5	1	2.5
Aug 2009	596	0.5	0.5	1.5
Sep 2009	1409	0.5	1	1.5
Oct 2009	2106	0.5	1	3
Nov 2009	397	0.5	1.5	4
Dec 2009	70	0.5	1.5	2.5
Jan 2010	83	0.5	1	3.5
Feb 2010	2554	0.5	2	5
Mar 2010	4306	0.5	1	3
Apr 2010	1199	0.5	1	2.5
May 2010	1268	0.5	1	2.5
Jun 2010	381	0.5	1	2.5
Jul 2010	1045	0.5	1	2
Aug 2010	634	0.5	0.5	1.5
Sep 2010	1046	0.5	1	2
Oct 2010	1663	0.5	1	3.5
Nov 2010	1870	1	2	4.5
Dec 2010	479	0.5	2	4
Jan 2011	709	0.5	1.5	4
Feb 2011	2042	0.5	1.5	4

Table 5.6: Monthly lower decile, median, and upper decile of Doppler spread (Hz) at 14.36 MHz

Month	No. of data	Doppler spread (Hz)		
		10%	50%	90%
Mar 2009	0	-	-	-
Apr 2009	5	-	-	-
May 2009	9	-	-	-
Jun 2009	55	0.5	0.5	1
Jul 2009	84	0.5	0.5	1
Aug 2009	17	-	-	-
Sep 2009	372	0.5	1.5	3.5
Oct 2009	790	1	3	6.5
Nov 2009	23	-	-	-
Dec 2009	1	-	-	-
Jan 2010	11	-	-	-
Feb 2010	605	1	2	4.5
Mar 2010	1178	0.5	2	5.5
Apr 2010	10	-	-	-
May 2010	95	0.5	0.5	2
Jun 2010	91	0.5	0.5	2
Jul 2010	162	0.5	0.5	2
Aug 2010	130	0.5	1	2
Sep 2010	1100	0.5	1.5	4
Oct 2010	895	1	2	4
Nov 2010	149	0.5	1.5	4.5
Dec 2010	29	0.5	1.5	3
Jan 2011	47	0.5	1	2.5
Feb 2011	546	1	2	5

With the exception of the lowest frequency where small to moderate value of upper decile Doppler spreads were observed, large upper decile values normally occurred from around September/October to March. These were apparent on 8.01 MHz, and from October 2010 to February 2011 (6.95 MHz), and also from November 2010 to February 2011 (11.12 MHz). Smaller upper decile range was observed on 10.39 MHz. This is illustrated in Figure 5.4 where the upper decile of both the lowest and highest is intentionally omitted in the plots due to the gaps of data on these frequencies.

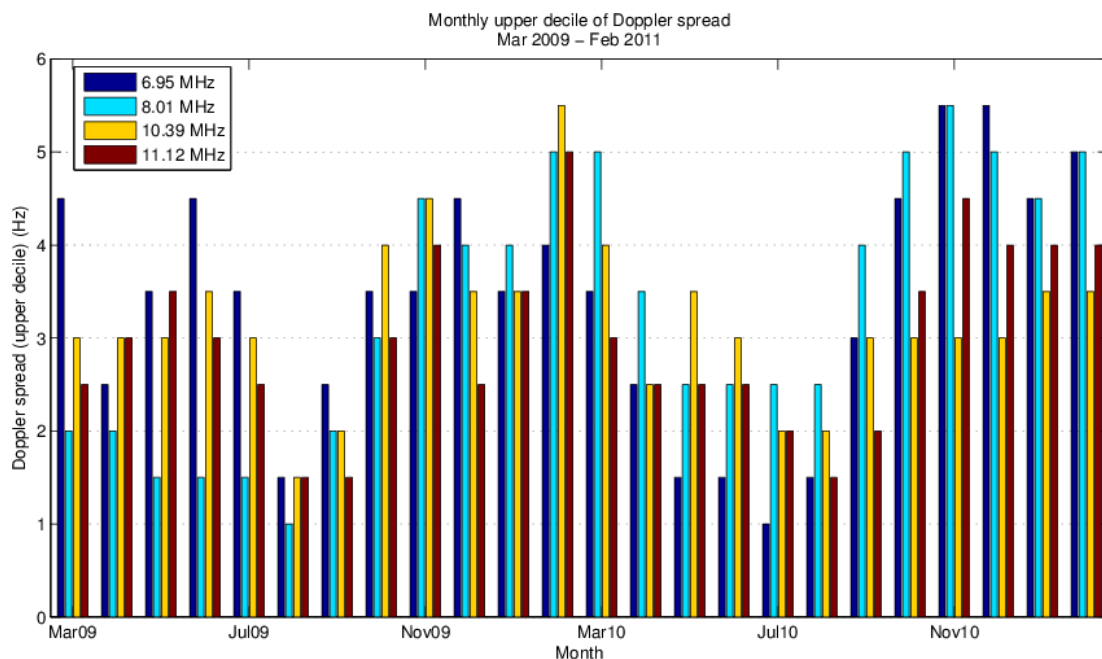


Figure 5.4: Monthly upper decile of Doppler spread from March 2009 to February 2011

Upper decile of 4.5 Hz was also observed outside the winter period, which was in June 2009 at 6.95 MHz. Meanwhile, only moderate upper decile Doppler spreads of 3-3.5 Hz were observed from September 2010 to January 2011 on 10.39 MHz.

Figure 5.4 also shows that larger upper decile of Doppler spread were measured on 6.95, 8.01 and 11.12 MHz during the second half of the observation periods from September to January, than during the same months of the first year of observations.

Meanwhile, smaller upper decile of Doppler spread was measured on 10.39 MHz during the same months (September to January) of the second half of the observation periods. Upper decile in February 2011 was larger than (on 6.95 MHz), equivalent with (on 8.01 MHz), and smaller than (on 10.39 and 11.12 MHz) the value in February 2010. Figure 5.4 also demonstrates that the increases of the upper decile of Doppler spread did not correspond to the increase of the frequency. This is in agreement with the work done by *Cannon et al.* [1995] where spreads were found to be higher on the lower frequencies.

Measurements conducted by *Warrington et al.* [2006] from 2003 to 2005 for the path Kirkenes-Kiruna revealed that the Doppler spreads tended to increase with increasing frequency. In another instance, *Angling et al.* [1998] concluded that Doppler spreads on all four high latitude paths were generally increasing with the increase of frequency, except on Isjford-Tuentangen during selected days between February-October 1995 where Doppler spread was the highest (~13 Hz) in the lowest band and the lowest (~8 Hz) in the highest band of frequency. *Angling et al.* [1998] suggested that this could be associated with the same mechanism that causes the multipath spreads to fall with increasing frequency on this path, that is a move from multihop to single-hop propagation.

Table 5.1 to Table 5.6 and Figure 5.4 only give general view of the monthly variability of Doppler spreads, more detailed variations based on hourly median and upper decile of Doppler spreads are discussed next. Figure 5.5 shows hourly median for Doppler spread computed for every observed month. Similar to the previous discussion, only hourly data of more than 25 cases are considered to compute hourly median. Increased median value of Doppler spread can be seen on the plots for generally on each frequency for certain months with the increasing of UT hour. The pattern is similar, however the exact period is difficult to deduce on each frequency due to the lack of number of meaningful detectable signals in every hour.

In general, median of Doppler spread was larger from September/October to March than the rest of the year. Diurnal variations during these months can also be seen where larger median of Doppler spread up to ~ 5 Hz (on 6.95 and 8.01 MHz) was observed around 0000 until 1400-1500 UT. Diurnal variation can still be observed on other months but for smaller median and shorter periods of relatively larger median. Despite a limited number of data, median of Doppler spread on 14.36 MHz reached up to 4.5 Hz in March 2010. Higher mean Doppler spread of ~ 7 -7.5 Hz was observed by Cannon *et al.* [1995] on the path from Isfjord to Tuentangen during 1800-2400 UT and 0000-0600 UT as opposed to the mean of ~ 1.9 -3.1 Hz at other time frame.

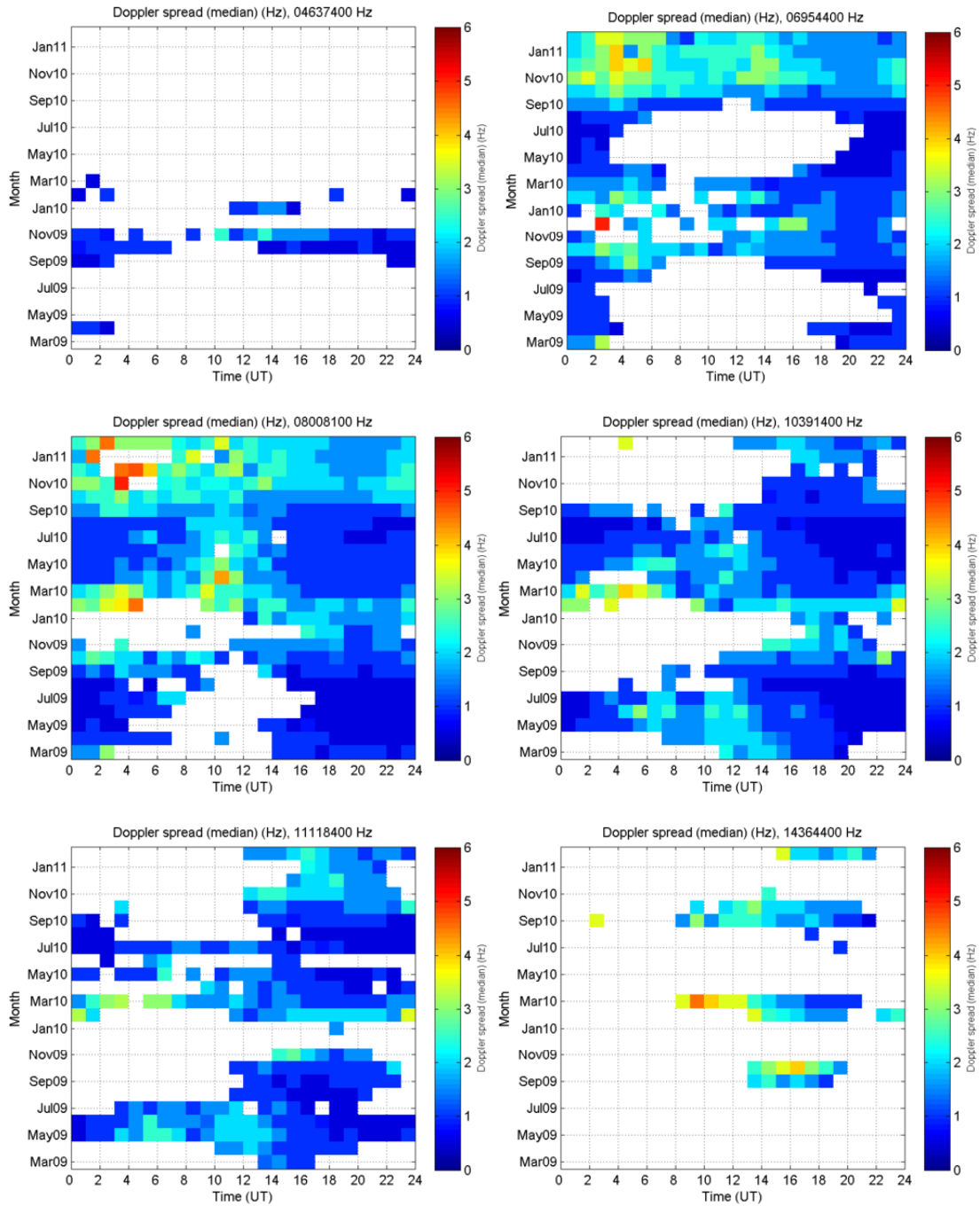


Figure 5.5: Median of Doppler spread computed hourly for every month from March 2009 to February 2011 on each frequency

Annual variations were also observed when data were sufficiently detectable especially on 6.95 and 8.01 MHz. For example, in general, median in October 2009 - February 2010 was smaller than during the same period of the following year, at least from 1200 UT onwards. Observations from 0000 to 1200 UT were not entirely

conclusive due to the lack of meaningful data during this period, but generally were in agreement with the previous observation, except in December 2009 from 1200 to 1300 UT (on 6.95 MHz) and between 0000 to 0500 UT in February 2010 (8.01 MHz). Unfortunately, observations on other frequencies for the same period were not possible due to the data gap. However, on 10.39 MHz, observations of median of Doppler spread from 0600 to 1400 UT in April to July 2010 was slightly smaller than during the same period of the previous year.

Since Doppler spreads were not uniformly distributed, it is better to look at the upper decile values to get a better understanding of Doppler spread distributions. Figure 5.6 shows the hourly upper decile of Doppler spread computed for every available month. Similar to the median, upper decile values of Doppler spreads are best looked on 6.95 and 8.01 MHz since meaningful data were insufficient on other frequencies, especially on the lowest and highest frequencies. In general, upper decile values from October to February were larger and covering longer period than in other months. Larger upper decile of Doppler spreads was observed from around 0000 to 1700 UT on 6.95 and 8.01 MHz. The values of hourly upper decile can reach up to 7-8.5 Hz (6.95 MHz) and 7-9.5 Hz (8.01 MHz).

As opposed to the median values where the largest median were observed mainly between 0100 to 0600 UT, the largest upper decile values during these months were scattered from 0000 to 1100 UT. March and September also demonstrated similar behaviour as in October-February but for slightly shorter period, until ~1500 UT for 8.01 MHz, and until ~1400 UT on March 2010 and ~0500 UT on September 2010 for 6.95 MHz. Data were not available for some times in March and September 2009

on this frequency. The largest upper decile of Doppler spread in an hour reached up to 5.5-9 Hz (6.95 MHz) and 6-8.5 Hz (8.01 MHz) in March and September.

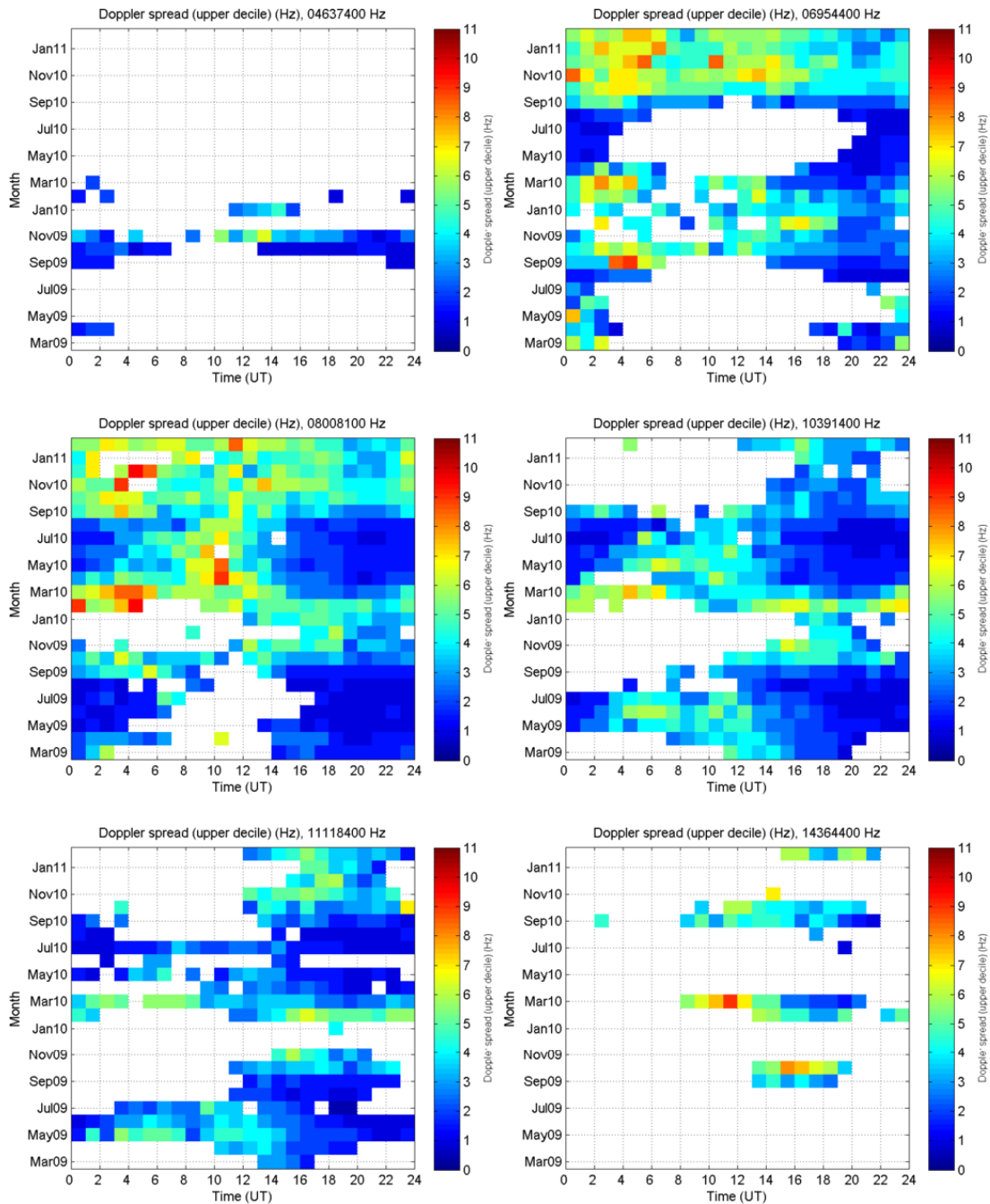


Figure 5.6: Upper decile of Doppler spread computed hourly for every month from March 2009 to February 2011 on each frequency

Although not for the whole period (e.g. in February on 8.01 MHz), values of upper decile on these two frequencies were most of the times larger in October 2010-February 2011 than in the previous year, where the differences was between 0.5 to 4.5 Hz (up to 6 Hz for 6.95 MHz in November). The difference is obtained by calculating the difference of upper decile values for each hour of the same month. The increase in the second year could due to the increasing solar activity. *Willink et al.* [1999] suggested that reduced solar activity may result in less variability on the measured channel characteristics compared to increased activity.

Meanwhile, the difference in these months was normally between 0.5 to 2 Hz larger for 11.12 MHz during these periods of the second year (based on October and November data only), while in February, the first year observations demonstrated larger upper decile values than in the second year. On 10.39 MHz, the upper decile values of Doppler spread, however, did not demonstrate dependence on the solar activity. The difference of the upper decile values was normally from 0.5 to 2.5 Hz between October-February of the first and the second year, and reached up to 4.5 Hz in November and February, where it normally larger in the first year.

Lack of detectable data between March and September makes it difficult to draw a conclusion of solar activity dependence during the observation months. However, based on the available data, larger upper decile of Doppler spreads on 8.01 MHz were observed in the second year for most of the times with 0.5-4 Hz differences from the first year. Meanwhile, for 6.95 and 11.12 MHz, larger upper decile of Doppler spreads were measured for at least half of the times during the first year of observations, with the differences from the following year were from 0.5 to 5 Hz

(6.95 MHz), and from 0.5 to 4 Hz (11.12 MHz). However, there is no apparent pattern of increasing upper decile values with the increase in solar activity on 10.39 MHz, with the difference of the available data for March-September of both years was between 0.5 and 2.5 Hz.

Larger upper decile of Doppler spread can be seen at the highest frequency, where the limited number of observed Doppler spreads tended to provide larger upper decile values when looking at the same time of occurrence as at other frequencies. Maximum of upper decile values reached 10.5 Hz on this frequency. Due to the lack of detectable data, conclusion on long term behaviour of the highest (and also the lowest) frequencies should not be made.

The number of Doppler spreads data on each observed month for every frequency as a function of time (UT) is illustrated in Figure 5.7. The left panel represents the number of all data of Doppler spreads in an hour for each month. Meanwhile, the right panel shows only for Doppler spreads exceeding 3 Hz. The 3-Hz threshold is chosen based on the maximum upper decile value of Doppler spread on 4.64 MHz, which is the frequency where Doppler spreads showed the least variation.

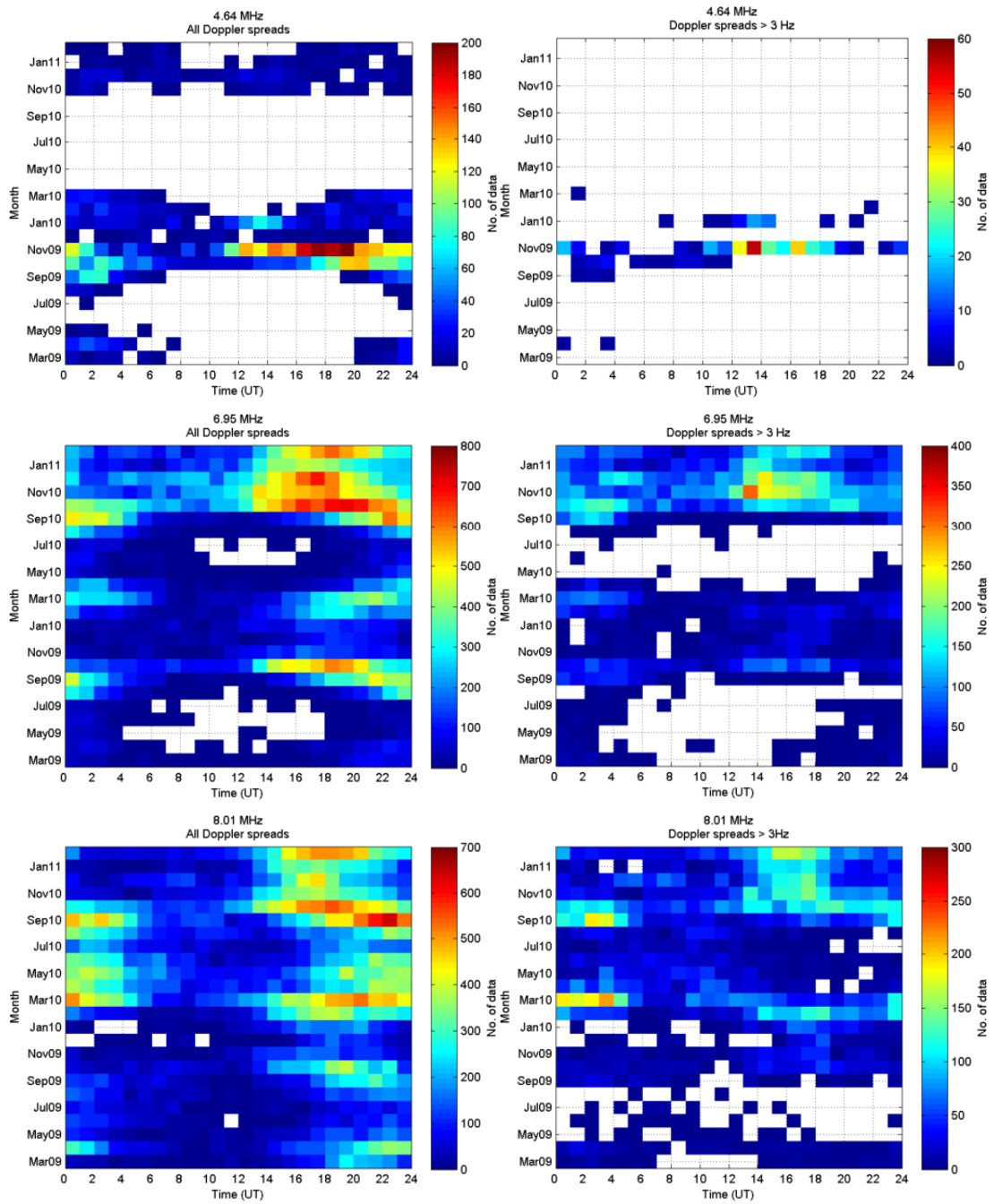


Figure 5.7 (i): The number of data for all Doppler spreads (left) and for Doppler spreads > 3 Hz (right) on 4.64, 6.95 and 8.01 MHz

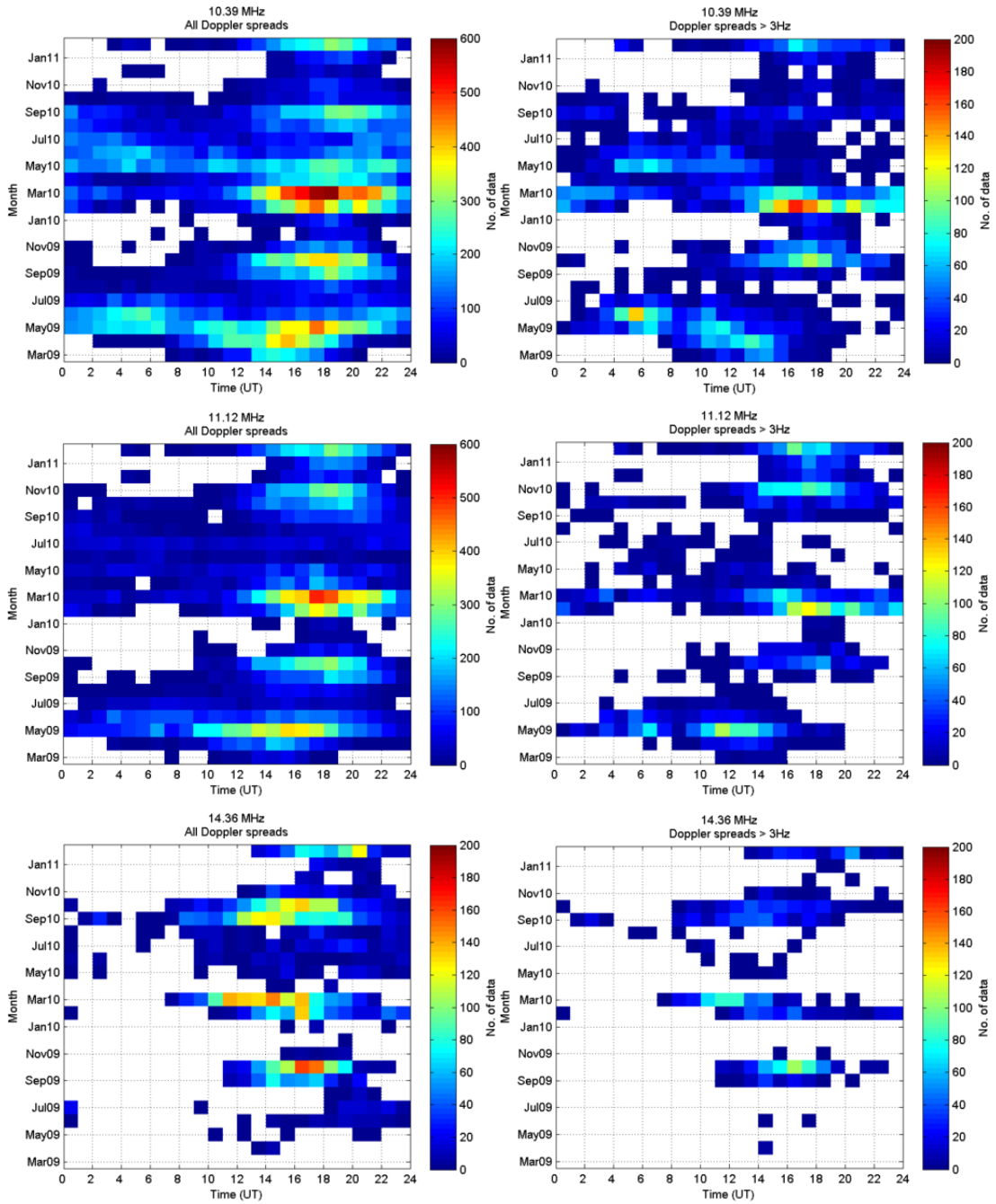


Figure 5.7 (ii): as of (i) but on 10.39, 11.12 and 14.36 MHz

As mentioned in earlier discussion, Doppler spreads were observed mostly on 8.01 and 6.95 MHz, followed by on 10.39 and 11.12 MHz. In term of Doppler spreads distribution on 8.01 MHz, even though the spreads distributed differently from one month to another, they were more likely to be observed from ~ 1400 UT onward until

~0400 UT (peaked at various hours), especially from March to October 2010. Meanwhile, Doppler spreads mostly observed from ~1300 UT until ~2300 UT from November 2010 to February 2011, also maximised at various hour during this period.

Similar pattern was also observed for the same month of the preceding year, except with less number of Doppler spreads. Diurnal behaviour of Doppler spreads on 6.95 MHz also demonstrated similarity with spreads observed on 8.01 MHz between November 2010 and February 2011. However, no data were detected for few hours around midday in April-July 2009 and June-July 2010.

On 10.39 and 11.12 MHz, there was a lack of detectable signals at the earlier hours of the day from March and April 2009, from September 2009 to January 2010, and from November 2010 to February 2011. The number of data of Doppler spreads peaked at ~1400 to ~2200 UT in May 2009 and March 2010.

Doppler spreads > 3 Hz on 6.95 MHz were observed at almost all day from September 2009 to April 2010, and also from September 2010 to February 2011. For 8.01 MHz, Doppler spreads > 3 Hz were observed at all months at almost all hours, except during May-August 2009. Even though the number of Doppler spreads > 3 Hz appears to be distributed for more hours on 10.34 MHz than on 11.12 MHz, but the actual percentage of Doppler spreads > 3 Hz is slightly larger on 11.12 MHz (Table 5.7).

Table 5.7: Percentage of Doppler spreads $3 > \text{Hz}$ on each frequency

Frequency (MHz)	Total no. of data	Total no. of Doppler spreads $> 3 \text{ Hz}$	Percentage of Doppler spreads $> 3 \text{ Hz}$ (%)
4.64	5626	391	7.0
6.95	75521	17011	22.5
8.01	82148	15965	19.4
10.34	54206	8021	14.8
11.12	32585	4912	15.1
14.36	6407	1952	30.5

Very few data on 4.64 MHz exceeded 3 Hz (equivalent to only 7.0% of total data), and while the number of total data on 14.36 MHz is only 6407, the percentage of Doppler spreads $> 3 \text{ Hz}$ is the highest at 30.5%. Insufficient detectable data and their non-uniform distributions throughout the whole day makes it impossible to draw conclusion of the distribution of Doppler spreads on these two frequencies.

Direct comparisons with the finding in the previous work conducted by, e.g. *Cannon et al.* [1995], *Broms* [1997], and *Angling et al.* [1998] perhaps should not be made as the recorded channel characteristics dependable on several factors, for example the geography of the path and system setting. The afore-mentioned authors conducted experiments over various path lengths at auroral and/or subauroral stations, therefore may demonstrate different characteristics than in this study which involves a transmitter in the polar cap region and the receiver in auroral/polar cap zone. For instance, measurements on a polar path from Isfjord (Svalbard) to Alert of 1383 km path length in January 1996 by *Warrington* [1998] showed greater spreads than those observed on Isfjord-Cricklade transauroral path.

5.2 Geomagnetic Activity Dependence

A total of 45 cases were found where the 3-hour K_p indices were considered as active geomagnetic activity. These cases were distributed in 23 days; including 3 days in 2009, 15 days in 2010 and 5 days in 2011. In addition, 31 cases were recognised as unsettled geomagnetic activities where $K_p = 4$ during these days. Table 5.8 lists out the geomagnetic activity level on the days where $K_p \geq 5$ from March 2009 to February 2011.

Table 5.8: Summary of geomagnetic activity where $K_p \geq 5$ from 14 March 2009 to February 2011

Date	3-hour K_p indices							
24 Jun 2009	2+	3	4	2-	2-	2+	5+	3-
22 Jul 2009	3	6-	5	4+	2-	2-	2+	1+
30 Aug 2009	2	1+	3-	2	3	6-	4+	3+
5 Apr 2010	3	3+	5+	8-	6-	5	4+	4-
6 Apr 2010	5	5+	5-	5-	4+	5+	5-	5-
12 Apr 2010	6-	4	3+	1+	1+	3	3-	1
14 Apr 2010	2-	1	0+	1	1-	1+	2+	5
2 May 2010	1	1	1+	4	6	5	6-	5+
3 May 2010	5	4	4-	3+	4-	3	3+	4-
29 May 2010	3-	4-	5+	4-	4+	4+	4+	3
30 May 2010	3-	2+	4	3-	2	4	5	4
4 Jun 2010	5-	4	2	3+	2-	1	1+	2-
3 Aug 2010	2+	2	2-	1+	1+	3+	5-	7-
4 Aug 2010	6+	4+	3-	5	5	4-	6+	5-
25 Aug 2010	4+	5-	2+	3-	3	3	2-	3
23 Oct 2010	4-	3-	4-	4+	5	4-	3	5-
11 Nov 2010	3+	1+	2	3+	3+	3+	3-	5-
27 Nov 2010	0	0	0	0+	1-	2-	5-	5-
7 Jan 2011	5	3-	2+	2+	2	2+	3	3
4 Feb 2011	2-	3+	2+	2-	2-	2+	5+	6-
5 Feb 2011	5	4-	3-	2+	1+	2+	3	3-
14 Feb 2011	0	0	0+	0+	1-	3	4	5+
18 Feb 2011	3	5-	5	4-	3	3	2+	2

Some of the cases in Table 4.4 are repeated here since period of observations of GPS and HF link were partly overlapped. Similar to the period of observations of the transionospheric data, only one event of $K_p=8-$, which was on 5 April 2010 and this was accompanied by minor/moderate storms (i.e. K_p from 5 to 6-) before and after. The whole $K_p > 4$ lasted 9 hours from 0600 to 1800 UT.

Table 5.9 shows the upper decile values of Doppler spreads of the day independent of occurrence time of the day. This means although the value may be high, it could possibly occur not at the same time as the active geomagnetic condition. Upper decile of Doppler spread in Table 5.9 were determined for daily value and not based on 3-hour K_p index because the number of cases could be too small to compute this value. Results presented in Table 5.9 show that Doppler spreads was not dependent on geomagnetic indices as the upper decile during geomagnetically disturbed days was a mixture of relatively low and high values.

The highest K_p index recorded on 5 April 2010 was preceded and followed by indices between 5 and 6-. However, Doppler spread availability during this period is very limited. Detailed observation on the Doppler spreads measured on this day on 6.95 and 8.01 MHz is shown in Figure 5.8. The maximum of Doppler spreads within this period only reached up to 2 Hz.

Table 5.9: Daily upper decile Doppler spread for each frequency during the days where $K_p \geq 5$ from 14 March 2009 to February 2011. Data was not available on 2 and 3 May 2010. Number of cases per day is in the brackets

Date	Doppler spread (upper decile) (Hz)					
	4.64 MHz	6.95 MHz	8.01 MHz	10.39 MHz	11.12 MHz	14.36 MHz
24 Jun 2009	- (0)	- (2)	- (3)	- (19)	- (0)	- (0)
22 Jul 2009	- (1)	- (6)	- (16)	- (20)	- (0)	- (0)
30 Aug 2009	- (3)	1.5 (86)	1 (30)	- (10)	- (1)	- (0)
5 Apr 2010	- (0)	2.5 (84)	3.5 (106)	- (9)	- (0)	- (0)
6 Apr 2010	- (0)	1.5 (104)	1.5 (90)	- (0)	- (0)	- (0)
12 Apr 2010	- (0)	2 (131)	2 (160)	- (1)	- (0)	- (0)
14 Apr 2010	- (0)	2 (154)	3.5 (279)	2.5 (46)	- (18)	- (0)
2 May 2010	no data					
3 May 2010	no data					
29 May 2010	- (0)	- (1)	1.5 (45)	- (20)	- (4)	- (11)
30 May 2010	- (0)	- (1)	1.5 (85)	- (22)	- (2)	- (3)
4 Jun 2010	- (0)	- (12)	2 (100)	1 (27)	- (0)	- (0)
3 Aug 2010	- (0)	- (0)	- (21)	- (6)	- (2)	- (17)
4 Aug 2010	- (0)	- (4)	1.5 (25)	- (1)	- (0)	- (2)
25 Aug 2010	- (0)	1.5 (100)	3 (280)	1.5 (58)	- (8)	- (0)
23 Oct 2010	- (0)	5.5 (442)	6 (342)	- (2)	6.5 (40)	- (0)
11 Nov 2010	- (0)	8 (455)	7 (257)	- (17)	4 (48)	- (9)
27 Nov 2010	- (1)	7 (352)	3 (61)	3.5 (26)	6 (45)	- (0)
7 Jan 2011	- (0)	3 (37)	4 (71)	- (0)	- (0)	- (0)
4 Feb 2011	- (1)	8 (172)	4 (118)	- (21)	3.5 (26)	- (4)
5 Feb 2011	- (8)	6 (224)	4.5 (110)	- (0)	- (0)	- (0)
14 Feb 2011	- (0)	6.5 (292)	5 (174)	5 (184)	4 (196)	6 (97)
18 Feb 2011	- (0)	8 (161)	6 (94)	- (22)	- (16)	- (0)

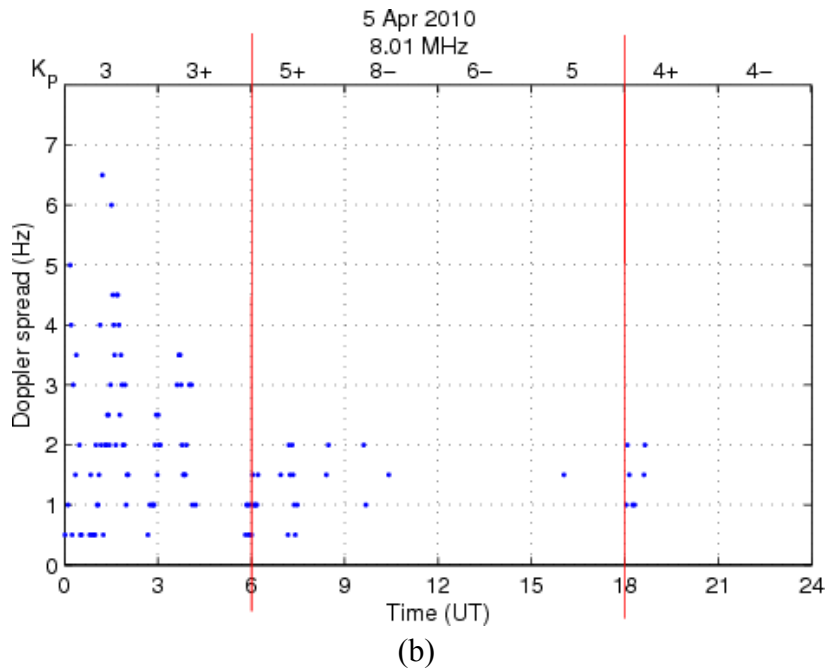
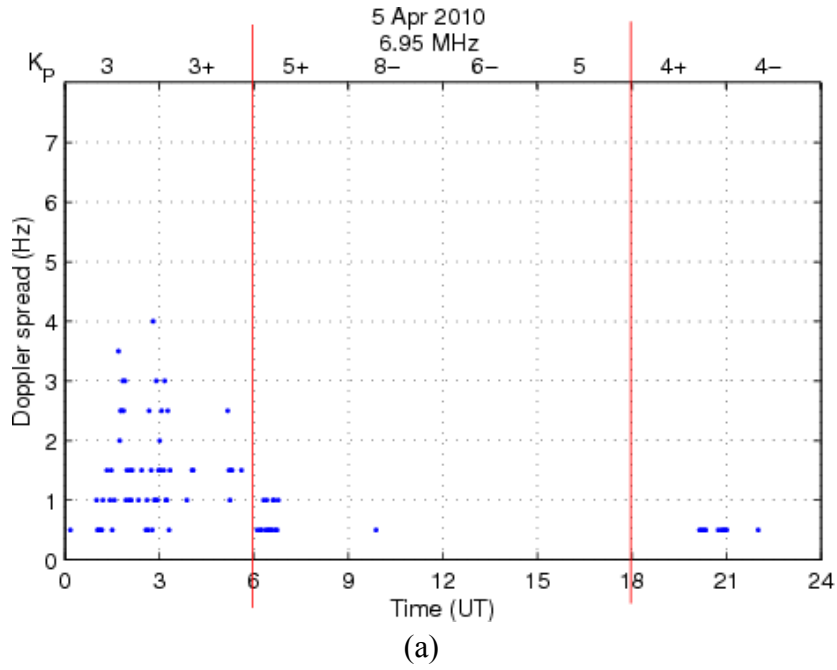


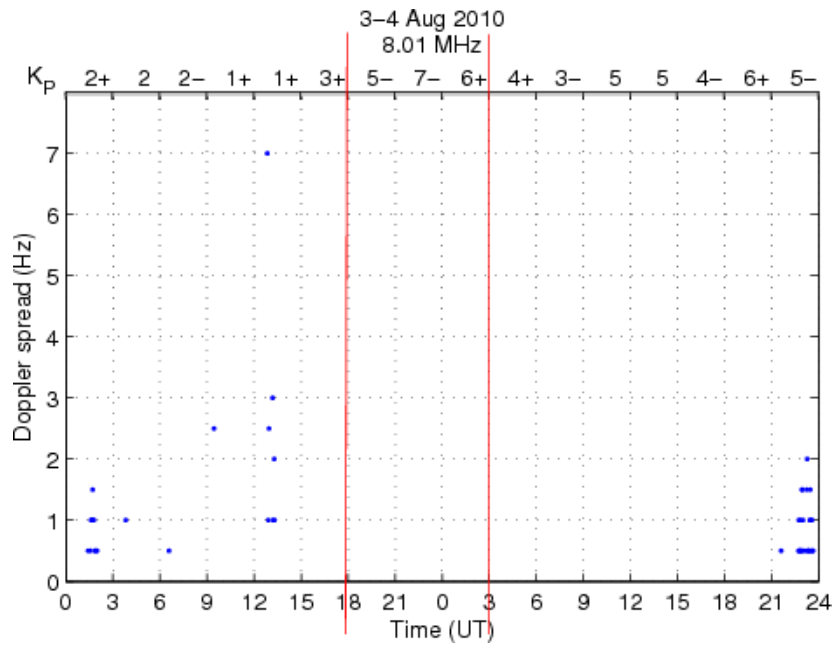
Figure 5.8: Doppler spreads on 5 April 2010 on (a) 6.95 MHz and (b) 8.01 MHz. The vertical lines represents the period where $K_p \geq 5$

The IMF components on this day are illustrated in Figure 4.19 while the variations of the magnetic data at Eureka and Resolute Bay are presented in Figure 4.20. IMF B_z component varied $\sim \pm 15$ nT during the period of observations from 0600 to 1200 UT.

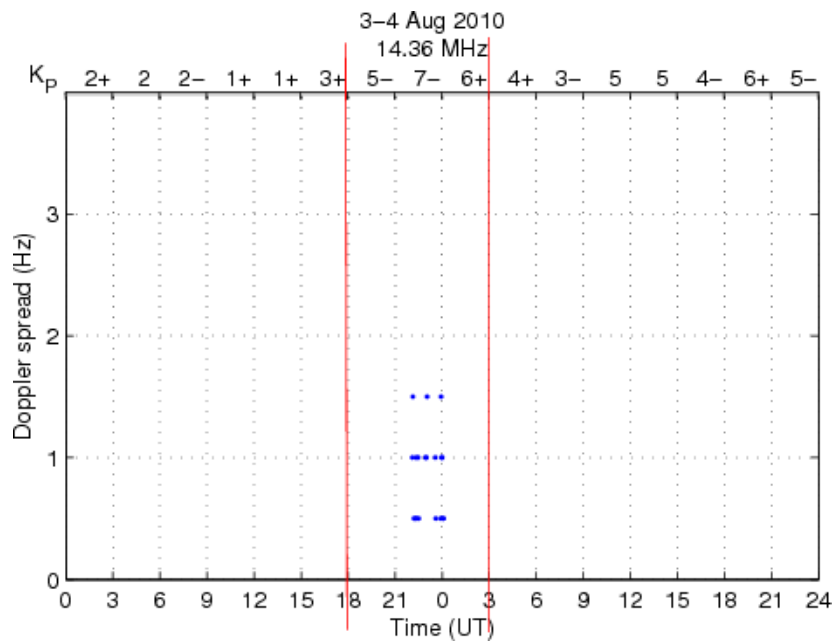
Each component of magnetic fields at both polar cap stations demonstrated large variations from its respective mean between 0500 and 1400 UT (for B_x), and between 0830 and 1800 UT (B_y). Meanwhile, B_z component at Resolute Bay showed large variations from its mean between 0900 and 1800 UT. B_z component at Eureka was relatively low compared to Resolute Bay but still reached up to ~ 180 nT.

Similar situation of low Doppler spreads was also observed during another high geomagnetic index occurrence on 3 and 4 August 2010. Doppler spreads availability on these days on any frequency were also very limited (refer Table 5.9). Doppler spreads on 6.95 and 14.36 MHz were shown in Figure 5.9, and the maximum of Doppler spreads only reached up to 2 Hz during the period of geomagnetic disturbances.

The IMF components on 3 August 2010 are shown in Figure 5.10 where all components started to vary from the background values from ~ 1800 UT, which where $K_p > 4$. Similar pattern can be observed on the magnetic data at Eureka and Resolute Bay where large variations of up to ± 500 nT can be registered during this period (Figure 5.11). Since the availability of Doppler spreads data were limited until the end of 3 August 2010 only, the magnetic field components on 4 August 2010 are not discussed.



(a)



(b)

Figure 5.9: Doppler spreads from 3 to 4 August 2010 on (a) 8.01 MHz and (b) 14.36 MHz. The vertical lines represents the period of interest where $K_p \geq 5$. Note that $K_p \geq 5$ also occurred at other times

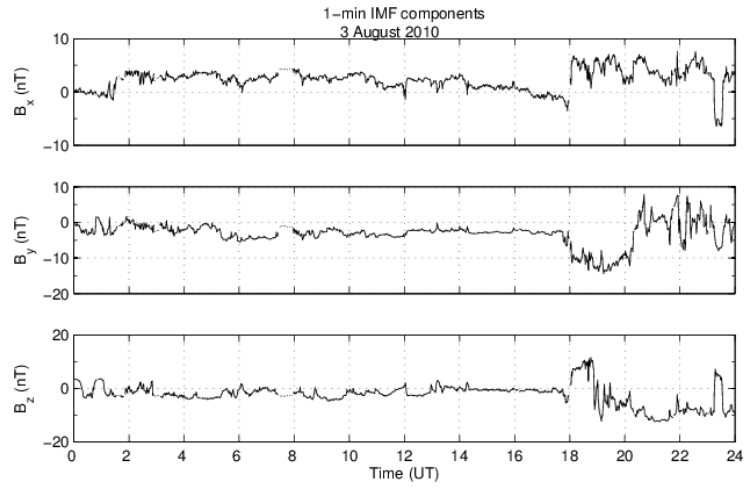
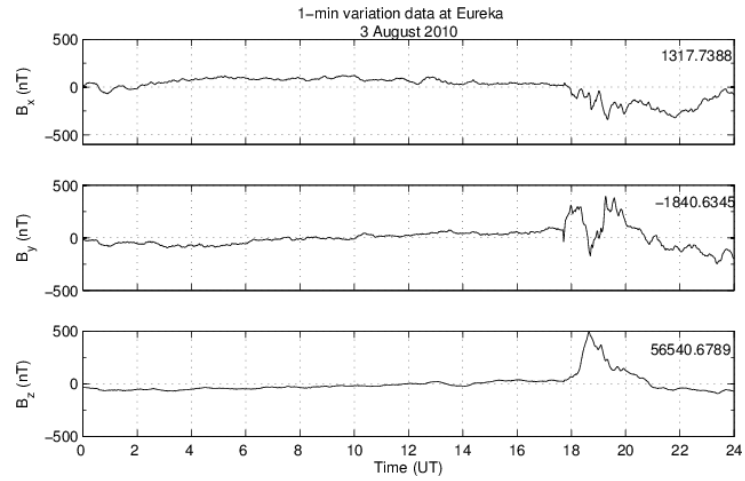
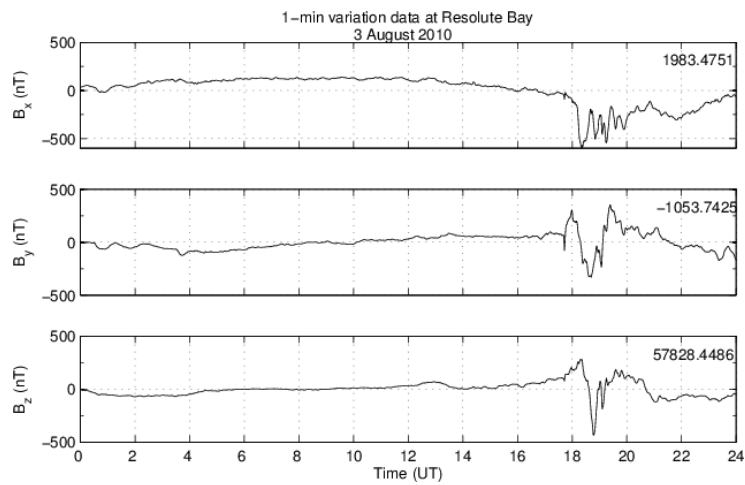


Figure 5.10: 1-minute IMF components on 3 August 2010



(a)



(b)

Figure 5.11: 1-minute variation data at (a) Eureka and (b) Resolute Bay on 3 August 2010

In another occasion on 4 and 5 February 2011 where K_p indices were between 5 and 6-, Doppler spreads were observed to reach up to 9.5 Hz on 6.95 and 8.01 MHz as presented in Figure 5.12 and Figure 5.13, respectively. However, the similar large Doppler spreads were also observed during the period of quiet geomagnetic conditions. The magnetic field variations of IMF and at Resolute Bay on 4 February 2011 are presented in Figure 5.14 and Figure 5.15, respectively. Magnetic field data for Eureka station were not available.

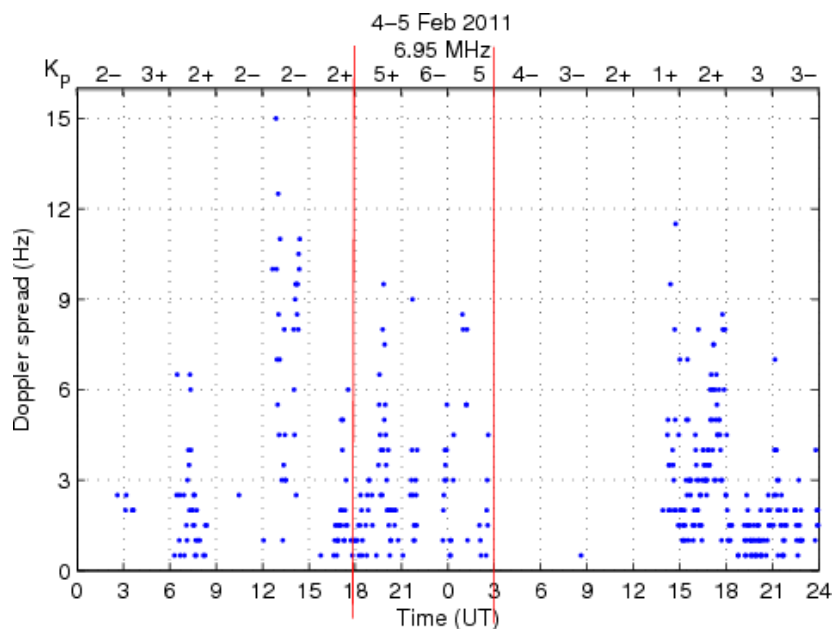


Figure 5.12: Doppler spreads from 4 to 5 February 2011 on 6.95 MHz. The vertical lines represents the period where $K_p \geq 5$

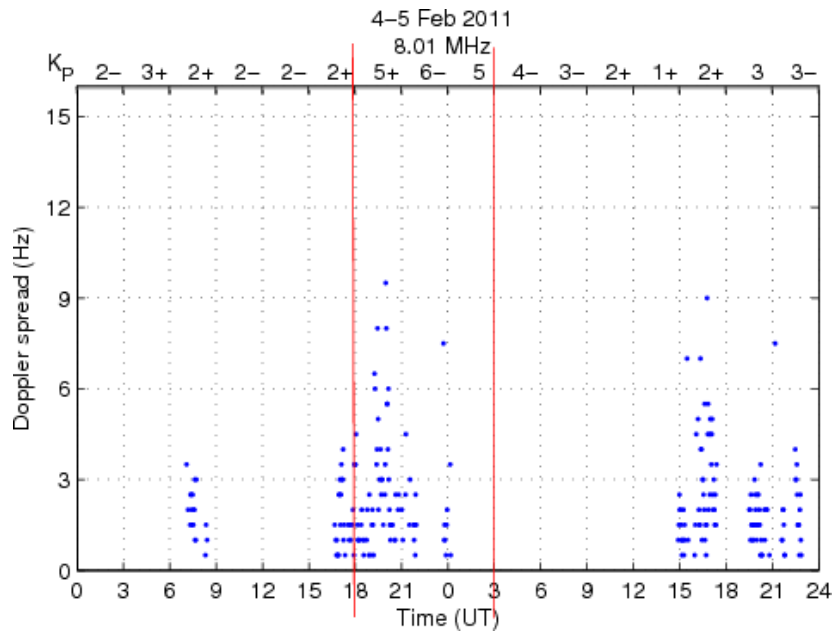


Figure 5.13: Doppler spreads from 4 to 5 February 2011 on 8.01 MHz. The vertical lines represents the period where $K_p \geq 5$

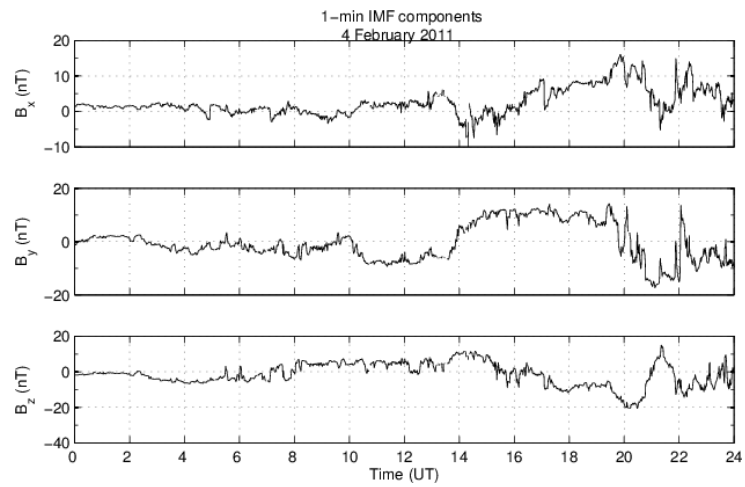


Figure 5.14: 1-minute IMF components on 4 February 2011

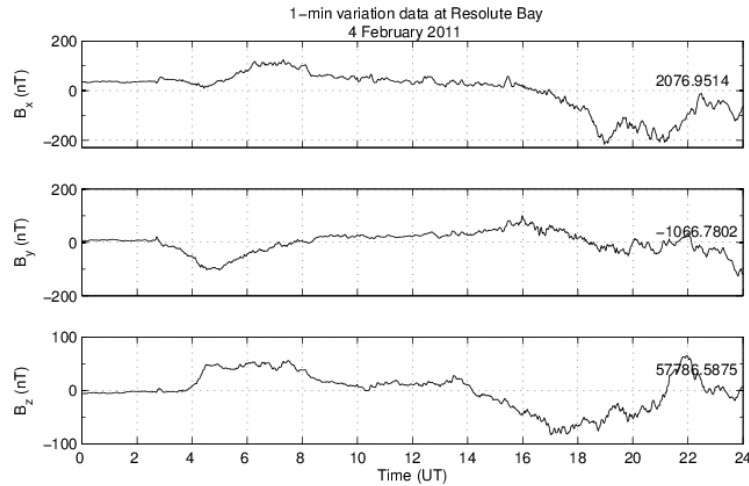


Figure 5.15: 1-minute variation data at Resolute Bay on 4 February 2011

Examples presented on 5 April 2010, 3-4 August 2010 and 4-5 February 2011 show that high geomagnetic conditions do not necessarily correlate with large Doppler spreads. *Jacobsen et al.* [2000] used ground-based magnetometer during magnetic disturbances and concluded that although several cases of good correspondence between increases on Doppler spread and magnetic variation, it cannot be registered at all times.

Meanwhile, *Broms et al.* [1997] studied the channel characteristics from 16 to 22 October 1995, which was the period of several ionospheric disturbances, over auroral zone from Harstad to Kiruna (194 km) and from Harstad to Tuentangen (1019 km), and concluded that in general, Doppler spreads and shifts were correlated to the level of ionospheric disturbances.

On the other hand, Doppler spreads generally shows increases with the increase of solar activities, as discussed in previous section. Upper decile of Doppler spreads was between 1 and 3.5 Hz from 24 Jun 2009 to 25 August 2010. Meanwhile it varied

from 3 to 8 Hz from 23 October 2010 onwards. Example on 4 and 5 February 2011 (Figure 5.13) clearly shows the increases in Doppler spreads regardless of geomagnetic conditions, whereas disturbed ionosphere on 5 April 2010 and from 3 to 4 August 2010 (Figure 5.8 and Figure 5.9) did not cause increases in Doppler spreads.

5.3 Concluding Remarks

The statistical analysis of Doppler spreads on all six frequencies for the data from March 2009 to February 2011 has been discussed in this chapter. Doppler spread was mostly less than ~5 Hz and rarely exceeded 15 Hz. Lower decile on any frequency never exceeded 1 Hz. Doppler spread median was between 0.5 to 1.5 Hz, except on several months where it reached between 2 and 3 Hz. Upper decile values showed more variability from 1-1.5 to 5.5 Hz, except on the lowest (where it maximised at only 3 Hz) and highest frequencies (where it maximised at 6.5 Hz on October 2009).

In general, large upper decile values normally occurred from around September/October to February/March between 0000 and 1700 UT on 6.95 and 8.01 MHz. The values of upper decile in an hour can reach up to 5.5-9 Hz (6.95 MHz) and 6-9.5 Hz (8.01 MHz). The increase of the upper decile of Doppler spread did not correspond to the increase of the frequency.

In general, Doppler spreads were increasing with the increase in solar activity, except on 10.39 MHz. Larger upper decile of Doppler spread of up to 4.5 Hz difference

were measured on 6.95, 8.01 and 11.12 MHz during the second half of the observation periods from September to January, than during the same months of the first year of observations.

However, disturbed ionosphere does not necessarily correlate with large Doppler spreads. Observations on 4 February 2011 from 1800 UT until the end of the day where K_p indices were between 5+ and 6- showed Doppler spreads can reach up to 9.5 Hz on 6.95 MHz (Table 5.10). However, higher geomagnetic indices on 5 April 2010 and 3 August 2010 corresponded to small Doppler spread of only up to 2 Hz. In addition, large Doppler spreads on 4 February 2011 were also registered during the period of quiet geomagnetic conditions.

Table 5.10: No. of Doppler spread data, the maximum Doppler spread during a specified 6-hour period for every case of $K_p > 4$

Date	Period	K_p	No. of Doppler spreads data	Max. Doppler spreads	Frequency (MHz)
5 Apr 2010	0600-1200	5+, 8-	21	2.00	8.01
3 Aug 2010	1800-0000	5-, 7-	17	1.50	14.34
4 Feb 2011	1800-0000	5+, 6-	73	9.50	6.95

Table 5.11 and Table 5.12 present the minimum and maximum values of all IMF components and also the variations of the magnetic field data at Eureka and Resolute Bay for the cases of $K_p > 4$. The IMF B_z components tended to give out the largest values for both minimum and maximum readings compared to the other two components, except on two occasions. No correlation can be found between the reading of magnetic fields at both stations and also of IMF, and the magnitude of the geomagnetic indices. For example, the highest K_p was on 5 April 2010 but the largest

magnitude of the minimum values of all magnetic field components was on 3 August 2010. Similarly, no correlation can be found between the intensity of the Doppler spreads and the magnitude of the magnetic field components, either the IMF or the local field. Polarities of the magnetic components (see Table 5.13) also did not demonstrate any relation to either the strength of the geomagnetic indices or the intensities of the Doppler spreads.

Table 5.11: Minimum value of each magnetic component of IMF, Eureka (EUA) and Resolute Bay (RES) for every case of $K_p > 4$ during a specified 6-hour period

Date	Period	Min. IMF			Min. EUA			Min. RES		
		B _x	B _y	B _z	B _x	B _y	B _z	B _x	B _y	B _z
5 Apr 2010	0600-1200	-6.1	-15.1	-15.0	-100.4	-95.9	-67.2	-121.2	-164.6	-108.8
3 Aug 2010	1800-0000	-6.4	-14.4	-12.5	-340.1	-247.5	-91.0	-610.5	-331.8	-435.2
4 Feb 2011	1800-0000	-5.3	-17.3	-20.6	n/a	n/a	n/a	-216.5	-126.9	-75.8

Table 5.12: Maximum value of each magnetic component of IMF, Eureka (EUA) and Resolute Bay (RES) for every case of $K_p > 4$ during a specified 6-hour period

Date	Period	Max. IMF			Max. EUA			Max. RES		
		B _x	B _y	B _z	B _x	B _y	B _z	B _x	B _y	B _z
5 Apr 2010	0600-1200	10.7	11.3	18.9	332.3	480.9	129.2	321.3	304.7	459.4
3 Aug 2010	1800-0000	7.7	7.8	11.6	-16.3	395.6	493.3	-40.8	351.3	282.7
4 Feb 2011	1800-0000	16.1	14.2	15.0	n/a	n/a	n/a	-11.0	32.6	65.6

Table 5.13: Percentage of positive polarity of each magnetic component of IMF, Eureka (EUA) and Resolute Bay (RES) for every case of $K_p > 4$ during a specified 6-hour period

Date	Period	IMF +ve (%)			EUA +ve (%)			RES +ve (%)		
		B _x	B _y	B _z	B _x	B _y	B _z	B _x	B _y	B _z
5 Apr 2010	0600-1200	90.0	15.8	57.6	90.0	32.7	44.9	90.0	43.2	51.2
3 Aug 2010	1800-0000	92.8	30.2	21.3	0.0	42.7	47.9	0.0	45.7	36.6
4 Feb 2011	1800-0000	94.7	38.0	18.6	n/a	n/a	n/a	0.0	21.9	33.5

Chapter Six: HF Link and Its Relations to Transionospheric Link

Selected events of Doppler spreads during the period of observations from March 2009 to February 2011 will be discussed in this chapter. Data from GISTM receivers at Alert and Svalbard (Ny-Ålesund and Longyearbyen) will also be used if available. Both sources of data (HF and transionospheric links) were overlapping from March 2009 to July 2010. Information of the geomagnetic conditions, IMF components, and geomagnetic field components at polar cap stations at Eureka and Resolute Bay will be utilised too.

6.1 Selected Events

This section will discuss selected events of Doppler spreads. These events will also include discussion on ionospheric variability detected by transionospheric means around the midpoint of HF link. Results from the dual-frequency GPS receivers at Alert and Svalbard (Ny-Ålesund and Longyearbyen) around the reflection point will be used when available. Table 6.1 gives the description for each event type used in this section.

Table 6.1: Description of each event type

Event Type	Description
B1	$K_p > 4$, Doppler spreads, TEC and scintillation variations
B2	TEC increase/decrease and/or σ_ϕ increase and/or Doppler spreads
B3	large TEC fluctuation and/or Doppler spreads
B4	Doppler spreads and no TEC and scintillation variations

Event Type B1

Event Type B1 discusses the Doppler spreads dependence on geomagnetic conditions and its relation with TEC variations and scintillation parameters around HF midpoint. The first event presented here is on 4 February 2011 from 1800 UT until 0300 UT on 5 February 2011 with K_p between 5 and 6-. This event was discussed in Chapter Five and Doppler spreads plots on 6.95 and 8.01 MHz during these two days were presented in Figure 5.12 and Figure 5.13, respectively. As discussed in Chapter Five, there were few large Doppler spreads during these hours. However, Doppler spreads were also large outside the period of geomagnetically disturbed ionosphere.

Figure 6.1 shows slant TEC and σ_ϕ of PRN21 observed over Ny-Ålesund from 1600 to 2200 UT on 4 February 2011 where $K_p > 4$ from 1800 UT until 0300 UT the following day. PRN21 was the closest satellite to HF midpoint between 1730 UT and 1930 UT. Paths of all visible satellites from 1800 UT to 1959 UT at ionospheric pierce point of 350 km of over Ny-Ålesund are illustrated in Figure 6.2. Slant TEC observed on PRN21 was fluctuating ~ 3 TECU from ~ 1830 UT until the end of satellite visibility at ~ 1930 UT. Phase scintillations reached ~ 0.17 rad around 1915 UT.

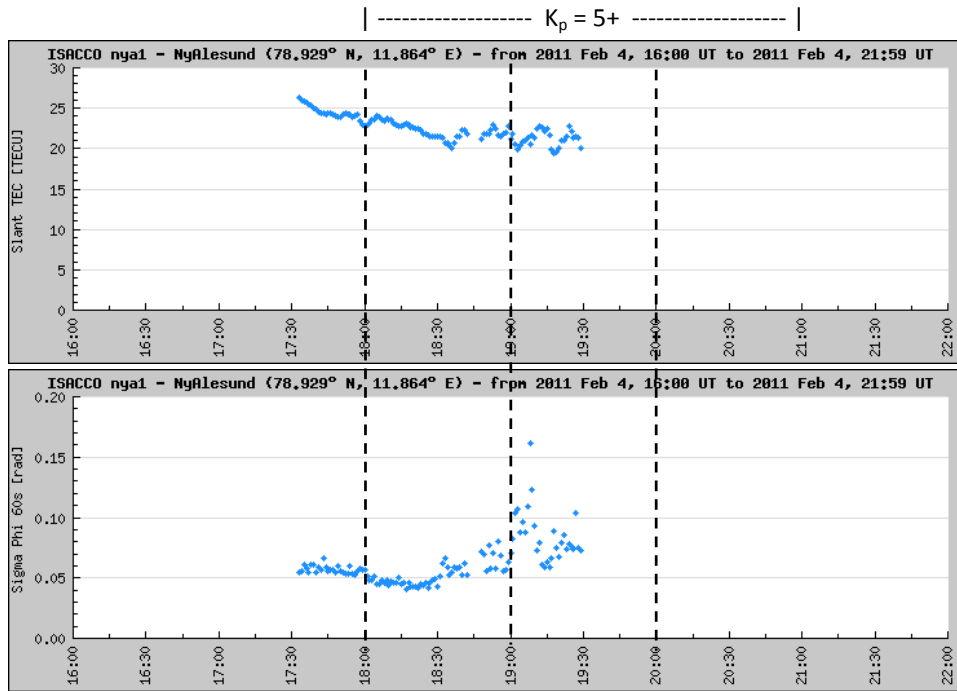


Figure 6.1: Slant TEC (top) and σ_ϕ (bottom) of PRN21 over Ny-Ålesund from 1600 to 2200 UT on 4 February 2011. The vertical lines indicates the period of interest where $K_p \geq 5$

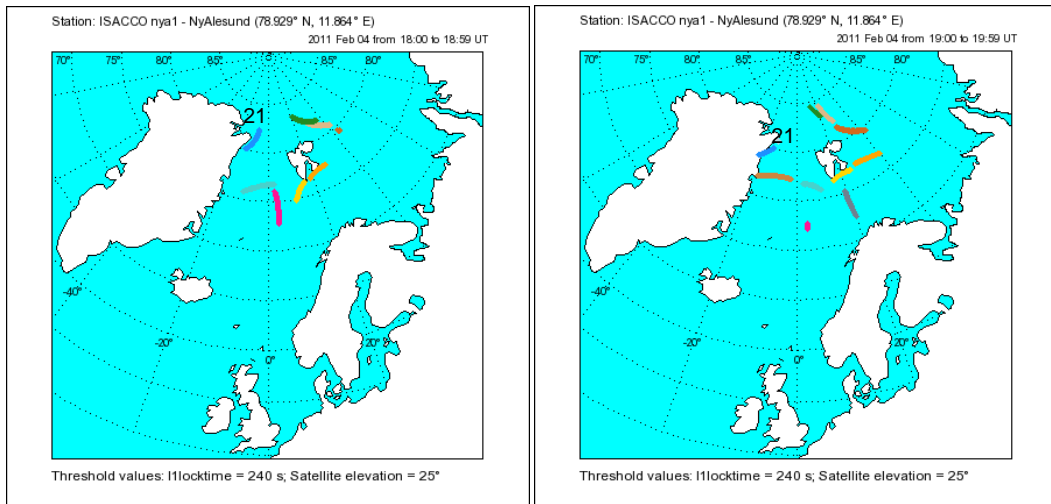


Figure 6.2: Colour-coded satellites path over Ny-Ålesund at 350 km on 4 February 2011 from 1800 to 1859 UT (left) and from 1900 to 1959 UT (right). The number denotes specific satellite number and also marks the beginning of the path

TEC variation and phase scintillations of PRN21 over Longyearbyen between 1600 UT and 2200 UT are shown in Figure 6.3. TEC fluctuated during the whole period when PRN21 was visible over Longyearbyen, which started 30 minutes earlier than the beginning of the disturbed ionosphere. σ_ϕ increased ~1850-1920 UT and reached ~0.32 rad. Paths of all visible satellites from 1800 UT to 1959 UT over Longyearbyen are illustrated in Figure 6.4.

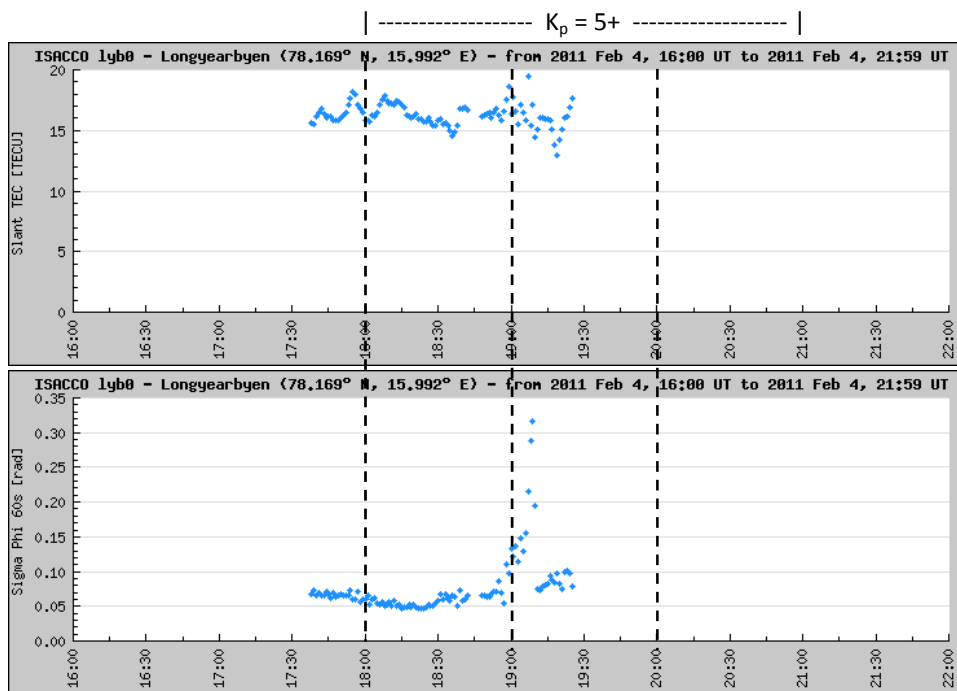


Figure 6.3: Slant TEC (top) and σ_ϕ (bottom) of PRN21 over Longyearbyen from 1600 to 2200 UT on 4 February 2011. The vertical lines indicates the period of interest where $K_p \geq 5$

Longyearbyen is located farther than Ny-Ålesund from the HF midpoint, therefore the path of PRN21 is also farther from the midpoint. Since the path orientations of all satellites are similar above Ny-Ålesund and Longyearbyen with only slight different in the distance from midpoint, only the paths over Ny-Ålesund will be shown in the

discussion of the following events. All plots regarding the GISTM receivers at Longyearbyen and Ny-Ålesund are generated from INGV website (<http://www.eswua.ingv.it>).

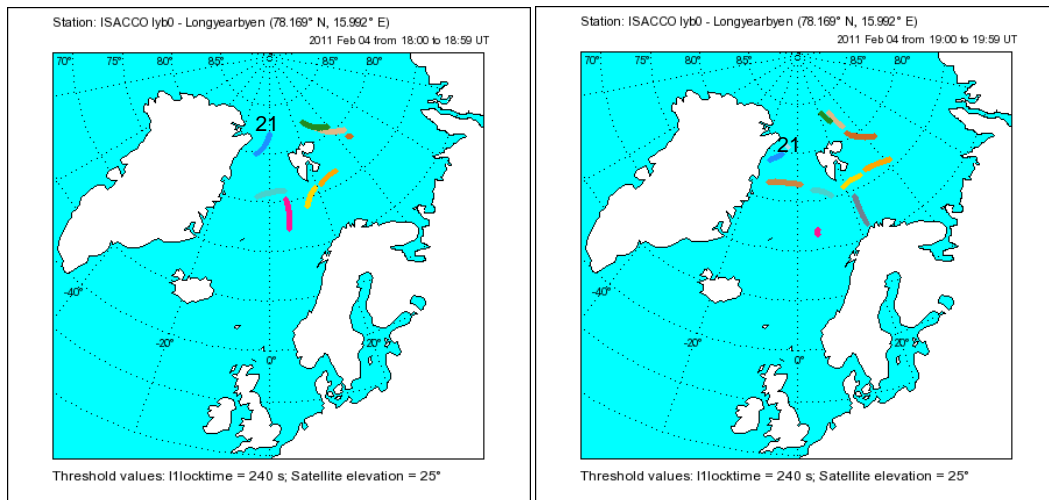


Figure 6.4: Colour-coded satellites path over Longyearbyen at 350 km on 4 February 2011 from 1800 to 1859 UT (left) and from 1900 to 1959 UT (right). The number denotes specific satellite number and also marks the beginning of the path.

Figure 6.5 and Figure 6.6 show Doppler spreads and SNR on 4 February 2011 from 1600 UT to 2200 UT on 6.95 MHz and 8.01 MHz, respectively. Doppler spreads between 1800 and 1900 UT were < 5 Hz, which corresponded to the less variable TEC and σ_{ϕ} on PRN21 during the same periods. Several larger Doppler spreads were observed in the following hour, earlier on 8.01 MHz than on 6.95 MHz. These coincided with the increasing TEC variations and phase scintillations on PRN21.

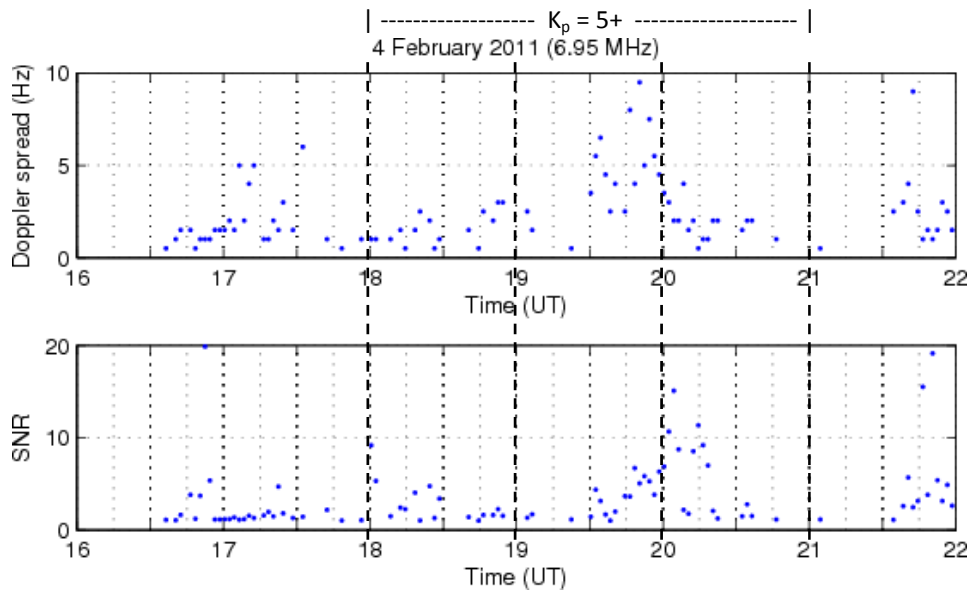


Figure 6.5: Doppler spread (top) and SNR (bottom) on 6.95 MHz from 1600 to 2200 UT on 4 February 2011. The vertical lines indicates the period of interest where $K_p \geq 5$

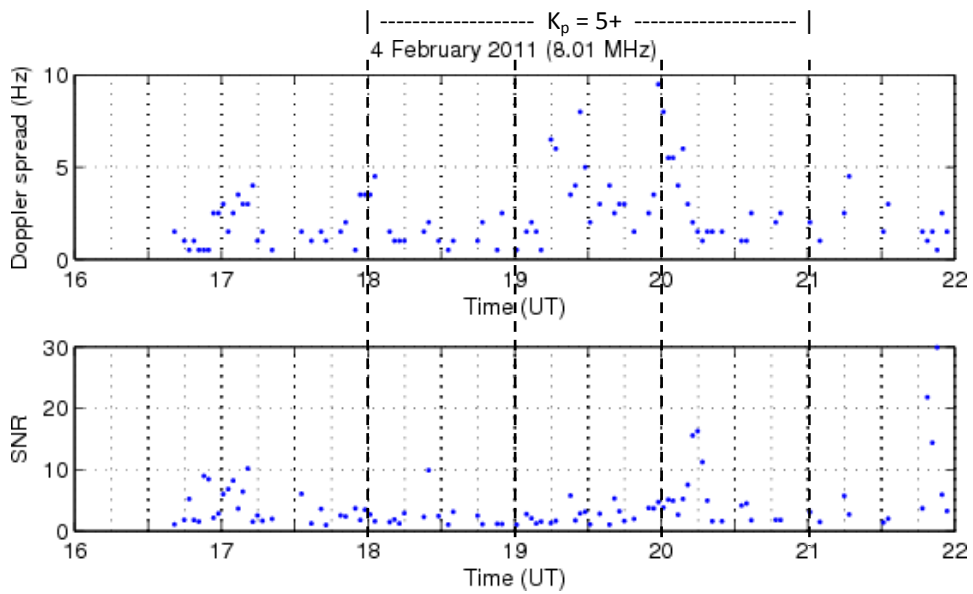


Figure 6.6: Doppler spread (top) and SNR (bottom) on 8.01 MHz from 1600 to 2200 UT on 4 February 2011. The vertical lines indicates the period of interest where $K_p \geq 5$

Figure 6.7 shows selected delay-Doppler spectra between 1900 and 2000 UT on 4 February 2011 as observed on 6.95 MHz. These spectra are chosen based on the strength of the received signal and also the intensity of the Doppler spreads. The Doppler spreads shown in Figure 6.7 varied from 5.5 to 9.5 Hz.

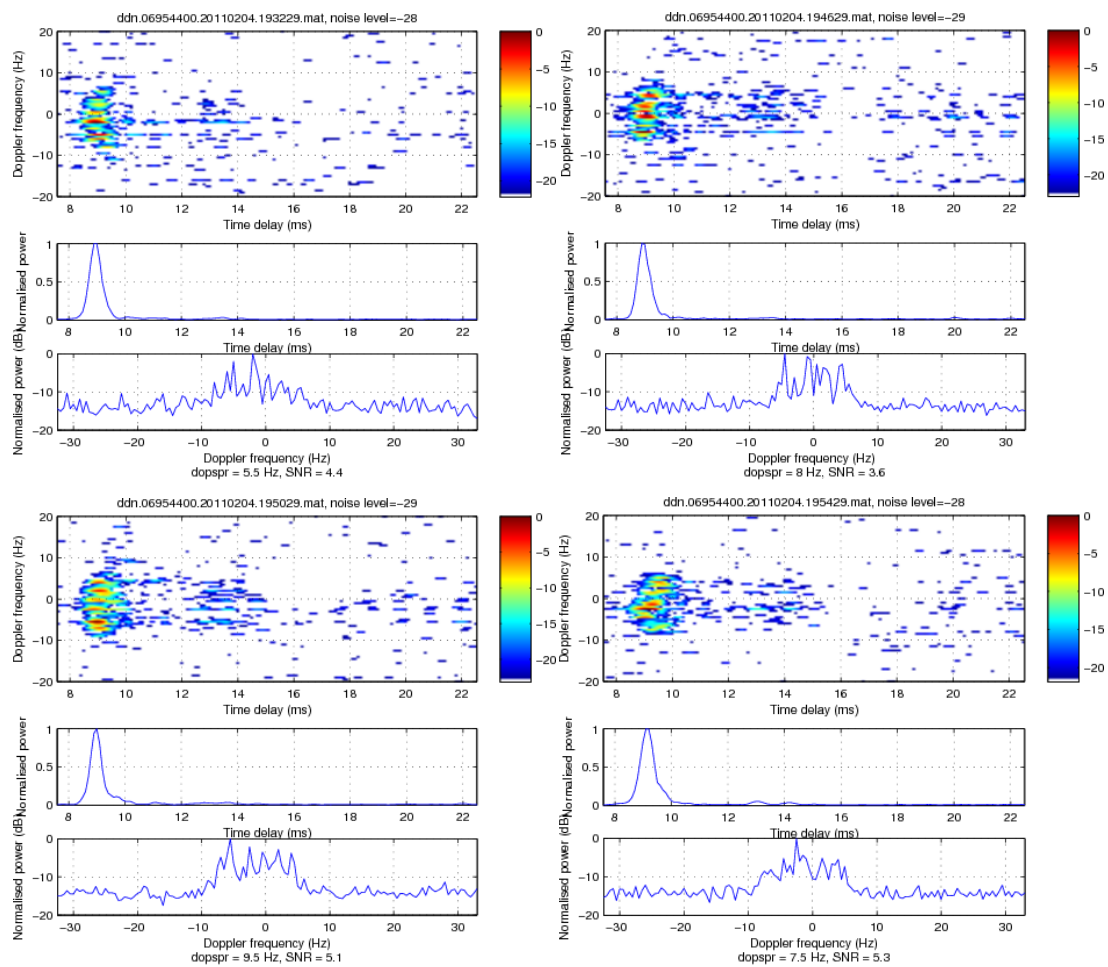


Figure 6.7: Selected delay-Doppler spectra on 6.95 MHz between 1900 and 2000 UT on 4 February 2011

Doppler spreads from 2000 UT to 2200 UT were mostly < 5 Hz, with few exceptions on 8.01 MHz at ~ 2000 UT. One large Doppler spread was observed on 6.95 MHz during this period but the signal was weak. In contrast, there were large TEC

fluctuations of up to ~ 8 TECU and also σ_ϕ increases up to ~ 0.17 rad on PRN18 and PRN22 during this period as observed on both GISTM receivers at Svalbard (refer Figure 6.8 and Figure 6.9). Paths of all visible satellites over Ny-Ålesund between 2000 and 2159 UT are illustrated in Figure 6.10.

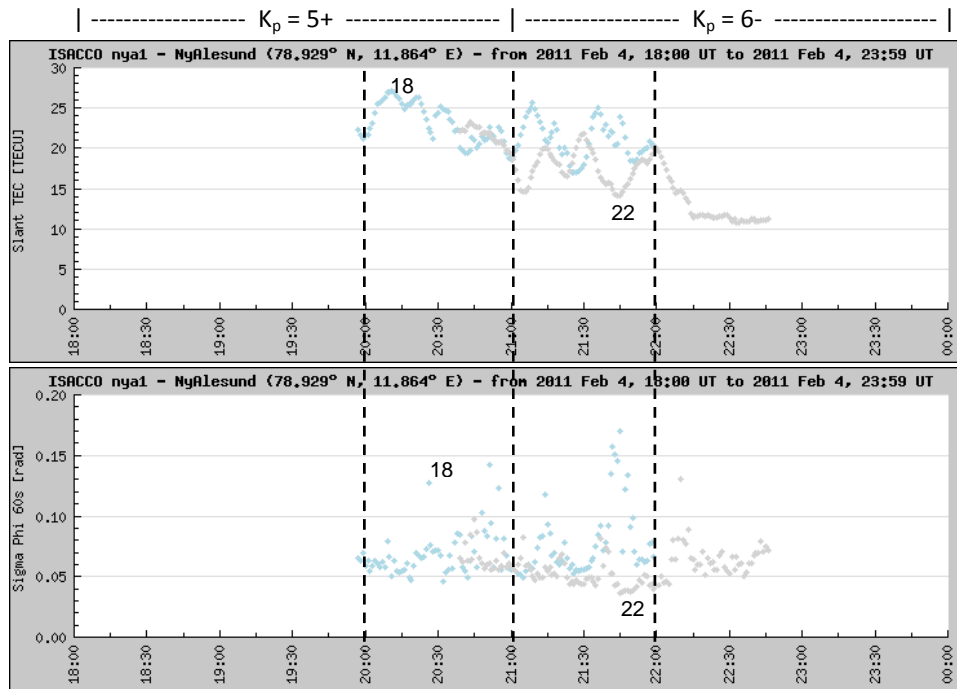


Figure 6.8: Slant TEC (top) and σ_ϕ (bottom) of PRN18 and PRN22 over Ny-Ålesund from 1800 to 0000 UT on 4 February 2011. The vertical lines indicates the period of interest where $K_p \geq 5$

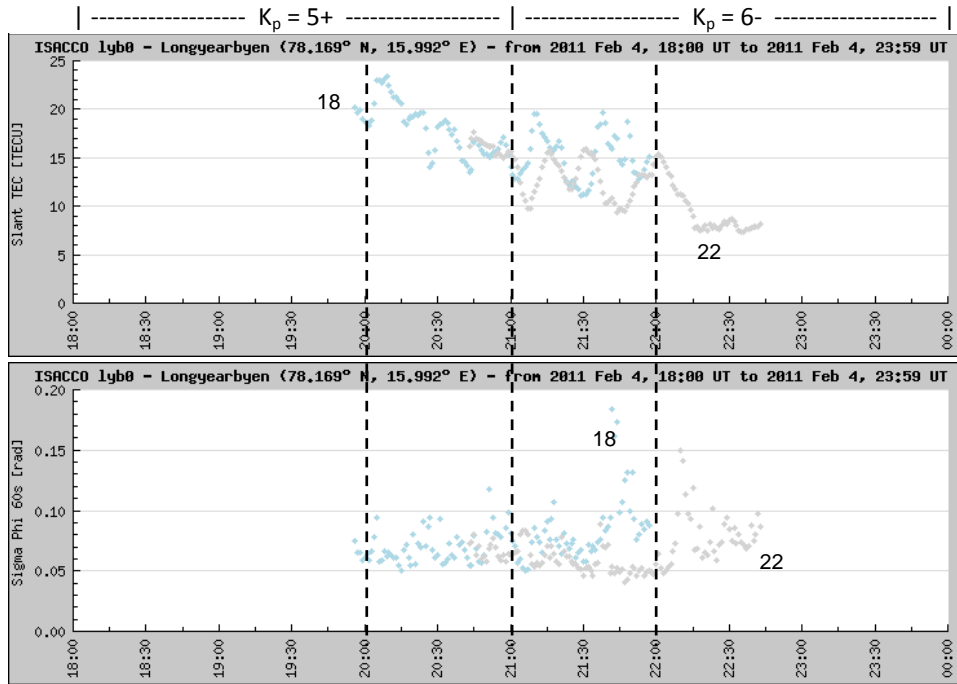


Figure 6.9: Slant TEC (top) and σ_{ϕ} (bottom) of PRN18 and PRN22 over Longyearbyen from 1800 to 0000 UT on 4 February 2011. The vertical lines indicates the period of interest where $K_p \geq 5$

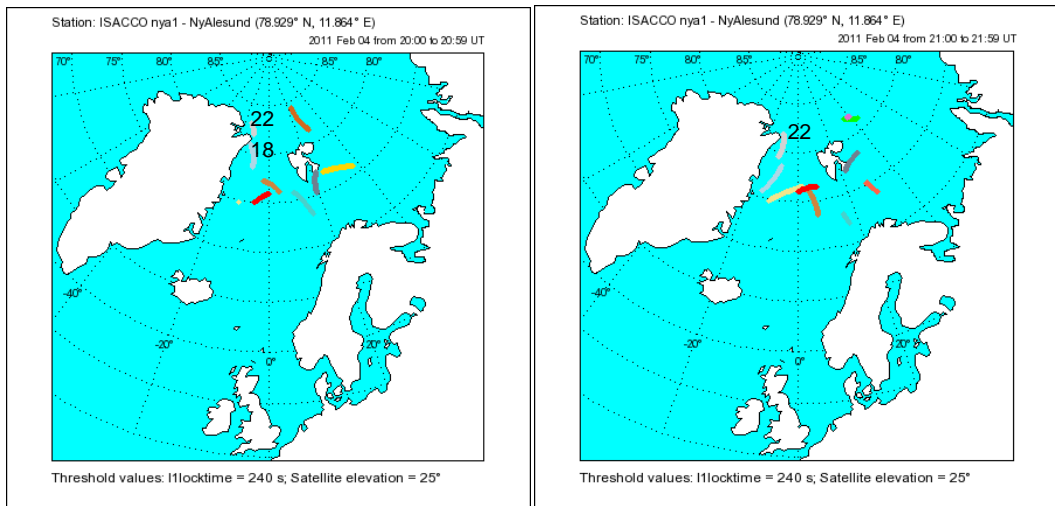


Figure 6.10: Colour-coded satellites path over Ny-Ålesund at 350 km on 4 February 2011 from 2000 to 2059 UT (left) and from 2100 to 2159 UT (right)

In the following time frame, PRN14 observed over Ny-Ålesund and Longyearbyen showed only a small long-period TEC increase between 2200 and 2359 UT as illustrated in Figure 6.11 and Figure 6.12, respectively. Paths of all visible satellites during this period are shown in Figure 6.13. Doppler spreads on 6.95 and 8.01 MHz of the same time frame as in Figure 6.11 and Figure 6.12 are shown in Figure 6.14 and Figure 6.15, respectively. Limited number of data of detectable Doppler spreads was observed between 2200 and 2359 UT and mostly less than 5 Hz. Doppler spreads on other frequencies are not shown here because of lack of meaningful data during this period.

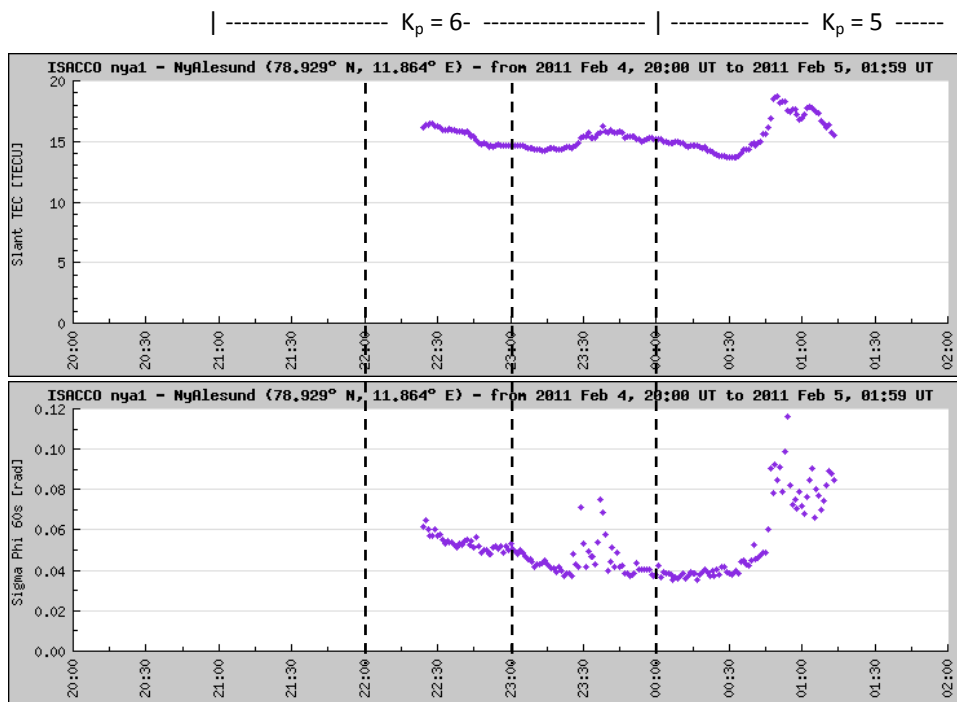


Figure 6.11: Slant TEC (top) and σ_ϕ (bottom) of PRN14 over Ny-Ålesund from 2000 UT on 4 February 2011 to 0200 UT on 5 February 2011. The vertical lines indicates the period of interest where $K_p \geq 5$

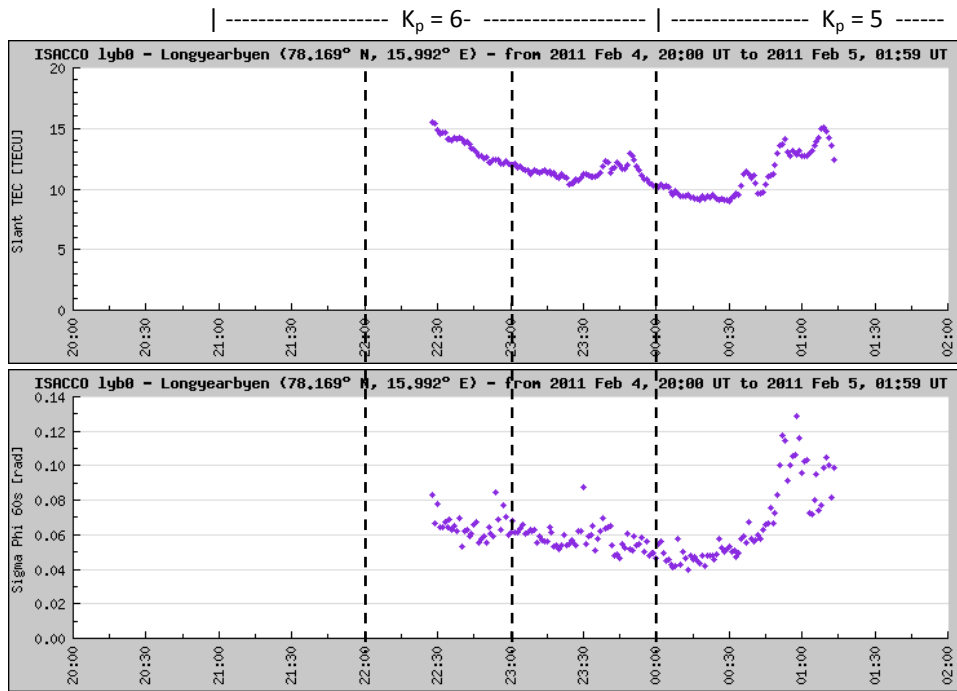


Figure 6.12: Slant TEC (top) and σ_ϕ (bottom) of PRN14 over Longyearbyen from 2000 UT on 4 February 2011 to 0200 UT on 5 February 2011. The vertical lines indicates the period of interest where $K_p \geq 5$

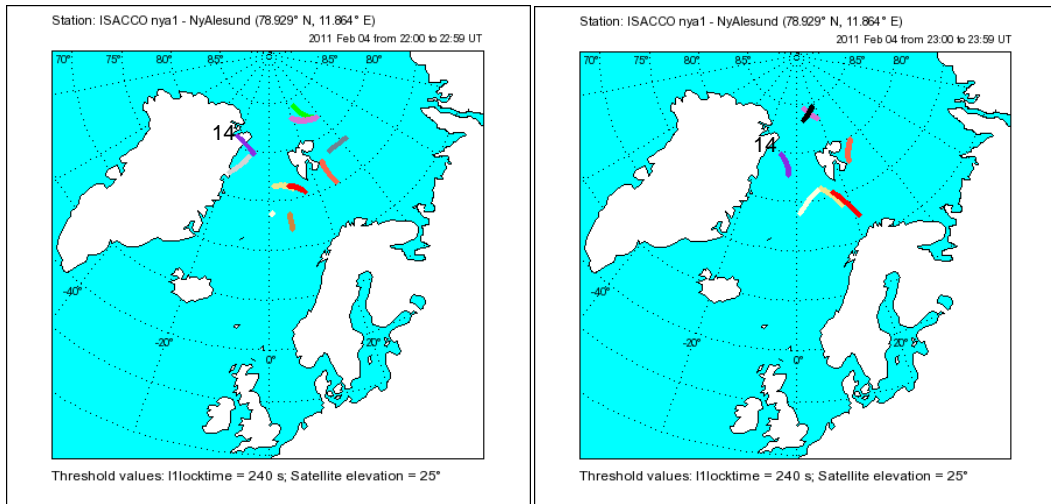


Figure 6.13: Colour-coded satellites path over Ny-Ålesund at 350 km on 4 February 2011 from 2200 to 2259 UT (left) and from 2300 to 2359 UT (right)

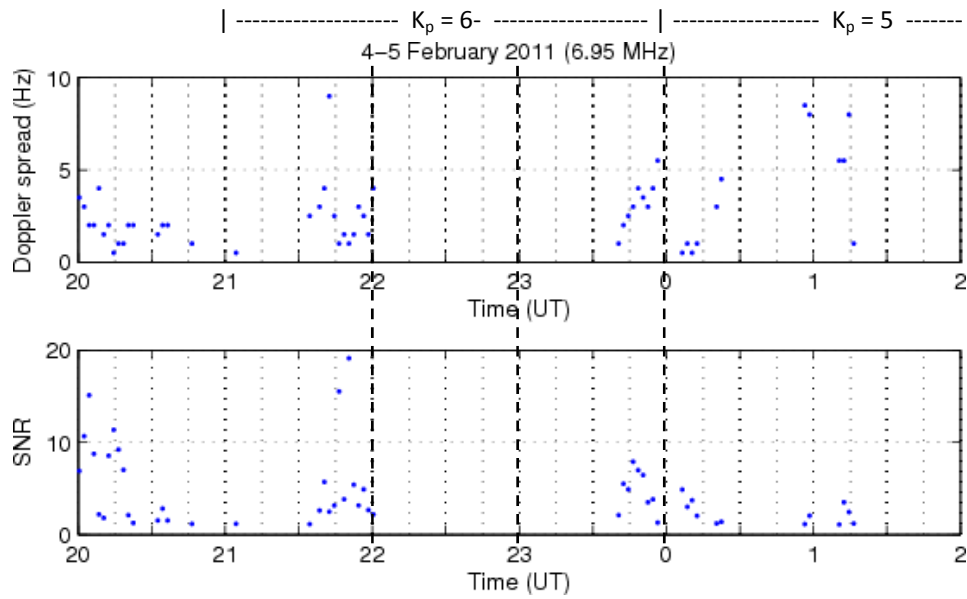


Figure 6.14: Doppler spread (top) and SNR (bottom) on 6.95 MHz from 2000 UT on 4 February 2011 to 0200 UT on 5 February 2011. The vertical lines indicates the period of interest where $K_p \geq 5$

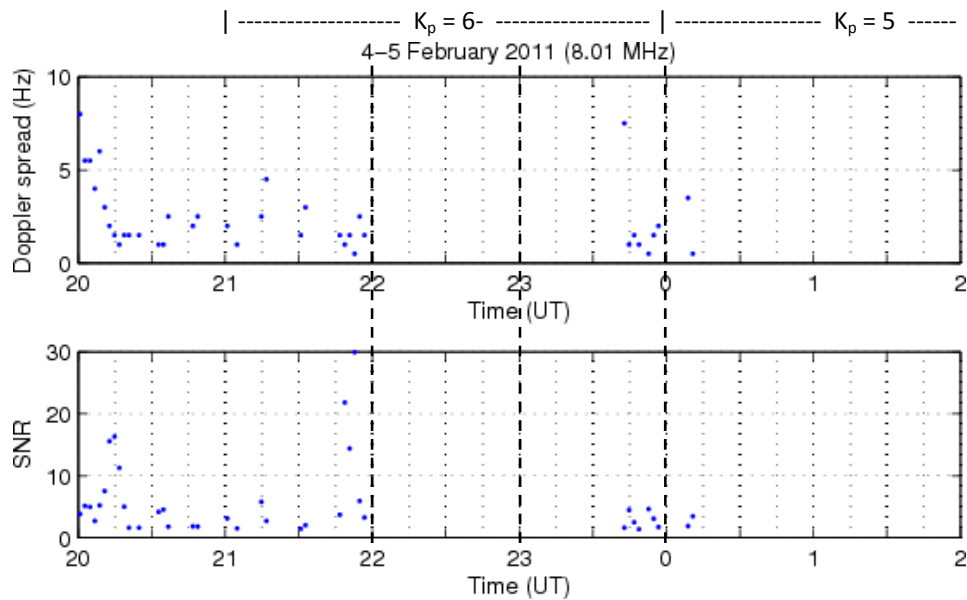


Figure 6.15: Doppler spread (top) and SNR (bottom) on 8.01 MHz from 2000 UT on 4 February 2011 to 0200 UT on 5 February 2011. The vertical lines indicates the period of interest where $K_p \geq 5$

Figure 6.16 and Figure 6.17 illustrate slant TEC and σ_ϕ of all visible satellites from 1800 UT to 2359 UT, over Ny-Ålesund and Longyearbyen, respectively. TEC fluctuation of up to ~ 7 TECU can be seen on most satellites especially between 1830 UT and 2230 UT. Increases in σ_ϕ were also observed during 1830-1930 UT, 2030-2230 UT, and 2330-2359 UT. At other times during the period of disturbed ionosphere until 0300 UT on 5 February 2011, slant TEC mostly shown less variations from the background values. Smaller TEC fluctuations of up to ~ 3 TECU were observed from 0300 to 0559 UT. These were during $K_p = 4+$. The limited number of data showed small Doppler spreads on both frequencies between 0000 and 0200 UT, except from ~ 0100 to ~ 0130 UT on 6.95 MHz, but these coming from weak signals (refer Figure 6.14 and Figure 6.15). The discussion here is limited until at the end of 4 February 2011 only in order to follow the 6-hour period of observations in the following case.

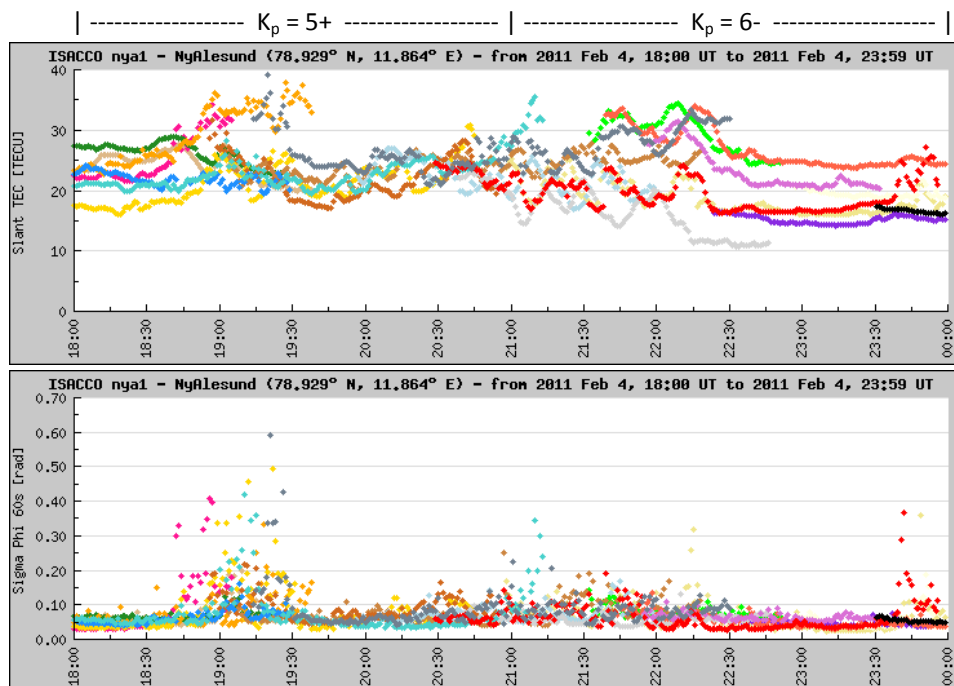


Figure 6.16: Slant TEC (top) and σ_ϕ (bottom) of all visible satellites over Ny-Ålesund from 1800 UT to 2359 UT on 4 February 2011

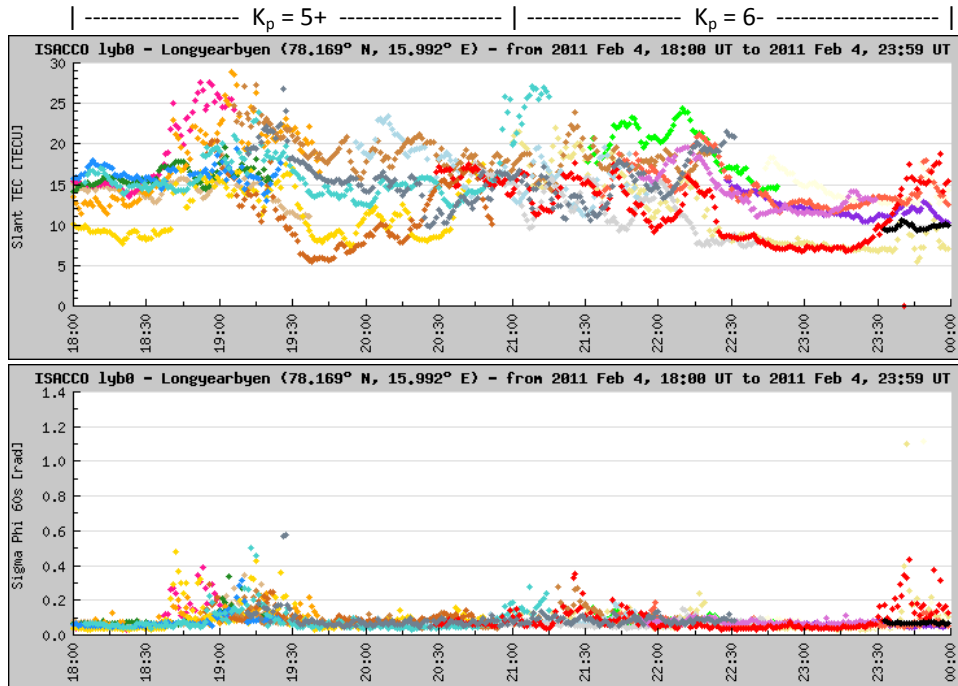


Figure 6.17: Slant TEC (top) and σ_ϕ (bottom) of all visible satellites over Longyearbyen from 1800 UT to 2359 UT on 4 February 2011

Event discussed here is an example of no direct correlation between geomagnetic conditions and Doppler spreads. Large Doppler spreads were found to occur at various times regardless of geomagnetic conditions during several hours on 4 and 5 February 2011 where these hours were during both quiet and disturbed ionosphere. No correlation was also found between geomagnetic conditions and both slant TEC and phase scintillations as has been discussed in Chapter Four. 4 and 5 February 2011 are outside the observation periods of GISTM receiver at Alert, therefore comparison is done using Svalbard's receivers only.

IMF B_z component was mostly northward from 1200 UT on 4 February 2011 until \sim 1500 UT and switched polarity and remained southward until \sim 2100 UT. After that, it fluctuated between polarities up to $\sim\pm 15$ nT (Figure 6.18). Meanwhile, Figure 6.19

illustrates the variation data of each northward, eastward, and vertical downward magnetic field at a polar cap station at Resolute Bay. B_x component varied up to ~ 200 nT from its mean value, B_y up to ~ 100 nT while B_z reached $\sim \pm 100$ nT during the period of observations. Magnetic data at Eureka station was not available during the observed period.

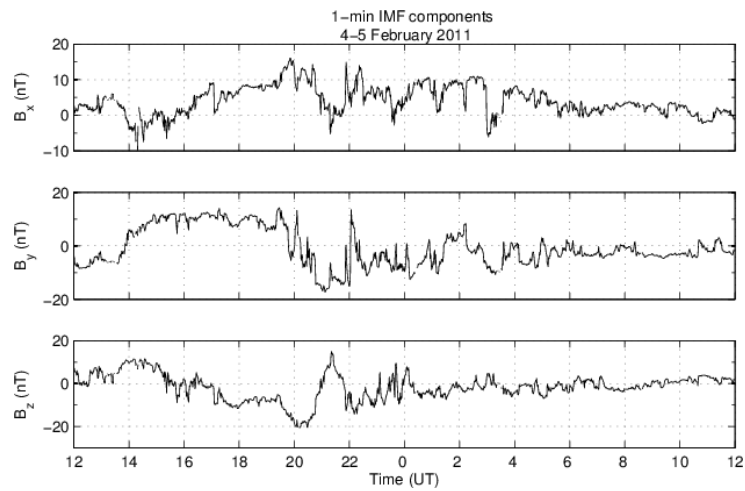


Figure 6.18: 1-minute IMF components from 1200 UT on 4 February 2011 to 1200 UT on 5 February 2011

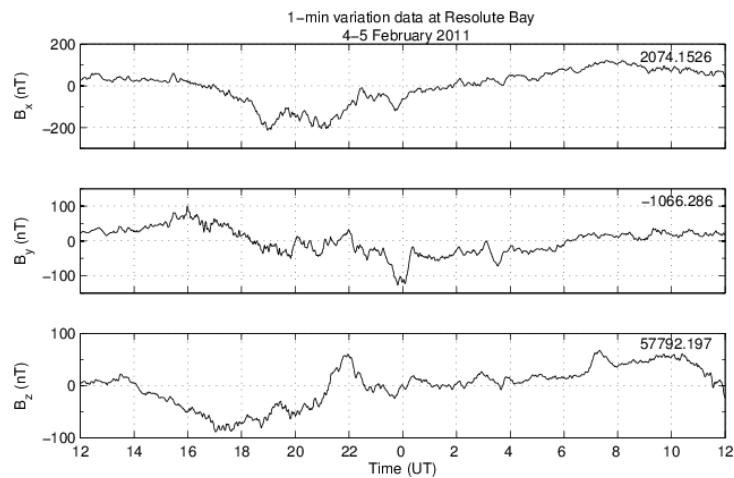


Figure 6.19: 1-minute variation data at Resolute Bay from 1200 UT on 4 February 2011 to 1200 UT on 5 February 2011. The number at the top right of each frame is the mean of its respective component

Another example for Event Type B1 is on 5 April 2010 where $K_p > 4$ between 0600 and 1800 UT. This event has been discussed in Chapter Four and Chapter Five. Here, the discussion is limited to only between 0600 and 0800 UT due to the lack of meaningful Doppler spread data in whole period. Figure 6.20 illustrates the slant TEC and σ_ϕ observed on PRN28 and PRN17 above Longyearbyen during 0600-0700 UT and 0700-0800 UT, respectively. These are the closest satellites to the HF midpoint. The paths of all visible satellites above Longyearbyen between 0600 and 0759 UT are illustrated in Figure 6.21. Data for Ny-Ålesund was not available on this day.

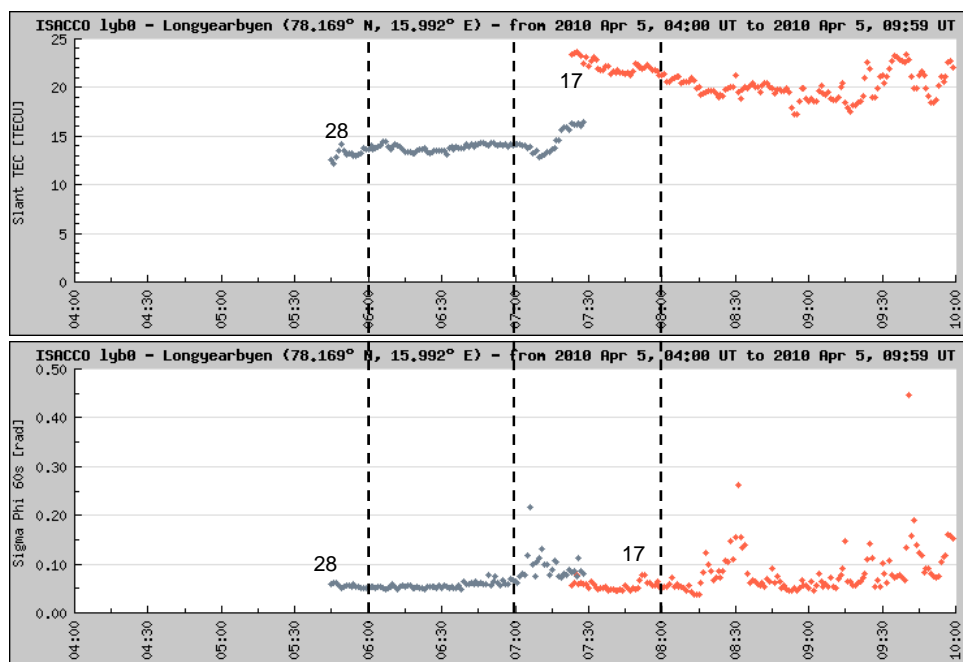


Figure 6.20: Slant TEC (top) and σ_ϕ (bottom) of PRN17 and PRN28 over Longyearbyen from 0400 to 1000 UT on 5 April 2010. The vertical lines indicates the period of interest

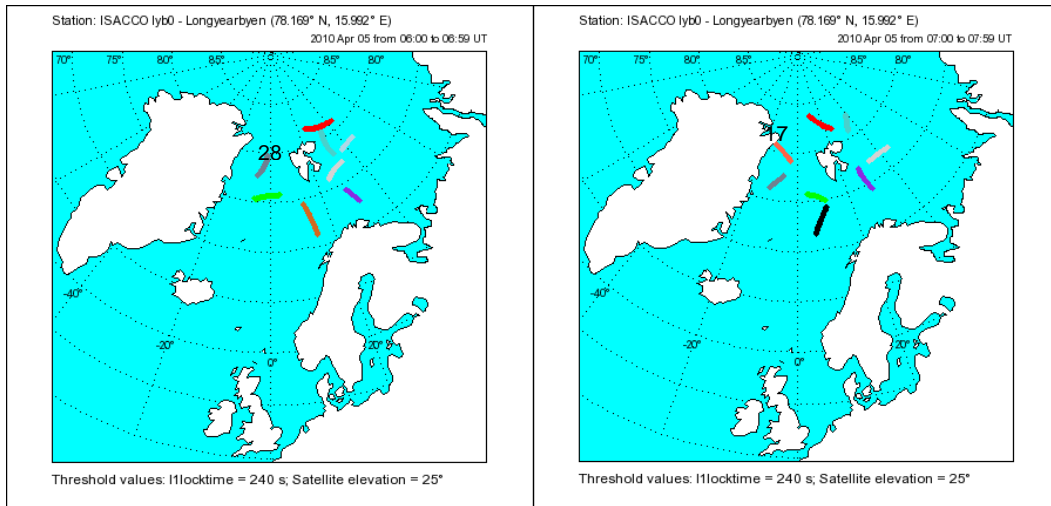


Figure 6.21: Colour-coded satellites path over Longyearbyen at 350 km on 5 April 2010 from 0600 to 0759 UT

No significant TEC variations and phase scintillations can be observed on both satellites during the period of observations. An increase of 0.22 rad can be seen on PRN28 but that was outside the observation period for this satellite. TEC changes up to ~5 TECU and increased σ_{ϕ} were detected on PRN17 but all these occurrences were observed outside the period of interest where PRN17 was far from the HF midpoint.

TEC variations and phase scintillations of satellites above Alert which were closest to the midpoint are illustrated in Figure 6.22. No significant TEC variations and phase scintillations can be observed on any on these satellites. The paths of all visible satellites between 0600 and 0800 UT can be referred in Figure 4.18. It can be seen from this figure that these satellites were not really close to the midpoint. Details of σ_{ϕ} , slant TEC, ROT, and ROTI of PRN19 are illustrated in Figure 6.23 where the period of interest was between 0600 and 0700 UT. It can be seen that only small TEC increase of ~1 TECU was registered during this period.

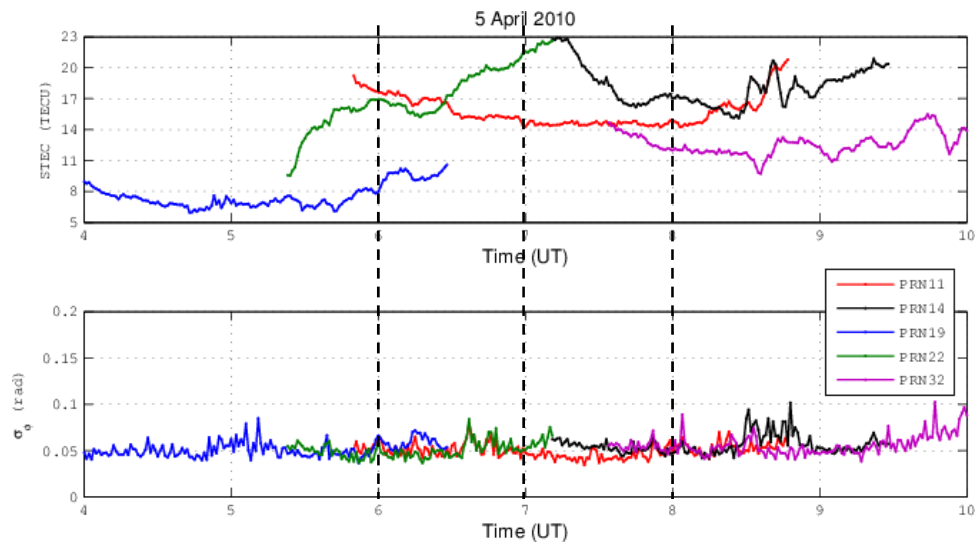


Figure 6.22: Slant TEC (top) and σ_ϕ (bottom) of several satellites over Alert from 0400 to 1000 UT on 5 April 2010. The vertical lines indicates the period of interest

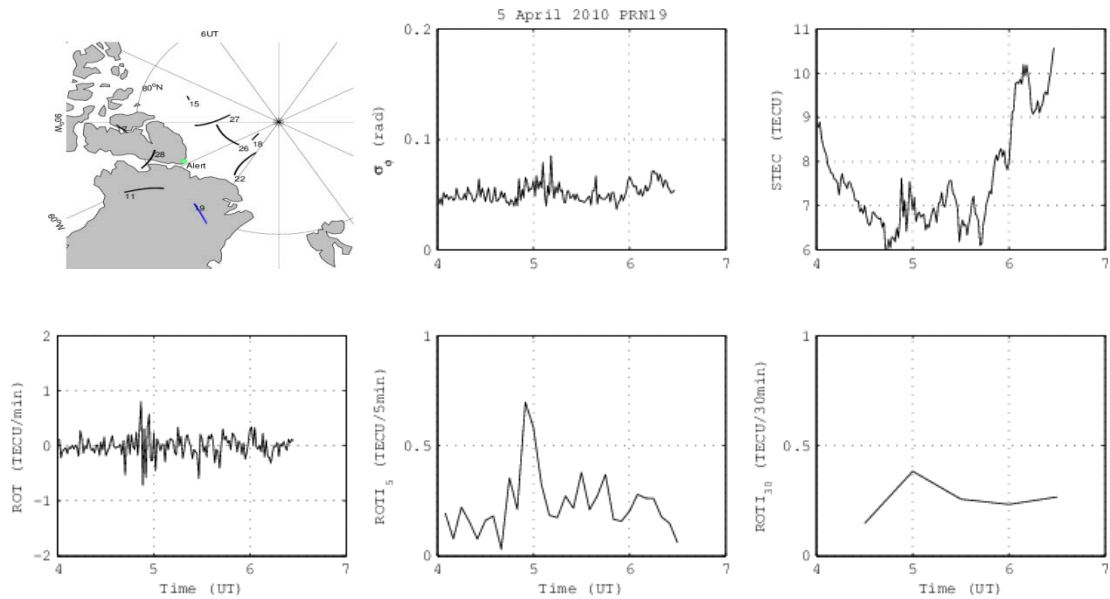


Figure 6.23: σ_ϕ , STEC, ROT, and ROTI of PRN19 on 5 April 2010. Paths of all visible satellites from 0600 to 0700 UT at 350 km are also shown

The same details for PRN32 and PRN14 are presented in Figure 6.24 and Figure 6.25, respectively where the period of interest is between 0700 and 0800 UT. No significant TEC increase was observed on PRN32 and only small increase of ~ 1 TECU was detected on PRN14 during this hour. Large TEC fluctuations of ~ 3 -6 TECU were registered afterwards on both satellites. No patches were observed on all three satellites between 0600 and 0800 UT, except one small patches of moderate intensity on PRN14. The IMF components and magnetic data over Eureka and Resolute Bay can be referred in Figure 4.19 and Figure 4.20, respectively.

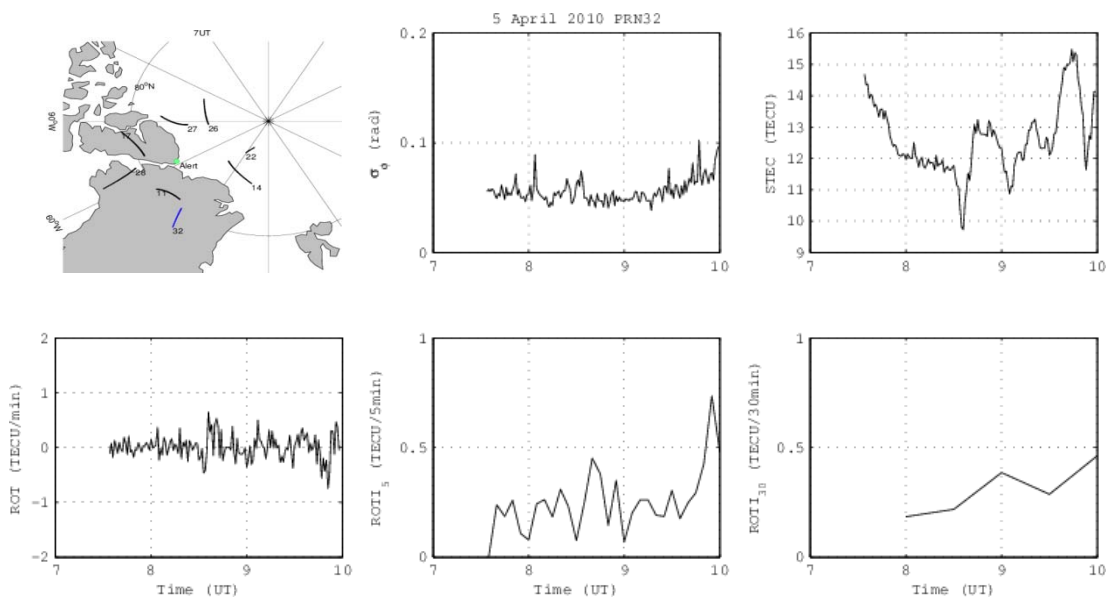


Figure 6.24: σ_ϕ , STEC, ROT, and ROTI of PRN32 on 5 April 2010. Paths of all visible satellites from 0700 to 0800 UT at 350 km are also shown

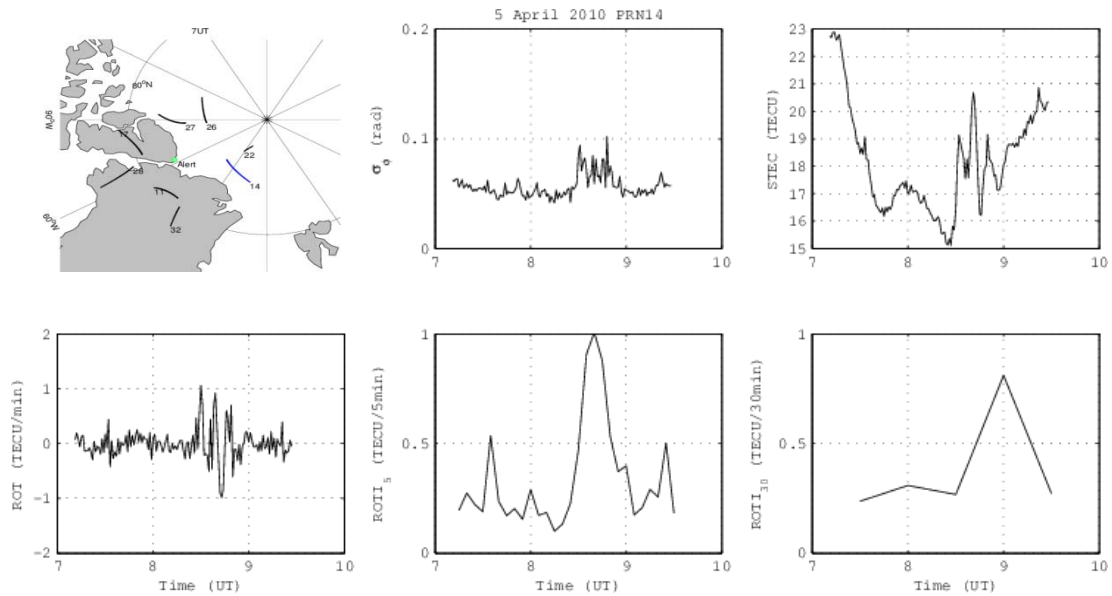


Figure 6.25: σ_ϕ , STEC, ROT, and ROTI of PRN14 on 5 April 2010. Paths of all visible satellites from 0700 to 0800 UT at 350 km are also shown

Event Type B2

A depletion of slant TEC of ~ 5 TECU was registered on PRN28 over Ny-Ålesund from 1815 to 1835 UT on 8 October 2009 (Figure 6.26). By using the speed of 600 m/s, the size of the irregularity is 720 km. The path of PRN28 and all other visible satellites during 1800-1859 UT is illustrated in Figure 6.27. PRN28 was the closest satellite to the HF midpoint. Similar depletion of ~ 7 TECU was observed on PRN28 over Longyearbyen for a longer duration from 1815 to 1845 UT. This is about 1080 km in terms of the size of the irregularity. The phase scintillation of PRN28 over Longyearbyen is not shown here as it gave erroneous reading.

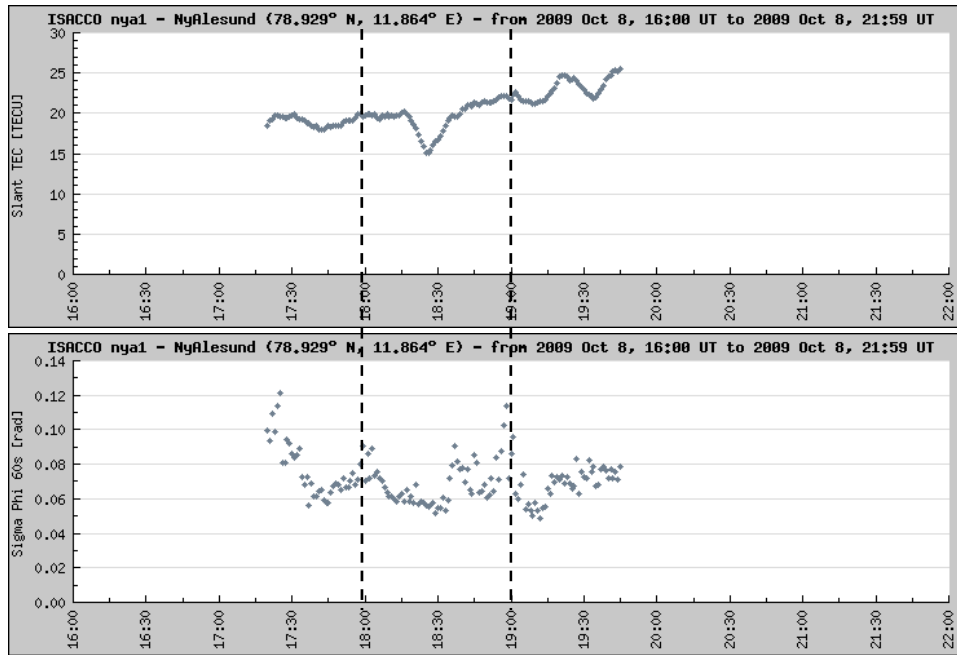


Figure 6.26: Slant TEC (top) and σ_ϕ (bottom) of PRN28 over Ny-Ålesund from 1600 to 2200 UT on 8 October 2009. The vertical lines indicates the period of interest

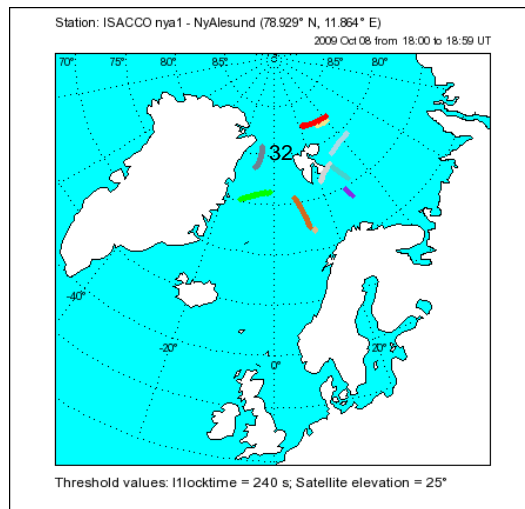


Figure 6.27: Colour-coded satellites path over Ny-Ålesund at 350 km on 8 October 2009 from 1800 to 1859 UT

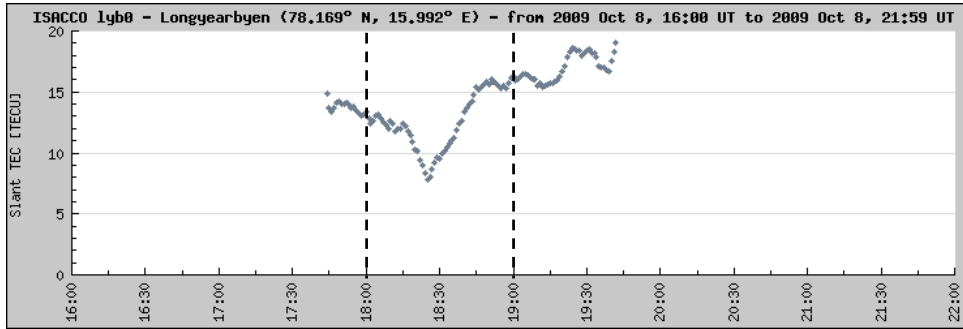


Figure 6.28: Slant TEC of PRN28 over Longyearbyen from 1600 to 2200 UT on 8 October 2009. The vertical lines indicates the period of interest

Meanwhile, over Alert, PRN19 and PRN22 were close to the HF midpoint (see Figure 6.29). Contrary to PRN28 which was observed over Ny-Ålesund and Longyearbyen, no significant TEC variations were registered on PRN19 and PRN22 above Alert, except small TEC fluctuation on both satellites (see Figure 6.30) that caused few patches as indicated in Figure 6.31 and Figure 6.31.

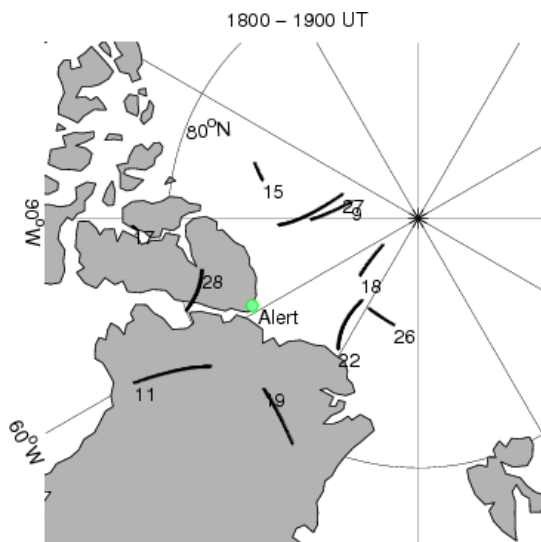


Figure 6.29: Satellites path over Alert at 350 km on 8 October 2009 from 1800 to 1900 UT

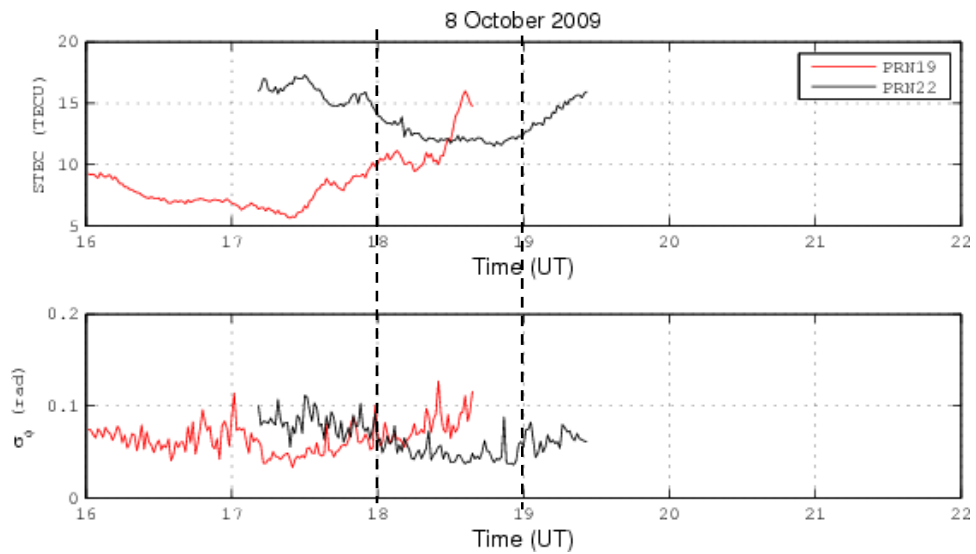


Figure 6.30: Slant TEC (top) and σ_ϕ (bottom) of PRN19 and PRN22 over Alert from 1600 to 2200 UT on 8 October 2009. The vertical lines indicates the period of interest

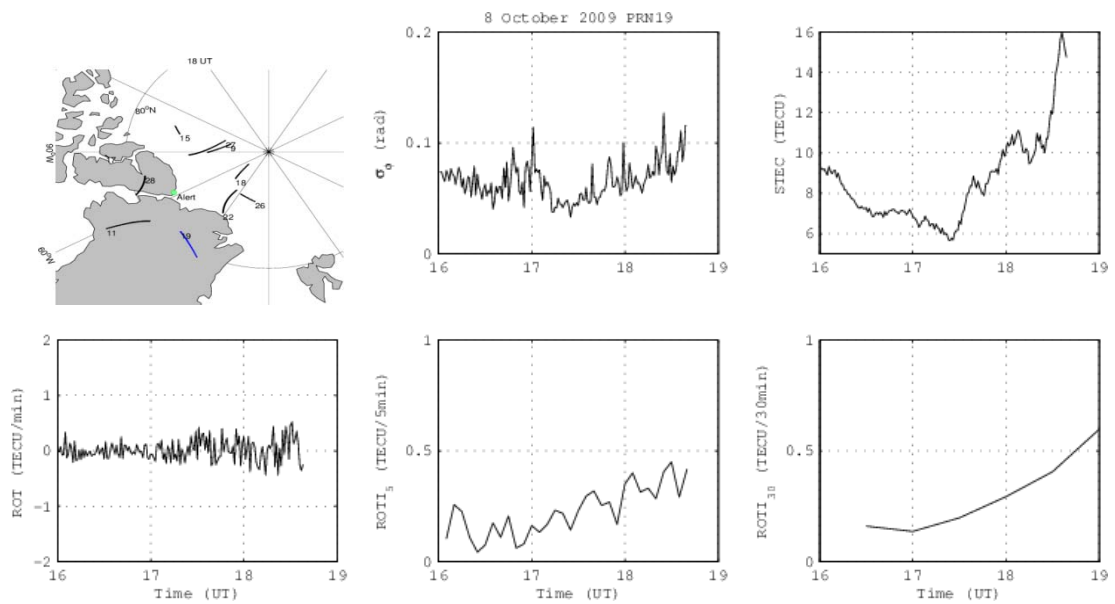


Figure 6.31: σ_ϕ , STEC, ROT, and ROTI of PRN19 on 8 October 2009. Paths of all visible satellites from 1800 to 1900 UT at 350 km are also shown

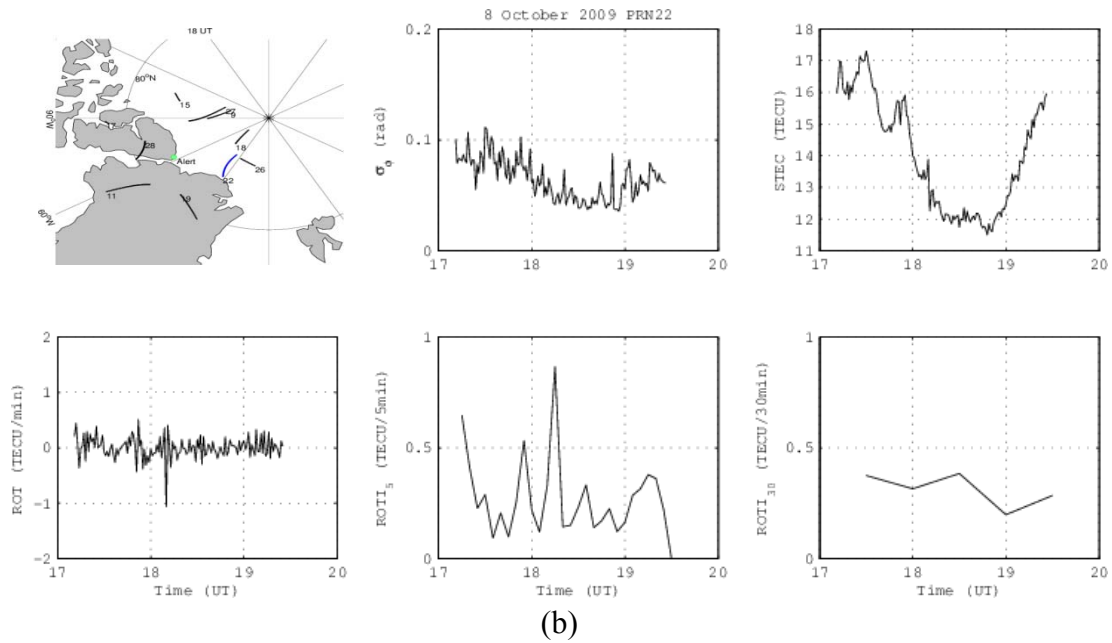


Figure 6.32: σ_ϕ , STEC, ROT, and ROTI of PRN22 on 8 October 2009. Paths of all visible satellites from 1800 to 1900 UT at 350 km are also shown

Doppler spreads on 14.36 MHz varied from 2 to 9.5 Hz between 1800 and 1900 UT (see Figure 6.33). The values range was from 4 to 6 Hz between 1803 and 1815 UT. Then, the SNR becoming less than the threshold until it resumed normally at 1824 UT but the Doppler spreads were < 5 Hz until 1829 UT. Doppler spreads increased up to 9 Hz until fall below 5 Hz again at 1851 UT. The period of large Doppler spreads was not simultaneous with the timing of TEC depletion on PRN28, but rather shifted later on.

A selection of delay-Doppler spectra on 14.36 MHz during 1800-1900 UT is shown in Figure 6.34. Doppler spreads observed on 6.95 and 8.01 MHz reached up to ~ 5 -6 Hz during this hour. Meanwhile, only few Doppler spreads of maximum 4 Hz met the SNR threshold of 0 dB on 10.39 and 11.12 MHz, and no meaningful Doppler spread on 4.64 MHz.

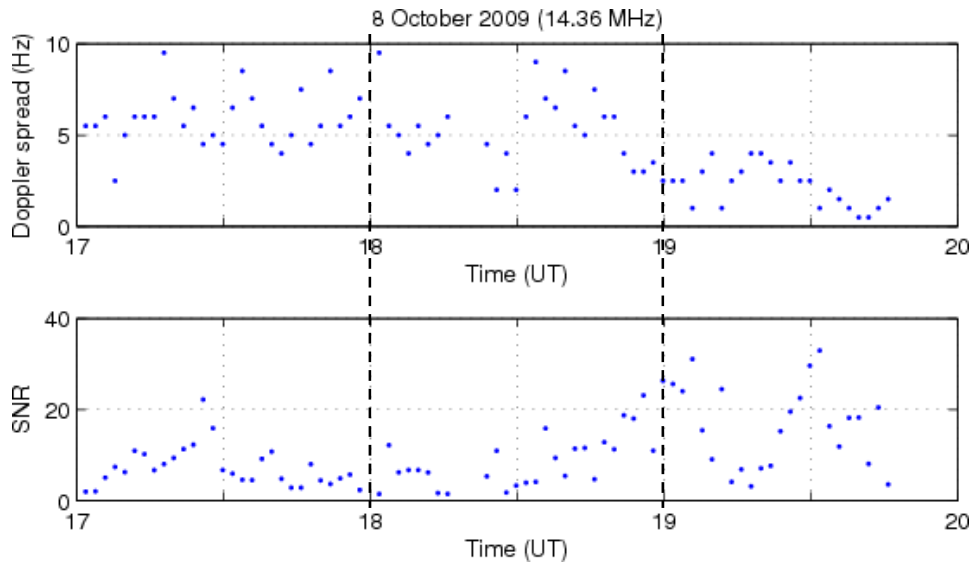


Figure 6.33: Doppler spread (top) and SNR (bottom) on 14.35 MHz from 1700 to 2000 UT on 8 October 2009. The vertical lines indicates the period of interest

The large Doppler spread during this hour may or may not be related to the depletion of TEC observed on PRN28. Furthermore, no significant TEC changes were recognised on PRN19 and PRN22, which were both observed over Alert. All three satellites were not close to each other and at different side of the midpoint. If the large Doppler spreads were actually related to the depletion of slant TEC on PRN28, then the actual reflection point might be nearby the path of PRN28. IMF B_z was mostly southward (i.e. -2.5 nT) from ~1700 UT until ~2200 UT (Figure 6.35). The variation of magnetic data at Eureka for each component did not exceed ± 25 nT from their respective means (Figure 6.36). Not enough magnetic data at Resolute Bay to be used for plotting. Meanwhile, K_p was between 0 and 1+ on this day.

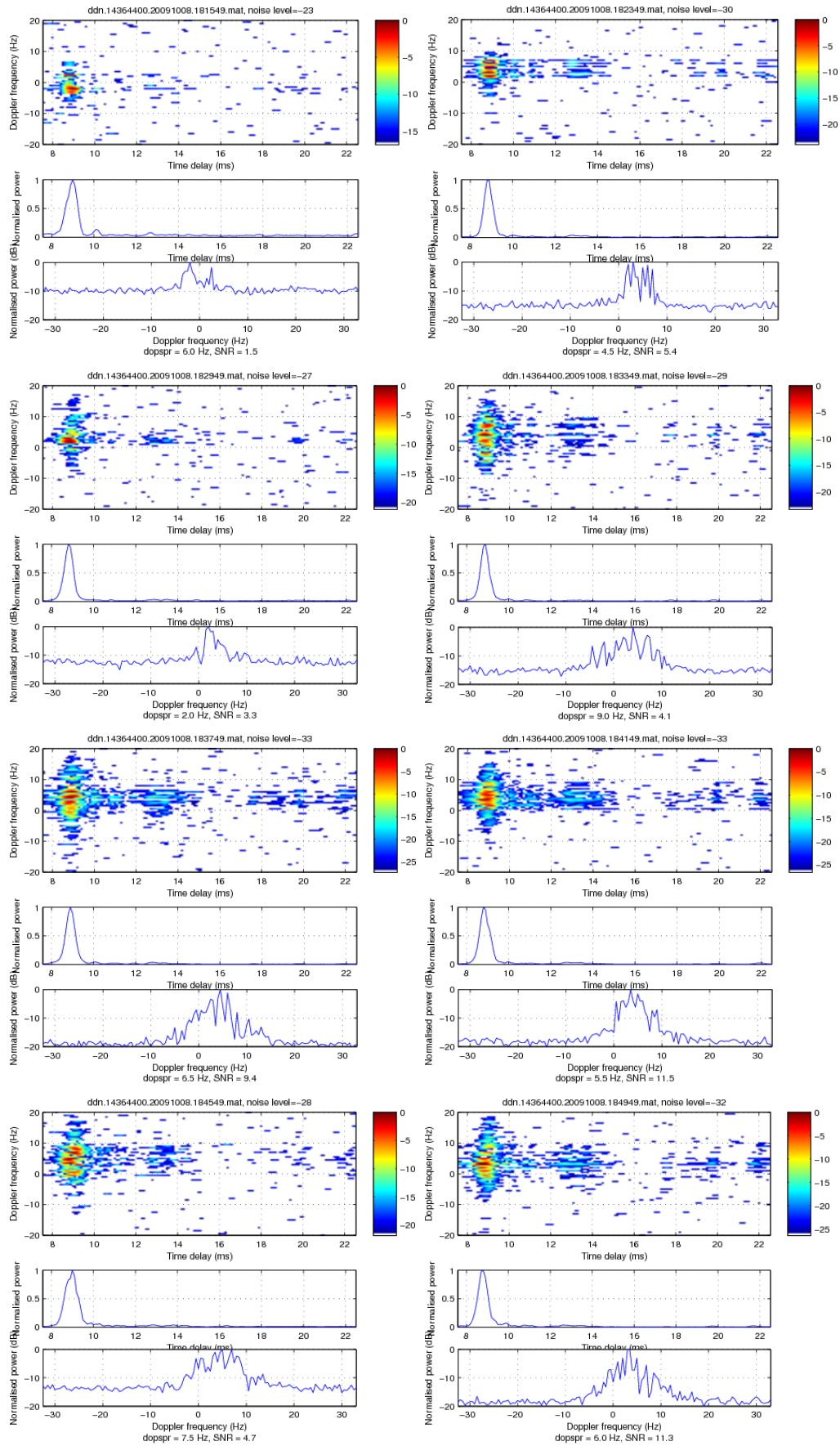


Figure 6.34: Selected SNR delay-Doppler spectra on 14.36 MHz between 1800 and 1900 UT on 8 October 2009

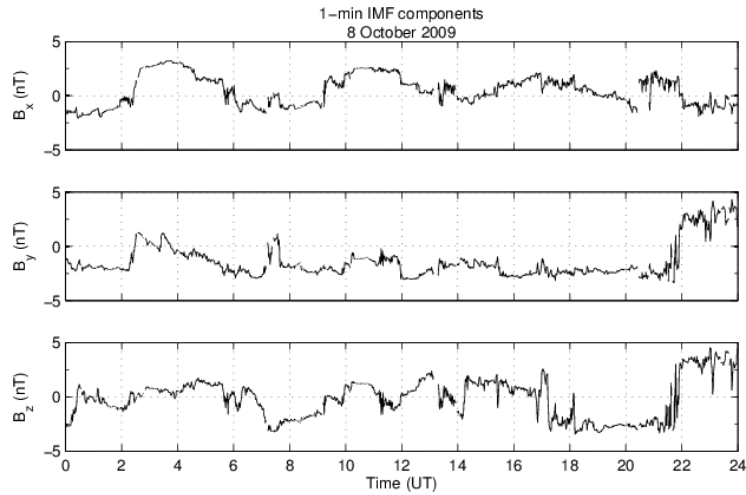


Figure 6.35: 1-minute IMF components on 8 October 2009

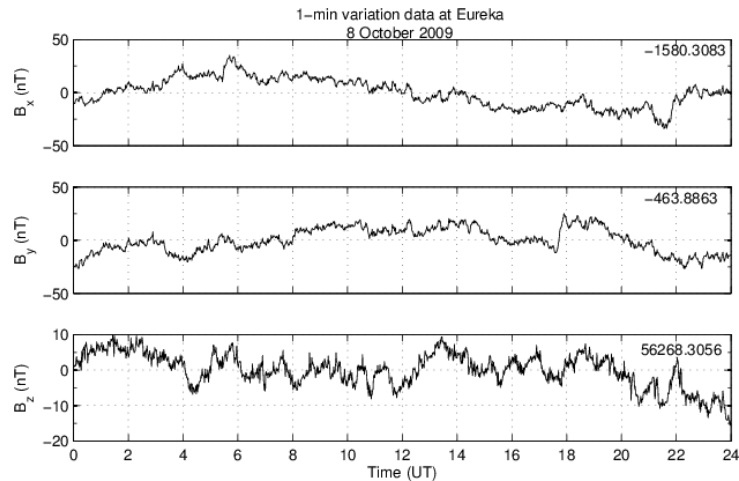


Figure 6.36: 1-minute variation data at Eureka on 8 October 2009

Another occurrence of Event Type B2 is on 4 October 2009 where details of σ_ϕ , slant TEC, ROT, and ROTI of PRN21, PRN16 and PRN6 on this day are illustrated in Figure 6.37, Figure 6.38 and Figure 6.39, respectively. These are the satellites nearby the HF midpoint between 1500 and 1700 UT. There were large TEC changes on PRN21 from ~ 1540 UT, together with increase in σ_ϕ of 0.24 rad from ~ 1600 to 1634 UT. The TEC changes ended at 1615 UT before increasing again and ended at

~1633 UT. However, PRN21, starting to move away from HF midpoint starting ~1600 UT (refer Figure 6.41 for path from 1500 to 1700 UT for each hour). Several patches of low to high intensities were observed on this satellite during the period of observations.

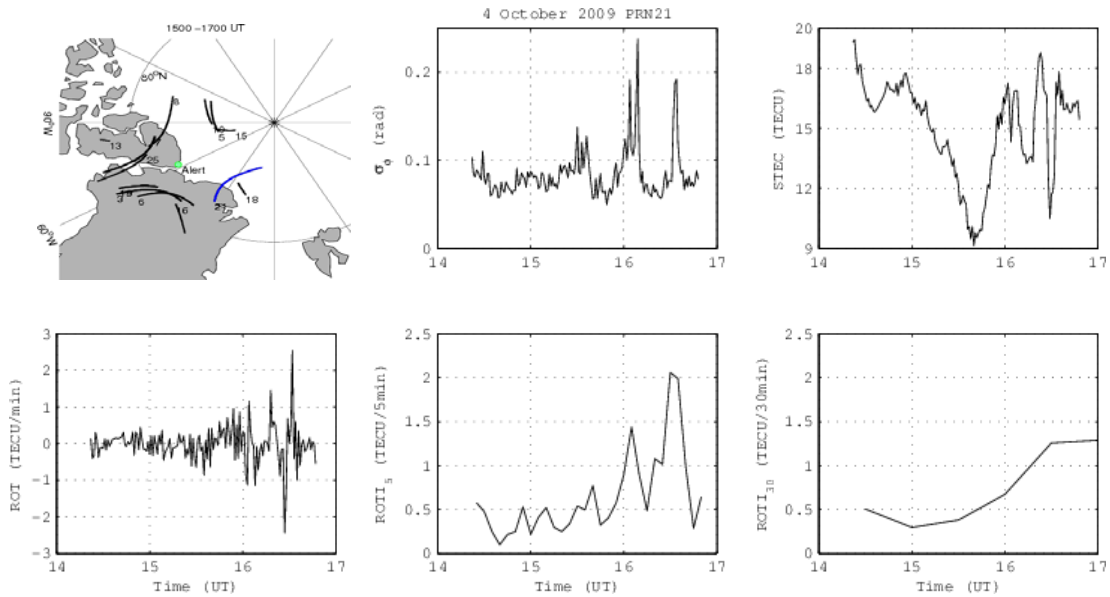


Figure 6.37: σ_p , STEC, ROT, and ROTI of PRN21 on 4 October 2009. Paths of all visible satellites from 1500 to 1700 UT at 350 km are also shown

PRN16 was experiencing a TEC decrease of ~2 TECU only that reached the minimum peak at ~1530 UT that caused low intensity patches. In addition, although large TEC fluctuations with moderate to high intensities patches occurred on PRN6 from ~1500 UT onwards, it was only approaching HF midpoint at the end of observation period. Most of the other visible satellites during this period did not demonstrate large TEC changes. Another satellite that was close to the midpoint was PRN18, but the details of this satellite is not shown here since its existence over Alert was only in brief during the period of observations. The plots of slant TEC and

σ_ϕ of all four satellites are shown in Figure 6.40 and the paths of all visible satellites between 1500 and 1700 UT are illustrated in Figure 6.41.

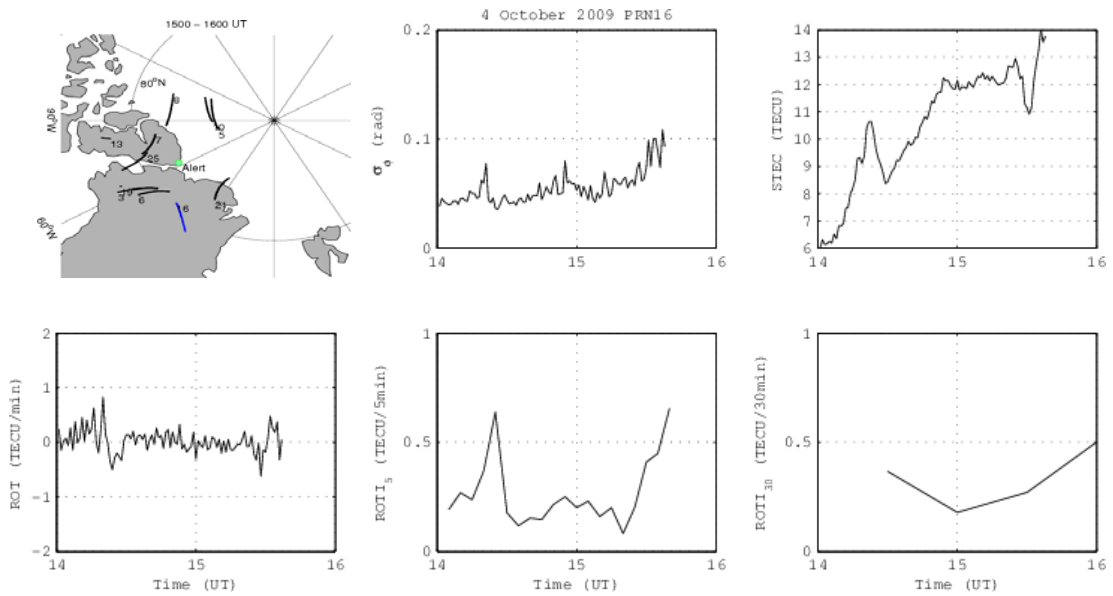


Figure 6.38: σ_ϕ , STEC, ROT, and ROTI of PRN16 on 4 October 2009. Paths of all visible satellites from 1500 to 1600 UT at 350 km are also shown

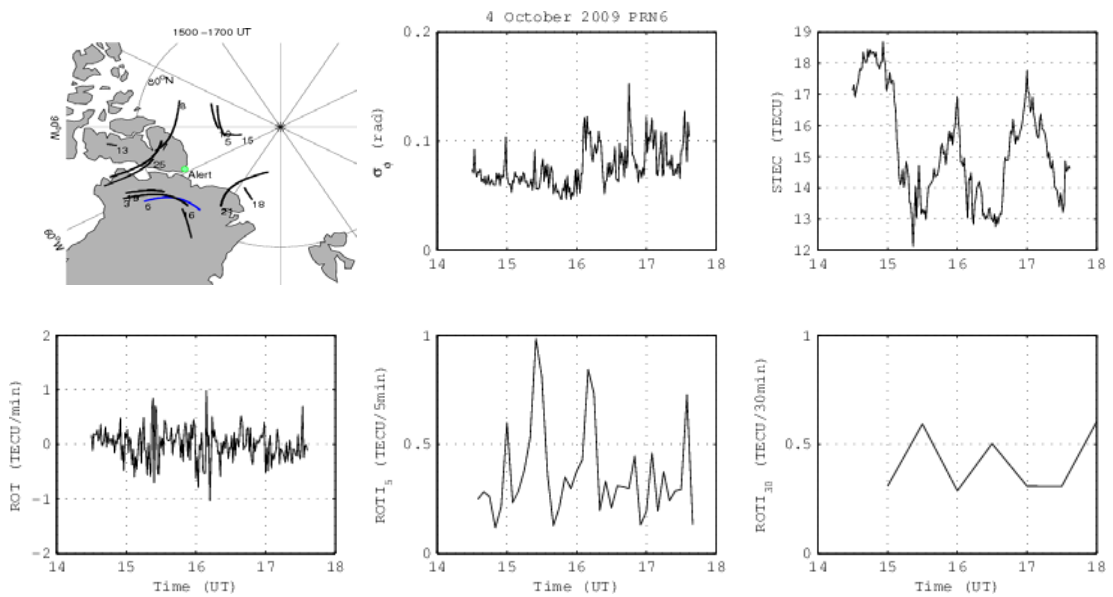


Figure 6.39: σ_ϕ , STEC, ROT, and ROTI of PRN6 on 4 October 2009. Paths of all visible satellites from 1500 to 1700 UT at 350 km are also shown

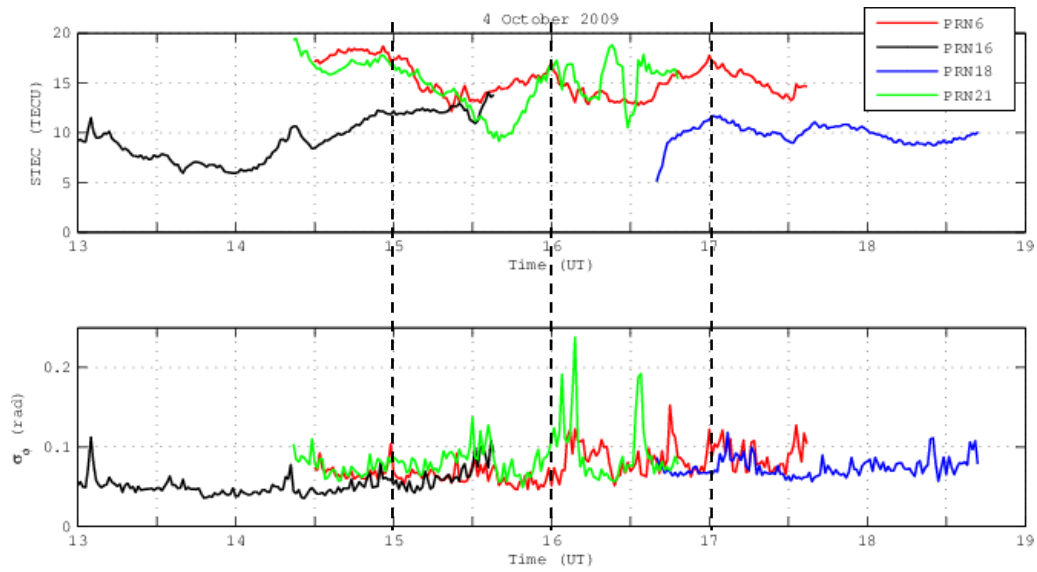


Figure 6.40: Slant TEC (top) and σ_ϕ (bottom) of PRN6, 16, 18 and 21 over Alert from 1300 to 1900 UT on 4 October 2009. The vertical lines indicates the period of interest

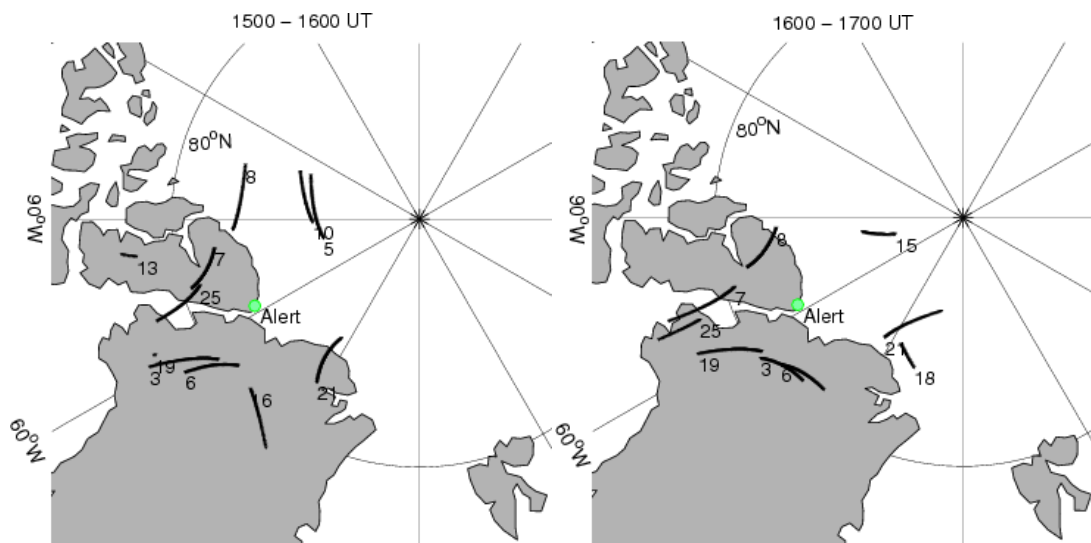


Figure 6.41: Satellites path over Alert at 350 km on 4 October 2009 from 1500 to 1700 UT

Changes of slant TEC and σ_ϕ on satellites over Svalbard observed near the HF midpoint during 1500-1700 UT are illustrated in Figure 6.42 and Figure 6.43. Small TEC fluctuation of ~ 2 TECU can be seen during 1500-1559 UT. TEC decrease of

~3-5 TECU was observed on PRN7 at ~1613 UT and also increase of ~2-3TECU on PRN8. σ_ϕ also increased from ~1530 to ~1630 UT at both Ny-Ålesund and Longyearbyen from 0.25 to 0.35 rad. Path of all visible satellites during these two hours are shown in Figure 6.44.

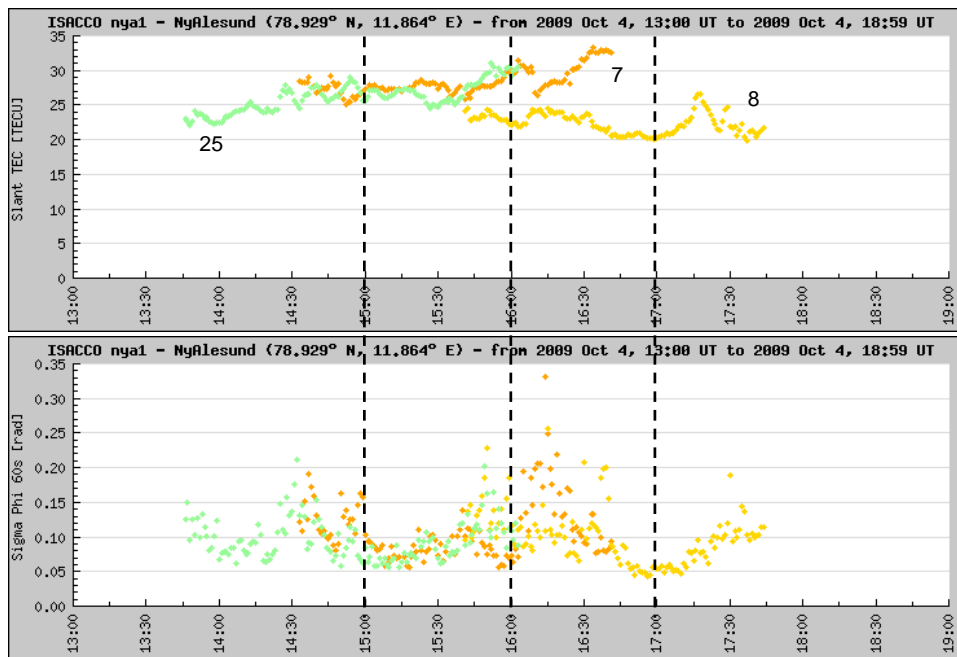


Figure 6.42: Slant TEC (top) and σ_ϕ (bottom) of PRN7, 8 and 25 over Ny-Ålesund from 1300 to 1900 UT on 4 October 2009. The vertical lines indicates the period of interest

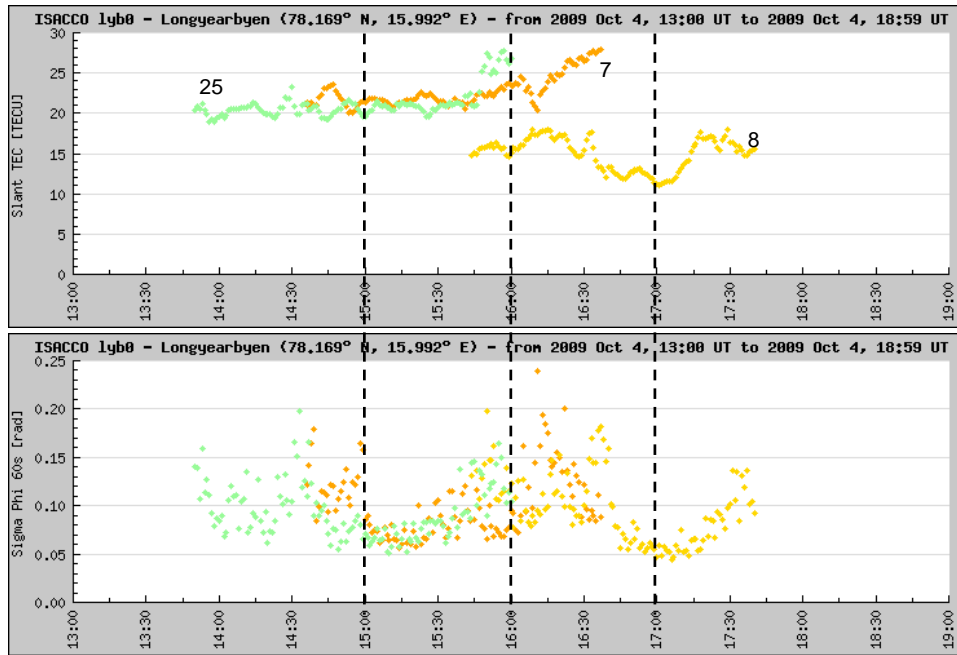


Figure 6.43: Slant TEC (top) and σ_ϕ (bottom) of PRN7, 8 and 25 over Longyearbyen from 1300 to 1900 UT on 4 October 2009. The vertical lines indicates the period of interest

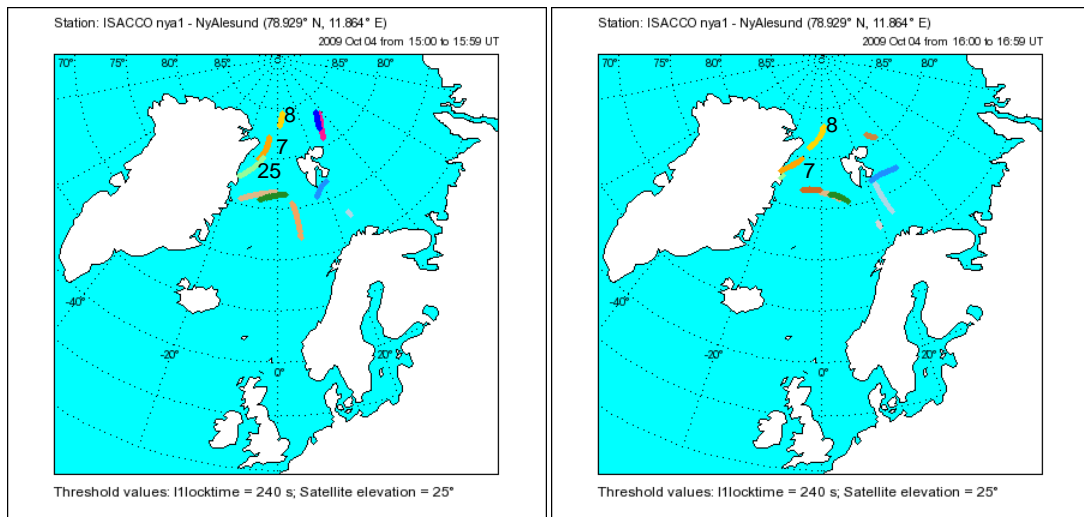


Figure 6.44: Colour-coded satellites path over Ny-Ålesund at 350 km on 4 October 2009 from 1500 to 1659 UT

Doppler spreads and SNR on 10.39 MHz from 1430UT to 1730 UT are shown in Figure 6.45. There was a gap of data on 10.39 MHz from 1600 to 1640 UT due to lack of significant data set. Doppler spreads were mostly < 5 Hz between 1500 and 1600 UT with one occurrence of 15 Hz. Although the values of Doppler spread started to increase ~ 1730 UT and reached a maximum of 10.5 Hz, they were mostly at the lower end of SNR. Selected delay-Doppler spectra between 1500 and 1700 UT are shown in Figure 6.46 and Figure 6.47.

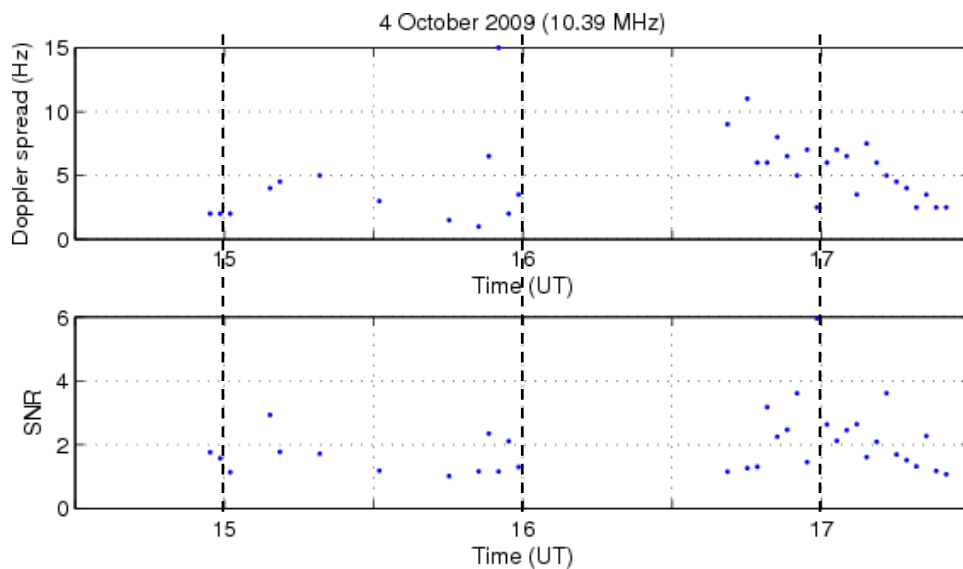


Figure 6.45: Doppler spread (top) and SNR (bottom) on 10.39 MHz from 1430 to 1730 UT on 4 October 2009. The vertical lines indicates the period of interest

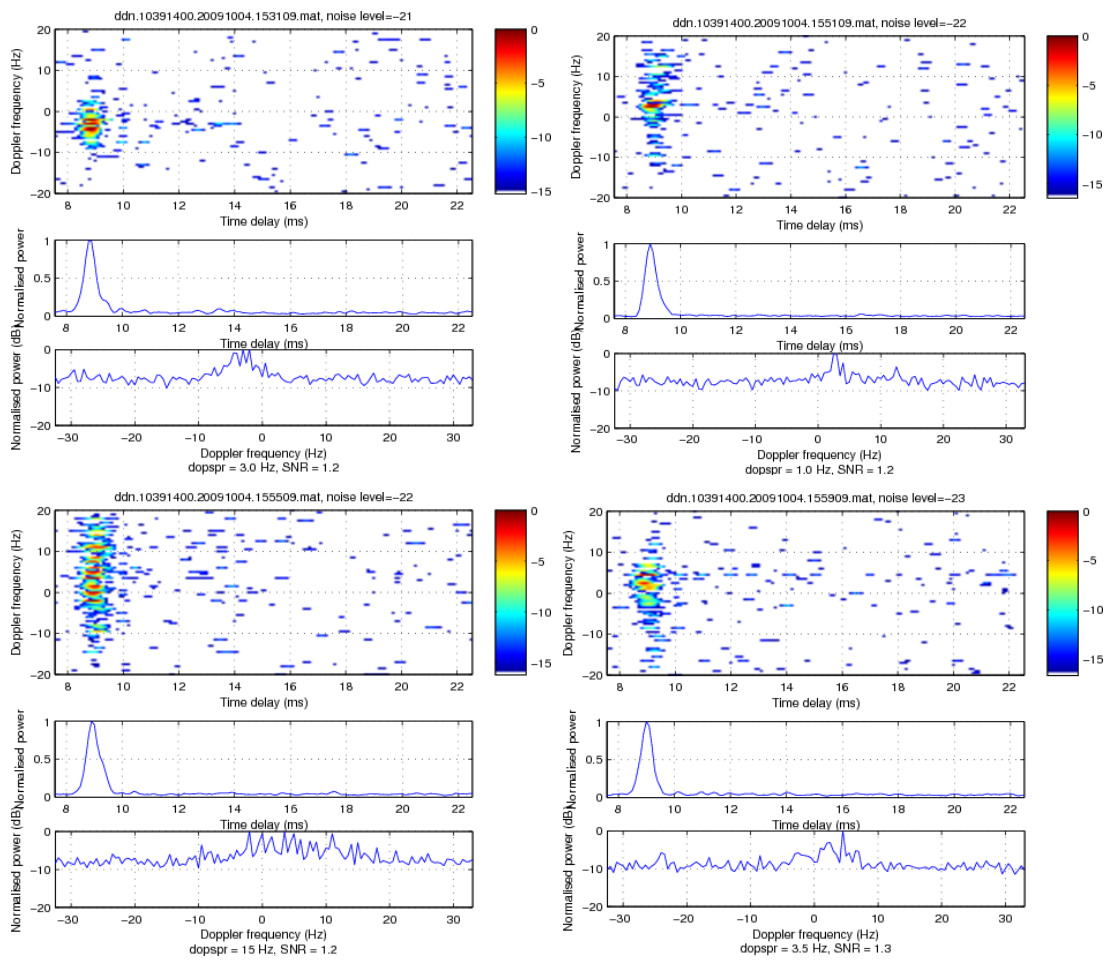


Figure 6.46: Selected delay-Doppler spectra on 10.39 MHz between 1500 and 1600 UT on 4 October 2009

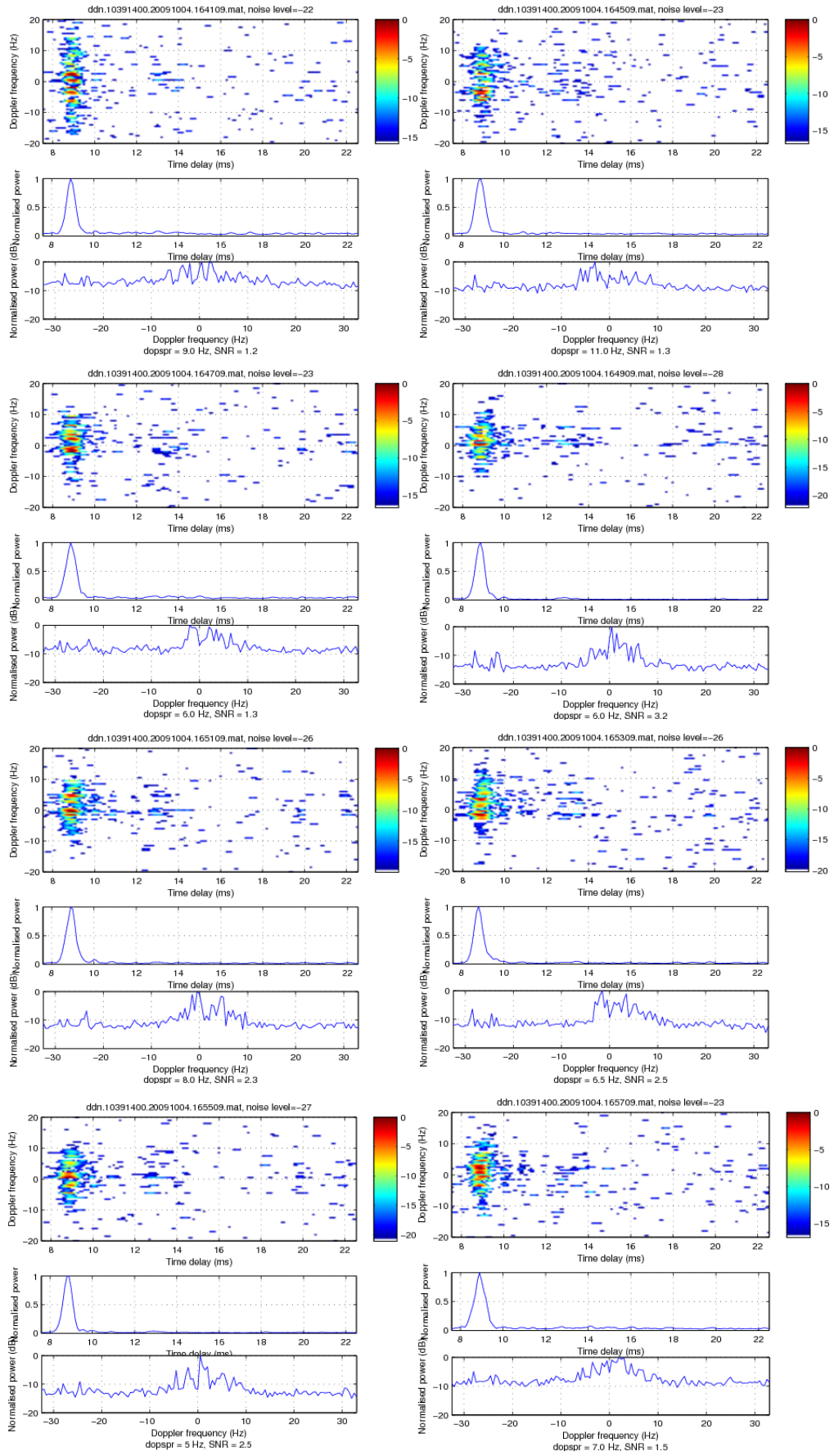


Figure 6.47: Selected delay-Doppler spectra on 10.39 MHz between 1600 and 1700 UT on 4 October 2009

IMF B_z component fluctuated between -5 nT and 5 nT during the period of observations (see Figure 6.48). Magnetic data at Eureka and Resolute Bay showed variations up to $\sim\pm 50$ nT from the mean (Figure 6.49). K_p was low between 0 and 2+ on this day.

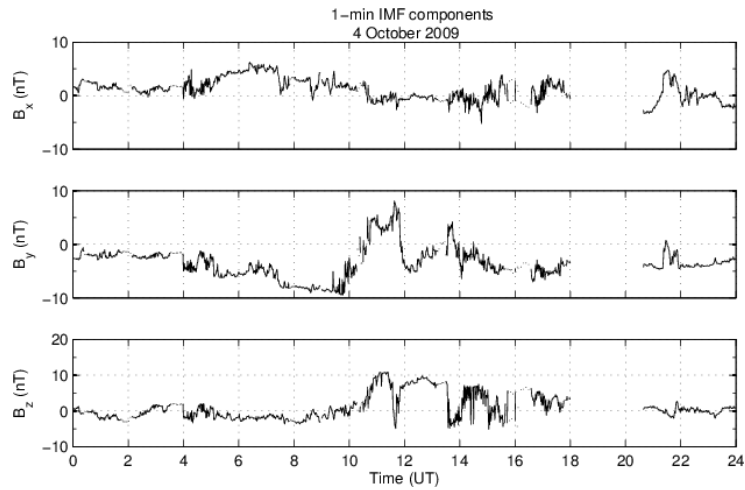
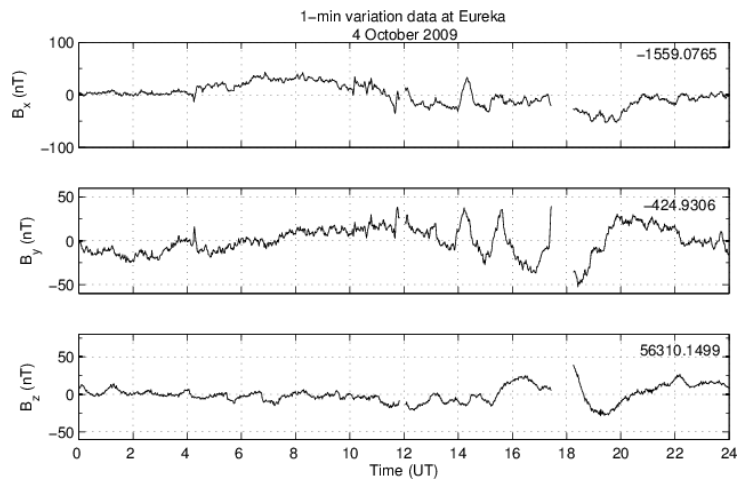


Figure 6.48: 1-minute IMF components on 4 October 2009



(a)

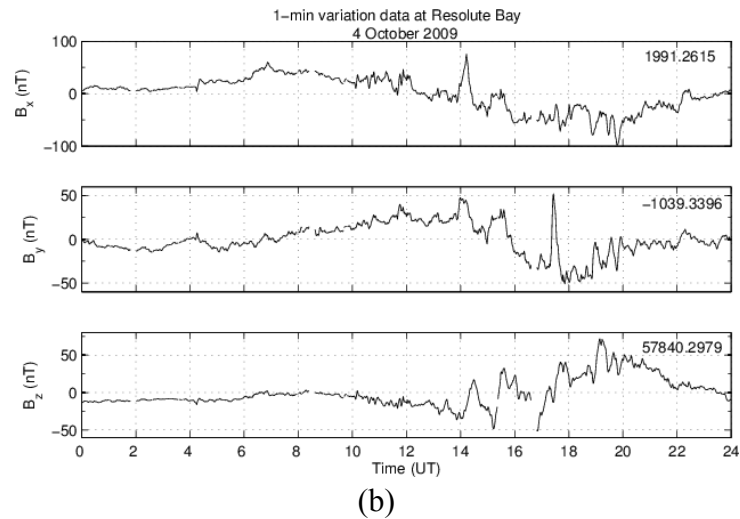


Figure 6.49: 1-minute variation data at (a) Eureka, and (b) Resolute Bay on 4 October 2009

Event Type B3

Event Type B3 discusses the Doppler spreads characteristics during large fluctuations of TEC on mostly all visible satellites including those around HF midpoint. An example of this event is on 15 February 2010, which also has been discussed in Chapter Four in Event Type A2. Similarly, the period of observation is set from 1600 to 2000 UT. Details of σ_{ϕ} , slant TEC and ROTI of visible satellites during this period can be found in Figure 4.40. Path of all visible satellites from 1600 to 2000 UT is illustrated in Figure 6.50. The slant TEC and phase scintillation of satellites close to the HF midpoint (i.e. PRN7, 8 and 13) are shown in Figure 6.51 where TEC fluctuations and increased phase scintillations were apparent.

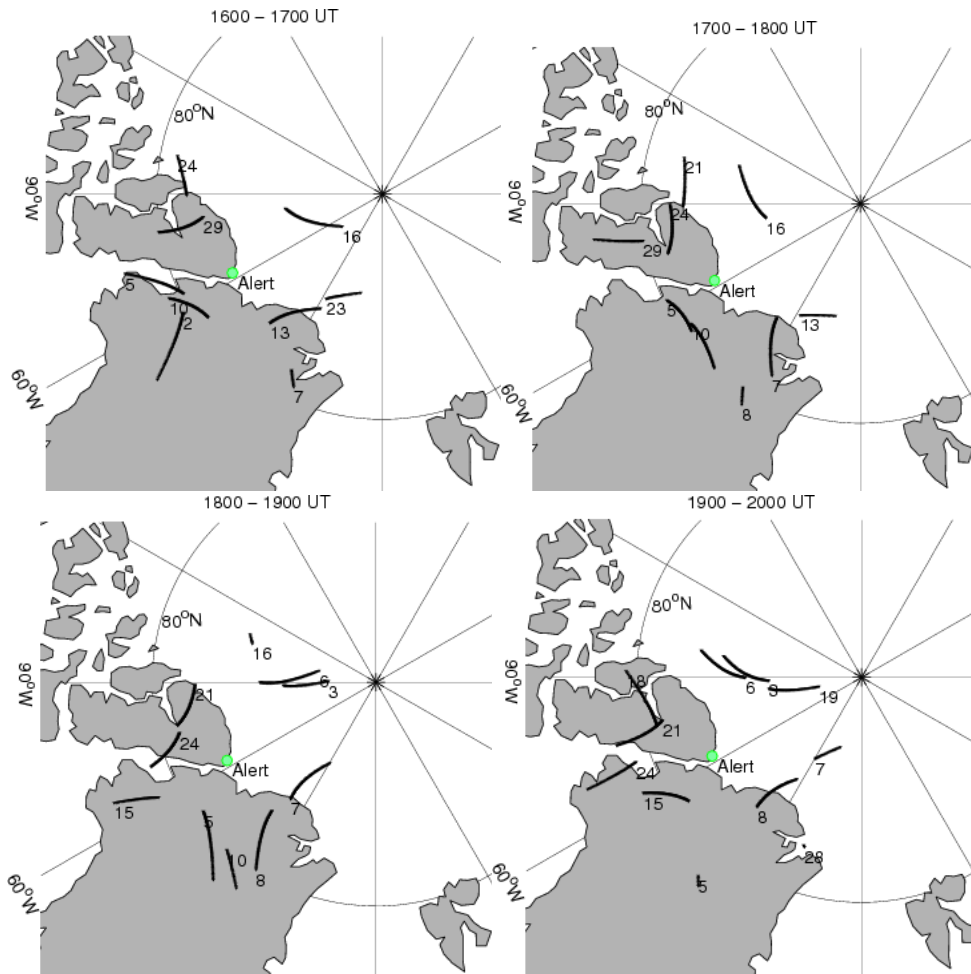


Figure 6.50: Satellites path over Alert at 350 km on 15 February 2010 from 1600 to 2000 UT

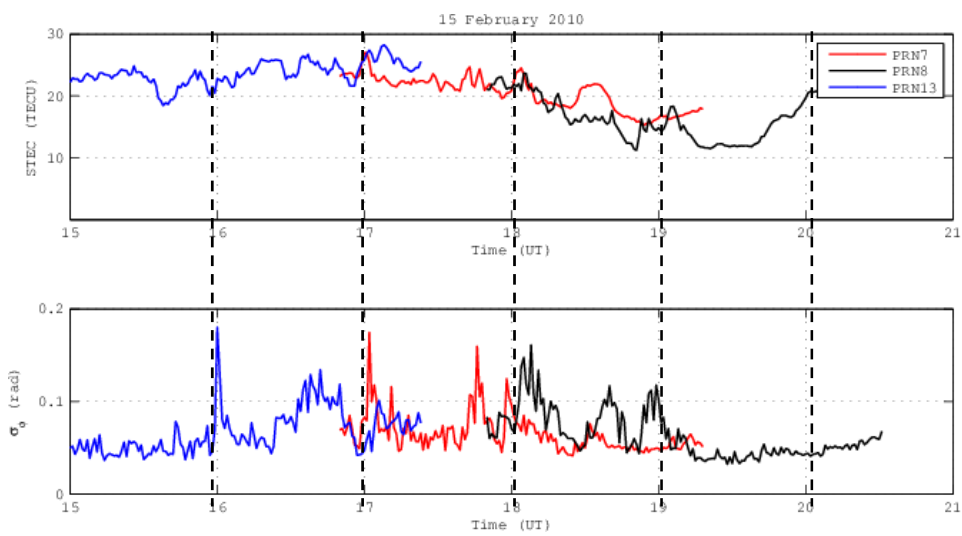


Figure 6.51: Slant TEC (top) and σ_ϕ (bottom) of PRN7, 8 and 13 over Alert from 1500 to 2100 UT on 15 February 2010. The vertical lines indicates the period of interest

Figure 6.52 and Figure 6.53 shows the Doppler spreads and SNR on 15 February 2010 from 1600 to 2000 UT on 10.39 and 11.12 MHz, respectively. The number of meaningful signals on 11.12 MHz were less than on 10.39 MHz, but both showed similar characteristics where most Doppler spreads < 5 Hz were between 1600 and 1730 UT. After that, larger Doppler spreads up to 8 Hz were registered until ~ 1810 UT (on 10.39 MHz) and until ~ 1815 UT (11.12 MHz). Doppler spreads becoming small up to only ~ 2 Hz until the end of observation periods.

Slant TEC on two satellites close to HF midpoint, PRN7 (see Figure 4.43) and PRN8 (see Figure 4.44) was fluctuating heavily until end of observation periods, and so were on most of other visible satellites. However, large Doppler spreads were observed at certain times only during the period of interest. Selected delay-Doppler spectra on 10.39 MHz between 1700 and 2000 UT can be seen in Figure 6.54, Figure 6.55 and Figure 6.56.

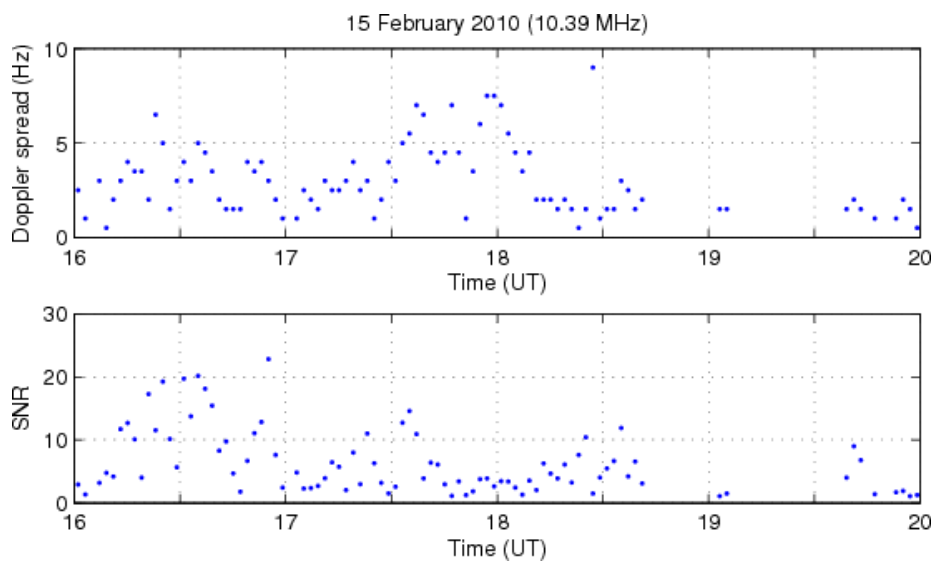


Figure 6.52: Doppler spread (top) and SNR (bottom) on 10.39 MHz from 1600 to 2000 UT on 15 February 2010

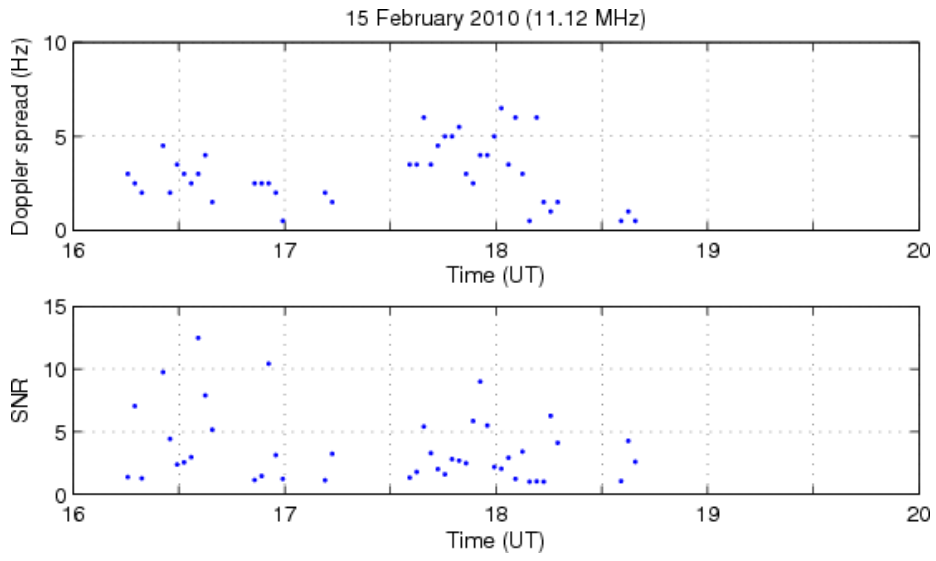


Figure 6.53: Doppler spread (top) and SNR (bottom) on 11.12 MHz from 1600 to 2000 UT on 15 February 2010

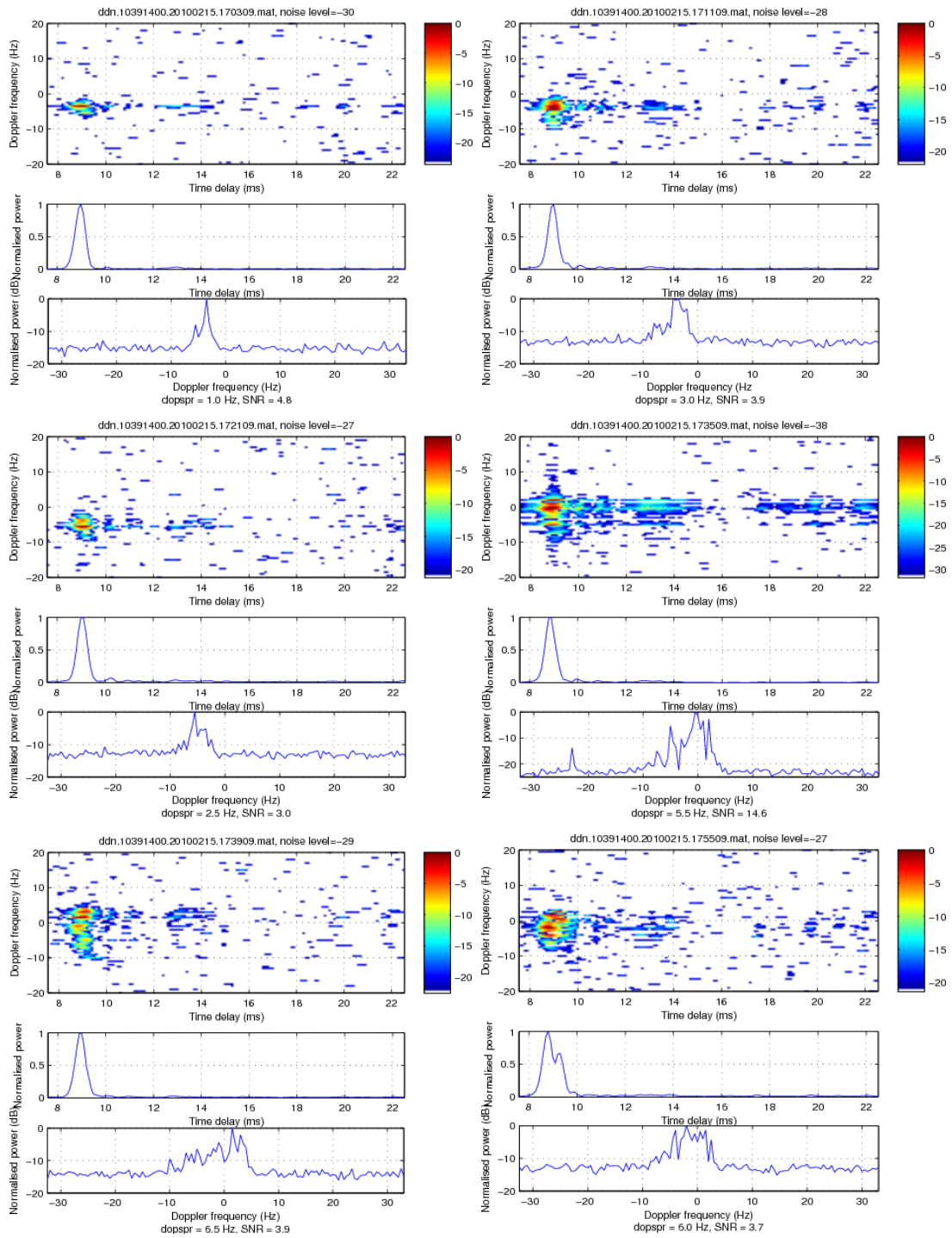


Figure 6.54: Selected delay-Doppler spectra on 10.39 MHz between 1700 and 1800 UT on 15 February 2010

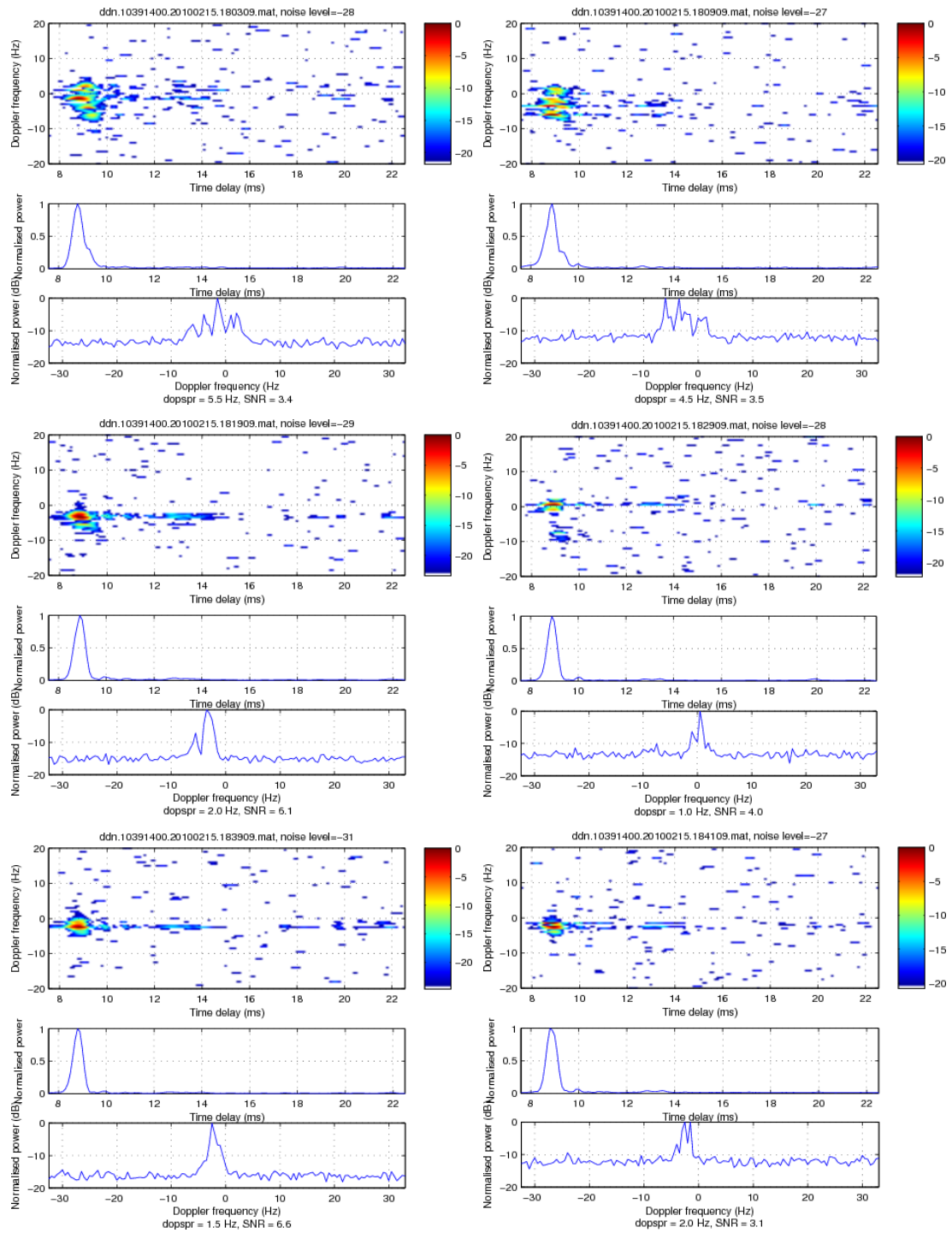


Figure 6.55: Selected delay-Doppler spectra on 10.39 MHz between 1800 and 1900 UT on 15 February 2010

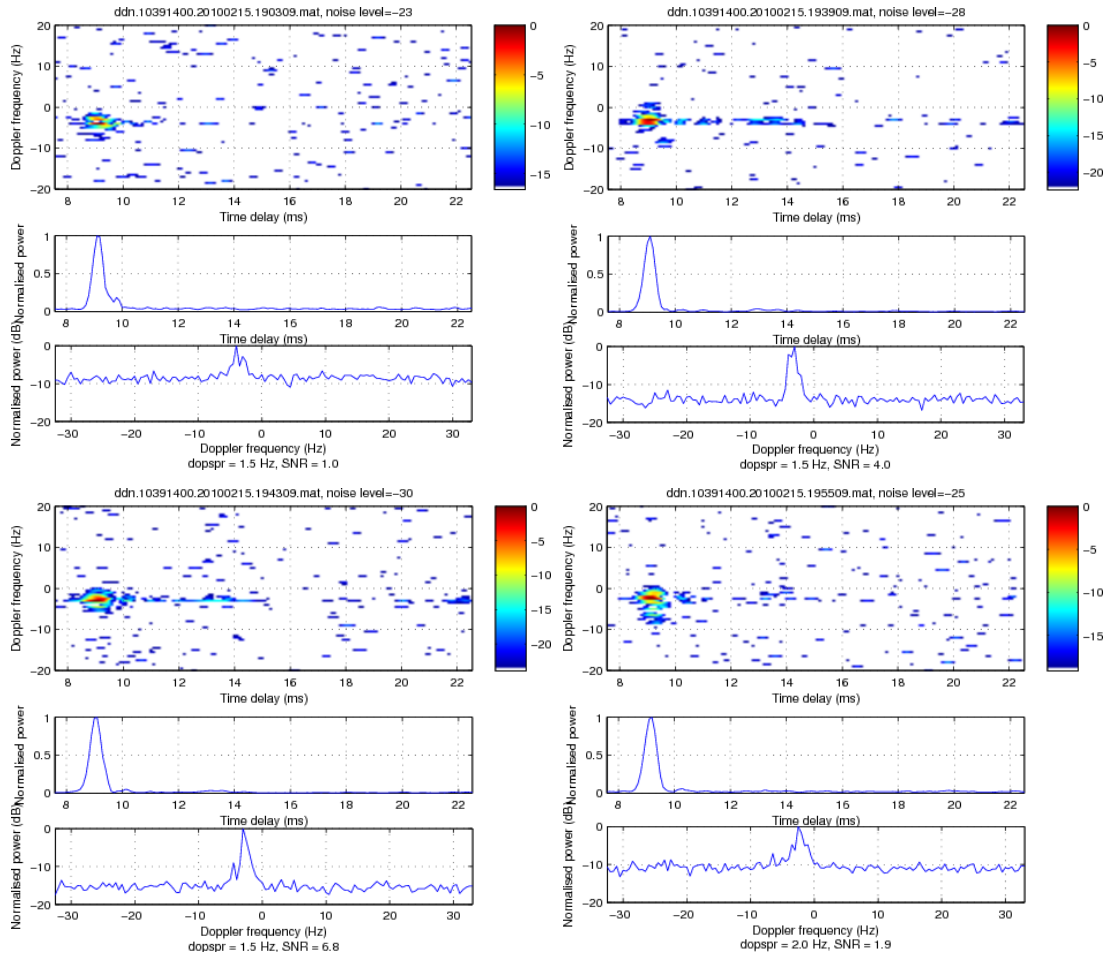


Figure 6.56: Selected delay-Doppler spectra on 10.39 MHz between 1900 and 2000 UT on 15 February 2010

Observations of slant TEC and σ_ϕ over Svalbard during the same period of time are presented in Figure 6.57 and Figure 6.58. TEC were found to be fluctuating on the satellites close to the HF midpoint. σ_ϕ were also increased until ~ 0.16 rad at various times. There were very little variations of slant TEC on other visible satellites until ~ 1800 UT. After that, variations of TEC and also σ_ϕ were registered on few other satellites, namely PRN3, PRN6 and PRN19, which were above Svalbard at roughly the same location (see Figure 6.59).

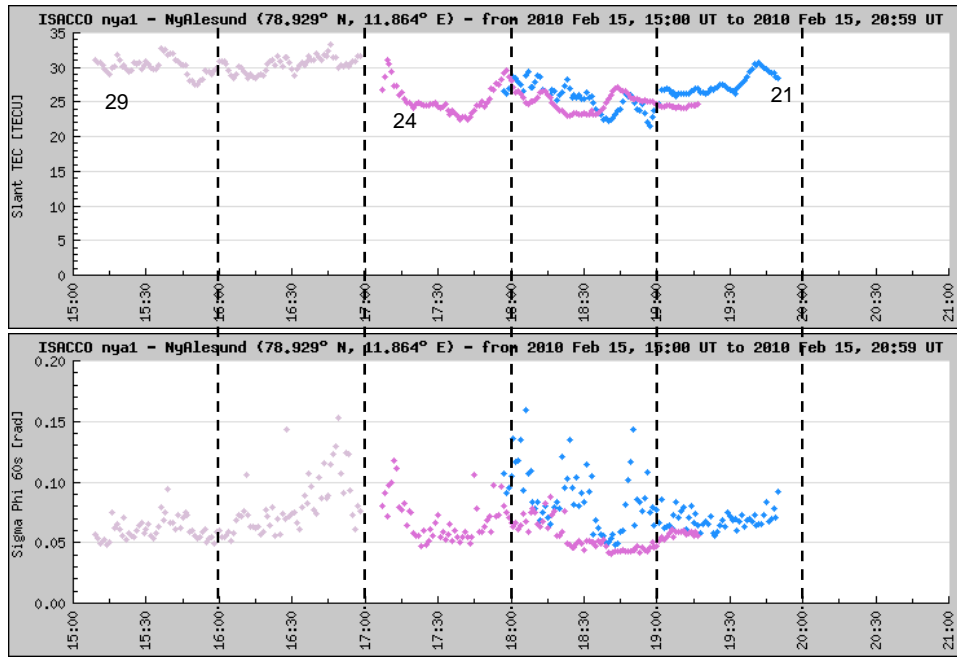


Figure 6.57: Slant TEC (top) and σ_ϕ (bottom) of PRN29, 21 and 24 over Ny-Ålesund from 1500 to 2000 UT on 15 February 2010. The vertical lines indicates the period of interest

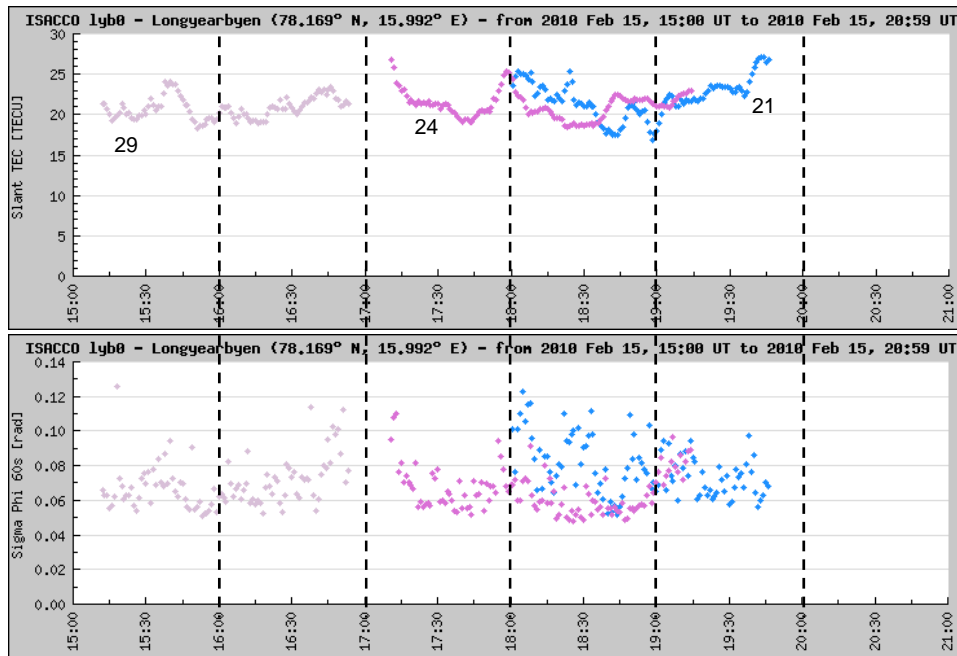


Figure 6.58: Slant TEC (top) and σ_ϕ (bottom) of PRN29, 21 and 24 over Longyearbyen from 1500 to 2000 UT on 15 February 2010. The vertical lines indicates the period of interest

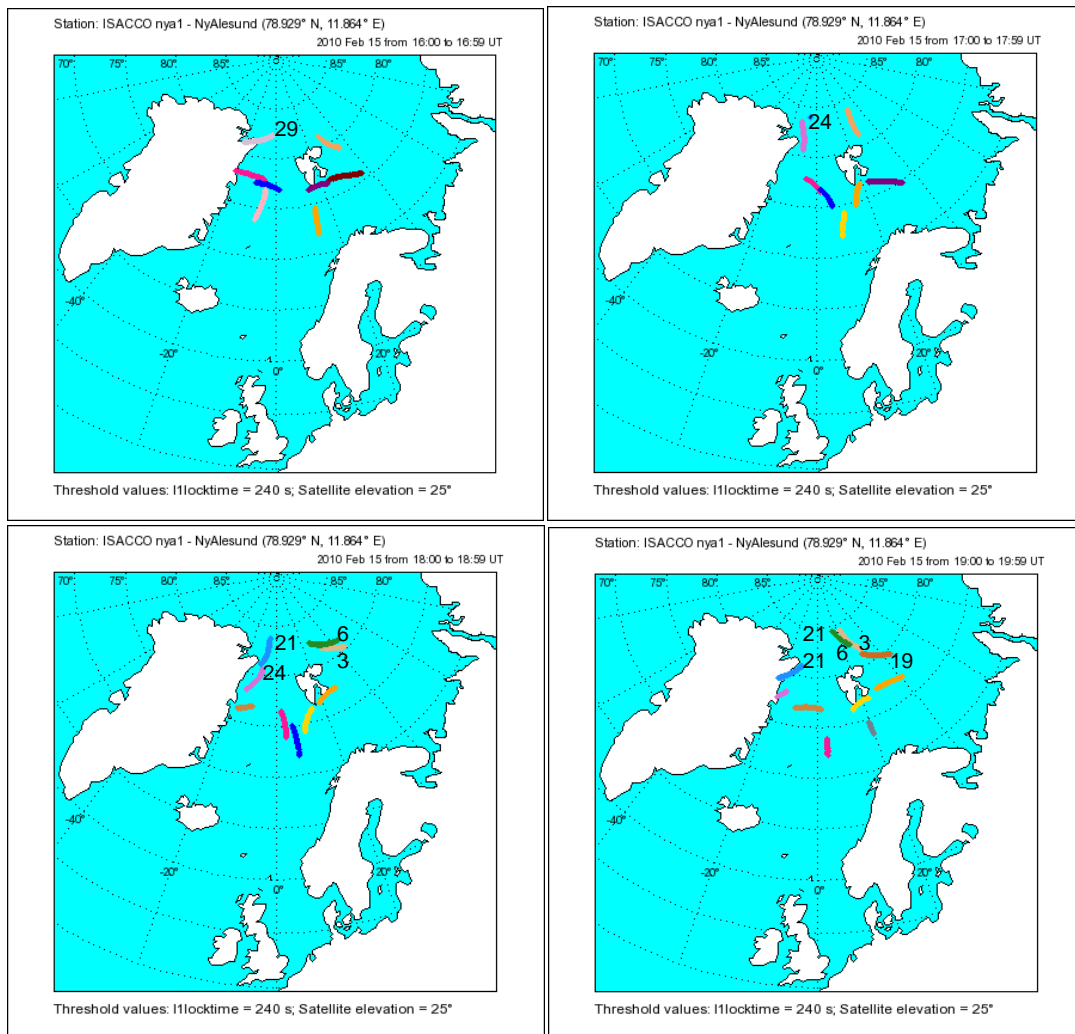


Figure 6.59: Colour-coded satellites path over Ny-Ålesund at 350 km on 15 February 2010 from 1600 to 1959 UT

Geomagnetic indices on 15 February 2010 were between 1+ and 4+ and IMF B_z was predominantly southwards (refer Figure 4.45). Magnetic field components at Eureka and Resolute Bay demonstrated changes from their background values up to $\sim\pm 60$ nT starting from ~ 1700 UT until ~ 2200 UT (refer Figure 4.46).

Another example of large TEC fluctuation on most of visible satellites over Alert on 11 April 2010 between 1700 and 2000 UT is shown in Figure 6.60 (b). The period of

observations is restricted for one hour only from 1900 to 2000 UT. Path of all visible satellites during this hour is illustrated in Figure 6.61. The slant TEC and phase scintillations of a satellite close to the HF midpoint are shown in Figure 6.62. The detail of these two parameters together with the rate of TEC and ROTI is demonstrated in Figure 6.63. Large TEC fluctuations of ~ 5 TECU can be seen clearly between 1900 and 2000 UT. No significant phase scintillation was detected in this hour. Patches were also observed during the observation periods.

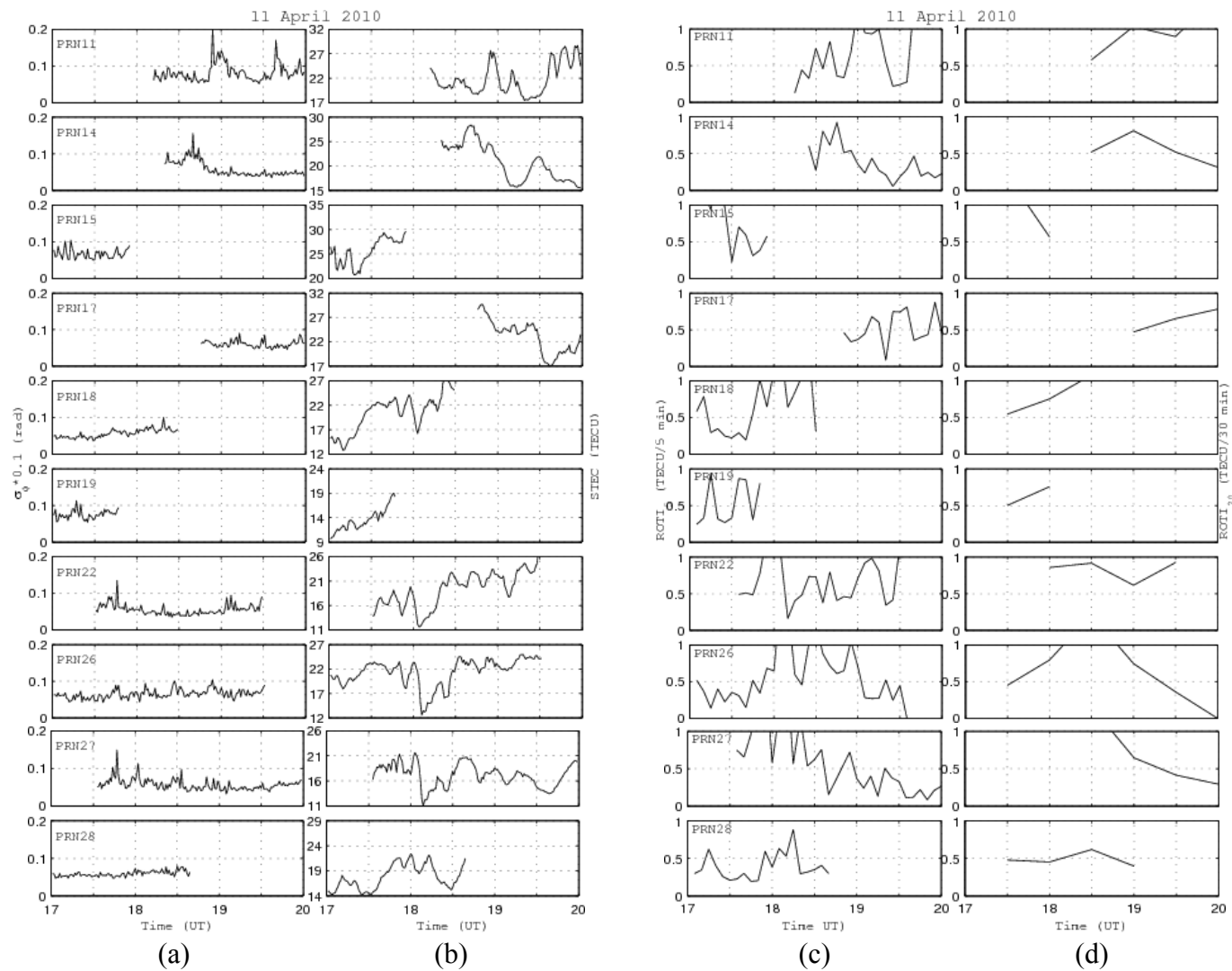


Figure 6.60: (a) σ_{ϕ} , (b) STEC, (c) ROTI₅ and (d) ROTI₃₀ observed on each visible satellite on 11 April 2010 from 1700 to 2000 UT. Note the different values on y-axis for STEC, but grid scale is equal

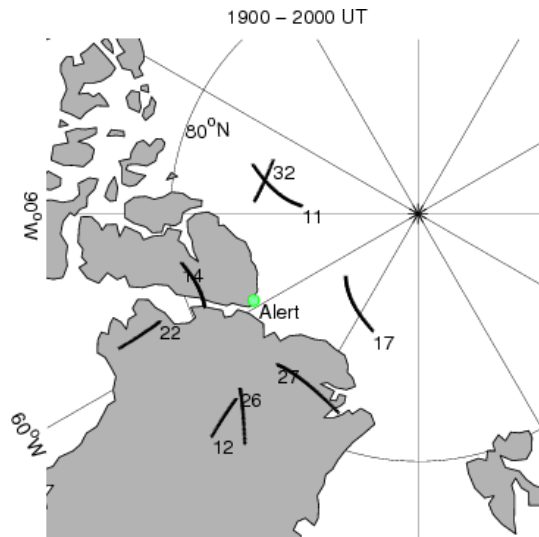


Figure 6.61: Satellites path over Alert at 350 km on 11 April 2010 from 1900 to 2000 UT

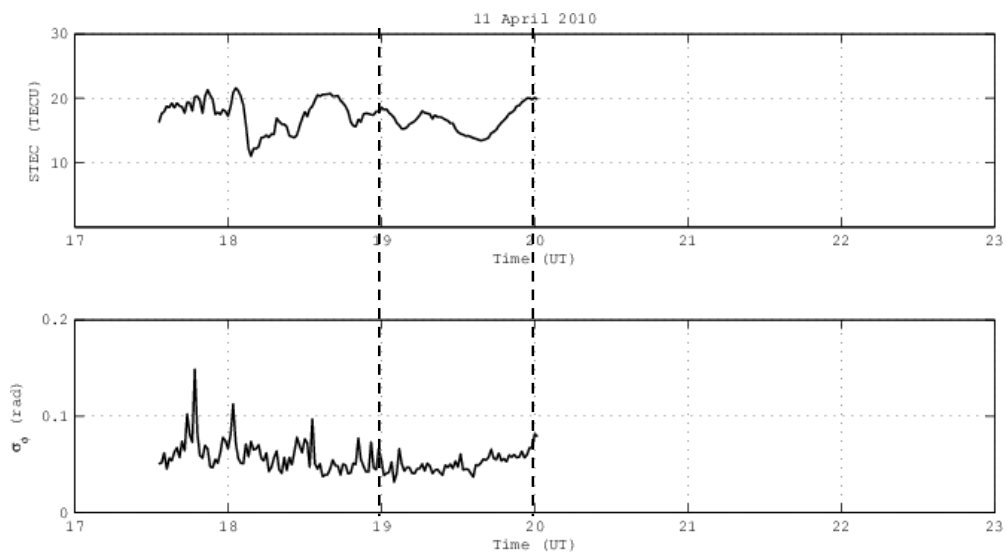


Figure 6.62: Slant TEC (top) and σ_{ϕ} (bottom) of PRN27 over Alert from 1700 to 2300 UT on 11 April 2010. The vertical lines indicates the period of interest

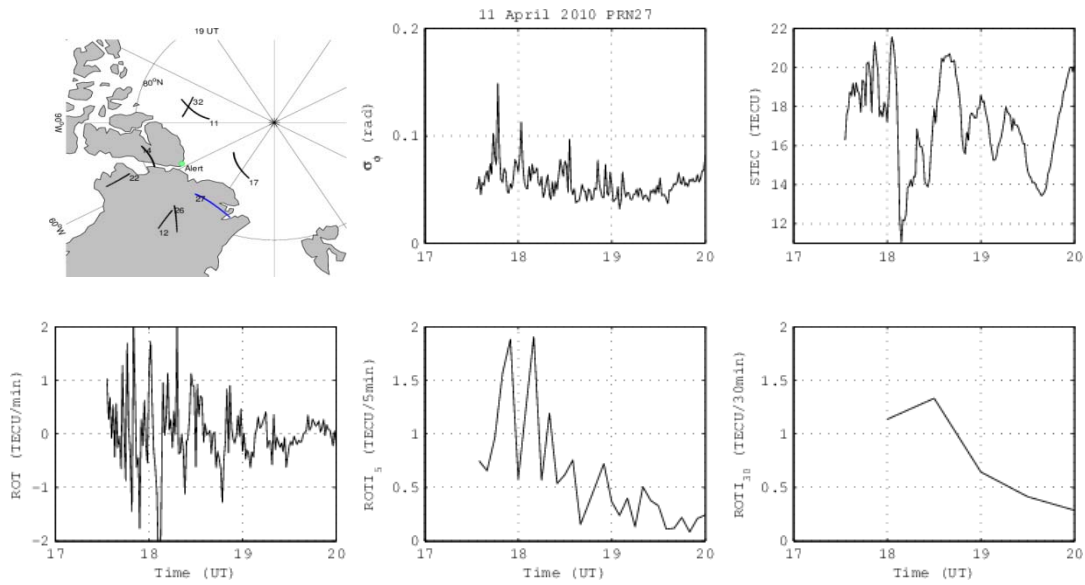


Figure 6.63: σ_ϕ , STEC, ROT, and ROTI of PRN27 on 11 April 2010. Paths of all visible satellites from 1900 to 2000 UT at 350 km are also shown

However, even though TEC behaviour is similar to the previous example, the Doppler spreads characteristic is different. Doppler spreads on 10.38 MHz were low, up to only 2.5 Hz during this hour, as shown in Figure 6.64. A selection of delay-Doppler spectra is illustrated in Figure 6.65.

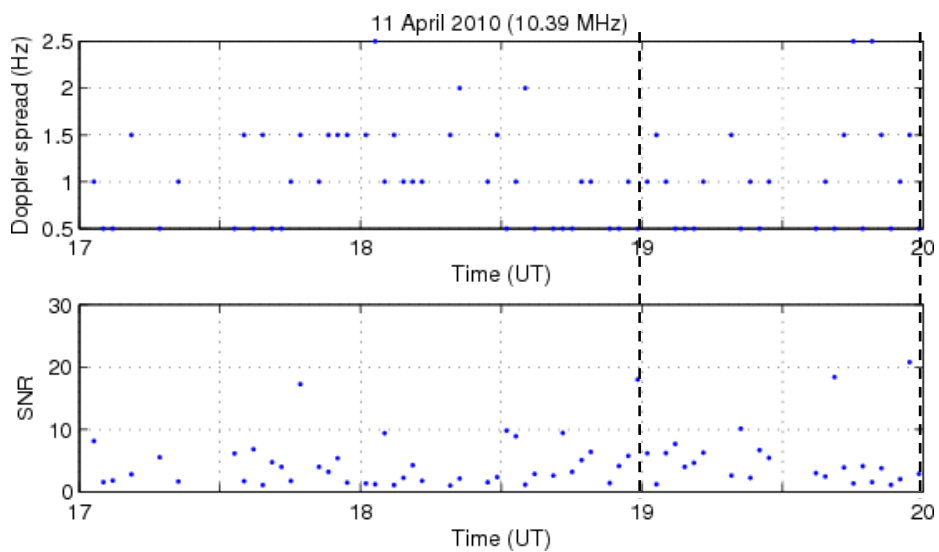


Figure 6.64: Doppler spread (top) and SNR (bottom) on 10.39 MHz from 1700 to 2000 UT on 11 April 2010. The vertical lines indicates the period of interest

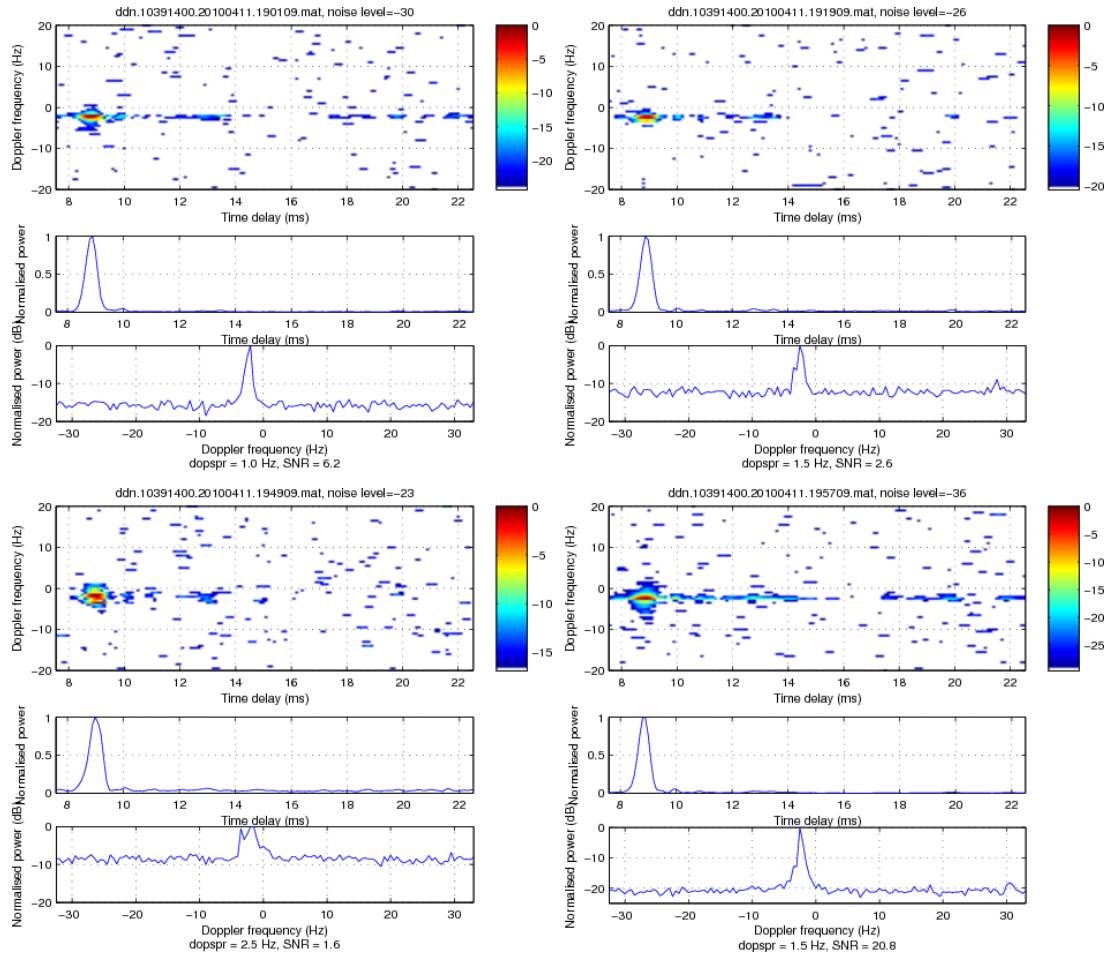


Figure 6.65: Selected delay-Doppler spectra on 10.39 MHz between 1900 and 2000 UT on 11 April 2010

Over Svalbard, the satellite closest to the HF midpoint, PRN14 did not demonstrate significant increase in both slant TEC and σ_{ϕ} (Figure 6.66 and Figure 6.67). Path of PRN14 and all other visible satellites between 1900 and 1959 UT is illustrated in Figure 6.68. B_z was southward until ~ 2000 UT and then fluctuated between negative and positive polarities until ~ 2200 UT (see Figure 6.69). Figure 6.70 shows that the magnetic fields at Eureka and Resolute Bay were mostly at the negative values up to ~ 110 nT. K_p was 4- during this hour.

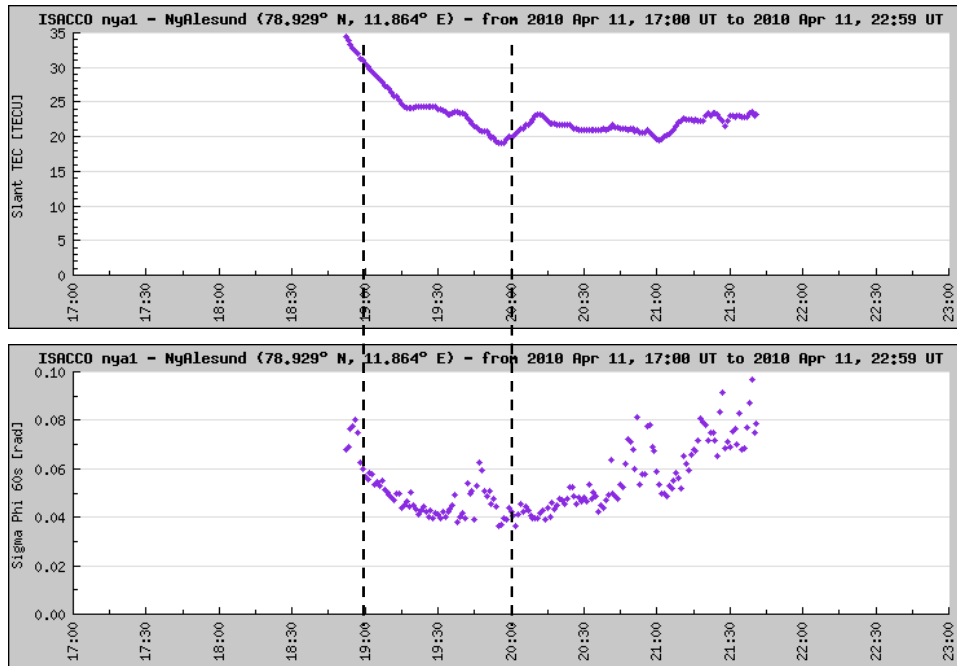


Figure 6.66: Slant TEC (top) and σ_ϕ (bottom) of PRN14 over Ny-Ålesund from 1700 to 2300 UT on 11 April 2010. The vertical lines indicates the period of interest

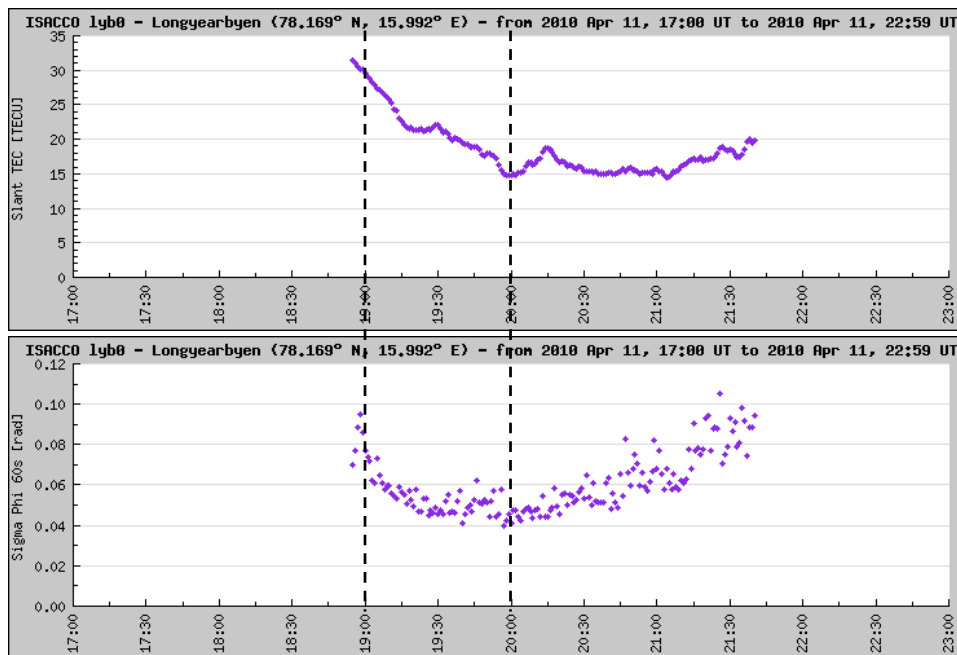


Figure 6.67: Slant TEC (top) and σ_ϕ (bottom) of PRN14 over Longyearbyen from 1700 to 2300 UT on 11 April 2010. The vertical lines indicates the period of interest

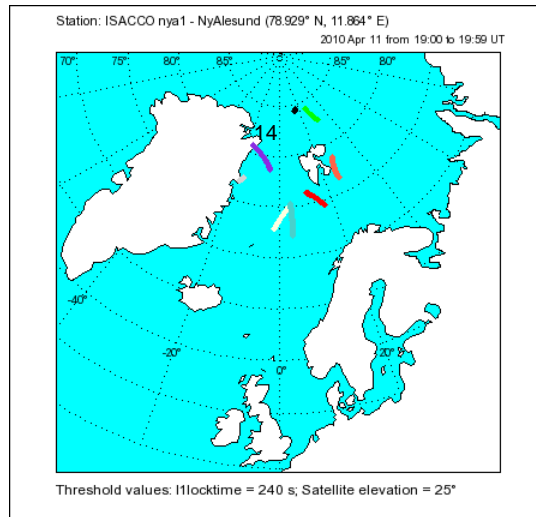


Figure 6.68: Colour-coded satellites path over Ny-Ålesund at 350 km on 11 April 2010 from 1900 to 1959 UT

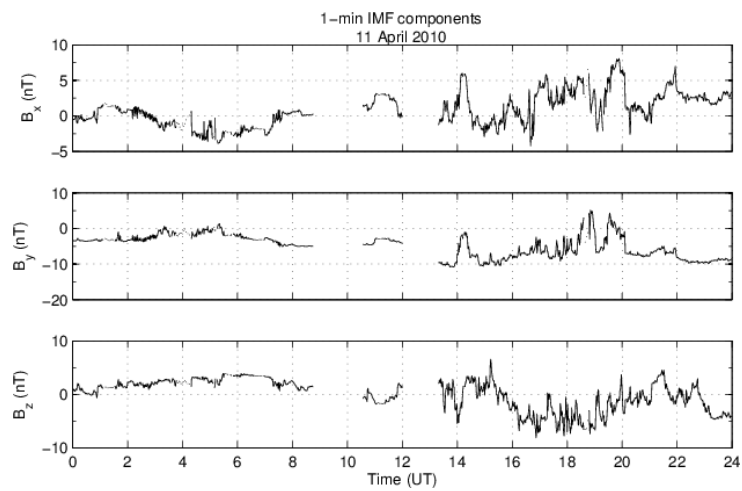


Figure 6.69: 1-minute IMF components on 11 April 2010

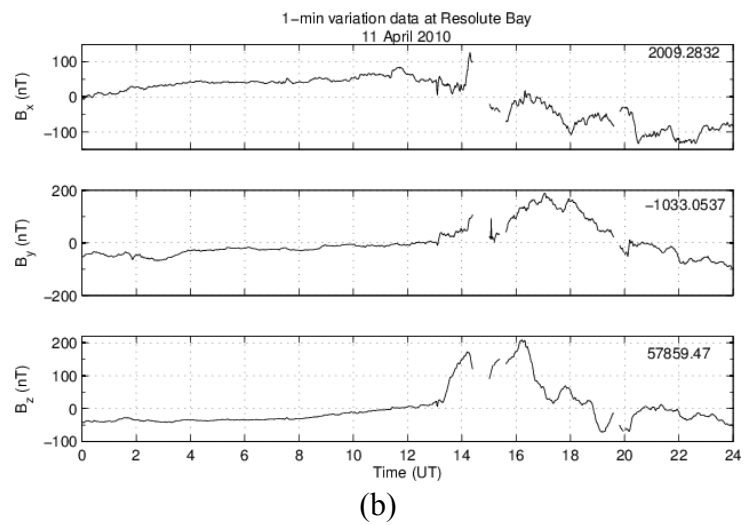
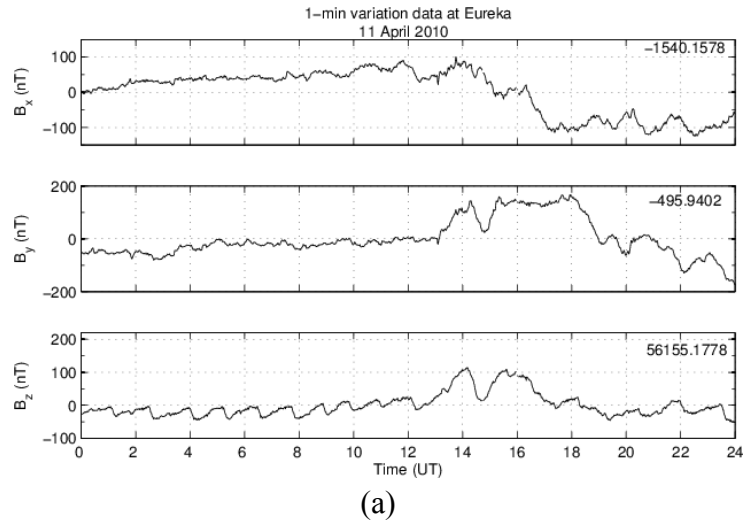


Figure 6.70: 1-minute variation data at (a) Eureka, and (b) Resolute Bay on 11 April 2010

Event Type B4

An example of large Doppler spreads but with no large TEC variations and phase scintillations is discussed next. Figure 6.71 shows the Doppler spreads and SNR of signals received on 14.36 MHz from 1500 to 1800 UT on 8 October 2009 (the same day was also discussed in Event Type B2 but for different time of interest). Doppler spreads were large, mostly > 5 Hz from ~ 1615 UT onwards. A selection of large Doppler spreads on 14.36 MHz between 1600 and 1700 UT is illustrated in Figure

6.72. Doppler spreads on 6.95, 8.01 and 11.12 MHz were all < 4 Hz, and no significant signals were received on 4.64 and 10.39 MHz.

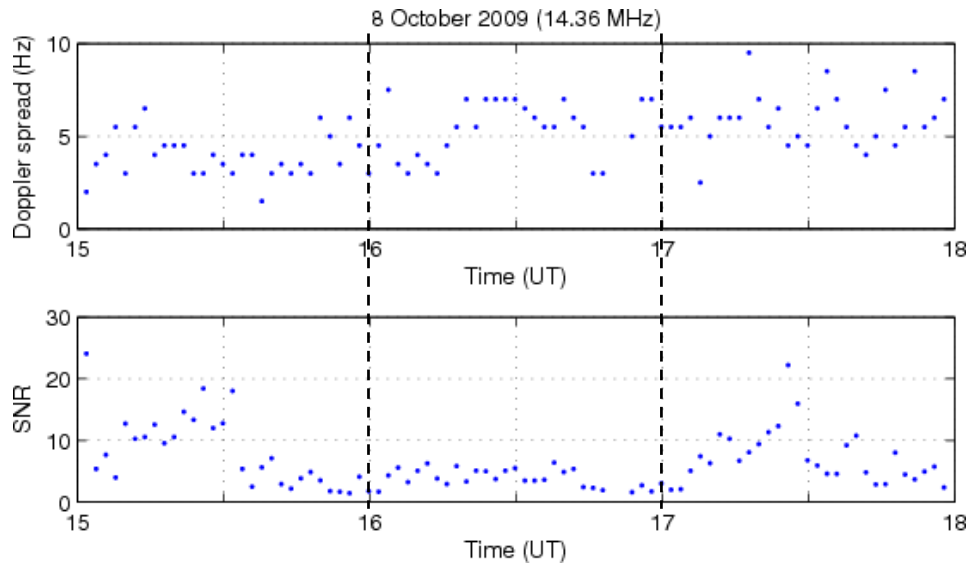


Figure 6.71: Doppler spread (top) and SNR (bottom) on 14.36 MHz from 1500 to 1800 UT on 8 October 2009. The vertical lines indicates the period of interest

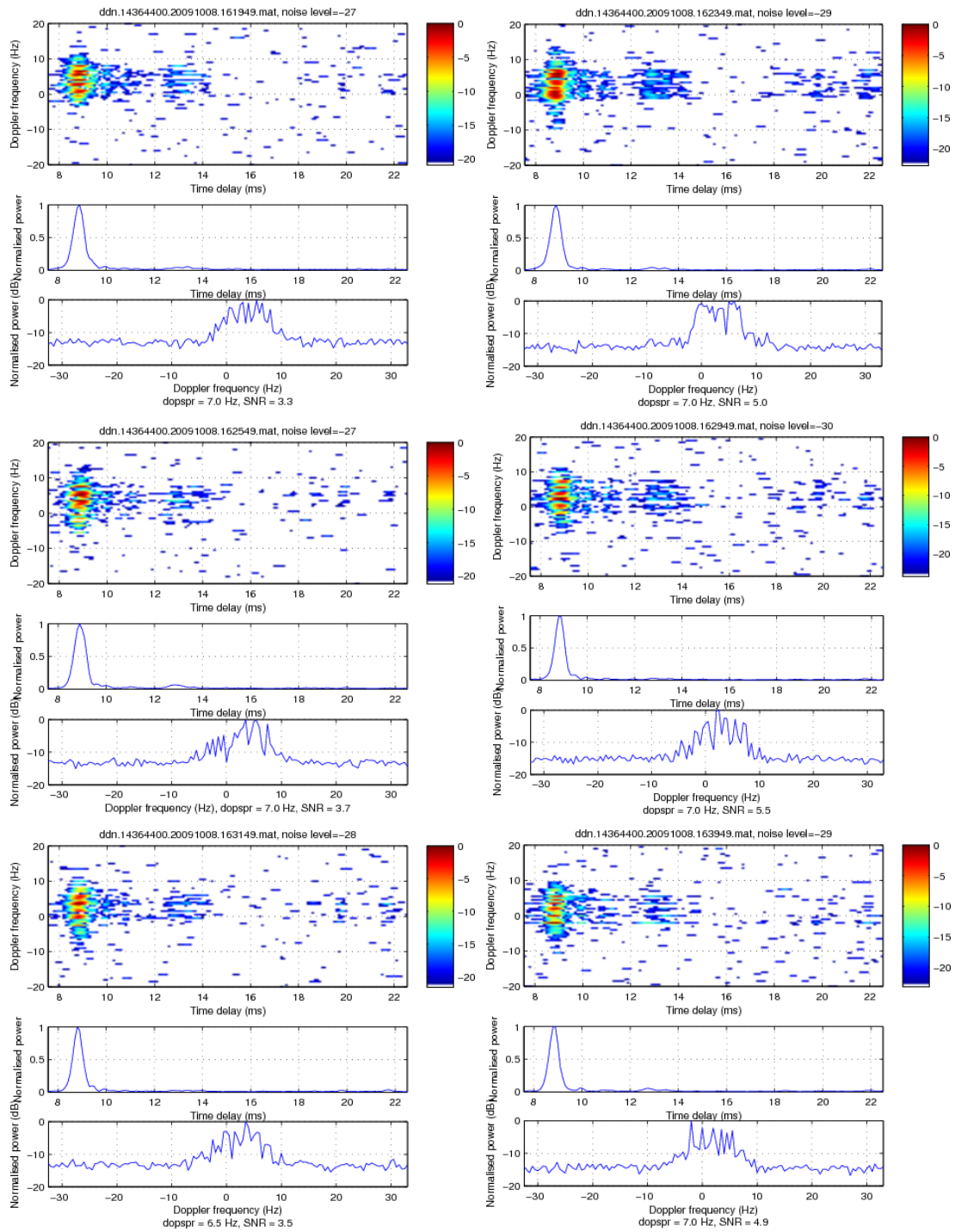


Figure 6.72: Selected delay-Doppler spectra on 14.36 MHz between 1600 to 1700 UT on 8 October 2009

Figure 6.73 illustrated the slant TEC and σ_ϕ of PRN7 and PRN8 with the period of interest from 1600 to 1700 UT. The path of all satellites over Ny-Ålesund during this hour is illustrated in Figure 6.74. PRN8 was closer to the HF midpoint compared to PRN7. Besides, PRN7 was only visible above Ny-Ålesund until ~1625 UT. Only a small increase of ~2 TECU of ~30-minute duration from ~1630 to ~1700 UT was observed on PRN8. σ_ϕ was also low during this hour. Data was not available for Longyearbyen during the period of observations.

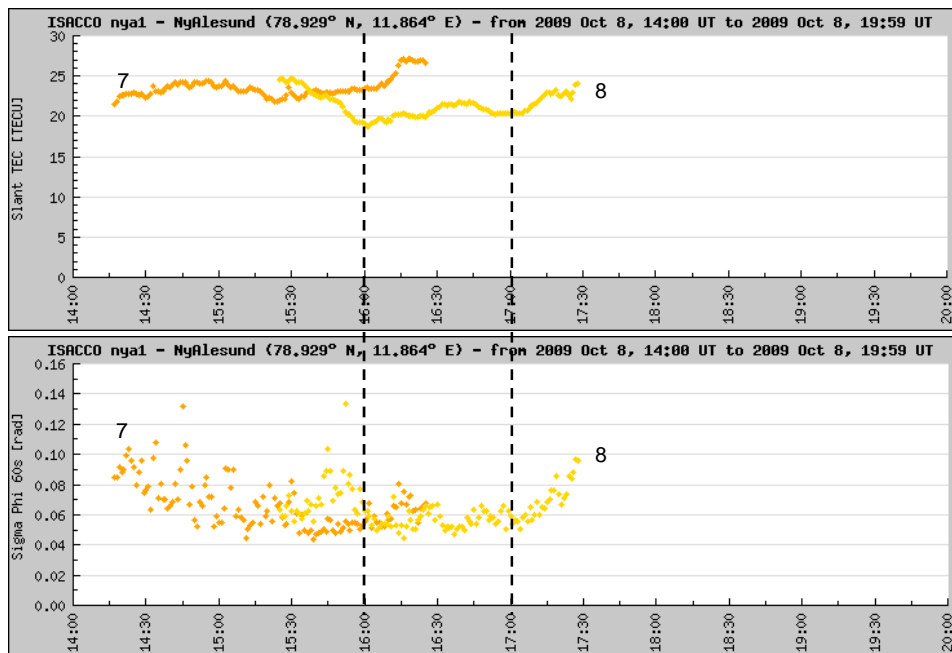


Figure 6.73: Slant TEC (top) and σ_ϕ (bottom) of PRN7 and PRN8 over Ny-Ålesund from 1400 to 2000 UT on 8 October 2009. The vertical lines indicates the period of interest

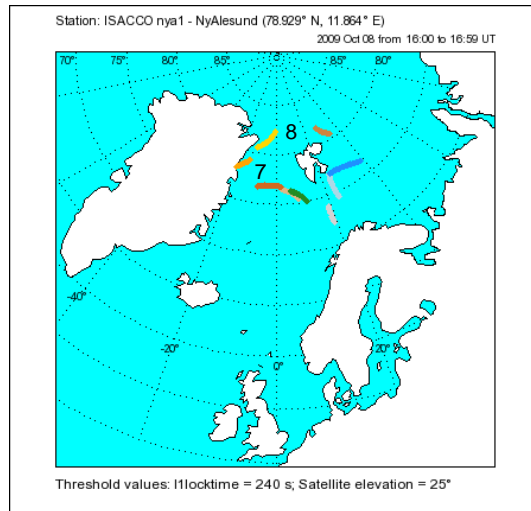


Figure 6.74: Colour-coded satellites path over Ny-Ålesund at 350 km on 8 October 2009 from 1600 to 1659 UT

Similar to PRN8 that was observed from the GISTM receiver in Ny-Ålesund, PRN6 also experienced a long-duration small increase of slant TEC as observed from Alert (Figure 6.75). PRN18 did not demonstrate any significant increase on the slant TEC and also on σ_{ϕ} . Since PRN3 was at the same track orientation as PRN6 (see Figure 6.76), the behaviour of slant TEC and σ_{ϕ} is also similar. Details of σ_{ϕ} , slant TEC, rate of TEC and ROTI for PRN6 and PRN18 are illustrated in Figure 6.77 and Figure 6.78, respectively. The rate of TEC indicates that there was no large variation of TEC per minute, and only small weak patches were observed based on ROTI illustration. B_z was mostly positive during 1600-1700 UT before changing polarity (refer Figure 6.35). Magnetic data at Eureka for each component did not exceed ± 25 nT from their respective means (refer Figure 6.36).

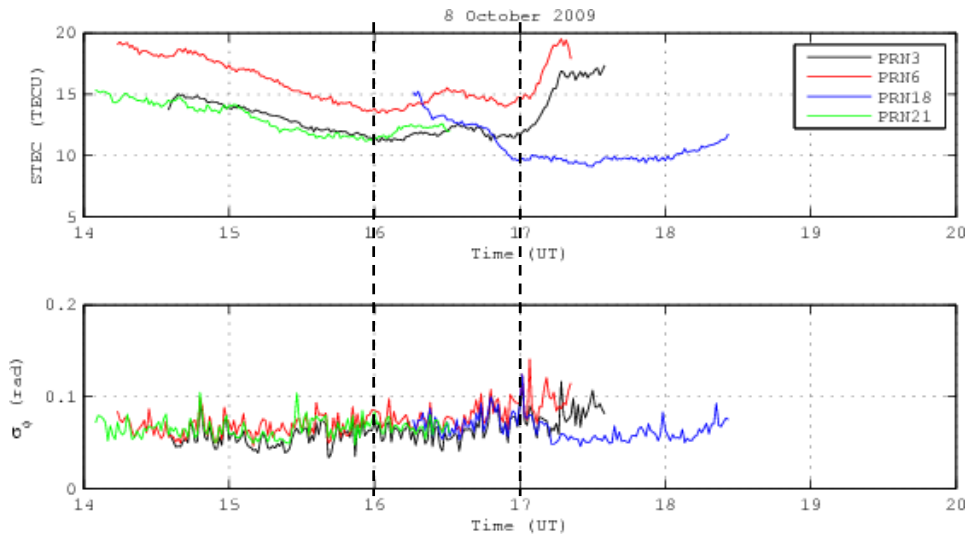


Figure 6.75: Slant TEC (top) and σ_ϕ (bottom) of PRN3, 6, 18 and 21 over Alert from 1400 to 2000 UT on 8 October 2009. The vertical lines indicates the period of interest

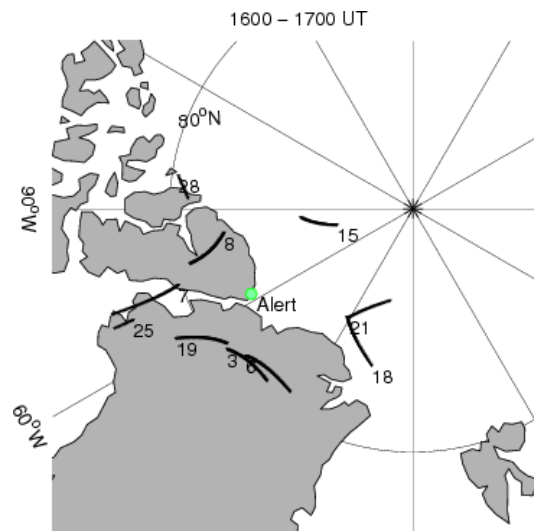


Figure 6.76: Satellites path over Alert at 350 km on 8 October 2009 from 1600 to 1700 UT

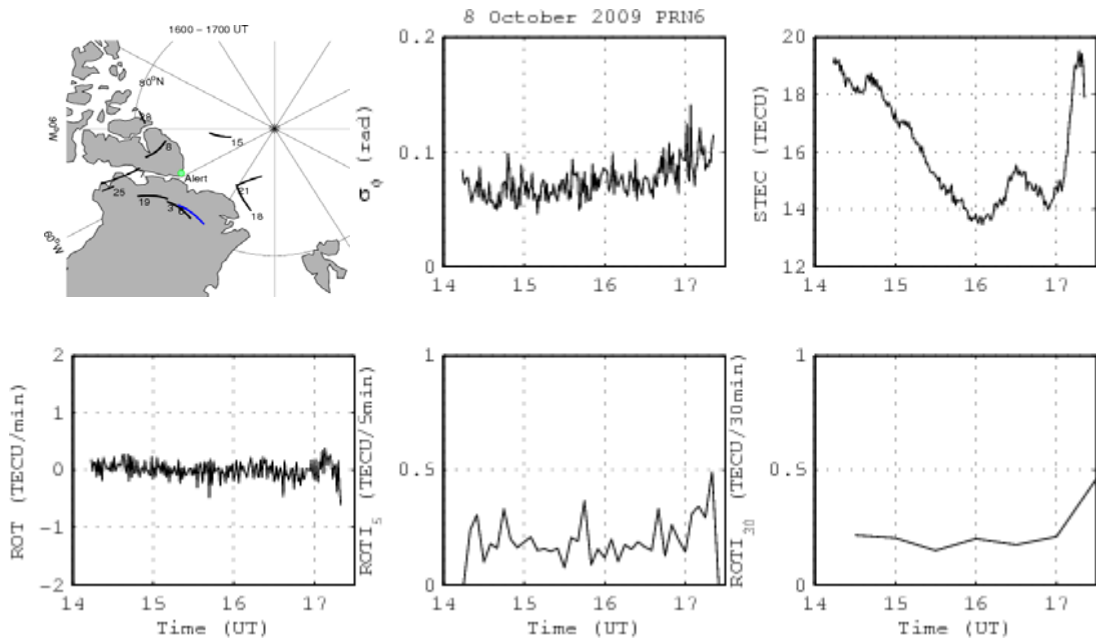


Figure 6.77: σ_ϕ , STEC, ROT, and ROTI for 5- and 30-min interval of PRN6 on 8 October 2009 from 1400 to 1730 UT. Paths of all visible satellites between 1600 and 1700 UT at 350 km are also shown

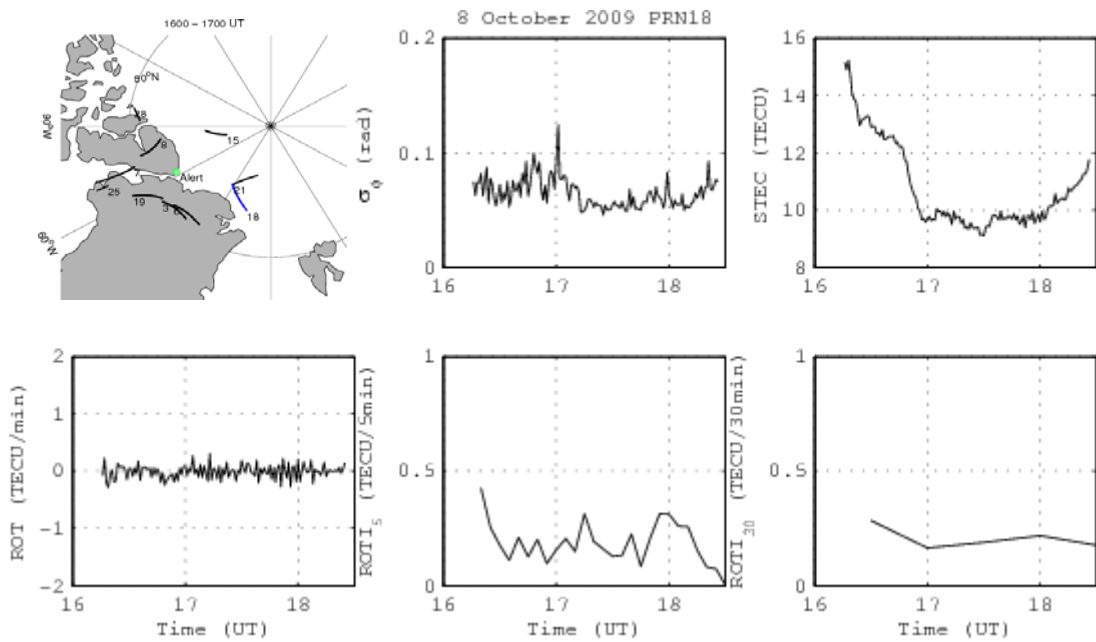


Figure 6.78: σ_ϕ , STEC, ROT, and ROTI for 5- and 30-min interval of PRN18 on 8 October 2009 from 1600 to 1830 UT. Paths of all visible satellites between 1600 and 1700 UT at 350 km are also shown

Another example for Event Type B4 is on 13 April 2010 between 0200 and 0300 UT. Large Doppler spreads of ~ 5 -10 Hz were detected on 6.95 MHz in this hour (see Figure 6.79 (a)). Similar Doppler spreads were also observed on 8.01 MHz but only between 0200 and 0215 UT (Figure 6.79 (b)).

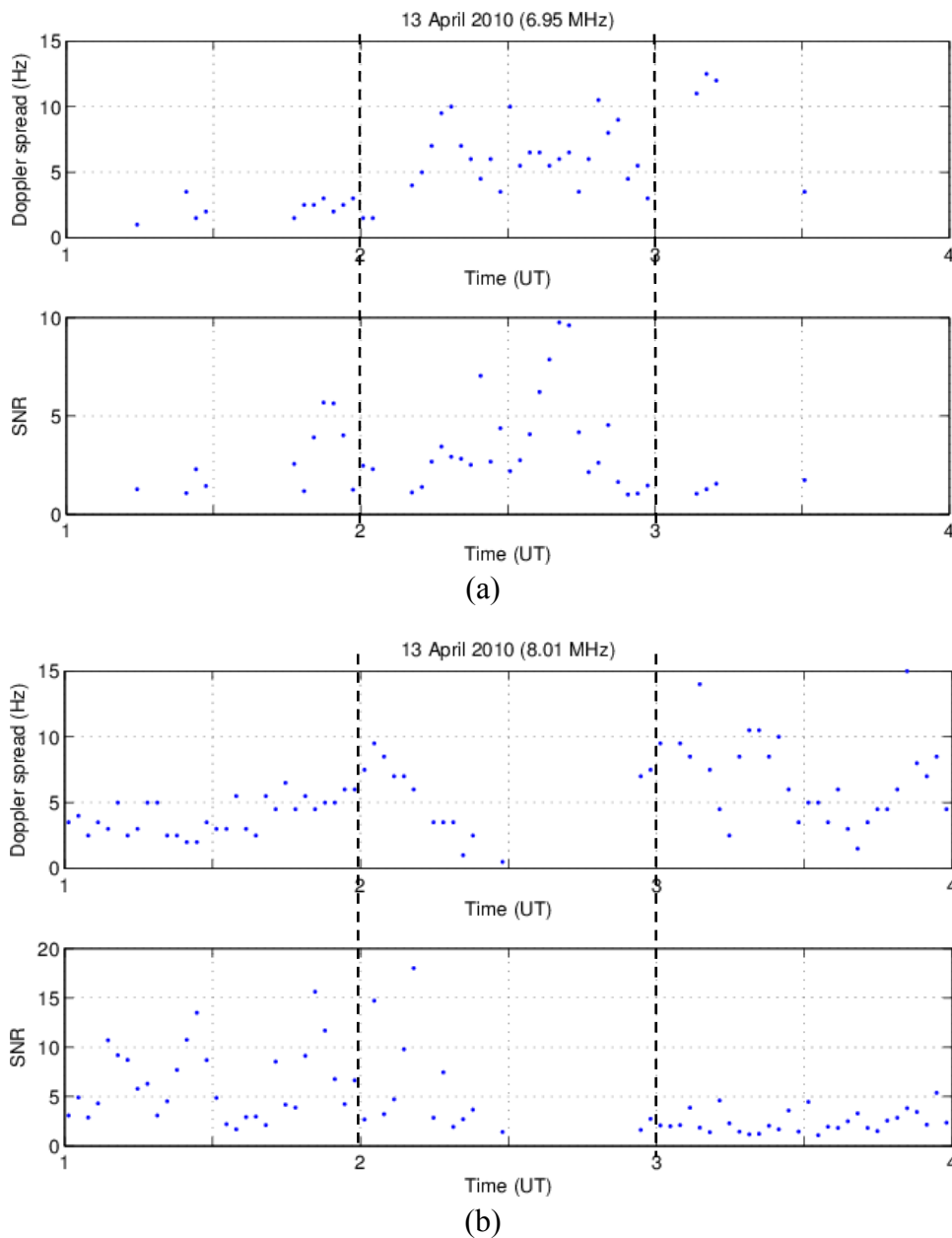


Figure 6.79: Doppler spread (top) and SNR (bottom) on (a) 6.95 MHz and (b) 8.01 MHz from 0100 to 0400 UT on 11 April 2010. The vertical lines indicates the period of interest

Figure 6.80 and Figure 6.81 illustrated the slant TEC and σ_ϕ of PRN7 above Ny-Ålesund and Longyearbyen, respectively with the period of interest from 0200 to 0300 UT. The path of all satellites over Ny-Ålesund during this hour is illustrated in Figure 6.82. No significant TEC variations can be observed on PRN7. σ_ϕ was also low during this hour which was less than 0.1 rad. Similar observations of TEC and σ_ϕ were registered on the satellites above Alert that were closest to the HF midpoint (i.e. PRN21 and PRN24) as demonstrated in Figure 6.83. The path of all visible satellites over Alert is shown in Figure 6.84.

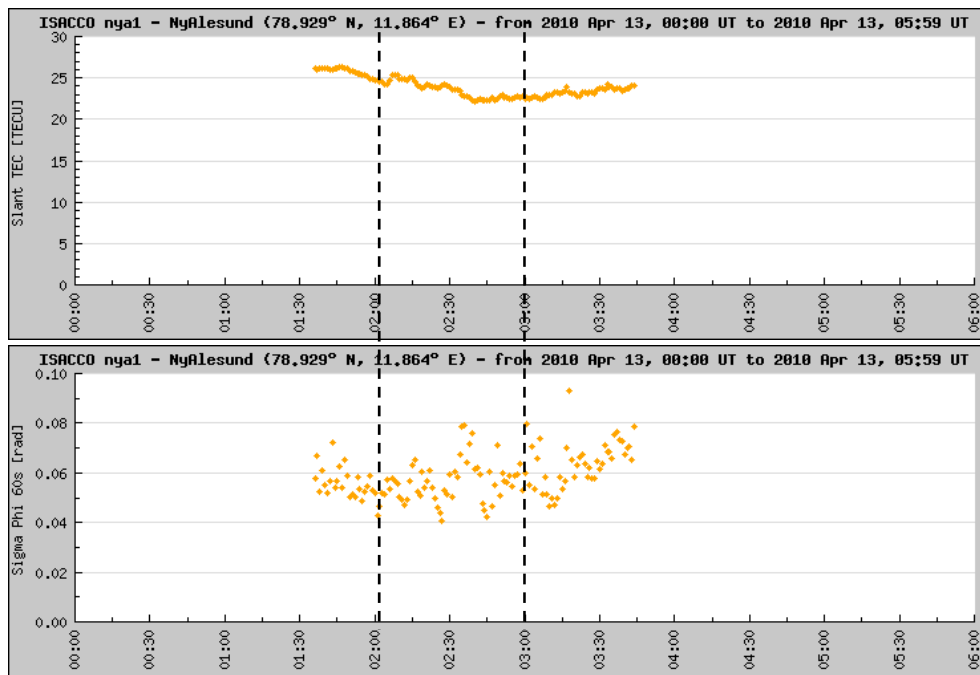


Figure 6.80: Slant TEC (top) and σ_ϕ (bottom) of PRN7 over Ny-Ålesund from 0000 to 0600 UT on 13 April 2009. The vertical lines indicates the period of interest

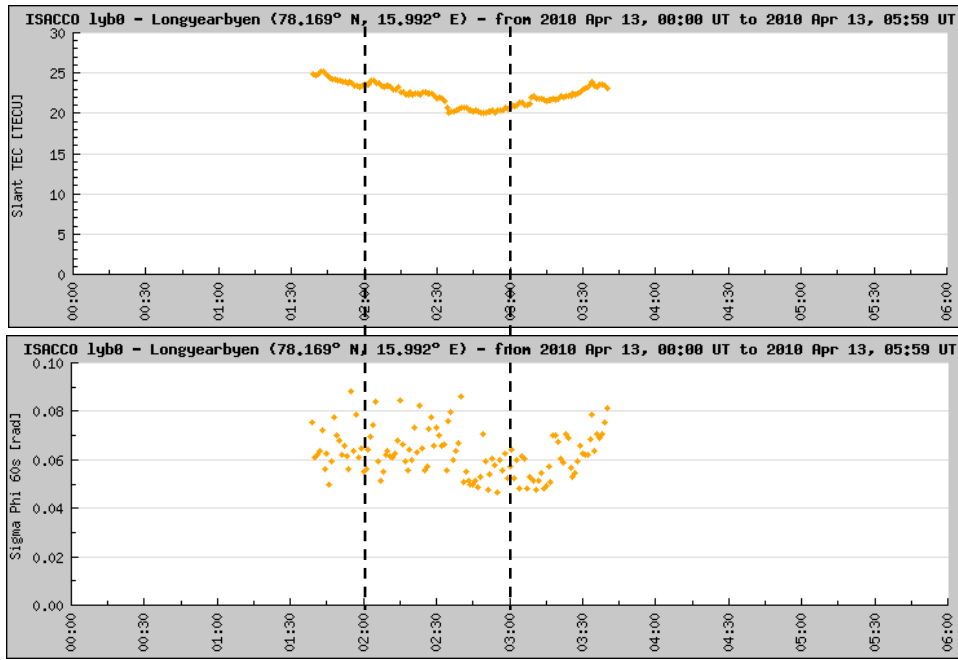


Figure 6.81: Slant TEC (top) and σ_ϕ (bottom) of PRN7 over Longyearbyen from 0000 to 0600 UT on 13 April 2009. The vertical lines indicates the period of interest

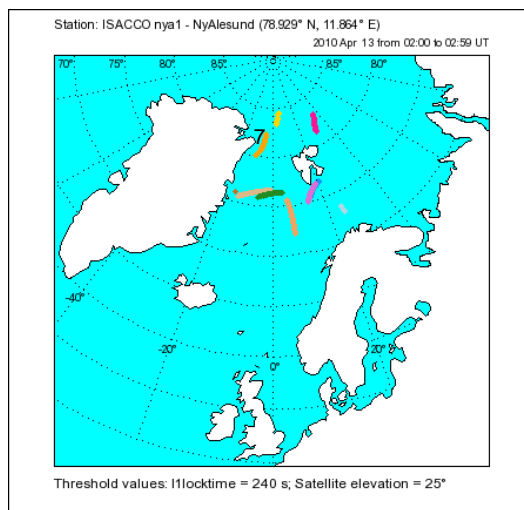


Figure 6.82: Colour-coded satellites path over Ny-Ålesund at 350 km on 13 April 2010 from 0200 to 0259 UT

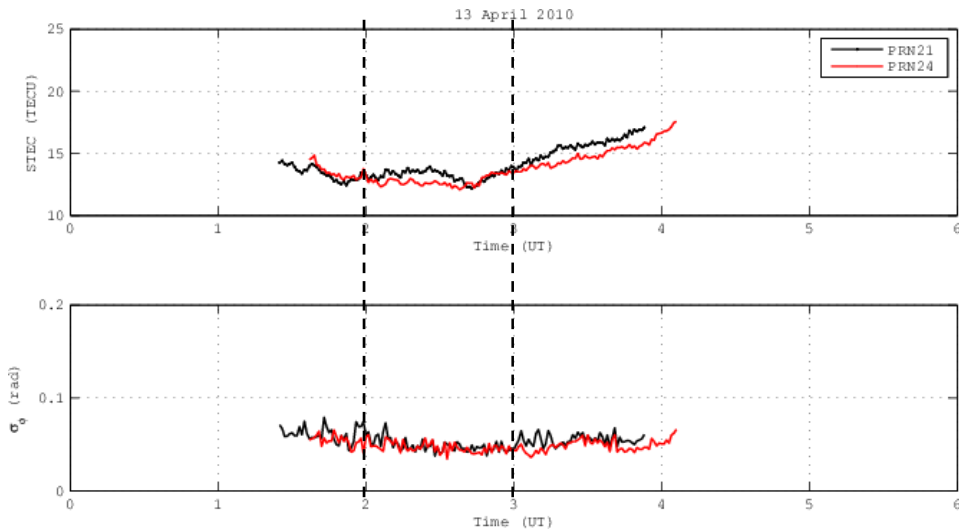


Figure 6.83: Slant TEC (top) and σ_ϕ (bottom) of PRN21 and PRN24 over Alert from 0000 to 0600 UT on 13 April 2010. The vertical lines indicates the period of interest

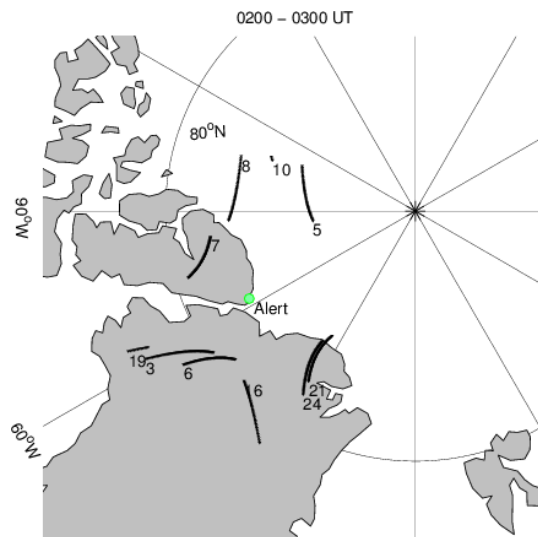


Figure 6.84: Satellites path over Alert at 350 km on 13 April 2010 from 0200 to 0300 UT

Detailed observation on the slant TEC of both satellites showed small TEC fluctuation of ~ 1 -1.5 TECU during the period of interest. No patches were registered in this hour except for one small weak patches on PRN24 (Figure 6.85). All IMF components around the period of observations did not exceed ± 5 nT (Figure 6.86)

while the variation of the magnetic data from their respective means at both Eureka and Resolute Bay were small with relatively more magnetic activities were observed at Eureka than at Resolute Bay (Figure 6.87).

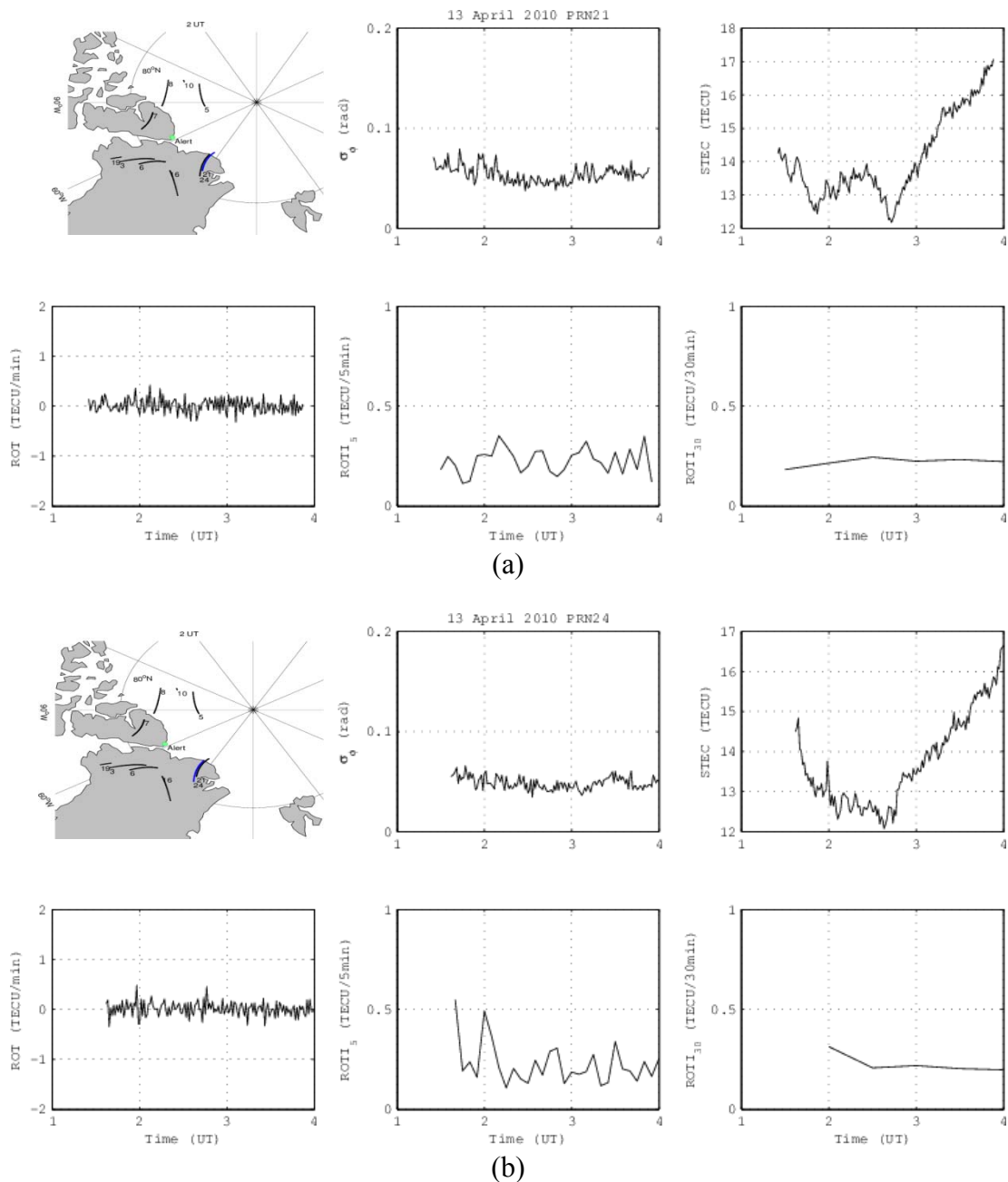


Figure 6.85: σ_0 , STEC, ROT, and ROTI for 5- and 30-min interval of (a) PRN21 and (b) PRN24 on 13 April 2010 from 0100 to 0400 UT. Paths of all visible satellites between 0200 and 0300 UT at 350 km are also shown

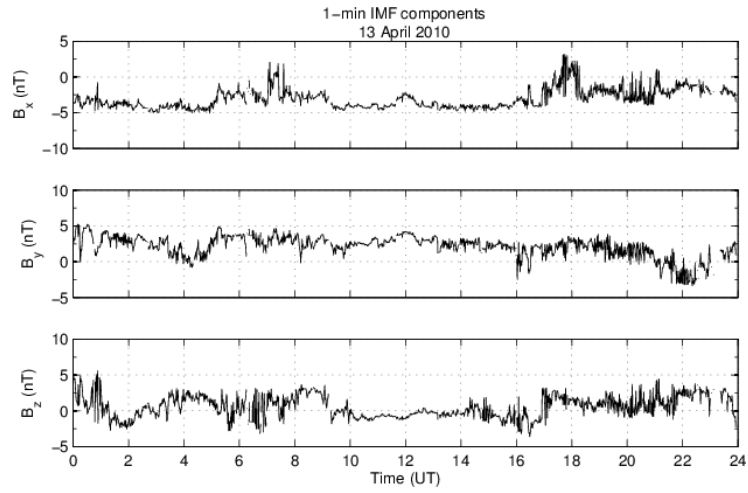
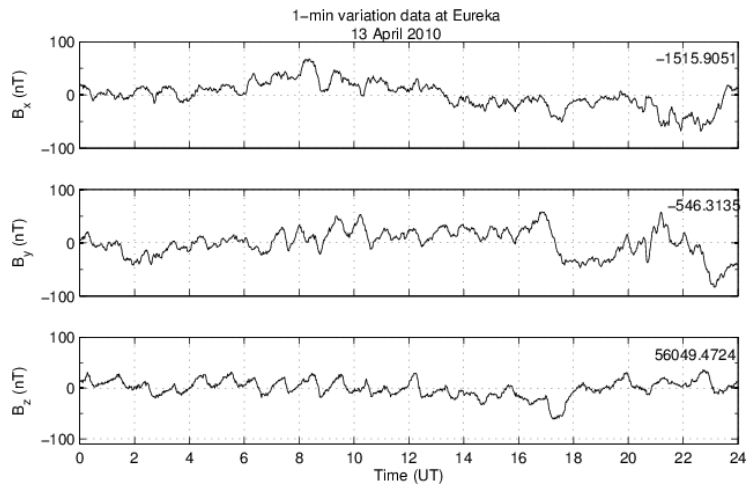
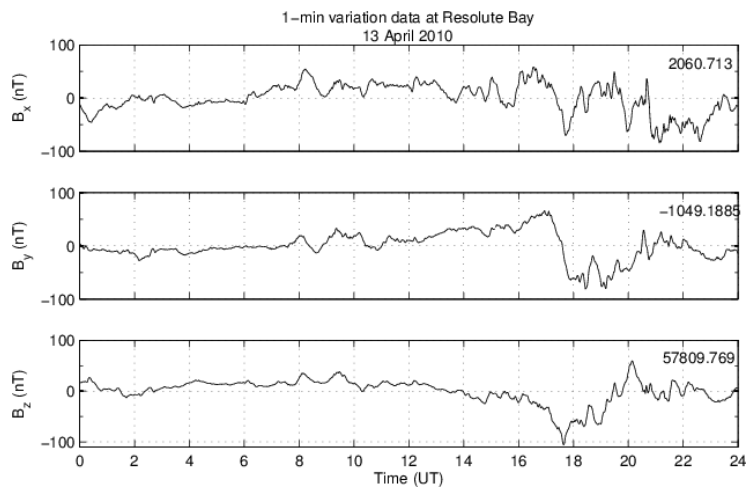


Figure 6.86: 1-minute IMF components on 13 April 2010



(a)



(b)

Figure 6.87: 1-minute variation data at (a) Eureka, and (b) Resolute Bay on 13 April 2010

6.2 Concluding Remarks

This chapter discusses the relation of the Doppler spreads with the TEC variations and phase scintillations around the HF midpoint. The dependence on various geomagnetic conditions was also observed, where it also have been discussed in Chapter Five. Selected events were chosen and then discussed in detail. Table 6.2 summarises the daily sunspot number, the maximum 3-hour geomagnetic indices and also the maximum 1-hour polar cap index for a particular day in each event type. Description of each event type can be found in Table 6.1. Event B1 is specifically to observe to effect of high geomagnetic indices on Doppler spread as has been discussed in Chapter Five. Event B3 was during the unsettled geomagnetic conditions while the other two event types were during quiet ionosphere.

Table 6.2: Sunspot number (SSN), maximum geomagnetic index (K_p) and maximum polar cap index ($PC(N)$) for every case in each event type

Event Type	Date	SSN	Max. K_p	Max. $PC(N)$
B1	4 Feb 2011	22	6-	4.3
	5 Apr 2010	26	8-	5.1
B2	8 Oct 2009	0	1+	0.7
	4 Oct 2009	0	2+	0.6
B3	15 Feb 2010	20	4+	3.8
	11 Apr 2010	8	4-	2.8
B4	8 Oct 2009	0	1+	0.7
	13 Apr 2010	7	2	0.9

Based on all the cases presented in this chapter, the relation between the irregularities observed at Alert via transionospheric link and HF link is complex. Large TEC fluctuations/increases and/or phase scintillations observed on satellite(s) close to HF midpoint may correspond to either small or large Doppler spreads as summarised in Table 6.3. Example presented on 15 February 2010 between 1600 and 1900 UT shows that large Doppler spread of up to 9 Hz was observed during the period of TEC fluctuations (as indicated by the ROT) that formed around 11-13 moderate to high intensity of small patches and also 2-3 large patches. Phase scintillations were also relatively high during this period.

Similar trait was observed on 4 October 2009 (1500-1700 UT) and 8 October 2009 (1800-1900 UT) where large Doppler spread of 9.5-15 Hz corresponded to 1-6 small patches of moderate to high intensity and 1-2 large patches. The difference with the previous case is on the intensity of the TEC fluctuations. This is reflected in the number of the patches formed on both cases.

However, the co-existence of patches and large Doppler spreads was not registered at all time. For example, large Doppler spread of up to 7.5-10.5 Hz on 13 April 2010 (0200-0300 UT) and 8 October 2009 (1600-1700 UT) did not trigger the formation of moderate to high intensity of either small or large patches on the satellites over the HF midpoint. In addition, even high geomagnetic indices did not guarantee the co-existence of patches and large Doppler spreads as in the case observed on 5 April 2010 where disturbed ionospheric conditions did not trigger either large Doppler spread or both small and large patches of moderate to high intensity. Phase scintillations however, reached up to ~ 0.2 rad on this day.

Table 6.3: No. of patches, minimum and maximum ROT, maximum σ_ϕ , and maximum Doppler spread for every case in each event type during a specified 1-hr period except on 4 February 2011. The Number of data for the satellites(s) in the specified period and the number of data of Doppler spread on a particular frequency are also included

Event Type	Date	Period (UT)	PRN	No. of data	No. of patches				Min. ROT (TECU/min)	Max. ROT (TECU/min)	Max. σ_ϕ (rad)	No. of data of Doppler spread	Max. Doppler spread (Hz)	Frequency (MHz)
					Small		Large							
					Low	Med-high	Low	Med-high						
B1	4 Feb 2011	1800-0000	n/a	n/a	n/a	n/a	n/a	n/a	n/a	n/a	73	9.5	6.95	
	5 Apr 2010	0600-0700	19	28	3	0	1	0	0.07	-0.23	0.20	7	1.5	8.01
		0700-0800	11, 32	85	7	0	0	0	0.07	-0.16	0.20	8	2.0	
		0800-0900	11, 32	106	15	0	4	0	0.09	-0.31	0.21	2	2.0	
B2	8 Oct 2009	1800-1900	19, 22	98	12	1	2	1	-0.56	0.45	0.13	21	9.5	14.36
	4 Oct 2009	1500-1600	16, 21	97	11	6	2	2	-0.41	0.51	0.14	11	15.0	10.39
		1600-1700	6, 18	79	9	2	3	0	-0.29	0.39	0.15	9	11.0	
B3	15 Feb 2010	1600-1700	7, 13	69	0	11	0	2	-0.58	1.03	0.13	29	6.5	10.39
		1700-1800	7, 8, 13	92	6	11	0	3	-0.80	0.62	0.17	29	7.5	
		1800-1900	7, 8	118	9	13	1	3	-0.70	0.80	0.16	21	9.0	
		1900-2000	8	59	3	2	1	1	-0.47	0.63	0.08	10	2.0	
	11 Apr 2010	1900-2000	27	59	7	1	2	0	-0.24	0.23	0.07	24	2.5	10.39
B4	8 Oct 2010	1600-1700	6, 18	103	7	0	2	0	-0.24	0.26	0.11	28	7.5	14.34
	13 Apr 2010	0200-0300	21, 24	118	14	0	3	0	-0.24	0.26	0.07	26	10.5	6.95

Observations on GPS data over Alert and Svalbard around the HF midpoint did not necessarily demonstrate total similarity since the closest satellite to the HF midpoint observed at each station is at different sides of the midpoint. This could be due, for example, to the size of the irregularities and also the area of occurrence. The number of patches observed on satellites above Svalbard could not be determined since TEC and scintillations data were plotted directly from INGV website.

IMF components do not show any particular effect on Doppler spreads intensities. Similar observations can be said regarding the magnetic field effects at Eureka and Resolute Bay. The minimum and maximum values of each component did not show correlation to the Doppler spreads in any event type (Table 6.4 and Table 6.5). However, large swing of magnetic components were observed on both stations on 4 February 2011 and 5 April 2010 where geomagnetic indices reached up to 6- and 8-. The magnitude of B_x and B_y components on both stations in Event Type B3 where both days corresponded to unsettled geomagnetic conditions (i.e. $K_p = 4$) were also higher than the rest of the cases. The magnitude of IMF components on Event Type B1 was also larger than in other event types.

The percentage of the positive polarities of each component is presented in Table 6.6. No specific pattern can be concluded on the relation between large Doppler spreads and the polarities of the magnetic components of IMF and also of the polar cap stations. Relation of magnetic field components and TEC variations and phase scintillations has been discussed in Chapter Four.

Table 6.4: Minimum values of each magnetic component of IMF, Eureka (EUA) and Resolute Bay (RES) for every case in each event type during a specified period. Different time frame was applied for each case, but mean value for each component at Eureka and Resolute Bay was calculated for 1-day period

Event Type	Date	Period (UT)	Min. IMF (nT)			Min. EUA (nT)			Min. RES (nT)		
			B _x	B _y	B _z	B _x	B _y	B _z	B _x	B _y	B _z
B1	4 Feb 2011	1800-0000	-5.3	-17.3	-20.6	n/a	n/a	n/a	-216.5	-126.9	-75.8
	5 Apr 2010	0600-1200	-6.1	-15.1	-15.0	-100.4	-95.9	-67.2	-121.2	-164.6	-108.8
B2	8 Oct 2009	1800-1900	0.0	-2.7	-3.4	-16.9	9.5	-0.8	-44.4	8.0	3.5
	4 Oct 2009	1500-1700	-3.2	-7.0	-5.1	-32.7	-36.9	-15.8	-56.5	-34.5	-51.3
B3	15 Feb 2010	1600-2000	-5.2	-11.2	-11.8	-101.2	24.6	-14.2	-89.7	27.3	-10.0
	11 Apr 2010	1900-2000	-2.2	-6.8	-6.7	-105.9	-62.1	-45.9	-84.1	-45.2	-71.6
B4	8 Oct 2009	1600-1700	0.6	-2.9	-2.4	-20.2	-4.8	-1.4	-15.7	8.7	-2.5
	13 Apr 2010	0200-0300	-5.0	1.4	-2.2	-15.8	-41.2	-19.6	-9.2	-28.0	-8.7

Table 6.5: As in Table 6.4 but for maximum values of each component

Event Type	Date	Period (UT)	Max. IMF (nT)			Max. EUA (nT)			Max. RES (nT)		
			B _x	B _y	B _z	B _x	B _y	B _z	B _x	B _y	B _z
B1	4 Feb 2011	1800-0000	16.1	14.2	15.0	n/a	n/a	n/a	-11.0	32.6	65.6
	5 Apr 2010	0600-1200	10.7	11.3	18.9	332.3	480.9	129.2	321.3	304.7	459.4
B2	8 Oct 2009	1800-1900	1.9	-1.8	0.4	-1.2	23.2	7.4	-33.7	18.8	16.1
	4 Oct 2009	1500-1700	3.8	-2.3	6.7	1.3	35.7	25.1	8.3	34.4	32.1
B3	15 Feb 2010	1600-2000	1.9	-2.9	-1.6	-5.1	123.2	15.4	15.1	114.3	51.6
	11 Apr 2010	1900-2000	8.1	4.3	3.7	-57.2	15.8	-17.1	-28.4	51.5	-14.2
B4	8 Oct 2009	1600-1700	2.1	-1.4	2.2	-12.0	4.1	7.0	-13.7	11.1	14.1
	13 Apr 2010	0200-0300	-3.0	3.9	1.1	16.9	-13.6	13.6	6.2	-5.2	7.1

Table 6.6: Percentage of positive polarity of each magnetic component of IMF, Eureka (EUA) and Resolute Bay (RES) for every case in each event type during a specified period

Event Type	Date	Period (UT)	IMF +ve (%)			EUA +ve (%)			RES +ve (%)		
			B _x	B _y	B _z	B _x	B _y	B _z	B _x	B _y	B _z
B1	4 Feb 2011	1800-0000	94.7	38.0	18.6	n/a	n/a	n/a	0.0	21.9	33.5
	5 Apr 2010	0600-1200	90.0	15.8	57.6	90.0	32.7	44.9	90.0	43.2	51.2
B2	8 Oct 2009	1800-1900	100.0	0.0	3.3	0.0	100.0	98.4	0.0	13.1	13.1
	4 Oct 2009	1500-1700	33.9	0.0	44.6	1.7	26.4	77.7	4.1	43.0	41.3
B3	15 Feb 2010	1600-2000	24.1	0.0	0.0	0.0	100.0	48.1	13.7	100.0	85.5
	11 Apr 2010	1900-2000	80.3	34.4	14.8	0.0	34.4	0.0	0.0	60.7	0.0
B4	8 Oct 2009	1600-1700	100.0	0.0	90.2	0.0	39.3	90.2	0.0	14.8	9.8
	13 Apr 2010	0200-0300	0.0	96.7	32.8	85.2	0.0	50.8	57.4	0.0	54.1

Chapter Seven: Summary

This study covers a period of observations from May 2008 until February 2011, where solar activity is starting to increase at the end of the observation period from very low activity at the beginning. Data from two different sources were utilised: a transionospheric link over Alert (data from May 2008 to July 2010), and a HF link from Qaanaaq to Svalbard (data from March 2009 to February 2011). In addition, data from GISTM receivers located at Svalbard (Ny-Ålesund and Longyearbyen) were also used. All selected events were discussed together with the activity indices (SSN) and geomagnetic parameters (K_p , and B_x , B_y , and B_z components of IMF and magnetic field at Eureka and Resolute Bay).

All observed months in 2010 showed higher mean of vertical TEC than in 2008 and 2009, except in February. However, mean VTEC in February 2010 was still higher than in February of the previous year. Monthly pattern can also be seen, where winter months showed lower mean vertical TEC than in summer and equinox months. This is expected as longer daylight is experienced. This is similar to the finding by *Prikryl et al.* [2010] when observing the TEC changes at high latitudes between September 2008 and August 2009.

Higher mean TEC in 2010 consequently caused more patches to be detected in 2010 for all UT hours as compared to the previous years. Low intensity patches of both small and large size were observed at all time during the period of observations, with small patches was more frequently registered. UT dependence can be seen for both small and large patches where ~80 large and ~300 small patches were identified

around 1000 to 2000 UT from June to October in both 2008 and 2009. The number of patches doubled in 2010. Even though it maximised around 1200 to 1800 UT, but a large number of weak patches were distributed all day in 2010. This may be related to the slight increase of solar activity and is in agreement with the finding in *Dandekar* [2002] where the number of patches is found to be dependent on sunspot number. As a note of caution, the number of patches may be overestimated as it is calculated based on individual satellite and added up. Therefore, different satellite(s) over or near the same path could see the same patch. *Krankowski et al.* [2006] concluded that the maximum patch activity occurred in the winter between 0300 and 1100 UT at four Antarctic stations. However, this observation was conducted in 2001, which was the period of high sunspot activity.

Patches were observed more in 2010 in any month, regardless of its size and intensity. The occurrence of both small and large patches of moderate to high intensity were found to be more than twice in February and March 2010 than in the other months of the same year. The difference of occurrence of small patches in each month of the same year was about 1-2% for low intensity patches and 1-10% for moderate-high intensity patches. This difference increased for large patches to 1-4% for low intensity and 1-12% for moderate-high intensity. The large differences were mostly contributed by the occurrence in February and March 2010.

Although patches were recognised all year regardless of the size, the seasonal pattern of weak patches was not clear. This is in agreement with the finding in *Dandekar* [2002] where no systematic seasonal dependence at medium to low sunspot activity can be observed. However, in this study, moderate to high intensity patches of any

size tended to occur more frequently in October and November, for both 2008 and 2009.

The number of patches displayed no significant dependence on geomagnetic latitude. Patches for each month were registered at all geomagnetic latitudes from 81° to 90°, except in February and March 2010 where most patches were observed from 85° to 90° of geomagnetic latitudes.

In terms of scintillation, amplitude scintillations index, S4 were very low in all observed months where at least ~99% of the S4 index were in the range of 0 to and 0.1. Only 0.01% of the S4 were between 0.2 and 0.3. Amplitude scintillations between 0 and 0.2 are usually considered as insignificant and therefore ignored.

Meanwhile, phase scintillations, σ_ϕ were also in the range of 0 to 0.1 rad for at least 93% of the time and can be up to ~100% in certain months. The remaining 7% varied from 0.1 to 0.7 rad, where it normally less than 0.2 rad. Only up to 0.2% of the σ_ϕ were between 0.15 and 0.2 rad. The effect of geomagnetic activity on the phase scintillations during the period of observations was very small. Overall, only 3.2% of all cases where $\sigma_\phi \geq 0.15$ rad occurred during $K_p \geq 5$.

Selected events were chosen and then discussed in detail in order to establish the relation between TEC variations and phase scintillations occurrences. The relationship of TEC fluctuations/increase and phase scintillations was found to be complex. There are few events where phase scintillations occurred simultaneously with the increase of slant TEC, but this was not frequent. A phase scintillation event

may not be necessarily observed at the same time as patches, either at the leading or trailing edge of a TEC increase, or even at the middle of it. Phase scintillations are smaller scale irregularity in comparison with patches. A smaller scale irregularity may cause localised phase scintillations while a strong one may cause patches of irregularities.

Based on the observed events, the irregularities at the high latitude were generally independent of geomagnetic activity. High TEC fluctuations/increase and/or phase scintillations can be observed at any time regardless of the level of the geomagnetic index. This is supported by finding of *Dandekar* [2002] where diurnal, seasonal and solar cycle dependence of polar patch occurrence is predominant and dependence on geomagnetic activity is found to be only secondary.

Similarly, irregularities are also found to be independent on the IMF B_z component. Large TEC fluctuations occurred either while B_z is dominantly southward or northward, or if it fluctuates between polarities. Existence of patches is often associated when B_z is southward, and arcs when B_z is northward [*Carlson*, 1994]. However, both patches and arcs may exist simultaneously, which is indicated when B_z switches polarities often [*Prikryl et al.*, 2010]. In this study, IMF components were found not to have any particular effect on the changes in TEC (and patches formation) and phase scintillations.

MacDougall and Jayachandran [2007] emphasised that the patches only show correlation with the IMF B_z component when there are very large swings of IMF B_z . No large value of IMF B_z was recorded in all event types. Similar observations can

be said regarding the magnetic field effects at Eureka and Resolute Bay. The minimum and maximum values of each component did not show correlation to any event type.

In regards to the HF link, monthly upper decile of Doppler spreads showed more variability from 1-1.5 to 5.5 Hz, except at the lowest and highest frequencies. The increases of the upper decile of Doppler spread were found not to correspond to the increase of the frequency. This is in agreement with the study conducted by *Cannon et al.* [1995] in 1994 where spreads were found to be higher on lower frequencies. However, observations by *Warrington et al.* [2006] from 2003 to 2005 for Kirkenes-Kiruna path revealed that the Doppler spreads tended to increase with increasing frequency. Similarly, *Angling et al.* [1998] concluded that Doppler spreads in 1995 on four high latitude paths were generally increasing with the increase of frequency, except on Isjford-Tuentangen path.

In general (except for the lowest frequency where low to moderate value of upper decile Doppler spreads were observed), high upper decile values normally occurred from around September/October to March. Higher upper decile of Doppler spreads was observed from around 0000 to 1700 UT on 6.95 and 8.01 MHz. The values of hourly upper decile can reach up to 7-8.5 Hz at 6.95 MHz and 7-9.5 Hz at 8.01 MHz. Doppler spreads are best looked on 6.95 and 8.01 MHz since data are insufficient on other frequencies, especially on the lowest and highest frequencies.

Although not for the whole period (e.g. in February on 8.01 MHz), values of upper decile on these two frequencies were most of the times larger in October 2010-

February 2011 than in the previous year, where the differences of hourly upper decile of the same month was between 0.5 to 4.5 Hz (up to 6 Hz for 6.95 MHz in November). The increase in the second year could be due to the increasing solar activity. This is in agreement with *Willink et al.* [1999] where it is suggested that reduced solar activity may result in less variability on the measured channel characteristics compared to increased activity.

Selected events were chosen and then discussed in order to observe the relation between the irregularities observed at Alert and Svalbard via transionospheric link and the HF link between Qaanaaq and Ny-Ålesund, which focused around the HF midpoint. The relation was found to be complex. Large TEC fluctuations/increases and/or phase scintillations observed on satellite(s) close to HF midpoint may correspond to either small or large Doppler spreads. This could be due, for example, to the size of the irregularities and also the area of occurrence. In addition, observations on GPS data over Alert and Svalbard around the HF midpoint did not necessarily demonstrate total similarity since the closest satellite to the HF midpoint observed at each station could be at different sides of the midpoint.

Doppler spreads were also independent of geomagnetic conditions. Higher Doppler spreads can occur during either quiet or disturbed ionospheric conditions. In addition, IMF components did not show any particular effect on the magnitude of the Doppler spreads. Similar observations can be said regarding the magnetic field effects at Eureka and Resolute Bay. The minimum and maximum values of each component did not show correlation to the Doppler spreads in any event type.

This study helps to gain a better understanding of the complex characteristics of the ionosphere. By understanding this, further usage, for example, warning, mitigating and/or predicting the effect of the space weather conditions at this region can be done accordingly. The study should be continued to understand the relation of TEC fluctuations/increase and phase scintillations, and also Doppler spreads at a very high latitude area. Furthermore, the study during the increasing solar activity would be informative in understanding the ever variable high latitude ionosphere.

References

Aarons, J., J.P. Mullen, H.E. Whitney, A.L. Johnson, and E.J. Weber (1981), UHF scintillation activity over polar latitudes, *Geophys.Res.Lett.*, 8(3), 277-280. Copyright 1983 American Geophysical Union.

Aarons, J., and B. Lin (1999), Development of high latitude phase fluctuations during the January 10, April 10-11, and May 15, 1997 magnetic storms, *J.Atmos.Solar Terr.Phys.*, 61(3-4), 309-327.

Angling, M.J., P.S. Cannon, T.C. Davies, T.J. Winink, V. Jodalen, and B. Lundborg (1998), Measurements of Doppler and multipath spread on oblique high-latitude HF paths and their use in characterizing data modem performance, *Radio Sci.*, 33(1), 97-108. Copyright 1998 American Geophysical Union.

Aquino, M., J.F.G. Monico, A.H. Dodson, H. Marques, G. De Franceschi, L. Alfonsi, V. Romano and M. Andreotti (2009), Improving the GNSS positioning stochastic model in the presence of ionospheric scintillation, *Journal of Geodesy*, 83 (10), 953-966, doi: 10.1007/s00190-009-0313-6

Basu, S., E.M. MacKenzie, S. Basu, E. Costa, P.F. Fougere, and H.E. Whitney (1987), 250 MHz/GHz Scintillation Parameters in the Equatorial, Polar, and Auroral Environments, *IEEE Journal on Selected Areas in Communications*, SAC-5(2), 102-115.

Basu, S., E.J. Weber, T.W. Bullett, M.J. Keskinen, E. MacKenzie, P. Doherty, R. Sheehan, H. Kuenzler, P. Ning, and J. Bongiolatti (1998), Characteristics of plasma structuring in the cusp/cleft region at Svalbard, *Radio Sci.*, 33(6), 1885-1899. Copyright 1998 American Geophysical Union.

Breed, A. M., P.L. Dyson, and R.J. Morris (2002), Structure and dynamics of polar patches above Casey, Antarctica, *J. Adv. Space Res.*, 30(11), 2551-2556, doi: 10.1016/S0273-1177(02)80338-6.

Broms, M., B. Lundborg, V. Jodalen, and T. Bergsvik (1997), Doppler effects on high latitude HF paths during an ionospheric disturbance, *Proceedings of the 1997 7th International Conference on HF Radio Systems and Techniques*, July 7-10, 1997.

Buchau, J., B.W. Reinisch, E.J. Weber, and J.G. Moore (1983), Structure and dynamics of the winter polar cap F region, *Radio Sci.*, 18(6), 995-1010. Copyright 1983 American Geophysical Union.

Cannon, P.S., G. Crowley, B.W. Reinisch, and J. Buchau (1992), Digisonde measurements of polar cap convection for northward interplanetary magnetic field, *J. Geophys. Res.*, 97(A11), 16877-16885. Copyright 1992 American Geophysical Union.

Cannon, P.S., N.C. Davies, M.J. Angling, V. Jodalen, K. W. Moreland, and B. Lundborg (1995), Initial results from DAMSON - a system to measure multipath,

Doppler spread and Doppler shift on disturbed HF channels, *IEE Conf. Pub.* 1995, v2-104.

Carlson, H.C., Jr., V.B. Wickwar, E.J. Weber, J. Buchau, J.G. Moore, and W. Whiting (1984), Plasma characteristics of polar cap F-layer arcs, *Geophys. Res. Lett.*, 1(9), 895-898. Copyright 1983 American Geophysical Union.

Carlson, H.C. (1994), The dark polar ionosphere: progress and future challenges, *Radio Sci.*, 29, 157-165. Copyright 1994 American Geophysical Union.

Crowley, G., A.J. Ridley, D. Deist, S. Wing, D.J. Knipp, B.A. Emery, J. Foster, R. Heelis, M. Hairston, and B.W. Reinisch (2000), Transformation of high-latitude ionospheric F region patches into blobs during the March 21, 1990, storm, *J. Geophys. Res.*, 105(A3), 5215-5230, doi: 10.1029/1999JA900357. Copyright 2000 American Geophysical Union.

Cumnock, J.A., L.G. Blomberg, I.I. Alexeev, E.S. Belenkaya, S.Y. Bobrovnikov, and V.V. Kalegaev (2006), Simultaneous polar aurorae and modelled convection patterns in both hemispheres, *Adv. Space Res.*, 38(8), 1685-1693, doi: 10.1016/j.asr.2005.04.105.

Dandekar, B.S. (2002), Solar cycle dependence of polar cap patch activity, *Radio Sci.*, 37(1), 1013, doi: 10.1029/2000RS002562. Copyright 2002 American Geophysical Union.

Dandekar, B.S., and T.W. Bullett (1999), Morphology of polar cap patch activity, *Radio Sci.*, 34(5), 1187-1205. Copyright 1999 American Geophysical Union.

Davies, K. (1990), *Ionospheric Radio*, Peter Peregrinus Ltd., London, UK.

De Franceschi, G., L. Alfonsi, V. Romano, M. Aquino, A. Dodson, C.N. Mitchell, P. Spencer, and A.W. Wernik (2008), Dynamics of high-latitude patches and associated small-scale irregularities during the October and November 2003 storms, *J. Atmos. Solar Terr. Phys.*, 70(6), 879-888, doi: 10.1016/j.jastp.2007.05.018.

Dubey, S., R. Wahi, and A.K. Gwal (2006), Ionospheric effects on GPS positioning, *Advances in Space Research*, 38(11), 2478-2484, doi: 10.1016/j.asr.2005.07.030.

Eastwood, J.P. (2008), The science of space weather, *Phil. Trans. R. Soc. A*, , 4489-4500, doi: 10.1098/rsta.2008.0161.

Friedrich, M., G. Egger, and K.M. Torkar (2006), First results of the polar cap ionosphere based on EISCAT Svalbard and Heiss Island rocket data, *J. Adv. Space Res.*, 37(5), 1097-1101, doi: 10.1016/j.asr.2005.01.033.

Gherm, V.E., N.N. Zernov, and H.J. Strangeways (2005), Propagation model for transionospheric fluctuating paths of propagation: Simulator of the transionospheric channel, *Radio Sci.*, 40, RS1003, doi: 10.1029/2004RS003097. Copyright 2005 American Geophysical Union.

Gherm, V.E., N.N. Zernov, S.M. Radicella, and H.J. Strangeways (2000), Propagation model for signal fluctuations on transionospheric radio links, *Radio Sci.*, 35(5), 1221-1232, doi:10.1029/1999RS002301. Copyright 2000 American Geophysical Union.

GSV GPS Silicon Valley (2007), GSV4004B GPS Ionospheric Scintillation & TEC Monitor (GISTM) User's Manual.

Gwal, A.K., and A. Jain (2011), GPS scintillation studies in the arctic region during the first winter-phase 2008 Indian Arctic Expedition, *Polar Science*, 4(4), 574-587, doi: 10.1016/j.polar.2010.08.001.

Hunsucker, R.D., and J.K. Hargreaves (2003), *The high latitude ionosphere and its effects on radio propagation*, Cambridge University Press, Cambridge, UK.

Jacobsen, B., V. Jodalen, P.S. Cannon, and M.J. Angling (2000), HF radio propagation at high latitudes under quiet and disturbed geomagnetic conditions, *8th International Conference on HF Radio Systems and Techniques*, July 10-13, 2000.

James, H.G., and J.W. MacDougall (1997), Signatures of polar cap patches in ground ionosonde data, *Radio Sci.*, 32(2), 497-513. Copyright 1997 American Geophysical Union.

Jayachandran, P.T., R.B. Langley, J.W. MacDougall, S.C. Mushini, D. Pokhotelov, A.M. Hamza, I.R. Mann, D.K. Milling, Z.C. Kale, R. Chadwick, T. Kelly, D.W. Danskin, and C.S. Carrano (2009), Canadian High Arctic Ionospheric Network (CHAIN), *Radio Sci.*, 44(RS0A03), doi: 10.1029/2008RS004046. Copyright 2009 American Geophysical Union.

Jones, J.B.L., R.D. Bentley, R. Hunter, R.H.A. Iles, G.C. Taylor, and D.J. Thomas (2005), Space weather and commercial airlines, *Advances in Space Research*, 36(12), 2258-2267, doi: 10.1016/j.asr.2004.04.017.

Krankowski, A., I.I. Shagimuratov, L.W. Baran, I.I. Ephishov, and N.J. Tepenitzyna (2006), The occurrence of polar cap patches in TEC fluctuations detected using GPS measurements in southern hemisphere, *J. Adv. Space Res.*, 38(11), 2601-2609, doi: 10.1016/j.asr.2005.12.006.

Li, G., B. Ning, Z. Ren, and L. Hu (2010), Statistics of GPS ionospheric scintillation and irregularities over polar regions at solar minimum, *GPS Solutions*, 14(4), 331-341, doi: 10.1007/s10291-009-0156-x.

MacDougall, J., and P.T. Jayachandran (2007), Polar patches: Auroral zone precipitation effects, *J. Geophys. Res.*, 112, A05312, doi: 10.1029/2006JA011930. Copyright 2007 American Geophysical Union.

McEwen, D.J., W. Guo, J.W. MacDougall, and P.T. Jayachandran (2004), The polar ionosphere, *J. Adv. Space Res.*, 34(9), 2080-2084, doi: 10.1016/j.asr.2004.06.011.

McEwen, D.J., and D.P. Harris (1996), Occurrence patterns of F layer patches over the north magnetic pole, *Radio Sci.*, 31(3), 619-628. Copyright 1996 American Geophysical Union.

Mitchell, C.N., L. Alfonsi, G. De Franceschi, M. Lester, V. Romano, and A.W. Wernik (2005), GPS TEC and scintillation measurements from the polar ionosphere during the October 2003 storm, *Geophys.Res.Lett.*, 32, L12S03, doi: 10.1029/2004GL021644. Copyright 2005 American Geophysical Union.

Momani, M.A., M.A. Mohd Ali, B. Yatim, M. Abdullah, and N. Misran (2008), GPS observations at quasi-conjugate points under disturbed conditions, *Acta Geophysica*, 56(4), 1179-1201, doi: 10.2478/s11600-008-0048-4.

Nava, B., S.M. Radicella, R. Leitinger, and P. Coisson (2007), Use of total electron content data to analyze ionosphere electron density gradients, *J. Adv. Space Res.*, 39(8), 1292-1297, doi: 10.1016/j.asr.2007.01.041.

Ngwira, C.M., L. McKinnell, and P.J. Cilliers (2010), GPS phase scintillation observed over a high-latitude Antarctic station during solar minimum, *J.Atmos.Solar Terr.Phys.*, 72(9-10), 718-725, doi: 10.1016/j.jastp.2010.03.014.

Pedersen, T.R., B.G. Fejer, R.A. Doe, and E.J. Weber (2000), An incoherent scatter radar technique for determining two-dimensional horizontal ionization structure in polar cap F region patches, *J. Geophys. Res.*, 105(A5), 10637-10655, doi:10.1029/1999JA000073. Copyright 2000 American Geophysical Union.

Pi, X., A.J. Mannucci, U.J. Lindqwister, and C.M. Ho (1997), Monitoring of global ionospheric irregularities using the worldwide GPS network, *Geophys.Res.Lett.*, 24(18), 2283-2286. Copyright 1997 American Geophysical Union.

Prikryl, P., P.T. Jayachandran, S.C. Mushini, D. Pokhotelov, J.W. MacDougall, E. Donovan, E. Spanswick, and J. St-Maurice (2010), GPS TEC, scintillation and cycle slips observed at high latitudes during solar minimum, *Annales Geophysicae*, 28(6), 1307-16, doi: 10.5194/angeo-28-1307-2010.

Rogers, N.C., E.M. Warrington, and T.B. Jones (2003), Oblique ionogram features associated with off-great circle HF propagation at high and sub-auroral latitudes, *IEE Proc Microwaves Antennas Propag.*, 150(4), 295-300, doi: 10.1049/ip-map:20030552.

Shagimuratov, I., I. Efishov, A. Krankowski, I. Zakharenkova, and G. Yakimova (2006), Monitoring of phase fluctuations of GPS signals in polar ionosphere, *Antennas and Propagation, 2006. EuCAP 2006. First European Conference on*, pp.1-6, 6-10 Nov. 2006, doi: 10.1109/EUCAP.2006.4584821.

Skone, S.H. (2001), The impact of magnetic storms on GPS receiver performance, *Journal of Geodesy*, 75 (9-10), 457-468, doi: 10.1007/s001900100198.

Skone, S., K. Knudsen, and M. De Jong (2001), Limitations in GPS receiver tracking performance under ionospheric scintillation conditions, *Phys. Chem. Earth (A) Solid Earth Geod.*, 26(6-8), 613-621, doi: 10.1016/S1464-1895(01)00110-7.

Spogli, L., L. Alfonsi, G. De Franceschi, V. Romano, M.H.O. Aquino, and A. Dodson (2009), Climatology of GPS ionospheric scintillations over high and mid-latitude European regions, *Annales Geophysicae*, 27(9), 3429-37, doi: 10.5194/angeo-27-3429-2009.

Stolle, C., S. Schluter, S. Heise, C. Jacobi, N. Jakowski, S. Friedel, D. Kurschner, and H. Luhr (2005), GPS ionospheric imaging of the north polar ionosphere on 30 October 2003, *J. Adv. Space Res.*, 36(11), 2201-2206, doi: 10.1016/j.asr.2005.08.047.

Vilella, C., D. Miralles, and J.L. Pijoan (2008), An Antarctica-to-Spain HF ionospheric radio link: sounding results, *Radio Sci.*, 43, RS4008, doi:10.1029/2007RS003812. Copyright 2008 American Geophysical Union.

Warnant, R., and E. Pottiaux (2000), The increase of the ionospheric activity as measured by GPS, *Earth Planets Space*, 52, 1055-1060.

Warrington, E.M. (1998), Observations of the directional characteristics of ionospherically propagated HF radio channel sounding signals over two high latitude paths, *IEE Proceedings-Microwaves, Antennas and Propagation*, 145(5), 379-85, doi: 10.1049/ip-map:19982068.

Warrington, E.M., A.J. Stocker, and D.R. Siddle (2006), Measurement and modeling of HF channel directional spread characteristics for northerly paths, *Radio Sci.*, 41, RS2006, doi: 10.1029/2005RS003294. Copyright 2006 American Geophysical Union.

Wernik, A.W., L. Alfonsi, and M. Materassi (2007), Scintillation modeling using in situ data, *Radio Sci.*, 42, RS1002, doi: 10.1029/2006RS003512. Copyright 2007 American Geophysical Union.

Willink, T.J., N.C. Davies, M.J. Angling, V. Jodalen, and B. Lundborg (1999), Robust HF data communications at high latitudes, *IEE Proc Microwaves Antennas Propag.*, 146(4), 263-269, doi: 10.1049/ip-map:19990575.

Zaalov, N.Y. (2004), Modelling of off-great circle propagation effects for HF radiowaves received over northerly paths, PhD, University of Leicester.

Zaalov, N.Y., E.M. Warrington, and A.J. Stocker (2005), A ray-tracing model to account for off-great circle HF propagation over northerly paths, *Radio Sci.*, 40, RS4006, doi: 10.1029/2004RS003183. Copyright 2005 American Geophysical Union.

Zou, Y. (2011), Ionospheric scintillations at Guilin detected by GPS ground-based and radio occultation observations, *J. Adv. Space Res.*, 47(6), 945-965, doi: 10.1016/j.asr.2010.11.016.